EXACT SERIES MODEL OF TRANSDUCERS WITH A STACK OF SOLID OR HOLLOW AXIALLY POLARIZED PIEZOELECTRIC AND ELASTIC CYLINDERS

A THESIS

submitted by

NISHAMOL P. A.

(Registration No. 4069)

for the award of the degree

of

DOCTOR OF PHILOSOPHY

NAVAL PHYSICAL AND OCEANOGRAPHIC LABORATORY
(Recognised Research Centre)
COCHIN UNIVERSITY OF SCIENCE AND TECHNOLOGY
KOCHI - 682022

OCTOBER 2018

EXACT SERIES MODEL OF TRANSDUCERS WITH A STACK OF SOLID OR HOLLOW AXIALLY POLARIZED PIEZOELECTRIC AND ELASTIC CYLINDERS

Ph.D. Thesis in the Field of Mathematical Acoustics

Author

Nishamol P. A.
Research Scholar, Registration No: 4069,
Naval Physical and Oceanographic Laboratory,
(Recognised Research Centre of CUSAT)
Defence Research and Development Organisation,
Thrikkakara, Kochi-682 021, India.
E-Mail: p.a.nishamol@gmail.com

Supervising Guide

Dr. D. D. Ebenezer
Scientist 'H', Associate Director,
Naval Physical and Oceanographic Laboratory,
Defence Research and Development Organisation,
Thrikkakara, Kochi-682 021, India.
E-Mail: d.d.ebenezer@gmail.com

October 2018

Dedicated to

My Guide

THESIS CERTIFICATE

This is to certify that the research work presented in this thesis entitled "***EXACT SERIES MODEL OF TRANSDUCERS WITH A STACK OF SOLID OR HOLLOW AXIALLY POLARIZED PIEZOELECTRIC AND ELASTIC CYLINDERS "*** submitted by **Mrs. Nishamol P. A.** to the Cochin University of Science and Technology, Kochi in partial fulfillment of the requirements for the award of the degree of Doctor of Philosophy under the Faculty of Science is a bonafide record of the research work carried out by her under my supervision and guidance at the Naval Physical and Oceanographic Laboratory (Recognized Research Centre of Cochin University of Science and Technology), DRDO, Thrikkakara, Kochi-682021. The contents of this thesis, in full or in parts, has not previously formed the basis for the award of any degree or diploma, associate-ship, fellow-ship, or any other similar title or recognition. The thesis has been modified to incorporate all the relevant corrections and modifications suggested by the audience and recommended by the Doctoral Committee during the pre-synopsis seminar.

Dr. D. D. Ebenezer
Supervising Guide
Scientist 'H',
Associate Director,
Naval Physical and Oceanographic Laboratory,
Kochi - 682021.

Kochi - 682021
01 Oct 2018

DECLARATION

I hereby declare that the work presented in this thesis entitled '***EXACT SERIES MODEL OF TRANSDUCERS WITH A STACK OF SOLID OR HOLLOW AXIALLY POLARIZED PIEZOELECTRIC AND ELASTIC CYLINDERS'*** is based on the original research work carried out by me under the supervision and guidance of **Dr. D. D. Ebenezer**, Scientist 'H', Associate Director, NPOL, Kochi, for the award of the degree of Doctor of Philosophy of Cochin University of Science and Technology. I further declare that the contents of this thesis, in full or in parts have not been submitted to any other University or Institute for the award of any degree or diploma.

NISHAMOL P. A.
Research Scholar,
Naval Physical and Oceanographic Laboratory,
Kochi- 682 021.

Kochi - 682021
01 Oct 2018

CERTIFICATE

This is to certify that this thesis entitled "***EXACT SERIES MODEL OF TRANSDUCERS WITH A STACK OF SOLID OR HOLLOW AXIALLY POLARIZED PIEZOELECTRIC AND ELASTIC CYLINDERS"*** submitted by **Mrs. Nishamol P. A. (Registration No. 4069)** was subjected to plagiarism detection using the software URKUND available at the CUSAT Central Library and found to have significant level of plagiarism of only 3% (Ref. Letter UL/109/2018-19 from The University Librarian dated 28.09.2018).

Dr. D. D. Ebenezer
Supervising Guide
Scientist 'H',
Associate Director,
Naval Physical and Oceanographic Laboratory,
Kochi - 682021.

Kochi - 682021
01 Oct 2018

ACKNOWLEDGEMENTS

First and foremost, I am grateful to my guide Dr. D. D. Ebenezer, Scientist 'H', Naval Physical and Oceanographic Laboratory, Kochi, for his continuous support of my Ph.D. and related research, for his patience, motivation, and immense knowledge. His dedication and keen interest, and above all his overwhelming attitude to help had been solely responsible for completing this work. His timely advice and scientific approach have helped me to a very great extent to accomplish this. I could not have imagined having a better advisor and mentor for my Ph.D.

I owe my deepest gratitude towards my mother-in-law, Smt. Fathima P. S. for her eternal support. Her infallible love and support has always been my strength. Her patience and sacrifice will remain my inspiration throughout my life. Without her help, I would not have been able to complete the thesis.

I express my sincere gratitude to Shri. S. Kedarnath Shenoy, Director, Naval Physical and Oceanographic Laboratory (NPOL), Shri. S. Ananthanarayanan, Former Director, NPOL, Dr. Subash Chandrabose, Group Director, Transducer Group, NPOL for facilitating this research work.

I gratefully acknowledge Dr. R. Ramesh, Division Head, Transducer Science, who consistently extended his research expertise throughout my work and Dr. D. Thomas for his advice and encouragement.

My special regards to my teachers, whose teaching at different stages of education has made it possible for me to see this day.

It is beyond words to express my immense gratitude to my colleagues Smt. Pushpa Abraham, Smt. Laly Joseph, and Shri. M. Ajesh Kumar for their constant support, earnest prayers, cheerful words and encouragement to do the work. Your support and friendship were vital to me. Thank you very much for being with me.

It is also a pleasure to mention my colleagues Dr. R. Rajesh, Shri. Jineesh George, and Shri. R. Krishnakumar for their support and encouragement.

A special word of gratitude to my former Division Head, Dr. K. P. B. Mooasd, for his valuable advice during the course of my study.

Sincere thanks are due to my Doctoral Committee (DC) members Prof. (Dr.) A. Vijayakumar, Dept. of Mathematics, Cochin University of Science and Technology, and Dr. P. V. Hareesh Kumar, Scientist 'G', NPOL, Kochi for their valuable help and fruitful suggestions.

My sincere thanks to Chairman and Members of Department Research Committee (DRC), NPOL for their valuable suggestions.

I thankfully bear in mind the support I received from Dr. A. Unnikrishnan and Dr. K. Sudarsan, my former DC members and former HRD Council Chairmen of NPOL.

I owe a lot to my parents, Shri. P. A. Aboobacker and Smt. Pathukutty T. M., my sister Jisha, and to my brother Ginish, who encouraged and helped me at every stage of my personal and academic life, and longed to see this achievement come true.

I am grateful to my husband, Dhilshad, for his moral support and for relieving me from many house-hold responsibilities during the writing of the thesis. I am also grateful to our children, Riyan and Ishika, for bearing my impatience while organizing the thesis.

All this would not have been possible without the grace of God. I thank him for all the blessings I received.

NISHAMOL P. A.

ABSTRACT

Keywords: analytical model, partial differential equation, boundary conditions, axially polarized hollow piezoelectric cylinder, piezoceramic rings, piezoceramic stacks, solid elastic cylinder, sandwich transducer, Langevin transducer, exact series, complete set of functions, transfer matrix, continuity condition.

The underwater electroacoustic resonant transducer is a very critical part of any active sonar system. An array of transducers is used in ships, submarines, and helicopters to radiate acoustic energy into the ocean; and, in ships, the same array of transducers is often used to receive the echo. The Tonpilz transducer is still the most commonly used acoustic radiator in ships and submarines. Models of transducers are necessary to design and develop transducers and arrays. Attempts to develop a transducer with a large number of components by using a trial and error approach and without using a good model are usually not very successful. A better model of a transducer can be built only by using better models of its components. In the present work, analytical models of an axially polarized hollow piezoelectric ceramic cylinder and a stack of hollow piezoceramic cylinders that is used in a Tonpilz transducer are developed. A classical Langevin transducer, a predecessor of the Tonpilz transducer, is also analyzed.

This thesis begins with an overview of underwater Tonpilz transducers and its components and the methods already existing in literature to analyze them. An axially polarized hollow piezoelectric cylinder (ring) is analyzed first. A method is presented to determine the response of a cylinder with arbitrary length to radius ratio and electrodes only on the top and bottom flat surfaces to electrical and mechanical excitations. The exact, linearized, two-dimensional, axisymmetric, governing partial differential equations of the cylinder are considered. The forms of the expressions for displacement and electric potential are obtained by using the method of separation of variables and they are products of Bessel and sinusoidal functions. Series solutions are formed by using complete sets in the radial and axial directions. All the functions of interest including displacements, electric potential, stresses and electric field displacements are expressed in terms of complete sets of functions. Therefore, it is possible to satisfy arbitrary piecewise continuous boundary conditions on all the surfaces. The coefficients in the series solutions are determined by using the boundary conditions.

An analytical model of a stack of identical, axially polarized, hollow piezoelectric cylinders is also presented in the thesis. A two-dimensional axisymmetric model of the stack is obtained by retaining only the leading terms in the series solution of the piezoceramic hollow cylinder. The model is used to develop a transfer matrix for one ring. The rings are arranged coaxially in the stack and at the flat interface between the two rings, the normal and shear stresses and the axial displacement are continuous. The transfer matrix of each individual ring is used to build a transfer matrix for the stack; and express the normal stress and normal displacement at one flat end of a stack in terms of the same functions at the other flat end and the electric potential. The input electrical admittance of the stack and electrical resonances are computed using the model.

An analytical model of a classical Langevin transducer, a stack of solid elastic and piezoelectric cylinders, is presented next. The axially polarized solid piezoelectric cylinder is sandwiched between two elastic solid cylinders. Exact series solutions to the exact equations of motion are used for both elastic and piezoelectric cylinders. Here, in contrast to the model of the stack, the normal and shear stresses and the normal and radial components of the displacement are continuous at the interfaces between the flat ends of the cylinders. Further, a large number of terms in each series is used to compute the numerical results. Transducers with identical elastic cylinders at the ends as well as those with a lighter head mass and a heavier tail mass are analyzed. The input electrical admittance, critical frequencies, and the components of displacement and stress at various cross-sections are computed.

Accurate models to determine the forced responses of axially polarized hollow piezoelectric ceramic cylinders, stacks of cylinders, and a classical Langevin transducer, all with internal losses, are developed in this thesis. Internal losses are modelled using complex piezoelectric coefficients. The electrical and mechanical functions of interest are computed using MATLAB. It is shown that the method is correct and that accurate numerical results are obtained by comparing the values of the critical frequencies, the frequency-dependent complex input electrical admittance, and the components of stress and displacement computed using the present method with those computed using the finite element software package ATILA [1]. These values are in excellent agreement upto many significant digits even at frequencies that are many times the fundamental resonance frequency. Results are shown for piezoelectric hollow cylinders with various sets of

boundary conditions, stacks of hollow cylinders, and stacks of solid cylinders of various dimensions. The accuracy is more than sufficient for most practical applications.

The analytical models developed here can be used to design components of transducers with specific resonance frequencies or other characteristics. The analytical models can also be used to determine the specific dimensions that result in the desired characteristics. These models can also be used to design other types of transducers with these components.

Table of Contents

LIST OF TABLES ..... **xiv**

LIST OF FIGURES ..... **xv**

NOMENCLATURE ..... **xix**

CHAPTER 1 INTRODUCTION **1**

1.1 INTRODUCTION **1**

1.2 MOTIVATION **2**

1.3 Literature Review **2**

1.3.1 Hollow Piezoceramic Cylinder 3

1.3.2 Stack of Piezoceramic Cylinders 8

1.3.3 Langevin Transducer 9

1.4 Objective and Organization of the Thesis **15**

CHAPTER 2 AXIALLY POLARIZED HOLLOW PIEZOCERAMIC CYLINDER **17**

2.1 Introduction **17**

2.2 Governing Equation **18**

2.3 Primary Variables: Exact series solution **20**

2.4 Secondary Variables **23**

2.5 Boundary Conditions **25**

2.6 Special Cases and Numerical Results **28**

2.6.1 Case 1: Zero axial displacement on flat surfaces 30

2.6.2 Case 2: Zero radial displacement on cylindrical surfaces 38

2.6.3 Case 3: Free flat and cylindrical surfaces 39

2.7 Conclusions **47**

CHAPTER 3 STACK OF AXIALLY POLARIZED HOLLOW PIEZOCERAMIC CYLINDERS **48**

3.1 Introduction **48**

3.2 An Exact Solution **50**

3.3 One Ring **52**

3.4 Stack **57**

3.5 Numerical Results **60**

3.5.1 Case 1 61

3.5.2 Case 2 64
3.5.3 Case 3 66
3.6 Conclusions 68
CHAPTER 4 CLASSICAL LANGEVIN TRANSDUCER 71
4.1 Introduction 71
4.2 Governing Equations 73
4.3 Solutions 75
4.3.1 Piezoelectric Ceramic Cylinder 75
4.3.2 Elastic Cylinder 80
4.4 Boundary and Continuity Conditions 84
4.4.1 Boundary Conditions 85
4.4.2 Continuity Conditions 91
4.5 Matrix Form 96
4.6 Numerical Results and Special Cases 96
4.6.1 Case 1 98
4.6.2 Case 2 100
4.6.3 Case 3 102
4.6.4 Case 4 113
4.7 Conclusions 115
CHAPTER 5 SUMMARY 116
CHAPTER 6 APPLICATIONS AND FUTURE WORK 120
REFERENCES 121
LIST OF PAPERS BASED ON THE THESIS 127
OTHER PUBLICATIONS AND CONFERENCE PROCEEDINGS 128
CURRICULUM VITAE 129

LIST OF TABLES

Table 2.1. Piezoceramic coefficients used to compute required coefficients. 29

Table 2.2. Computed PZT coefficients. 29

Table 2.3. Resonance and anti-resonance frequencies of a (50, 38, 8) cylinder for Case 1. The values of G and R in mS and Ohms, respectively are shown in parenthesis. 32

Table 2.4. Critical frequencies and associated electrical parameters for Case 1. The dimensions of the rings are (12, 6, 3) and (100, 80, 6). 37

Table 2.5. Computed resonances of a (10, 5, 10) cylinder for Case 1. 37

Table 2.6. Resonance and anti-resonance frequencies of a (50, 38, 8) ring for Case 2. 38

Table 2.7. Critical parameters of a (50, 25, 50) cylinder for Case 3. 40

Table 2.8. First two resonance and antiresonance frequencies of hollow piezoelectric cylinders of various dimensions for Case 3. 45

Table 2.9. Critical parameters of (12, 6, 3) and (12, 6, 6) cylinders for Case 3. 46

Table 3.1. G and B in the neighborhood of the first three resonances of the four ring stack of (12, 6, 3) rings. 64

Table 3.2. Critical parameters in the neighborhood of the length mode resonance of various stacks of (50, 38, 8) rings. 66

Table 3.3. Critical parameters in the neighborhood of the first two resonances of various stacks of (100, 80, 6) rings. 67

Table 4.1. Different cases considered for the analysis. 98

Table 4.2. Critical frequencies and G and *B* values of the transducer in Case 1. 99

Table 4.3. Critical frequencies and *G* and *B* values of the transducer in Case 2. 101

Table 4.4. Critical frequencies and G and B values of the transducer in Case 3. 103

Table 4.5. Convergence studies for the transducer in Case 3. 104

Table 4.6. Critical frequencies and the G, B values of the transducer in Case 4. 113

LIST OF FIGURES

Fig. 1.1. 2-D schematic of a Tonpilz transducer. 1

Fig. 1.2. Schematic of a stack of axially polarized hollow piezoceramic cylinders. 8

Fig. 1.3. Schematic of a Langevin transducer. 10

Fig. 2.1. A hollow piezoceramic cylinder of length *L*, inner radius *a*, and outer radius *b*. 18

Fig. 2.2. (a) f-G, (b) f-R, (c) G-B, and (d) R-X in the neighborhood of the second resonance frequency of a (50, 38, 8) cylinder for Case 1 computed using the model. 33

Fig. 2.3. (a) f-G, (b) f-R, (c) G-B, and (d) R-X plots in the neighborhood of the fifth resonance frequency of a (50, 38, 8) cylinder for Case 1 computed using the model. 33

Fig. 2.4. Equivalent circuit of a piezoelectric ceramic transducer with two resonances in the band of interest. 34

Fig. 2.5. The G-B characteristics derived from the equivalent circuit of a piezoelectric ceramic transducer with two resonances in the band of interest [77]. 35

Fig. 2.6. Axial and radial displacement, electric potential, conductance, susceptance, and resistance for Case 1. The dimensions of the cylinder are (50, 38, 8). Solid line: Model and Dots: ATILA. 36

Fig. 2.7. Contour maps of the axial and radial displacements of a (50, 25, 50) mm cylinder at its first resonance 25.20 kHz. (a) Real and (b) imaginary part of the axial displacement; (c) real and (b) imaginary part of the radial displacement; (e) real and (f) imaginary part of the total displacement in wireframe view; and (g) real and (h) imaginary part of the electric potential. 42

Fig. 2.8. Contour maps of the axial and radial displacements of a (50, 25, 50) cylinder at its second resonance 30.86 kHz. (a) Real and (b) imaginary part of the axial displacement; (c) real and (b) imaginary part of the radial displacement; (e) real and (f) imaginary part of the total displacement in wireframe view; and (g) real and (h) imaginary part of the electric potential. 43

Fig. 2.9. Contour maps of the axial and radial displacements of a (50, 25, 50) cylinder at its third resonance 38.30 kHz. (a) Real and (b) imaginary part of the axial

displacement; (c) real and (b) imaginary part of the radial displacement; (e) real and (f) imaginary part of the total displacement in wireframe view; and (g) real and (h) imaginary part of the electric potential. 44
Fig. 2.10. Contour maps of the axial and radial displacements a (50, 25, 50) cylinder at its fourth resonance 113.10 kHz. (a) Real and (b) imaginary part of the axial displacement; (c) real and (b) imaginary part of the radial displacement. 44
Fig. 2.11. Susceptance (B) for Case 3. The dimensions of the cylinder are (a) (50, 25, 50) and (b) (50, 38, 50). Solid line: Model and Dots: ATILA. 45
Fig. 3.1. Schematic of a stack of piezoelectric ceramic rings. 50
Fig. 3.2(a). Conductance in the 100-600 kHz band of a (12, 6, 3) ring. Red Line: Model; Dots: ATILA; and Green Line: 1-D model. 62
Fig. 3.2(b). Conductance in the neighborhood of the first resonance of a (12, 6, 3) ring. Red Line: Model; Dots: ATILA; and Green Line: 1-D model. 62
Fig. 3.3(a). Displacements at the first resonance, 121.6 kHz, of the (12, 6, 3) ring. Red line: Radial and blue line: axial displacements. 63
Fig. 3.3(b). Displacements at the second resonance, 481 kHz, of the (12, 6, 3) ring. Red line: Radial and blue line: axial displacements. 63
Fig. 3.4(a). Conductance of a stack of four (12, 6, 3) rings. Red Line: Present Method, Dots: ATILA, and Green Line: 1-D model. 63
Fig. 3.4(b). Susceptance of a stack of four (12, 6, 3) rings. Red Line: Present Method, Dots: ATILA, and Green Line: 1-D model. 63
Fig. 3.5(a). Susceptance of a stack of two (50, 38, 8) mm rings. Red Line: Model, Dots: ATILA, and Green Line: 1-D model. 65
Fig. 3.5(b). Conductance of a stack of ten (50, 38, 8) mm rings at the length mode resonance of 17.09 kHz. Red Line: Model, Dots: ATILA, and Green Line: 1-D model. 65
Fig. 3.6(a). Conductance in the neighborhood of the second and third resonances of the stack of ten (50, 38, 8) rings. Red Line: Model, Blue Dots: ATILA, and Green Line: 1-D model. 65
Fig. 3.6(b). Susceptance at the first three resonances of a stack of ten (50, 38, 8) rings. Red Line: Model, Blue Dots: ATILA, and Green Line: 1-D model. 65
Fig. 3.7(a). Conductance of a stack of twelve (100, 80, 6) rings. Red Line: Model, Dots: ATILA, and Green Line: 1-D model. 68

Fig. 3.7(b). Susceptance of a 22 ring stack of (100, 80, 6) rings at its length mode resonance. Red Line: Model, Dots: ATILA, and Green Line: 1-D model. 68
Fig. 4.1. Schematic of a Langevin Transducer. 71
Fig. 4.2. (a) Conductance (*G*) and (b) Susceptance (*B*) of the transducer in Case 1. Solid line: Present Method and Dots: ATILA. 99
Fig. 4.3. (a) Real and (b) imaginary parts of the axial displacement, U, on the axis of the transducer at its first resonance frequency, 55.66 kHz. Solid line: Present Method and Dots: ATILA. 100
Fig. 4.4. (a) Conductance (*G*) and (b) Susceptance (*B*) of the Langevin transducer in Case 2. Solid line: ATILA and Dots: Present Method. 101
Fig. 4.5. (a) Real and (b) imaginary parts of the axial displacement U at the centre of the PZT cylinder of the asymmetric transducer in Case 2. Solid line: Present Method and Dots: ATILA. 102
Fig. 4.6 (a) Conductance (*G*) and (b) susceptance (*B*) of the transducer in Case 3. Solid line: ATILA and Dots: Present Method. 103
Fig. 4.7. Case 3. Contributions of terms associated with coefficients shown in the legend to the normal stress component T_{zz} at the top flat surface of the piezoceramic cylinder at 67 kHz. 105
Fig. 4.8. (a) Real and (b) imaginary parts of the normal component of stress T_{zz} along the axis of the transducer at 67 kHz. Solid line: Present method and Dots: ATILA. 106
Fig.4.9. Axial displacement U along the axis of the transducer at its first resonance, 67 kHz. Solid line: Present Method and dots:ATILA. 107
Fig. 4.10. Axial displacement U at the top piezoceramic-elastic cylinder interface at 67 kHz. (a) Real part and (b) Imaginary part. Solid line: Present method and dots: ATILA. 108
Fig. 4.11. Real part of T_{zz} at the piezoceramic - top elastic cylinder interface. Solid line: average T_{zz} of the PZT and elastic cylinders at the interface computed analytically, Dashed line: T_{zz} at the bottom of the top elastic cylinder computed analytically, Circles: T_{zz} at the top of the piezoceramic cylinder computed analytically. Dots: ATILA. 109
Fig. 4.12. Imaginary part of T_{zz} at the piezoceramic - top elastic cylinder interface Solid line: average T_{zz} of the PZT and elastic cylinders at the interface computed

analytically, Dashed line: T_{zz} at the bottom of the top elastic cylinder computed analytically, Circles: T_{zz} at the top of the piezoceramic cylinder computed analytically. Dots: ATILA. 110

Fig. 4.13. T_{zz} at 100 kHz for the transducer in Case 3; (a) at the center of the bottom elastic cylinder, (b) at the center of the top elastic cylinder. Solid line: Present Method and Dots: ATILA. 111

Fig. 4.14. Stress values at the free ends of the elastic cylinders at 100 kHz; (a) T_{zz} at the bottom flat surface of the bottom elastic cylinder, (b) T_{zz} at the top flat surface of the top elastic cylinder. Solid line: Present Method and Dots: ATILA. 111

Fig. 4.15. Stress values at the free ends of the elastic cylinders at the first resonance frequency, 67 kHz; (a) T_{zz} at the bottom flat surface of the bottom elastic cylinder, (b) T_{zz} at the top flat surface of the top elastic cylinder. Solid line: Present Method and Dots: ATILA. 112

Fig. 4.16. (a) Conductance (*G*) and (b) Susceptance (*B*) of the transducer for Case 4 in 1-500 (kHz) frequency band. Solid line: Present Method and Dots: ATILA. 114

Fig. 4.17. (a) Real and (b) imaginary parts of the axial displacement *U* at *r=0* at the top interface of the transducer. Solid line: Present Method and Dots: ATILA. 114

NOMENCLATURE

English Symbols

Symbols	Description
a	Inner radius of the hollow piezoelectric cylinder/ Radius of the solid cylinder
A, A_1, A_2, A_{ms}	Coefficients in the series expansion
b	Outer radius of the hollow piezoelectric cylinder
$B, B_1, B_2, B_{ms}, B_{qs}$	Coefficients in the series expansion/ B is susceptance also
B_{max}	Local maxima of B
B_{min}	Local minima of B
C, C_{ms}, C_{qs}	Coefficients in the series expansion
$C_\nu, \nu = 0,1$	Generalized Bessel functions
$C'_\nu, \nu = 0,1$	Derivative of C_ν
c_{ij}^E	Elastic stiffness coefficients
c_{33}^D	Piezoelectric coefficient
c_s	Wave velocities
cos	Cosine function
D	Coefficient in the series expansion
d_{ij}	Piezoelectric coefficients
D_i	Components of electric displacements
E	Coefficient in the series expansion
e_{ij}	Piezoelectric coefficients
E_i	Components of electric field
$f_s, f_p, f_m, f_n, f_{-1/2s}, f_{1/2s}$	Critical frequencies
F	Coefficient matrix
G	Constant matrix/ conductance
G_{max}	Local maxima of G
I	Current
$J_\nu, \nu = 0,1$	Bessel function of first kind
$J'_\nu, \nu = 0,1$	Derivative of J_ν
$k_{z0}, k_{r0}, k_{rms}, k_{zms}, k_s$	Wave numbers
$k_{rm}, k_{zq}\ k_{zm}, K_{zm}, K_{rms}$	Arbitrary values
L	Length of cylinders
$m, n, q, s, N, M_r, M_q, M_z$	Whole numbers
P, P_{ms}	Coefficients
Q_1, Q_2, Q_{ms}	Coefficients

r	Radial coordinate
R	Resistance
S_{ij}	Strain components
s_{ij}^{E}	Elastic compliance coefficients
sin	Sine function
t	Time
T_{ij}	Stress components
U	Axial displacement
v^{D}, v^{E}	Velocities
W	Radial displacement
X	Matrix of coefficients
Y	Admittance/ Young's modulus
Y_{ν}, $\nu = 0{,}1$	Bessel function of the second kind
z	Axial coordinate
Z	Impedance

Greek Symbols

α_{ms}, β_{ms}, ς_{ms}, η_{ms}	Weighting functions of elastic cylinder
ε_{jj}^{S}, ε_{jj}^{T}	Piezoelectric permittivity coefficients
θ	Angular displacement
ψ_{ms}, χ_{ms}, ϕ_{ms}, γ_{ms} ν_{ms}, ζ_{ms}, υ_{ms}, ϑ_{ms}	Weighting functions of the piezoelectric cylinder
λ, μ	Lame's constants
ρ	Density
ω	Angular frequency
$\emptyset$	Electric potential

CHAPTER 1

INTRODUCTION

1.1 INTRODUCTION

The underwater sonar electroacoustic transducer is a vibrating device which, as a projector, is set into motion by electrical means causing it to alternately compress and rarefy the water it is in contact with and radiate sound. An array of projectors is used in sonar systems to radiate acoustic energy into the ocean. The transducers in these arrays are usually mounted on a plane, cylindrical, or spherical surface and enclosed in an acoustic window in the hull of a ship, a submarine, or a towed body. The design and development of underwater electro acoustic transducer is a challenging task as it comprises a large number of components of different shapes, sizes, and material properties. The task is made more challenging by the need to finalize acoustic and electrical specifications for the transducer in consultation with designers of other sub-systems of the sonar and to deliver a large number of transducers that meet the specifications.

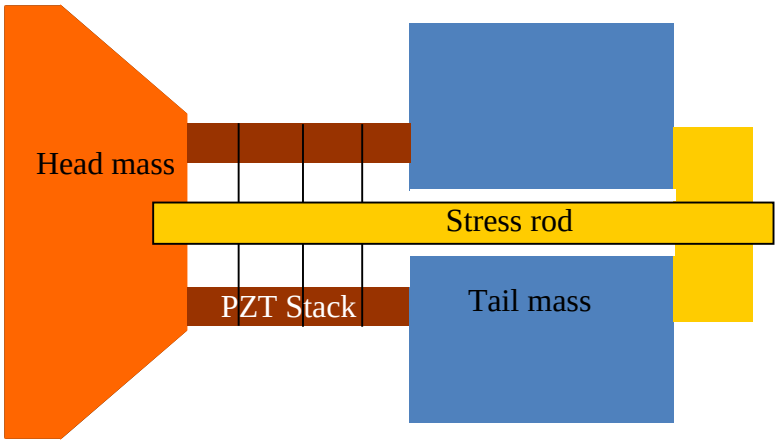

Fig. 1.1. 2-D schematic of a Tonpilz transducer.

The Tonpilz transducer is still the most commonly used acoustic radiator in ships and submarines. It is a sandwich-type transducer that comprises piezoelectric cylinders and other elastic components. A Tonpilz transducer has a stack of axially polarized hollow piezoelectric ceramic cylinders sandwiched between two elastic metal masses: the tail and the head. The tail is often a solid elastic circular cylinder and the head is a frustum of a cone with a circular or square cylinder at it end. Axially polarized hollow piezoelectric ceramic cylinders are bonded to each other using adhesives to form the stack. An elastic circular cylindrical stress rod is used to pre-stress the stack. A schematic of the Tonpilz

transducer is shown in Fig. 1.1. It typically resonates at a few kHz and is often preferred when the acoustic energy is to be radiated in a specific direction of interest.

1.2 MOTIVATION

Models of transducers are necessary to design and develop transducers and arrays. Attempts to develop a transducer with a large number of components by using a trial and error approach and without using a good model are usually not very successful. About 50 years ago, one-dimensional models of components of a Tonpilz transducer were first used to build a model of a Tonpilz transducer [2]. The model yields accurate results near the fundamental resonance frequency of the transducer when its length to diameter ratio is, say, 10. However, Tonpilz transducers seldom have such large ratios. Therefore, a better model is required.

A better model of a transducer can be built only by using better models of its components. The model of the components and the transducer are required not only to design the transducer but also to develop acceptance tests for the components. The transducer is assembled and tested in stages and a good model of the sub-assembly is also required.

The piezoelectric hollow cylinder used in Tonpilz and other sonar transducers has a length to diameter ratio that is less than one and a wall thickness to diameter ratio that is not small enough to use a simple model. It is commonly known as a piezoelectric ring. The primary motivation for this thesis is the need for an accurate model of an axially polarized hollow piezoelectric cylinder (ring) as it is the basic building block of the transducer. Another motivation is the need for a model of a stack of hollow piezoelectric cylinders used in the transducer that is better than the currently available one-dimensional model. A third motivation is the need to develop a method to model a stack of solid piezoelectric and elastic cylinders and show that it is accurate. The Langevin transducer has this type of construction and is the predecessor of the more modern Tonpilz transducer. The models of building blocks developed and validated in this thesis and other models developed later will lead to an accurate model of a Tonpilz transducer that has non-cylindrical components also.

1.3 LITERATURE REVIEW

The analytical models of axially polarized hollow piezoelectric ceramic cylinders and a stack of axially polarized hollow piezoelectric ceramic cylinders are developed in the thesis as components of a Tonpilz transducer. A model of a classical Langevin transducer,

a sandwich transducer, in air is also developed. The existing literature and the evolution of analysis on each of these is extensively reviewed.

1.3.1 Hollow Piezoceramic Cylinder

The piezoceramic stack in the Tonpilz transducer is comprised of several axially polarized piezoelectric ceramic rings. Each ring is a hollow cylinder. The length of the ring is approximately equal to the wall thickness and a small fraction of the inner radius. A model of the ring is of interest.

The piezoelectric ceramics have randomly oriented dipoles due to lack of symmetry in its ionic structure, which can be aligned by an applied electric field. They can generate electric voltage by applying pressure and vice versa. Vibrations of piezoelectric materials are of great importance because of their wide applications in transducers. The mechanical driving unit of the transducers is stacks of piezoceramic materials - slabs, disks, and rings.

The analysis of piezoceramics in an electrical system can be described through equivalent circuit analysis. Mason [3] analyses a long thin piezoelectric ceramic rod with electrodes at the ends. He uses the one-dimensional approximation and presents expressions for the displacement, stress, and current when it is electrically excited. He also presents an equivalent circuit.

Langevin [4] presents a derivation of the voltage or pressure sensitivity of cylindrical ceramic tubes for the axial, radial, and tangential polarizations and three different boundary conditions. He determines the voltage generated when hydrostatic pressure acts on the surface shells of finite length and arbitrary thickness cylinders after neglecting anisotropy. Therefore, his sensitivity calculation is valid only for frequencies well below the lowest resonance frequency of the structure. He uses elastic theory alone to calculate the sensitivity.

Martin [5] analyses longitudinally polarized ceramic tubes including the lateral interaction. The electrodes are placed on the annular surfaces. The longitudinal displacement is expressed in terms of trigonometric functions that depends only on the axial coordinate. A new equivalent circuit is obtained which is similar to that of Mason [3], except that the latter ignores lateral effects.

Paul [6] presents solutions for the exact governing equations of an axially polarized hollow piezoelectric circular cylinder belonging to 6mm crystal class. Each solution is a

product of a sinusoidal and a Bessel function. He derives the frequency equation for hollow cylinders.

Rogers [7] develops a mathematical model for the acoustical and electrical responses of a free-flooded, radially polarized piezoelectric cylinder. The cylinder is driven by a sinusoidal voltage. The solutions are expressed as the sum of a series in terms of its natural modes of a non-piezoceramic material and a particular solution corresponds to piezoelectricity. But this model uses membrane theory to model the cylinder.

Buchanan and Peddieson analyze infinite piezoceramic isotropic [8] and anisotropic [9] cylinders by applying the finite element analysis. The displacement components and the potential are expanded as a trigonometric series using shape functions. In their analysis, the boundary conditions are limited to stress free and short circuit conditions at the surface of the cylinder. They computed the natural frequencies of piezoceramics. They also analyzed the effect of a thin elastic coating on piezoceramic cylinders on natural frequencies.

Kunkel *et al*. [10] calculate the length, radial and edge vibration modes of axially symmetric piezoelectric ceramic disks (PZT-5H) by the finite-element method. The dependence of these vibrational modes on the disk diameter-to-thickness ratio has been studied. An analysis of the complete spectrum of vibrational modes as a function of diameter to thickness ratio is presented that include the identification of radial, edge, length, thickness shear, and thickness extensional vibrations. From this analysis, they optimize the disk diameter to thickness ratio.

Brissaud [11] uses pure modes to analyze thickness polarized piezoelectric disks, rings, and plates. The displacement in a particular direction depends only on the corresponding coordinate. He presents an axisymmetric model but neither the exact governing equations nor all boundary conditions are satisfied by the solutions that contain only two coefficients. The stress and strain components and the electrical impedance are obtained for rectangular and cylindrical geometries. He concludes that, the wave velocities and permittivity depend neither on the geometry nor on the mode that is considered.

Lamberti and Pappalardo [12] develop an approximate 2-D model of an axially polarized hollow piezoceramic cylinder. The displacements are two orthogonal wave functions in the x and z directions expressed in terms of sinusoidal functions and are similar to those proposed by Brissaud. The stress free boundary conditions are satisfied in an integral way by equating the surface integral of stresses to zero. Their model predicts the

lateral mode resonance in addition to the length mode resonance predicted by the one-dimensional model [3].

Iula *et al*. [13] describe an approximated axisymmetric model of solid axially polarized piezoelectric cylinders with electrodes on its flat surfaces. They use two orthogonal wave functions in r and z directions as Brissaud's solutions [11]. The boundary conditions on stress and electric potential are satisfied in an average sense.

Mancic and Radmanovic [14] present an approximated axisymmetric model of a axially polarized hollow piezoceramic cylinder. Their solutions are also based on those presented by Brissaud [11] and satisfy the boundary conditions on stress only in an average sense.

Lin and co-workers analyze thickness polarized piezoelectric ceramic rectangular plates [15,16], axially polarized solid cylinders [17], and hollow cylinders [18, 19,20] by using Brissaud-type solutions [11]. They present equivalent circuits and study the effect of dimensions on the effective piezoelectric coupling coefficient.

Feng *et al*. [21] develop a 2-D equivalent circuit of longitudinally polarized piezoelectric ceramic rings. They ignore shearing stress and torsion. The equivalent circuit includes the effect of both axial and radial vibrations. The continuity between the stresses and external forces is satisfied in an average sense at the mechanical boundaries. The predicted radial and thickness mode resonances are comparable with experimental values when the disk or ring is thin.

In Refs. 11 - 21, shear stress is zero everywhere and the equipotential boundary condition on the flat electroded surfaces is not exactly satisfied.

Ying *et al*. [22] focus on the random vibration analysis of a thick piezoelectric, radially polarized, axisymmetric, hollow cylinder in plane strain conditions. They consider the Gauss electrostatic condition [23] in their analysis. The displacements are expanded as a Legendre series and the electric field boundary conditions are homogenous. The frequency response characteristics and electrical and mechanical coupling properties are explored.

Jalili and Goudarzi [24] use the force-velocity boundary conditions and force - voltage equivalence to derive the equivalent electro mechanical impedance matrix of an axially polarized piezoceramic ring. The determinant of the impedance matrix is minimum in resonant condition and is maximum in anti-resonant condition. They compute the resonance and anti-resonance frequencies and present only two or three vibration modes.

Brissaud [25] presents a 3-D model of piezoelectric materials - rectangular and cylindrical elements - based on an approximate description of the potential and electric field inside the material. The displacements along the three coordinate axes and electrical impedance are calculated for each geometry and the resonance conditions are stated.

Ebenezer and Abraham [26] present a thin shell analytical model of axially polarized piezoelectric ceramic finite cylinders with internal losses. Governing equations for a thin shell are first derived by using the Flugge approximations, assuming that the electric potential has a quadratic variation between the curved surfaces, and using Hamilton's principle extended to piezoelectric media. A finite series solution to the displacement-potential equations is presented. The analytical values of resonance frequencies and the input electrical admittance of thin shells are in excellent agreement with finite element results. In the model, the radial stress is assumed to be zero on the surfaces of the cylinder and therefore inside the thin shell also. However, when the wall thickness of the shell is comparable to the length, it cannot be neglected at the upper branch resonance frequency.

Ebenezer and Abraham [27] use eigenfunctions to analyze radially polarized cylindrical membranes. They show that the infinite series solution converges to the wrong value when the radial displacement is specified to be zero at the ends of the cylinder. Correct solutions, without discontinuities in the radial displacement, are obtained by expressing the displacements as a weighted sum of eigenfunctions plus the low-frequency solution. They use infinite series to analyze radially [28] polarized thin piezoelectric cylindrical shells with internal losses also.

Ebenezer and Ramesh [29] present a few exact solutions, with four coefficients, to the governing equations of solid axially polarized piezoelectric cylinders. They show that only these solutions are required to exactly satisfy certain uniform boundary conditions and approximately satisfy others in an average sense. The uniform potential boundary conditions are exactly satisfied.

Ramesh and Ebenezer [30] present an axisymmetric analytical model of hollow axially polarized piezoelectric ceramic cylinders with radius a few times the wall-thickness and the length. They assume that the axial displacement and electric potential are functions of only the axial coordinate and the radial displacement is a function of the radial coordinate. Using exact solutions to the exact governing equations, the boundary conditions on electric potential are satisfied exactly and the others are satisfied in an average sense. The computed

complex input electrical admittance is in good agreement with Finite Element Analysis results in the neighborhood of both lower and upper branch resonance frequencies.

Ebenezer and Ramesh [31] present a method to analyze solid axially polarized piezoelectric ceramic cylinders with arbitrary length to radius ratio. They use infinite series expressions for the axial and radial displacements and the electric potential. Each term in the series is an exact solution to the exact governing equations. Every function of interest is expressed in terms of a complete set of orthogonal functions in the radial direction. Therefore, it is possible to satisfy arbitrary boundary conditions on the flat surfaces. On the curved surface, zero shear stress, specified uniform radial displacement, and zero normal component of charge density are satisfied exactly and other more general boundary conditions are satisfied in an average sense. The displacement, stress, and potential fields within the cylinder are in good agreement with finite element results obtained using ATILA [1].

Ebenezer *et al*. [32] analyze the forced vibration of solid finite axially polarized piezoelectric ceramic cylinders. They use exact solutions to the exact axisymmetric governing equations. Each term in the solution is a product of a sinusoidal function and a Bessel function. These functions form complete sets in the axial and radial directions respectively. The weights in the solution are determined by using the orthogonal properties of the functions and are used to satisfy specified, arbitrary, axisymmetric boundary conditions on all the surfaces. All numerical results including those for a free cylinder of length and diameter 10 mm are in excellent agreement with those computed using ATILA [1]. The aspect ratio of the cylinder is one and other approximate models do not yield accurate results for this case. The method can be extended to analyze hollow cylinders and composite transducers.

In the present work, the forced response of axially polarized finite piezoelectric hollow cylinders with arbitrary length to radius ratios and electrodes only on the top and bottom flat surfaces is analyzed. Internal losses are included in the model using complex dielectric, elastic and piezoelectric coefficients. Exact, linearized, axisymmetric governing equations for the piezoceramic cylinder and Gauss electrostatic condition in cylindrical coordinates are considered. Exact series solutions are used for displacements and electric potential with each term in the series is a solution to the governing equations. They are products of trigonometric and Bessel functions and are not pure modes as that in Brissaud [11]. The solutions form complete orthogonal [33] sets in both radial and axial directions. Therefore,

the response to arbitrary and piecewise continuous boundary conditions can be determined. The boundary conditions are satisfied in a weighted average sense using orthogonal and complete weights. Each boundary condition is multiplied by an infinite set of complete orthogonal sets and integrated over the surfaces. The model developed is an accurate one to determine the forced responses of piezoceramic cylinders. Numerical values of the complex input electrical admittance and the complex displacement are computed and compared with those obtained using the finite element package ATILA. They are in excellent agreement.

1.3.2 Stack of Piezoceramic Cylinders

The cylinder or ring is a common piezoelectric ceramic element which, when stacked axially and cemented together with a piston head mass and inertial rear tail mass, forms the common Tonpilz piston transducer. In the stack, the rings are normally connected electrically in parallel to decrease the impedance compared to a single element. Each component is coated with electrodes on both its flat ends and then glued together to form the stack. When a voltage is applied across the stack, each component receives the same voltage and individual expansions sum, allowing large expansions for a reasonable voltage. The schematic of a piezoceramic stack is shown in Fig. 1.2.

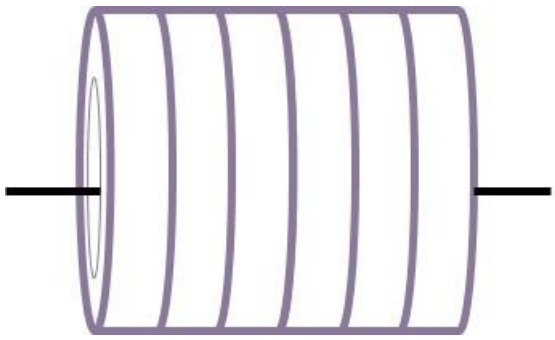

Fig. 1.2. Schematic of a stack of axially polarized hollow piezoceramic cylinders.

Martin [34] develops an equivalent circuit of a stack or segment of identical rings. The circuit for one ring is obtained by using Mason's model [3] or Martin's model [11]. The stress, displacement, and strain distributions at the interfaces are computed. His segmented system is thin to ensure very high radial mode resonance frequency. His analysis does not consider the losses at the joints as reported by Toulis [35].

Sherrit *et al*. [36] uses Martin's model [34] to develop a model of the stack and piezoelectric coefficients are calculated from the model impedance data using inversion techniques.

Nowotny *et al*. [37] present a one-dimensional transfer matrix description of layered piezoelectric structures with two electrodes. The piezoceramic layer is in between the two electrodes and there are non-piezoceramic layers, one on each side of the piezoceramic layer. The continuity of stresses and displacement along the axial direction is applied between the layers and a transfer matrix is derived for the multi-layered structure. Later Nowotny *et al*. [38] extend their work to multi-layered structures with *N* electrodes.

Flint *et al*. [39] presents electrical power predictions of piezoceramic stack actuators with respect to its host structure. They derive the electrical impedance of the stack using a one-dimensional model and the influence of host structure is incorporated as an external impedance term. The electrical behaviour of elements in the stack are analyzed separately. The theory is experimentally validated with a particular host structure.

The models existed in literature are all based on one-dimensional models. An improved two-dimensional analytical model of a stack of axially polarized hollow piezoelectric ceramic cylinders with internal losses is presented in the thesis. A few exact solutions to the exact equations of motion of hollow piezoelectric cylinders and the Gauss electrostatic condition is used. Complex piezoelectric coefficients will be used to model internal losses. Transfer matrix approach is used in the analysis. The model of a single piezoceramic ring is modified to form a transfer matrix for one ring and this is extended to develop a transfer matrix for the stack. The continuity of the axial stress and displacement at the flat interfaces between two rings in the stack is used to develop the transfer matrix. The input electrical admittance and current in the stack are computed by specifying zero stresses at the boundaries.

1.3.3 **Langevin Transducer**

The Langevin transducer is a sandwich transducer that comprises one or more pairs of piezoelectric rings or cylinders sandwiched between two metal masses. It is considered to be a predecessor of the Tonpilz transducer. In the thesis, a classical Langevin transducer is analyzed in vacuum. The transducer comprises an axially polarized solid piezoelectric cylinder sandwiched between two elastic solid cylinders. All three cylinders are of the same diameter. The elastic cylinders and piezoceramic cylinders are reviewed here.

The classical one-dimensional model of longitudinal vibration of long, thin, elastic cylinders, developed during the 18th century, is the simplest model of cylinders [40]. In this model, it is assumed that only the longitudinal stress is non-zero. When the ends of the rod are excited, two waves travel along the axis in opposite directions and cause displacement and normal stresses, along the axis of the rod, that are independent of radial distance from the axis of the rod.

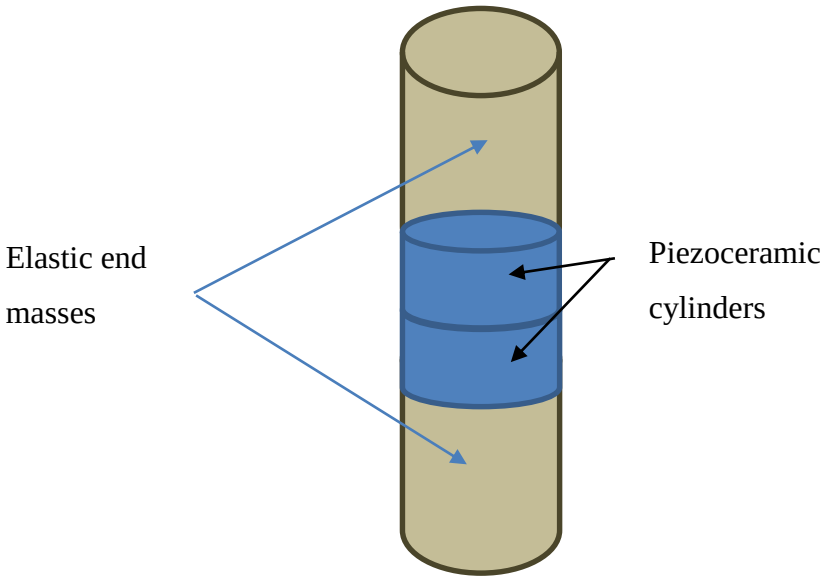

Fig. 1.3. Schematic of a Langevin transducer.

Pochhammer and Chree [41,42] independently present models for free axisymmetric vibration of an infinite circular cylinder, governed by exact one-dimensional equations of elasticity, and with zero normal and shear stress on the curved surface. In this model, the axial and radial displacements are functions of both axial and radial coordinates, travelling along the axis, in opposite directions. When this model is used to analyze transducers, continuity of only average stress and average displacement, along the axis, can be ensured at the plane interface between components.

Filon [43] presents a static model of elastic cylinders in which the solution to the biharmonic [44] equation is expressed as the sum of an infinite series. Each term in the series is an exact solution to the exact equation of elasticity and is a product of sinusoidal function of the axial coordinate and Bessel function of the radial coordinate. The sinusoidal functions form a complete set in the axial direction and are used to satisfy arbitrary boundary conditions on the curved surface. However, on the flat ends, only some boundary conditions are satisfied exactly and the others are satisfied only at some points or in a

weighted average sense. He presented several numerical results after truncating the infinite series.

Purser [45] presents a model of static finite cylinder with specified uniform normal stress and zero shear stress on the surfaces. In the model, dilatation is expressed as the sum of two series. Each term in both the series is an exact solution to the exact governing equation. The sinusoidal functions in the first series form a complete set in the axial direction and Bessel functions in the series form a complete set in the radial direction. The series solutions are used to satisfy all the boundary conditions exactly or with high accuracy in a weighted - average sense.

Aggarwal [46] analyses the free vibration of a finite elastic disk. His solution is a single term and is the product of sinusoidal and Bessel functions. The coefficients in the solution are determined for two cases. In the first case, zero-stress boundary conditions on the flat surfaces are satisfied exactly. Further, on the curved boundary, the zero shear stress is satisfied exactly or the normal stress is satisfied only at the rims. Numerical results are presented to illustrate the magnitude of the normalized residual stresses on the curved boundary. In the second case, zero-stress boundary conditions on the curved surface are satisfied exactly.

Hutchinson extends Purser's approach to analyze free vibration of finite elastic cylinders with certain specified uniform boundary conditions. The axial and radial components of displacement are expressed in terms of complete sets of functions. The infinite series is simply truncated and each term in the solution satisfies the boundary conditions on the axial displacement exactly. Some boundary conditions are satisfied exactly and others are approximately satisfied by orthogonalization on the boundaries. He analyzes cylinders with zero displacements at the boundaries [47] and zero stress at the boundaries [48] and presents several resonance frequencies for each case.

Grinchenko [49] analyzes a hollow static cylinder of finite length with specified non zero normal stress on the outer and inner curved surfaces. The other stresses are zero. All components of stress are expressed as sums of two infinite series. The coefficients in the series are determined without truncating the series.

McMahon [50] analyzes the free axisymmetric vibrations of solid, isotropic, elastic cylinders by using finite-difference method. In this method, the differential equations and boundary condition equations are transformed into finite-difference equations by substituting difference expressions for the derivatives. When the solid has free boundaries,

the set of equations is homogeneous and the roots of the determinant of coefficients yield the resonant frequencies. For forced vibrations, the equations are non-homogeneous and are solved to yield displacements and stresses.

Grinchenko and Meleshko [51] analyze the forced axisymmetric vibration of a circular elastic disk. They use infinite series solutions and the sum of the series is approximated by using the asymptotic values of some coefficients. This model predicts the edge resonances.

Leissa and So [52,53] present a variational Ritz method for 3-D analysis of finite solid circular elastic cylinders. In this method, the components of displacement are expressed as sums of Fourier series in the circumferential coordinate. The coefficients in the series are expressed as weighted sums of complete sets of polynomial functions in the radial and axial directions. They present extensive tables of natural frequencies of cylinders with various length to radius ratios. The flat boundaries are either free or fixed and the curved boundary is free.

Meleshko [54] revisits Filon's static problem and expresses the components of displacements as sums of two infinite series. He considers the axisymmetric distribution of stresses and displacements in a finite elastic cylinder under non-uniform and discontinuous loading on its curved surface. The coefficients in the series are determined by using the boundary conditions. In one approach the series are simply truncated. In another approach, a modification of the method presented by Grinchenko [49] is used to achieve rapid convergence of the series solution for a special case.

Ebenezer *et al*. [55,56] present a method to determine the vibratory response of a solid, finite, elastic cylinder with arbitrary length to radius ratio. In their analysis, the axial and radial displacements are expressed in terms of complete sets of functions. The components of stress are also expressed in terms of complete sets. They present natural frequencies of free cylinders that are in good agreement with those presented by Leissa and So [53] and those obtained using ATILA. They also determine the forced response for various cases of non-uniform loads on the flat and curved surfaces and show that they are in good agreement with those obtained using ATILA. Only a few terms of the infinite series are needed to compute a large number of resonance frequencies as well as determine the response to high frequency loads on the flat and curved surfaces of cylinders.

Sburlati [57] analyzes static cylinders by expressing the Love function in the form of a Fourier-Bessel series. All the Bessel functions are zero on the curved surface and therefore cannot be used to correctly represent any non-zero value there. To overcome this difficulty,

she uses two auxiliary terms that are dependent only on the axial coordinate. She presents analytical solutions for the case of specified radial displacement on the curved surface and zero stress on the flat surfaces. Numerical results are presented to show that all the boundary conditions are satisfied.

In our analysis of elastic cylinders, the method used by Purser [45] to analyze static elastic cylinders and by Hutchinson [47, 48] to study the free vibration of elastic cylinders is extended to determine the forced vibration response of solid, elastic, isotropic cylinders to excitations that are neither symmetric nor antisymmetric about the plane that is midway between the flat ends of the cylinder. The method is based on the use of two infinite series solutions to the governing equations. Each term in the two series is an exact solution to the governing equations. The two series consist of terms that are orthogonal and form complete sets of functions in the axial and radial directions. The components of stress are also expressed in terms of complete sets of functions and hence arbitrary boundary conditions can be satisfied on the boundaries of the cylinder.

Axially polarized solid piezoceramic cylinders are analyzed using exact series solutions to the exact governing equations. The displacements and electric potential are expressed in terms of complete orthogonal functions. They are expressed as the product of Bessel and trigonometric functions where the former form a complete set in the axial direction and the latter form a complete set in the radial direction. Both symmetric and antisymmetric components are used. The response of the cylinder to symmetric excitations is analyzed in Ref. [32]. They used radial displacement that is symmetric about the center of the cylinder. In the present analysis, the antisymmetric radial displacement is also considered.

The design of a sandwich transducer is discussed by Stansfield [58]. Woollett [59] analyzes transducers using circuit network analysis and as a longitudinal vibrator. Underwater sandwich transducers are optimized for their performance using Mason's one-dimensional equivalent circuit model [60,61]. Decarpigny *et al*. [62] present a mixed model of axisymmetric Tonpilz transducers in vacuum. They use a finite element model of the head and a plane wave or rod model of other components. Continuity conditions are used to match the stress and displacement at the interface. Finite element methods are also used to optimize underwater electroacoustic sandwich transducers [63].

Iula *et al*. [64] present an approximate axisymmetric analytical model of the Langevin transducer in vacuum and discuss its improvements over 1-D models. Their model, based

on Brissaud's work [11], is used to predict radial and thickness extensional modes. They use an axisymmetric analytical model of the piezoceramic cylinder in which the displacements represent pure mode propagation and shear stress is zero everywhere in the transducer. Electrical and mechanical boundary conditions are satisfied in an average sense. The piezoceramic cylinder is described as 4 port system with 3 mechanical and one electrical port and the two end masses are described using 3 port systems. The full Langevin model is obtained by loading the mechanical ports with the mechanical impedance of the surrounding media, the continuity of the velocities at the interfaces, and applying an alternating voltage to the electric port. The frequency spectrum, impedance and displacement modes are computed and are experimentally validated.

Iula *et al*. [65] present a finite element analysis of the vibrational behaviour of the Langevin transducer in vacuum and its dependence on the length to diameter ratio of the transducer. Transducers with total length greater than, comparable to, and smaller than the diameter are studied and the frequency spectrum are shown. They conclude that, the product of the radiating area and the displacement is a little higher for transducers with comparable longitudinal and lateral dimensions than it is for transducers with length much greater than diameter.

Lin [66] proposes an approximate analytic method to analyze the coupled vibration of sandwich piezoelectric transducer with a large cross-section in air. He uses pure modes. The coupled resonance frequency equations for the radial resonances of the piezoceramic and elastic cylinders and the longitudinal vibration of the transducer are derived. His analysis ignores the shear and torsional strains and assumes that the mechanical coupling coefficient is a constant. The disadvantage of the model is that it cannot be used to accurately determine the displacement distribution and the stresses and strains in the transducer. Later he uses this pure mode model to study the multimode behaviour of Langevin transducers with large cross section [67].

Arnold [68] uses Mason's equivalent circuit of the transducer to study the effect of stress rod in Langevin transducers. His results show that the stress rod does not have a significant effect on the fundamental resonance. However, certain higher order resonances can be predicted only if the stress rod is included in the model. Besides, the central bolt reduces the electromechanical coupling factor because it represents a load for the transducer.

Liang *et al*. [69] analyze the electrical limit for a typical Langevin ultrasonic transducer. They propose to use piezoceramic rings with different thicknesses at different locations in a transducer to improve the electrical limit and service life. The calculation process of the electric field energy densities of piezoceramic rings by using ANSYS is introduced, and a design example is presented.

Butler [70] designs a sandwich transducer with inactive and active material components to achieve wide band response. A plane wave model is used to compute the transmitting and receiving characteristics and an equivalent circuit is further developed.

In the thesis, a classical Langevin transducer in vacuum is modelled using exact solutions to the exact governing equations for both elastic and piezoelectric cylinders. Two infinite series solutions are used for each component of the Langevin transducer; one represents the symmetric part and other the antisymmetric response. Unlike stacks, here stresses and displacements are in series form. The continuity of the axial, radial displacements, and normal and shear stresses are used at the two flat interfaces of the Langevin transducer. The boundary and continuity conditions are satisfied in the weighted average sense using orthogonal Bessel and trigonometric functions as weights. The resonance frequencies and electrical and mechanical parameters of interest are computed. Langevin transducers with identical and different end masses are analyzed.

1.4 OBJECTIVE AND ORGANIZATION OF THE THESIS

Though there are various finite element models and approximate one-, two-, and three-dimensional analytical models of piezoelectric transducers and their components; there is an increasing demand for exact analytical models to analyze them. The primary objective in this work is to develop an improved two-dimensional axisymmetric analytical model of a piezoelectric hollow cylinder and a model of stacks of cylinders. In this work, only stacks with hollow piezoelectric cylinders of the same inner and outer radii and stacks of solid cylinders with the same diameter that are either elastic or piezoelectric are considered.

In the model of one cylinder [71], the boundary conditions are to be satisfied on flat and curved surfaces, in contrast to one-dimensional models in which the boundary conditions are satisfied at two points. In the model of a stack of cylinders [72] that is used as the driver in a Tonpilz transducer, in addition to the boundary conditions at the flat ends of the stack and the inner and outer surfaces, continuity conditions are satisfied at each interface between flat ends of the cylinders.

Accurate models of axisymmetric stacks of cylinders that are either hollow or solid are presented in the thesis. The flat ends of the cylinders are in contact with each other. All the cylinders have the same outer diameter. If the cylinders are hollow, all of them have the same inner diameter also. Models of a stack of piezoelectric rings used in Tonpilz transducers and Langevin transducers [73] are presented to illustrate the procedure. The numerical results generated by these models are compared with those computed by using ATILA - a finite element package to analyze underwater electroacoustic transducers [1].

The thesis has been structured into six chapters. A brief introduction to transducers and their components is presented and the methods already existing in literature to analyze them are extensively reviewed in **Chapter 1**. **Chapter 2** is devoted to the analysis of electrically or mechanically excited, axially polarized, axisymmetric, hollow piezoelectric ceramic cylinders. Both the electrical and mechanical responses are analyzed with arbitrary boundary conditions. In **Chapter 3**, an analytical model is presented of a stack of identical, axially polarized, hollow piezoelectric ceramic cylinders. The stack is excited by applying a voltage across the electrodes that are on the flat surfaces. A transfer matrix is developed for each cylinder in the stack and is used to build a transfer matrix for the stack. In **Chapter 4**, an analytical model of a classical Langevin transducer with an axially polarized piezoelectric cylinder sandwiched between two elastic cylinders is presented. All the three cylinders in the transducer are solid and of the same diameter. Exact series solutions to the exact equations of motion are used for both elastic and piezoelectric cylinders. In **Chapter 5,** a summary of the thesis and the significance of the contribution are presented. The thesis concludes with **Chapter 6** where the applications and the direction in which future work may progress is presented.

CHAPTER 2
AXIALLY POLARIZED HOLLOW PIEZOCERAMIC CYLINDER

2.1 INTRODUCTION

Axially polarized piezoelectric ceramic hollow cylinders (rings) are often used as electro-mechanical transformers in electro-elastic transducers. They are preferred because it is necessary to pre-stress the piezoceramic and an axisymmetric structure is obtained by passing a rod through the center of the ring to pre-stress it. A stack of axially polarized piezoceramic rings is used in Tonpilz type transducers that are often used for generation of underwater sound. The length of the ring in a stack is approximately equal to the wall thickness and a small fraction of the inner radius.

In this chapter, axially polarized hollow piezoceramic cylinders of arbitrary length to radius ratio are analyzed. A model of the cylinder with arbitrary boundary conditions is presented. A method is presented to determine the forced response of the cylinders with electrodes only on the top and bottom flat surfaces. Electrical and mechanical excitations are considered. Internal losses are included in the model using complex dielectric, elastic, and piezoelectric coefficients. The exact, linearized, two-dimensional, axisymmetric governing equations are obtained in cylindrical coordinates by using two equations of dynamic equilibrium and the Gauss electrostatic condition. The resulting equations are Partial Differential Equations in the axial and radial coordinates. The response of the cylinder to arbitrary and piecewise continuous excitation of the boundary is determined by using complete, orthogonal, infinite sets of functions. All components of the primary variables - displacement and electric potential - are expressed as a sum of series solutions and each term in each series is an exact solution to the exact governing equations of motion and the Gauss condition. The terms in the expressions for components of displacement and electric potential are products of Bessel and sinusoidal functions and are orthogonal to each other. The coefficients in the series solutions are computed by specifying boundary conditions on the surfaces of the cylinder. Complete sets of functions in the radial and axial directions are formed by appropriately choosing the arguments of Bessel and trigonometric functions, respectively. Therefore, arbitrary piecewise boundary conditions can be satisfied on all surfaces of the piezoceramic ring. Numerical values of the complex input electrical

admittance, the complex displacements, and stresses are computed and compared with those computed by the finite element package ATILA. Both are in excellent agreement. The method can be extended to analyze a stack of axially polarized hollow cylinders, sandwich, and Tonpilz transducers.

2.2 GOVERNING EQUATION

Consider a hollow, piezoelectric, isotropic cylinder of finite length *L*, inner radius *a*, and outer radius *b* as shown in Fig. 2.1. Forced vibrations of the cylinder with specified axisymmetric boundary conditions and the response of the cylinder to arbitrary but axisymmetric stresses or displacements specified on the surfaces of the cylinder are analyzed. The origin of the cylindrical local coordinate system is placed at the geometric center of the cylinder.

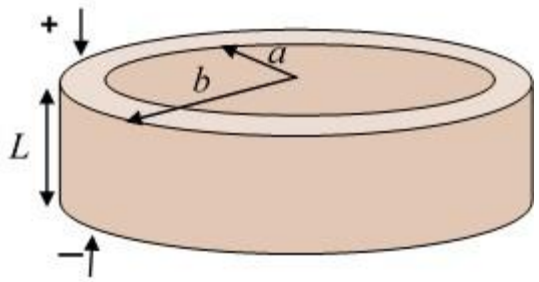

Fig. 2.1. A hollow piezoceramic cylinder of length *L*, inner radius *a*, and outer radius *b*.

The excitation and the boundary conditions, and therefore, the response of the circular cylinder are axisymmetric. The axisymmetric dynamic equilibrium equations [74] expressed in cylindrical coordinates (r, θ, z) as,

$$\frac{\partial T_{zz}}{\partial z} + \frac{\partial T_{rz}}{\partial r} + \frac{1}{r} T_{rz} = -\rho\omega^2 U \tag{2.1a}$$

and

$$\frac{\partial T_{rr}}{\partial r} + \frac{\partial T_{rz}}{\partial z} + \frac{1}{r}(T_{rr} - T_{\theta\theta}) = -\rho\omega^2 W \tag{2.1b}$$

where U and W are the axial and radial components of displacements, respectively. T_{rr}, T_{zz}, and $T_{\theta\theta}$ are the normal components of stress in the radial, axial, and tangential directions, respectively, and T_{rz} is a shear component of stress. Here, ρ is the density and ω is the angular frequency. The excitation and response are time-harmonic, and $e^{j\omega t}$ where t denotes time, is suppressed in all the equations for convenience. The components of strain [74] are expressed as,

$$[S_{rr}, \quad S_{\theta\theta}, \quad S_{zz}, \quad S_{rz}] = \left[\frac{\partial W}{\partial r}, \quad \frac{W}{r}, \quad \frac{\partial U}{\partial z}, \quad \frac{\partial U}{\partial r} + \frac{\partial W}{\partial z}\right] \tag{2.2a}$$

and the components of electric field are expressed as,

$$[E_r, \quad E_z] = -\left[\frac{\partial \emptyset}{\partial r}, \quad \frac{\partial \emptyset}{\partial z}\right] \tag{2.2b}$$

where $\emptyset$ is the electric potential. The constitutive relations for a piezoelectric material of 6mm crystal class [74] are written as,

$$\begin{Bmatrix} T_{rr} \\ T_{\theta\theta} \\ T_{zz} \\ T_{rz} \\ D_r \\ D_z \end{Bmatrix} = \begin{bmatrix} c_{11}^E & c_{12}^E & c_{13}^E & 0 & 0 & -e_{31} \\ c_{12}^E & c_{11}^E & c_{13}^E & 0 & 0 & -e_{31} \\ c_{13}^E & c_{13}^E & c_{33}^E & 0 & 0 & -e_{33} \\ 0 & 0 & 0 & c_{44}^E & -e_{15} & 0 \\ 0 & 0 & 0 & e_{15} & \varepsilon_{11}^S & 0 \\ e_{31} & e_{31} & e_{33} & 0 & 0 & \varepsilon_{33}^S \end{bmatrix} \begin{Bmatrix} S_{rr} \\ S_{\theta\theta} \\ S_{zz} \\ S_{rz} \\ E_r \\ E_z \end{Bmatrix}. \tag{2.3}$$

Here, c_{11}^E, c_{12}^E, c_{13}^E, c_{33}^E, and c_{44}^E are the elastic stiffness coefficients; e_{31}, e_{33}, and e_{15} are the piezoelectric stress coefficients, and ε_{11}^S and ε_{33}^S are dielectric permittivity coefficients of the piezoceramic material. Since there is no net charge enclosed by the piezoceramics, the components of electric displacement, D_r and D_z, must satisfy the Gauss condition [23],

$$\frac{\partial (rD_r)}{r\partial r} + \frac{\partial D_z}{\partial z} = 0. \tag{2.4}$$

Substituting Eqs. (2.2) and (2.3) in Eqs. (2.1) and (2.4) yield

$$\begin{bmatrix} c_{33}^E \frac{\partial^2}{\partial z^2} + c_{44}^E \left\{\frac{\partial^2}{\partial r^2} + \frac{1}{r}\frac{\partial}{\partial r}\right\} + \rho\omega^2 & (c_{13}^E + c_{44}^E)\left\{\frac{\partial^2}{\partial r \partial z} + \frac{1}{r}\frac{\partial}{\partial z}\right\} & e_{33}\frac{\partial^2}{\partial z^2} + e_{15}\left\{\frac{\partial^2}{\partial r^2} + \frac{1}{r}\frac{\partial}{\partial r}\right\} \\ (c_{13}^E + c_{44}^E)\frac{\partial^2}{\partial r \partial z} & c_{11}^E\left\{\frac{\partial^2}{\partial r^2} + \frac{1}{r}\frac{\partial}{\partial r} - \frac{1}{r^2}\right\}\frac{\partial^2}{\partial z^2} + c_{44}^E\frac{\partial^2}{\partial z^2} + \rho\omega^2 & (e_{31} + e_{15})\frac{\partial^2}{\partial r \partial z} \\ e_{33}\frac{\partial^2}{\partial z^2} + e_{15}\left\{\frac{\partial^2}{\partial r^2} + \frac{1}{r}\frac{\partial}{\partial r}\right\} & (e_{31} + e_{15})\left\{\frac{\partial^2}{\partial r\, \partial z} + \frac{1}{r}\frac{\partial}{\partial z}\right\} & -\varepsilon_{33}^S\frac{\partial^2}{\partial z^2} - \varepsilon_{11}^S\left\{\frac{\partial^2}{\partial r^2} + \frac{1}{r}\frac{\partial}{\partial r}\right\} \end{bmatrix}$$

$$\begin{Bmatrix} U \\ W \\ \emptyset \end{Bmatrix} = \begin{Bmatrix} 0 \\ 0 \\ 0 \end{Bmatrix}. \tag{2.5}$$

In this analysis, the piezoceramic cylinder is modeled with internal losses using complex values of the material coefficients. The coefficients are represented as the sum of real and imaginary parts. For example, c_{11}^E is represented as $c_{11}^E = c_{11}^{E\prime} + \mathrm{j}c_{11}^{E\prime\prime}$, where $'$ denotes the real part and $''$ denotes the imaginary part, and $j^2 = -1$. Standard book values are used for the real parts. The imaginary parts of these complex quantities are not arbitrarily chosen. In fact, they must satisfy Holland's conditions [75] separately. Holland

derived the following conditions that are to be satisfied by the imaginary parts of complex coefficients of piezoelectric materials:

$$s_{11}^{E''} \geq 0, s_{33}^{E''} \geq 0, s_{44}^{E''} \geq 0\,, s_{66}^{E''}, \varepsilon_{11}^{T'} \geq 0, \varepsilon_{33}^{T'} \geq 0, s_{11}^{E''} \geq |s_{12}^{E''}|$$

$$s_{11}^{E''} s_{33}^{E''} \geq \left(s_{13}^{E''}\right)^2, s_{11}^{E''} \varepsilon_{33}^{T''} \geq (d_{31}'')^2,\ s_{33}^{E''} \varepsilon_{33}^{T''} \geq (d_{33}'')^2, s_{44}^{E''} \varepsilon_{11}^{T''} \geq (d_{24}'')^2$$

$$s_{33}^{E''}\left(s_{11}^{E''} + s_{12}^{E''}\right) \geq 2\left(s_{13}^{E''}\right)^2,\ \varepsilon_{33}^{T''}\left(s_{11}^{E''} + s_{12}^{E''}\right) \geq 2(d_{31}'')^2. \tag{2.6}$$

where ε_{11}^{T} and ε_{33}^{T} are dielectric permittivity coefficients; s_{11}^{E}, s_{12}^{E}, s_{13}^{E}, s_{33}^{E}, and s_{44}^{E} are elastic compliance coefficients; d_{31}, d_{33}, and d_{15} are piezoelectric coefficients. When some other equivalent set of coefficients is used it is convenient to determine the above coefficients and ensure that the conditions are satisfied.

2.3 PRIMARY VARIABLES: EXACT SERIES SOLUTION

The solution to Eq. (2.5) is obtained by the method of separation of variables [76]. The form of the solution is found to be products of Bessel and trigonometric functions. Bessel functions of both kinds are included here because the cylinder is hollow. Series solutions are used and each term in each series is an exact solution to the exact governing equations of motion. It is easily verified that

$$[U \quad W \quad \emptyset]^T = [U_1 \quad W_1 \quad \emptyset_1]^T + [U_2 \quad W_2 \quad \emptyset_2]^T + [U_3 \quad W_3 \quad \emptyset_3]^T + [U_4 \quad W_4 \quad \emptyset_4]^T \tag{2.7a}$$

is the sum of four independent exact solutions to Eq. (2.5). The four independent solutions are

$$\begin{bmatrix} U_1 \\ W_1 \\ \emptyset_1 \end{bmatrix} = \begin{bmatrix} A\ \sin(k_{z0}z) \\ 0 \\ A\frac{e_{33}}{\varepsilon_{33}^S}\sin(k_{z0}z) \end{bmatrix} + \begin{bmatrix} \sum_{m=1}^{M_r}\sum_{s=1}^{3} A_{ms}C_0(k_{rm}r)\sin(k_{zms}z) \\ \sum_{m=1}^{M_r}\sum_{s=1}^{3} A_{ms}\psi_{ms}C_1(k_{rm}r)\cos(k_{zms}z) \\ \sum_{m=1}^{M_r}\sum_{s=1}^{3} A_{ms}\chi_{ms}C_0(k_{rm}r)\sin(k_{zms}z) \end{bmatrix}, \tag{2.7b}$$

where $k_{z0} = \omega/v^D$, $v^D = \left(\frac{c_{33}^E + {e_{33}}^2/\varepsilon_{33}^S}{\rho}\right)^{1/2} = \left(\frac{c_{33}^D}{\rho}\right)^{1/2}$;

$C_0(k_{rm}r) = J_0(k_{rm}r) + \zeta_m Y_0(k_{rm}r)$, $C_1(k_{rm}r) = J_1(k_{rm}r) + \zeta_m Y_1(k_{rm}r)$ and $J_n(.)$ and $Y_n(.)$, $n = 0, 1$ are the nth order Bessel functions of the first and second kind, respectively;

$$\begin{bmatrix} U_2 \\ W_2 \\ \emptyset_2 \end{bmatrix} = \begin{bmatrix} 0 \\ BJ_1(k_{r0}r) \\ 0 \end{bmatrix} + \begin{bmatrix} \sum_{q=1}^{M_z}\sum_{s=1}^{3} B_{qs}J_0(k_{rqs}r)\sin\left(k_{zq}z\right) \\ \sum_{q=1}^{M_z}\sum_{s=1}^{3} B_{qs}\phi_{qs}J_1(k_{rqs}r)\cos\left(k_{zq}z\right) \\ \sum_{q=1}^{M_z}\sum_{s=1}^{3} B_{qs}\gamma_{qs}J_0(k_{rqs}r)\sin\left(k_{zq}z\right) \end{bmatrix}$$

where $k_{r0} = {\omega}/{v^E}$, $v^E = \left(\frac{c_{11}^E}{\rho}\right)^{1/2}$; (2.7c)

$$\begin{bmatrix} U_3 \\ W_3 \\ \emptyset_3 \end{bmatrix} = \begin{bmatrix} 0 \\ CY_1(k_{r0}r) \\ 0 \end{bmatrix} + \begin{bmatrix} \sum_{q=1}^{M_z}\sum_{s=1}^{3} C_{qs}Y_0(k_{rqs}r)\sin(k_{zq}z) \\ \sum_{q=1}^{M_z}\sum_{s=1}^{3} C_{qs}\phi_{qs}Y_1(k_{rqs}r)\cos(k_{zq}z) \\ \sum_{q=1}^{M_z}\sum_{s=1}^{3} C_{qs}\gamma_{qs}Y_0(k_{rqs}r)\sin(k_{zq}z) \end{bmatrix}, \quad (2.7d)$$

and

$$\begin{bmatrix} U_4 \\ W_4 \\ \emptyset_4 \end{bmatrix} = \begin{bmatrix} 0 \\ 0 \\ Dz + E \end{bmatrix}. \quad (2.7e)$$

Here; A, B, C, D, E, A_{ms}, B_{qs}, and C_{qs}; m= 1, 2, …, M_r and q= 1, 2, …, M_z are the coefficients to be determined. The $Dz + E$ term in Eq. (2.7e) is required in the expression for $\emptyset$ to satisfy the non - zero potential condition even when the displacements are zero under clamped boundary conditions.

The trigonometric and Bessel functions form an orthogonal complete sets of functions in the axial and radial directions, respectively. The orthogonality properties of the sin functions [77] are shown below.

$$\int_{-b/2}^{b/2} \sin(Xz)\sin\left(k_{zq}z\right)dz =$$

$$\begin{cases} 0, \; X = k_{zq}, q \neq n \\ b/2\,, \; X = k_{zn}, q = n \\ 2\left[\frac{X\sin(k_{zn}b/2)\cos\left(\frac{Xb}{2}\right) - k_{zn}\cos(k_{zn}b/2)\sin\left(\frac{Xb}{2}\right)}{k_{zn} - X^2}\right], X \neq k_{zn}, n = 1,2,3,\ldots \end{cases} \quad (2.8)$$

Similarly, for q = 0, 1, 2, 3,…, and $M_z = \infty$, the terms in $\cos\left(k_{zq}z\right)$ are orthogonal, i.e.,

$$\int_{-\frac{L}{2}}^{\frac{L}{2}} \cos(Xz)\cos(k_{zn}z)\,dz =$$

$$\begin{cases} 0, \;\; X = k_{zm} \text{ and } m \neq n \\ L/2, \;\; X = k_{zm} \text{ and } m = n = 1,2,3,\ldots \\ \frac{2(-1)^{n+1}XL^2}{4n^2\pi^2 - X^2L^2}\sin\left(\frac{XL}{2}\right) \; or \; 2\left[\frac{k_{zn}\sin(k_{zn}b/2)\cos\left(\frac{Xb}{2}\right) - X\cos(k_{zn}b/2)\sin\left(\frac{Xb}{2}\right)}{{k_{zn}}^2 - X^2}\right], \;\; X \neq k_{zn} \,\&\, n = 1,2,3,\ldots \end{cases} \quad (2.9)$$

It is noted that the m = 0 term in the cosine series is 1 and is contained in the leading terms of Eqs. (2.7c) and (2.7d).

A set of orthogonal functions is a complete set, when clearly not all the coefficients in the expansion of a nonzero function in terms of these orthogonal functions can be zero; and

thus no nontrivial function can have a trivial expansion. The expansion of a function in terms of the members of a complete set converges and can be integrated and differentiated term by term and the sum of the series cannot differ from the function over any interval of finite length [78]. Hollow cylinders can be analyzed using two different sets of functions [79] that are complete in the axial direction. In the first set, k_{zq} are chosen such that $k_{zq}\,L/2 = q\pi, q = 0, 1, 2, 3, \ldots, M_z$. Here, the series begin with the $q = 0$ term. In the first term, W is zero, but U is a function of k_{z0}. In the second set, k_{zq} are chosen such that $k_{zq}\,L/2 = (2q-1)\,\pi/2\,,\ q = 1, 2, 3, \ldots, M_z$, where M_z is ∞. In both sets, for $M_z = \infty$, $\sin(k_{zq}z)$ and $\cos(k_{zq}z)$ are complete sets of functions that are orthogonal.

Bessel functions in the solutions are chosen such that they form an orthogonal and complete set in the radial direction. The values of k_{rm} and ζ_m are chosen such that they are the solutions to $C_1(k_{rm}a) = 0$ and $C_1(k_{rm}b) = 0$. For m = 0, 1, 2, 3, …, M_r = ∞, the terms in the C_0 series are orthogonal [77] , i.e.,

$$\int_a^b C_0(k_{rm}r)\,C_0(k_{rn}r)rdr = \begin{cases} 0; & m \neq n \\ 0.5(b^2-a^2); & m = n = 0 \\ 0.5r^2\{C_0^2(k_{rn}r) + C_1^2(k_{rn}r)\}|_a^b; & m = n = 1,2,3,\ldots \end{cases} \quad (2.10)$$

The m = 0 term in the C_0 series is 1 and is contained in the leading terms of Eqs. (2.7c) and (2.7d). The terms in the $C_1(k_{rm}r)$series are also orthogonal [77],

$$\int_a^b C_1(k_{rm}r)\,C_1(k_{rn}r)rdr =$$

$$\begin{cases} 0; & m \neq n \\ \left[0.5r^2\{(1-(k_{rn}r)^{-2})C_1^2(k_{rn}r) + C_1'^2(k_{rn}r)\}\right]_a^b; & m = n = 1,2,3,\ldots \end{cases} \quad (2.11)$$

and they form a norm-wise complete set of functions. In Eq. (2.12), the prime denotes derivative with respect to the argument.

The frequency-dependent values of k_{zms} are now determined by substituting Eq. (2.7b) in Eq. (2.5) and equating the determinant of the resulting equation to zero. The characteristic equation is cubic in ${k_{zms}}^2$ and is solved for m = 1, 2, …, M_r to obtain the values of k_{zms}, $s = 1,2,3$. Similarly, by substituting Eq. (2.7c) in Eq. (2.5) and equating the determinant of the resulting equation to zero, the frequency-dependent values of k_{rqs} are determined. Then, substituting Eq. (2.7b) in Eq. (2.5) yields the following expressions:

$$\psi_{ms} = \frac{(\rho\omega^2 - c_{33}^E\,{k_{zms}}^2 - c_{44}^E\,{k_{rm}}^2)(\varepsilon_{33}^S\,{k_{zms}}^2 + \varepsilon_{11}^S\,{k_{rm}}^2) - (e_{33}{k_{zms}}^2 + e_{15}{k_{rm}}^2)^2}{(e_{33}{k_{zms}}^2 + e_{15}{k_{rm}}^2)(e_{31}+e_{15})k_{rm}k_{zms} + (\varepsilon_{33}^S\,{k_{zms}}^2 + \varepsilon_{11}^S\,{k_{rm}}^2)(c_{13}^E + c_{44}^E)k_{rm}k_{zms}} \quad (2.12a)$$

and

$$\chi_{ms} = \frac{(\rho\omega^2 - c_{33}^E k_{zms}^2 - c_{44}^E k_{rm}^2)(e_{31}+e_{15})k_{rm}k_{zms} + (c_{13}^E + c_{44}^E)k_{rm}k_{zms}(e_{33}k_{zms}^2 + e_{15}k_{rm}^2)}{(e_{33}k_{zms}^2 + e_{15}k_{rm}^2)(e_{31}+e_{15})k_{rm}k_{zms} + (\varepsilon_{33}^S k_{zms}^2 + \varepsilon_{11}^S k_{rm}^2)(c_{13}^E + c_{44}^E)k_{rm}k_{zms}}. \quad (2.12b)$$

Similarly, substituting Eq. (2.7c) in Eq. (2.5) yields the following expressions for ϕ_{qs} and γ_{qs}:

$$\phi_{qs} = \frac{(\rho\omega^2 - c_{33}^E k_{zq}^2 - c_{44}^E k_{rqs}^2)(\varepsilon_{33}^S k_{zq}^2 + \varepsilon_{11}^S k_{rqs}^2) - (e_{33}k_{zq}^2 + e_{15}k_{rqs}^2)^2}{(e_{33}k_{zq}^2 + e_{15}k_{rqs}^2)(e_{31}+e_{15})k_{rqs}k_{zq} + (\varepsilon_{33}^S k_{zq}^2 + \varepsilon_{11}^S k_{rqs}^2)(c_{13}^E + c_{44}^E)k_{rqs}k_{zq}} \quad (2.12c)$$

and

$$\gamma_{qs} = \frac{(\rho\omega^2 - c_{33}^E k_{zq}^2 - c_{44}^E k_{rqs}^2)(e_{31}+e_{15})k_{rqs}k_{zq} + (e_{33}k_{zq}^2 + e_{15}k_{rqs}^2)(c_{13}^E + c_{44}^E)k_{rqs}k_{zq}}{(e_{33}k_{zq}^2 + e_{15}k_{rqs}^2)(e_{31}+e_{15})k_{rqs}k_{zq} + (\varepsilon_{33}^S k_{zq}^2 + \varepsilon_{11}^S k_{rqs}^2)(c_{13}^E + c_{44}^E)k_{rqs}k_{zq}}. \quad (2.12d)$$

The axial displacement, U, and the potential, $\emptyset$, are anti-symmetric about the plane midway between the ends of the cylinder in Eqs. (2.7b) - (2.7d) and are expressed in terms of sine functions. The radial displacement, W, in these equations is symmetric because it is expressed in terms of cosine functions. Axial displacement and the potential that are symmetric and radial displacement that is anti-symmetric, can also be modelled. But, here the axisymmetric excitation to the single cylinder induces anti-symmetric axial vibrations only.

2.4 SECONDARY VARIABLES

The secondary variables of interest are the components of stress and electric field displacement. They are determined by using stress-strain and strain-displacement relations in Eqs. (2.3) and (2.2), respectively. The normal components of stress are expressed as

$$T_{rr} = A\left(c_{13}^E + \frac{e_{31}e_{33}}{\varepsilon_{33}^S}\right)k_{z0}\cos(k_{z0}z) + B\left\{c_{11}^E k_{r0} J_0(k_{r0}r) + \frac{c_{12}^E - c_{11}^E}{r} J_1(k_{r0}r)\right\} +$$
$$C\left\{c_{11}^E k_{r0} Y_0(k_{r0}r) + \frac{c_{12}^E - c_{11}^E}{r} Y_1(k_{r0}r)\right\} + De_{31} + \sum_{m=1}^{M_r}\sum_{s=1}^{3} A_{ms}\left\{[c_{11}^E \psi_{ms}k_{rm} + (c_{13}^E + e_{31}\chi_{ms})k_{zms}]C_0(k_{rm}r) + \frac{c_{12}^E - c_{11}^E}{r}\psi_{ms}C_1(k_{rm}r)\right\}\cos(k_{zms}z) +$$
$$\sum_{q=1}^{M_z}\sum_{s=1}^{3} B_{qs}\left\{\left[c_{11}^E \phi_{qs}k_{rqs} + \left(c_{13}^E + e_{31}\gamma_{qs}\right)k_{zq}\right]J_0\left(k_{rqs}r\right) + \frac{c_{12}^E - c_{11}^E}{r}\phi_{qs}J_1\left(k_{rqs}r\right)\right\}\cos\left(k_{zq}z\right) + \sum_{q=1}^{M_z}\sum_{s=1}^{3} C_{qs}\left\{\left[c_{11}^E \phi_{qs}k_{rqs} + \left(c_{13}^E + e_{31}\gamma_{qs}\right)k_{zq}\right]Y_0\left(k_{rqs}r\right) + \frac{c_{12}^E - c_{11}^E}{r}\phi_{qs}Y_1\left(k_{rqs}r\right)\right\}\cos\left(k_{zq}z\right), \quad (2.13)$$

and

$$T_{zz} = A\left(c_{33}^{E} + \frac{{e_{33}}^{2}}{\varepsilon_{33}^{S}}\right)k_{z0}\cos(k_{z0}z) + Bc_{13}^{E}k_{r0}J_0(k_{r0}r) + Cc_{13}^{E}k_{r0}Y_0(k_{r0}r) + De_{33} +$$
$$\sum_{m=1}^{M_r}\sum_{s=1}^{3}A_{ms}\left[c_{13}^{E}\psi_{ms}k_{rm} + (c_{33}^{E} + e_{33}\chi_{ms})k_{zms}\right]C_0(k_{rm}r)\cos(k_{zms}z) +$$
$$\sum_{q=1}^{M_z}\sum_{s=1}^{3}B_{qs}\left[c_{13}^{E}\phi_{qs}k_{rqs} + \left(c_{33}^{E} + e_{33}\gamma_{qs}\right)k_{zq}\right]J_0\left(k_{rqs}r\right)\cos\left(k_{zq}z\right) +$$
$$\sum_{q=1}^{M_z}\sum_{s=1}^{3}C_{qs}\left[c_{13}^{E}\phi_{qs}k_{rqs} + \left(c_{33}^{E} + e_{33}\gamma_{qs}\right)k_{zq}\right]Y_0\left(k_{rqs}r\right)\cos\left(k_{zq}z\right). \quad (2.14)$$

The shear stress is expressed as

$$T_{rz} = -\sum_{m=1}^{M_r}\sum_{s=1}^{3}A_{ms}\left[c_{44}^{E}\left(k_{rm} + \psi_{ms}k_{zms}\right) + e_{15}\chi_{ms}k_{rm}\right]C_1(k_{rm}r)\sin(k_{zms}z) -$$
$$\sum_{m=1}^{M_q}\sum_{s=1}^{3}B_{qs}\left[c_{44}^{E}\left(k_{rqs} + \phi_{qs}k_{zq}\right) + e_{15}\chi_{qs}k_{rqs}\right]J_1\left(k_{rqs}r\right)\sin\left(k_{zq}z\right)$$
$$-\sum_{m=1}^{M_q}\sum_{s=1}^{3}C_{qs}\left[c_{44}^{E}\left(k_{rqs} + \phi_{qs}k_{zq}\right) + e_{15}\chi_{qs}k_{rqs}\right]Y_1\left(k_{rqs}r\right)\sin\left(k_{zq}z\right). \quad (2.15)$$

The components of electric field displacement are expressed as,

$$D_r = \sum_{m=1}^{M_r}\sum_{s=1}^{3}A_{ms}\left[-e_{15}\left(k_{rm} + \psi_{ms}k_{zms}\right) + \varepsilon_{11}^{S}\chi_{ms}k_{rm}\right]C_1(k_{rm}r)\sin(k_{zms}z) +$$
$$\sum_{m=1}^{M_q}\sum_{s=1}^{3}B_{qs}\left[-e_{15}\left(k_{rqs} + \phi_{qs}k_{zq}\right) + \varepsilon_{11}^{S}\chi_{qs}k_{rqs}\right]J_1\left(k_{rqs}r\right)\sin\left(k_{zq}z\right) +$$
$$\sum_{m=1}^{M_q}\sum_{s=1}^{3}C_{qs}\left[-e_{15}\left(k_{rqs} + \phi_{qs}k_{zq}\right) + \varepsilon_{11}^{S}\chi_{qs}k_{rqs}\right]Y_1\left(k_{rqs}r\right)\sin\left(k_{zq}z\right) \quad (2.16)$$

and

$$D_z = Be_{31}k_{r0}J_0(k_{r0}r) + Ce_{31}k_{r0}Y_0(k_{r0}r) - D\varepsilon_{33}^{S} + \sum_{m=1}^{M_r}\sum_{s=1}^{3}A_{ms}\left[(e_{33} -\right.$$
$$\left.\varepsilon_{33}^{S}\chi_{ms}\right)k_{zms} + e_{31}\psi_{ms}k_{rm}]C_0(k_{rm}r)\cos(k_{zms}z) + \sum_{q=1}^{M_z}\sum_{s=1}^{3}B_{qs}\left[\left(e_{33} -\right.\right.$$
$$\left.\left.\varepsilon_{33}^{S}\gamma_{qs}\right)k_{zq} + e_{31}\phi_{qs}k_{rqs}\right]J_0\left(k_{rqs}r\right)\cos\left(k_{zq}z\right) + \sum_{q=1}^{M_z}\sum_{s=1}^{3}C_{qs}\left[\left(e_{33} - \varepsilon_{33}^{S}\gamma_{qs}\right)k_{zq} +\right.$$
$$\left.e_{31}\phi_{qs}k_{rqs}\right]Y_0\left(k_{rqs}r\right)\cos\left(k_{zq}z\right). \quad (2.17)$$

Finally, the current is expressed as

$$I = -\int_a^b j\omega D_z 2\pi r dr = -2\pi j\omega Be_{31}[bJ_1(k_{r0}b) - aJ_1(k_{r0}a)] -$$
$$2\pi j\omega Ce_{31}[bY_1(k_{r0}b) - aY_1(k_{r0}a)] + 2\pi j\omega D\varepsilon_{33}^{S}(b^2 - a^2). \quad (2.18a)$$

and the admittance is

$$Y = G + jB = \frac{I}{\emptyset_0}, \quad (2.18b)$$

where G is the real part of admittance, the conductance, and B is the imaginary part of admittance, the susceptance.

All the components of displacement and stress are expressed in terms of functions that are complete in both axial and radial directions. In the radial direction U, T_{rr}, T_{zz}, and D_z are expressed as a weighted sum of $C_0(k_{rm}r),\ m = 0, 1, 2, \ldots, \infty$ and other terms. Further, $C_1(k_{rm}r),\ m = 1, 2, \ldots, \infty$ are all zero at $r = a$ and b, and form a complete set of functions: W, T_{rr}, and D_r are expressed as a weighted sum of these functions and other terms. Similarly, in the axial direction, the components of displacements and stresses are expressed as the sum of either complete sets of sin or cos functions or other terms. In general, the components of displacement and stress are expressed in terms of complete sets of functions. It therefore follows that the response of the hollow piezoceramic cylinder can be determined for arbitrary excitations.

2.5 BOUNDARY CONDITIONS

On the flat, electroded surfaces, U and T_{zz} are expressed in terms of $C_0(k_{rm}r)$, m=0,1,2,...; and W and T_{rz} are expressed in terms of $C_1(k_{rm}r)$, m=1,2,.... On the curved, unelectroded surfaces, U and T_{rz} are expressed in terms of $\sin(k_{zq}z)$, q=1,2,...,M_z; and W and T_{rr} are expressed in terms of $\cos(k_{zq}z)$,q = 0,1,2,... M_z.

All fields on the flat and curved surfaces are denoted using a flat over-bar and a curved frown, respectively. For example,

$T_{zz} = \bar{T}_{zz}$ and $T_{rz} = \bar{T}_{rz}$ on $a \le r \le b, z = \pm L/2,$ (2.19a, 2.19b)

$T_{rr} = \hat{T}_{rra}$ and $T_{rz} = \hat{T}_{rza}$ on $r = a, |z| \le L/2,$ (2.20a, 2.20b)

and

$T_{rr} = \hat{T}_{rrb}$ and $T_{rz} = \hat{T}_{rzb}$ on $r = b, |z| \le L/2.$ (2.21a, 2.21b)

A similar notation is used for the components of displacements U and W. The boundary conditions are satisfied in a weighted-average sense by using complete orthogonal weights. Both sides of each boundary condition is multiplied with the weights and are integrated. As a large number of weights are used to satisfy the conditions in an average sense, the conditions are nearly satisfied at every point on the surface. The complete orthogonal Bessel functions are the weights on the boundary conditions specified on the flat surfaces and trigonometric functions are on those specified on the curved surfaces.

The boundary condition on T_{zz} in Eq. (2.19a) is satisfied in by using the orthogonal property of $C_0(k_{rn}a)$ in Eq. (2.10). T_{zz}, in Eq. (2.14), is multiplied both sides by $rC_0(k_{rn}r)$ and integrating over r from a to b yields

$$A\left(c_{33}^{E}+\frac{{e_{33}}^{2}}{\varepsilon_{33}^{S}}\right)k_{z0}\cos(k_{z0}L/2)\frac{b^{2}-a^{2}}{2}+Bc_{13}^{E}\{bJ_{1}(k_{r0}b)-aJ_{1}(k_{r0}a)\}+$$
$$Cc_{13}^{E}\{bY_{1}(k_{r0}b)-aY_{1}(k_{r0}a)\}+De_{33}\frac{b^{2}-a^{2}}{2}+\sum_{q=1}^{M_z}\sum_{s=1}^{3}B_{qs}\left\{c_{13}^{E}\phi_{qs}k_{rqs}+\left(c_{33}^{E}+\right.\right.$$
$$\left.\left.e_{33}\gamma_{qs}\right)k_{zq}\right\}\cos\left(k_{zq}{}^{L}/_{2}\right)\left\{bJ_{1}\left(k_{rqs}b\right)-aJ_{1}\left(k_{rqs}a\right)\right\}/k_{rqs}+$$
$$\sum_{q=1}^{M_z}\sum_{s=1}^{3}C_{qs}\left\{c_{13}^{E}\phi_{qs}k_{rqs}+\left(c_{33}^{E}+\right.\right.$$
$$\left.\left.e_{33}\gamma_{qs}\right)k_{zq}\right\}\cos\left(k_{zq}{}^{L}/_{2}\right)\left\{bY_{1}\left(k_{rqs}b\right)-aY_{1}\left(k_{rqs}a\right)\right\}/k_{rqs}=\int_{a}^{b}\bar{T}_{zz}rdr\ \text{ for } n=0, \tag{2.22a}$$

and

$$Bc_{13}^{E}{k_{r0}}^{2}\{bC_{0}(k_{rn}b)J_{1}(k_{r0}b)-aC_{0}(k_{rn}a)J_{1}(k_{r0}a)\}/({k_{r0}}^{2}-{k_{rn}}^{2})+$$
$$Cc_{13}^{E}{k_{r0}}^{2}\{bC_{0}(k_{rn}b)Y_{1}(k_{r0}b)-aC_{0}(k_{rn}a)Y_{1}(k_{r0}a)\}/({k_{r0}}^{2}-{k_{rn}}^{2})+$$
$$\sum_{s=1}^{3}A_{ns}\{c_{13}^{E}\psi_{ns}k_{rn}+$$
$$(c_{33}^{E}\ e_{33}\chi_{ns})k_{zns}\}\,C_{0}(k_{rm}a)\cos\left(k_{zns}{}^{L}/_{2}\right)\left\{b^{2}{C_{0}}^{2}(k_{rn}b)-a^{2}{C_{0}}^{2}(k_{rn}a)\right\}/2+$$
$$\sum_{q=1}^{M_z}\sum_{s=1}^{3}B_{qs}\left\{c_{13}^{E}\phi_{qs}k_{rqs}+\left(c_{33}^{E}+\right.\right.$$
$$\left.\left.e_{33}\gamma_{qs}\right)k_{zq}\cos\left(k_{zq}{}^{L}/_{2}\right)k_{rqs}\right\}\left\{bC_{0}(k_{rn}b)J_{1}\left(k_{rqs}b\right)-aC_{0}(k_{rn}a)J_{1}\left(k_{rqs}a\right)\right\}/({k_{rqs}}^{2}-$$
$${k_{rn}}^{2})+\sum_{q=1}^{M_z}\sum_{s=1}^{3}C_{qs}\left\{c_{13}^{E}\phi_{qs}k_{rqs}+\left(c_{33}^{E}+\right.\right.$$
$$\left.\left.e_{33}\gamma_{qs}\right)k_{zq}\cos\left(k_{zq}{}^{L}/_{2}\right)k_{rqs}\right\}\left\{bC_{0}(k_{rn}b)Y_{1}\left(k_{rqs}b\right)-aC_{0}(k_{rn}a)Y_{1}\left(k_{rqs}a\right)\right\}/({k_{rqs}}^{2}-$$
$${k_{rn}}^{2})=\int_{a}^{b}\bar{T}_{zz}rC_{0}(k_{rn}r)dr;\ \text{ for }\ n=1,2,3,\dots,M_{r}. \tag{2.22b}$$

The boundary condition on U on the flat surfaces is also satisfied in the same way. Multiplying both sides of U by $rC_0(k_{rn}a)$ and integrating over r yields:

$$A\sin(k_{z0}L/2)\ =\int_{a}^{b}\bar{U}rdr,\ \text{for}\ \ n=0, \tag{2.23a}$$

and

$$\sum_{s=1}^{3}A_{ns}\sin(k_{zns}L/2)\{b^{2}C_{0}^{2}(k_{rn}b)-a^{2}C_{0}^{2}(k_{rn}a)\}/2=\int_{a}^{b}\bar{U}rC_{0}(k_{rn}r)dr,\text{for}\ n=1,2,\dots,M_{r}. \tag{2.23b}$$

The boundary condition on T_{rz} in Eq. (2.19b) is satisfied by using the orthogonal property of $C_1(k_{rn}r)$ in Eq. (2.11). Multiplying both sides of Eq. (2.19b) by $rC_1(k_{rn}r)$ and integrating over r yields

$\sum_{s=1}^{3} A_{ns} \sin\left(k_{zns} {}^{L}/_{2}\right) \{c_{44}^{E}(k_{rn} + \psi_{rn} k_{zns}) + e_{15}\chi_{ns} k_{rn}\}\{b^2 C_0^2(k_{rn} b) - a^2 C_0^2(k_{rn} a)\}/2 =$

$\int_a^b \bar{T}_{rz} r C_1(k_{rn} r) dr$, for $n = 1,2, \ldots, M_r$. (2.24)

The orthogonal property of $\cos\left(k_{zq} z\right)$ in Eq. (2.9) is used to satisfy the boundary condition on $\hat{T}_{rra}$ in Eq. (2.20a). Multiplying both sides of the above equation by $\cos\left(k_{zq} z\right)$ and integrating over z yields

$A\left(c_{13}^{E} + \frac{e_{31} e_{33}}{\varepsilon_{33}^{S}}\right) 2 \sin(k_{z0} L/2) + BL\left\{c_{11}^{E} k_{r0} J_0(k_{r0} a) + \frac{c_{12}^{E} - c_{11}^{E}}{a} J_1(k_{r0} a)\right\} +$

$CL\left\{c_{11}^{E} k_{r0} Y_0(k_{r0} a) + \frac{c_{12}^{E} - c_{11}^{E}}{a} Y_1(k_{r0} a)\right\} + DLe_{31} + \sum_{m=1}^{M_r} \sum_{s=1}^{3} 2\, A_{ms} \left\{c_{11}^{E} \psi_{ms} \frac{k_{rm}}{k_{zms}} + \right.$

$\left. c_{13}^{E} + e_{31}\chi_{ms}\right\} C_0(k_{rm} a) \sin\left(k_{zms} {}^{L}/_{2}\right) = \int_{-L/2}^{L/2} \hat{T}_{rra} dz$ when $q = 0$, (2.25a)

and

$A\left(c_{13}^{E} + \frac{e_{31} e_{33}}{\varepsilon_{33}^{S}}\right) 2 \frac{(-1)^{n+1} k_{z0}{}^2 L^2}{4n^2\pi^2 - k_{z0}{}^2 L^2} \sin(k_{z0} L/2) + \sum_{m=1}^{M_r} \sum_{s=1}^{3} A_{ms} \{c_{11}^{E} \psi_{ms} k_{rm} + (c_{13}^{E} +$

$e_{31}\chi_{ms}) k_{zms}\} C_0(k_{rm} a) 2 \frac{(-1)^{n+1} k_{zms} L^2}{4n^2\pi^2 - k_{zms}{}^2 L^2} \sin\left(k_{zms} {}^{L}/_{2}\right) + \sum_{s=1}^{3} B_{qs} \left\{\left[c_{11}^{E} \phi_{qs} k_{rqs} + \left(c_{13}^{E} + \right.\right.\right.$

$\left.\left.\left. e_{31}\gamma_{qs}\right) k_{zq}\right] J_0\left(k_{rqs} a\right) + \frac{c_{12}^{E} - c_{11}^{E}}{a} \phi_{qs} J_1\left(k_{rqs} a\right)\right\} \frac{L}{2} + \sum_{s=1}^{3} C_{qs} \left\{\left[c_{11}^{E} \phi_{qs} k_{rqs} + \left(c_{13}^{E} + \right.\right.\right.$

$\left.\left.\left. e_{31}\gamma_{qs}\right) k_{zq}\right] Y_0\left(k_{rqs} a\right) + \frac{c_{12}^{E} - c_{11}^{E}}{a} \phi_{qs} Y_1\left(k_{rqs} a\right)\right\} \frac{L}{2} = \int_{-L/2}^{L/2} \hat{T}_{rra} \cos\left(k_{zq} z\right) dz;$

for $q = 1,2, \ldots, M_z$. (2.25b)

Similarly, the boundary condition on $\hat{T}_{rza}$ is satisfied by using the orthogonal property of $\sin\left(k_{zq} z\right)$ in Eq. (2.8). Multiplying both sides of Eq. (2.20b) by $\sin\left(k_{zq} z\right)$ and integrating over z yields

$-\sum_{s=1}^{3} B_{ns} \{[c_{44}^{E}(k_{rns} + \phi_{ns} k_{zn}) + e_{15}\gamma_{ns} k_{rns}] J_1(k_{rns} a)\} \frac{L}{2} - \sum_{s=1}^{3} C_{ns} \{[c_{44}^{E}(k_{rns} +$

$\phi_{ns} k_{zn}) + e_{15}\gamma_{ns} k_{rns}] Y_1(k_{rns} a)\} \frac{L}{2} = \int_{-L/2}^{L/2} \hat{T}_{rza} \sin\left(k_{zq} z\right) dz$ for $q = 1,2, \ldots, M_z$.

(2.26)

The boundary conditions in Eq. (2.21) are obtained in a similar way by replacing a in Eqs. (2.25) and (2.26) by b. The conditions on electric potential,$\emptyset$, on the flat surfaces are satisfied by using the orthogonality properties of $C_0(k_{rn} a)$. Multiplying $\emptyset$ by $r C_0(k_{rn} a)$ and integrating over r yields;

$-A \frac{e_{33}}{\varepsilon_{33}^{S}} \sin\left(k_{z0} \frac{L}{2}\right) - D \frac{L}{2} + E = \int_a^b \bar{\emptyset} r dr$, when $n = 0$ and at $z = \frac{-L}{2}$, (2.27a)

$$A\frac{e_{33}}{\varepsilon_{33}^{S}}\sin\left(k_{z0}\frac{L}{2}\right)+D\frac{L}{2}+E=\int_a^b\bar{\emptyset}rdr,\ \text{when}\ \ n=0\ \text{and at}\ z=\frac{L}{2}, \tag{2.27b}$$

and

$$\sum_{s=1}^{3}A_{ns}\chi_{ns}\sin\left(k_{zns}\,{}^{L}/_{2}\right)\{b^2C_0^2(k_{rn}b)-a^2C_0^2(k_{rn}a)\}/2=\int_a^b\bar{\emptyset}rC_0(k_{rn}r)dr,$$

$$\text{for}\ n=1,2,3,\ldots,M_r\ \text{and at}\ z=\pm\frac{L}{2}. \tag{2.28}$$

The equations thus obtained through the boundary conditions by using the orthogonal properties of Bessel and trigonometric functions are combined, truncated, and expressed in matrix form as

$$[F]\{X\}=\{G\} \tag{2.29a}$$

where

$$\{X\}^T=[A,B,C,D,E,A_{11},A_{12},A_{13},A_{21},A_{22},A_{23},\ldots,A_{M_r1},A_{M_r2},A_{M_r3},B_{11},B_{12},B_{13},\ldots,$$

$$B_{M_z1},B_{M_z2},B_{M_z3},\ldots,C_{11},C_{12},C_{13},\ldots,C_{M_z1},C_{M_z2},C_{M_z3}\,]. \tag{2.29b}$$

$[F]$ is a square matrix of size $[3M_r+6M_z+5, 3M_r+6M_z+5]$, and M_r and M_z are now finite. The elements of the column matrix $\{G\}$ are zeros when there is no displacement or stress on the boundaries. In some cases, the normal displacement is specified and in some cases normal stresses are specified and Eq. (2.29) is assembled using the appropriate equations.

2.6 SPECIAL CASES AND NUMERICAL RESULTS

The forced vibration responses of hollow piezoelectric cylinders to a few excitations are presented. Three special cases are considered in the analysis to illustrate the method. Numerical results are presented for axially polarized piezoceramic hollow cylinders of various length to diameter ratios to illustrate the method. The dimensions, in mm, of the cylinder are specified by the triplet (Outer diameter, Inner diameter, Length). PZT-4 material with internal losses represented by complex coefficients is used in all the cases. A set of piezoelectric coefficients used in the analysis is presented in Table 2.1. The real parts of these coefficients are from Ref. [80]. The imaginary parts satisfy the conditions mentioned by Holland [75]. The computed results are compared with those computed using ATILA. Second order, eight-noded, quadrilateral, piezoelectric elements are used in the axisymmetric model in ATILA.

Table 2.1. Piezoceramic coefficients used to compute required coefficients.

Material property	**Value**
ρ (kg/m^3)	7500
s_{11}^E(pm^2/N)	12.3 (1 - j0.005)
s_{12}^E	-4.05(1 - j 0.005)
s_{13}^E	-5.31 (1 - j 0.005)
s_{33}^E	15.5 (1 - j 0.005)
s_{44}^E	39 (1 - j 0.005)
d_{31} (pC/N)	-123(1 - j 0.005)
d_{33}	289(1 - j 0.005)
$d_{15} = d_{24}$	496(1 - j 0.005)
ε_{33}^T(C/Vm)	1300 ×8.854e^{-12}(1- j 0.004)
ε_{11}^T	1475×8.854e^{-12}(1- j 0.004)
v^D(m/s)	4533+ j 10.22
v^E	4305+ j 10.76

Table 2.2. Computed PZT coefficients.

Material property	Value
c_{11}^E (GPa)	139 (1 + j 0.005)
c_{12}^E	77.835(1 + j 0.005)
c_{13}^E	74.282 (1 + j 0.005)
c_{33}^E	115.41 (1 + j 0.005)
c_{44}^E	25.64(1 + j 0.005)
e_{31} (C/m^2)	-5.2028(1 - j0.005)
e_{33}	15.0804 (1 - j 0.005)
e_{15}	12.7179(1 - j 0.005)
ε_{33}^S (C/Vm)	663.21 × 8.854e^{-12}(1 - j 0.004)
ε_{11}^S	762.54 × 8.854e^{-12}(1 - j 0.004)

Ten coefficients are used in ATILA. Eight of them are the first eight in Table 2.1. The other two, ε_{33}^S and ε_{11}^S, are computed using the values in Table 2.1. In the analytical model, the ten piezoelectric coefficients in Eq. (2.5) are used. They are computed using the values

in Table 2.1. The eight coefficients present in the analytical model are c_{11}^E, c_{12}^E, c_{13}^E, c_{33}^E, c_{44}^E, e_{31}, e_{33}, and e_{15}. The computed values of these coefficients are given in Table 2.2. The significant digits of these coefficients are different from those in Table 2.1 because the former is generated from the latter using MATLAB code. In ATILA, the results are obtained using $I \times J$ elements: I elements in the axial direction and J elements in the radial direction. The number of finite elements that is necessary for accurate analysis is determined through convergence studies.

In all cases, the frequency, f_s, at which the conductance, G, reaches a local maximum, the value of G at this frequency, G_{max}; and the frequency, f_p, at which the resistance, R, reaches a local maximum, and the value of R at this frequency, R_{max}, are computed. The frequencies $f_{-\frac{1}{2s}}$ and $f_{\frac{1}{2s}}$ at which the susceptance, B, reaches a local maximum and minimum, respectively, the values of B at these frequencies, B_{max} and B_{min}, are presented for some cases. They are computed using the present method and ATILA, and are compared. The frequencies f_s and f_p are referred to as resonance and anti-resonance frequencies, respectively. In all the analyses, k_{zq} are chosen such that $k_{zq}\, L/2 = q\pi$, $q = 0, 1, 2, 3, \ldots, M_z$.

2.6.1 **Case 1: Zero axial displacement on flat surfaces**

In this case, the axial displacement is specified and is zero on the flat surfaces of the hollow piezoceramic cylinder. Normal and shear stresses on the curved surfaces and shear stress on the flat surfaces are zero. A potential is applied on the top flat surface of the hollow piezoceramic cylinder. The boundary conditions are: $\bar{U} = 0$, $\bar{T}_{rz} = 0$, $\hat{T}_{rra} = 0$, $\hat{T}_{rza} = 0$, $\hat{T}_{rrb} = 0$, $\hat{T}_{rzb} = 0$, $\emptyset = 0$ on $z = -L/2$ and $\emptyset = \emptyset_0$ on $z = L/2$.

It is seen by using Eq. (2.23) that the boundary conditions on axial displacement imply that the coefficients A and A_{ms} are zeros. Similarly, it is seen from Eq. (2.26) that the boundary conditions on $\hat{T}_{rz}$ imply that B_{ms} and C_{ms} are zero. Then, using A = 0 in Eq. (2.27) yields $E = 0.5$ and $D = 1/L$. The coefficients B and C are determined by using the following two conditions on $\hat{T}rr$:

$$BL\left\{c_{11}^E k_{r0} J_0(k_{r0} r) + \frac{c_{12}^E - c_{11}^E}{a} J_1(k_{r0} r)\right\} + CL\left\{c_{11}^E k_{r0} Y_0(k_{r0} r) + \frac{c_{12}^E - c_{11}^E}{a} Y_1(k_{r0} r)\right\} + DLe_{31} = 0, \text{ for } r = a, b. \tag{2.30}$$

It is thus seen that none of the terms in the series are necessary to satisfy the boundary conditions and a closed-form solution is obtained for this special case. Only four of the coefficients are non-zero and this implies that $U = 0$ everywhere, W is independent of z, and $\emptyset$ varies linearly with respect to z. The numerical results obtained from the exact analytical solution are used to test the convergence of the finite element results by increasing the number of elements.

Computed resonance and anti-resonance frequencies of a (50, 38, 8) hollow cylinder that are less than 5 MHz are presented in Table 2.3. For this cylinder, the L/D ratio, where D is the average diameter, is 0.18. For the first four resonance and anti-resonance frequencies in Table 2.3, it is seen that 16×12 finite elements yields values of frequencies, G and R that are correct to four significant digits. At the highest of these frequencies (f_{max} =1078 kHz) and the lower of the two phase velocities in Table 2.1, the side of each finite element (0.5 mm) is approximately $\lambda^E/8$ where $\lambda^E = v^E/f_{max}$. For the next 10 resonance and anti-resonance frequencies in Table 2.3, it is seen that the fourth significant digit of the values of frequencies computed using ATILA and the analytical model differ by at most 1 when 80×60 finite elements are used. The fourth significant digit of the values of G and R differ by at most 2. At the highest of these frequencies (f_{max} =4664 kHz) and the lower of the two phase velocities in Table 2.1, the side of each finite element (0.1 mm) is approximately $\lambda^E/9$ where $\lambda^E = v^E/f_{max}$.

It is noted that f_s is the frequency at which the conductance, G, reaches a local maximum, and f_p is the frequency at which the resistance, R, reaches a local maximum. For the lossless case, f_s and f_p do not exist. f_m and f_n are the frequencies at which the magnitudes of admittance and the impedance, respectively, are maximum. They exist for the lossy and the loss-less cases. The results obtained using the present method and ATILA show that $f_{sn} > f_{pn}$ for n = 5, 7, 9, 11, and 13 where n is the mode number. However, for both the lossy and the loss-less cases, f_m is always less than the corresponding f_n. It is also noted that f_{sn} is approximately n-1 times f_{s2} for $n \geq 3$. It is concluded by computing the resonance frequencies of a few cylinders that f_{s1} is inversely proportional to the mean diameter and f_{s2} is inversely proportional to the wall thickness of the cylinder.

Table 2.3. Resonance and anti-resonance frequencies of a (50, 38, 8) cylinder for Case 1. The values of G and R in mS and Ohms, respectively are shown in parenthesis.

	Model		ATILA			
Mode No.	f_s (kHz)	f_p (kHz)	f_s (kHz) I=16, J=12	f_s (kHz) I=80, J=60	f_p (kHz) I=16, J=12	f_p (kHz) I=80, J=60
1	26.06 (0.1906)	26.18 (177.7k)	26.06 (0.1906)	26.06 (0.1906)	26.18 (177.8k)	26.18 (177.8k)
2	359.63 (7.332)	364.35 (3.714k)	359.63 (7.332)	359.63 (7.332)	364.35 (3.714k)	364.35 (3.714k)
3	717.93 0.0257	717.94 (3.414)	717.93 0.0257	717.93 0.0257	717.95 (3.414)	717.95 (3.414)
4	1076.53 (2.460)	1078.13 (144.4)	1076.81 (2.460)	1076.53 (2.459)	1078.13 (144.4)	1078.13 (144.4)
5	1435.22 (0.0257)	1435.21 (0.8544)	1436.35 (0.0258)	1435.22 (0.02575)	1436.35 (0.8544)	1435.21 (0.8543)
6	1793.91 (1.489)	1794.88 (31.58)	1797.31 (1.496)	1793.92 (1.489)	1798.19 (31.62)	1794.88 (31.58)
7	2152.66 (0.03145)	2152.61 (0.4639)	2160.69 (0.03156)	2152.69 (0.03145)	2160.69 (0.4625)	2152.61 (0.4639)
8	2511.36 (1.0785)	2512.05 (11.68)	2528.19 (1.0909)	2511.39 (1.0785)	2528.81 (11.67)	2512.08 (11.68)
9	2870.17 (0.03859)	2870.02 (0.32016)	2901.39 (0.03893)	2870.21 (0.03859)	2901.31 (0.31642)	2870.12 (0.3201)
10	3228.83 (0.8538)	3229.37 (5.5944)	3282.18 (0.8569)	3228.94 (0.8539)	3282.69 (5.4382)	3229.47 (5.5941)
11	3587.71 (0.04629)	3587.43 (0.2458)	3671.5 (0.04691)	3587.92 (0.04629)	3671.31 (0.2381)	3587.54 (0.2458)
12	3946.31 (0.7139)	3946.75 (3.1319)	4062.12 (0.5487)	3946.62 (0.7140)	4062.39 (2.2725)	3947.00 (3.1318)
13	4305.30 (0.05429)	4304.80 (0.2002)	4747.69 (0.05987)	4305.71 (0.05429)	4747.0 (0.1808)	4305.20 (0.2002)
14	4663.79 (0.6196)	4664.16 (1.9464)	5042.08 (1.2368)	4664.47 (0.6198)	5042.89 (3.3231)	4664.84 (1.9465)

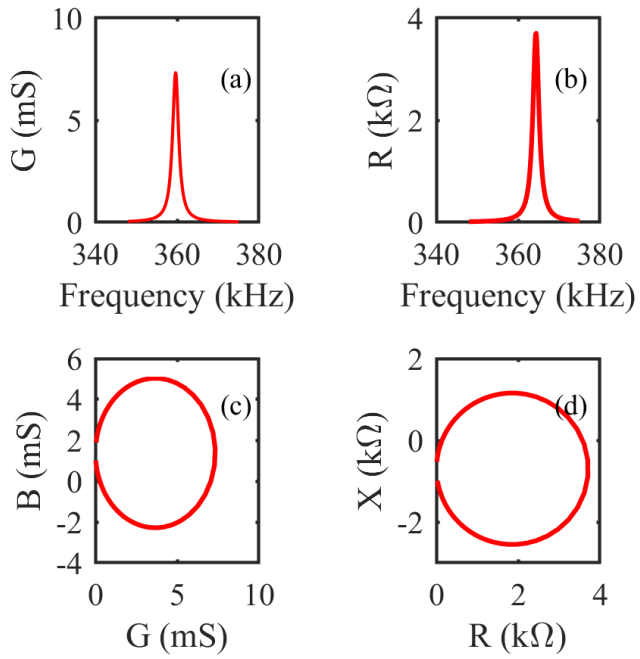

Fig. 2.2. (a) f-G, (b) f-R, (c) G-B, and (d) R-X in the neighborhood of the second resonance frequency of a (50, 38, 8) cylinder for Case 1 computed using the model.

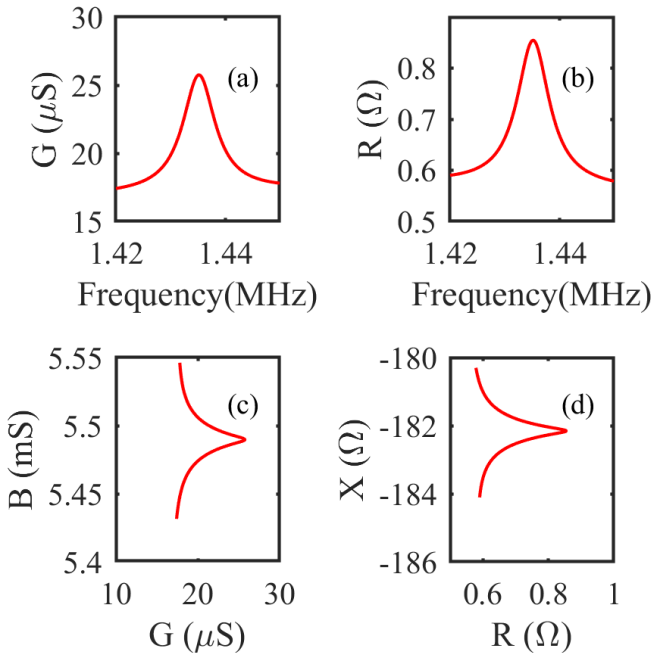

Fig. 2.3. (a) f-G, (b) f-R, (c) G-B, and (d) R-X plots in the neighborhood of the fifth resonance frequency of a (50, 38, 8) cylinder for Case 1 computed using the model.

The conductance, G, and reactance, R, in the neighborhoods of f_{s2} =359.63 kHz and f_{p2} = 364.35 kHz, respectively, of (50, 38, 8) cylinder are shown in Figs. 2.2(a) and 2.2(b), respectively. The conductance (G) - susceptance (B) plot in the neighborhood of f_{s2} and

the resistance (R) - reactance (X) plot in the neighborhood of f_{p2}, are shown in Figs. 2.2(c) and 2.2(d), respectively. In this case, $f_{s2} < f_{p2}$ and the familiar loops are seen in Figs. 2.2(c) and 2.2(d). Corresponding figures are shown in the neighborhoods of f_{s5} and f_{p5} in Figs. 2.3(a) to 2.3(d). In this case, $f_{s5} > f_{p5}$ and the G-B and R-X loops degenerate as shown in Figs. 2.3(c) and 2.3(d), respectively. The basic form of the equivalent circuit of a piezoelectric device with one resonance has a capacitor in one arm of the circuit and a capacitor, an inductor, and a resistor in a parallel arm. When the resistor has a moderate value, the admittance of the circuit has the characteristics shown in Fig. 2.2 and $f_s < f_p$. When the resistor has a high value, the admittance of the circuit has the characteristics shown in Fig. 2.3 and $f_s > f_p$.

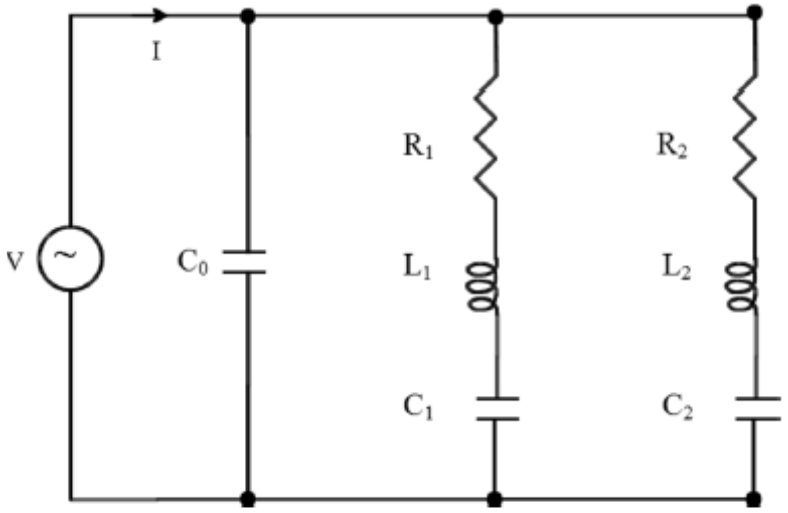

Fig. 2.4. Equivalent circuit of a piezoelectric ceramic transducer with two resonances in the band of interest.

The form of the equivalent circuit for underwater transducers with two resonances [81] is shown in Fig. 2.4. It is valid when the resonance is like the one in Fig. 2.2 or like the one in Fig. 2.3. To illustrate this, the values of the equivalent circuit components that correspond to the first resonance in Ref. [81] (Set I: C_0 = 15.25e-9; R_1 = 2.468e3; L_1 = 0.1150; C_1 = 1.005e-9) are used to compute the G-B and shown using a red line in the Fig.2.5 below. There is moderate loss (R_1 = 2.468e3) in Set I. In Set II [C_0 = 15.25e-9; R_1 = 3×2.468e3; L_1 = 0.1150; C_1 = 1.005e-9], the loss is high and the G-B is shown using a blue line in the Fig.2.5 below. The red line corresponds to moderate loss and the G-B curve looks like the one in Fig. 2.2(c). The blue line corresponds to higher loss and the G-B looks like the one in Fig. 2.3(c). Thus, both Figs. 2.2 and 2.3 have realistic equivalent circuits.

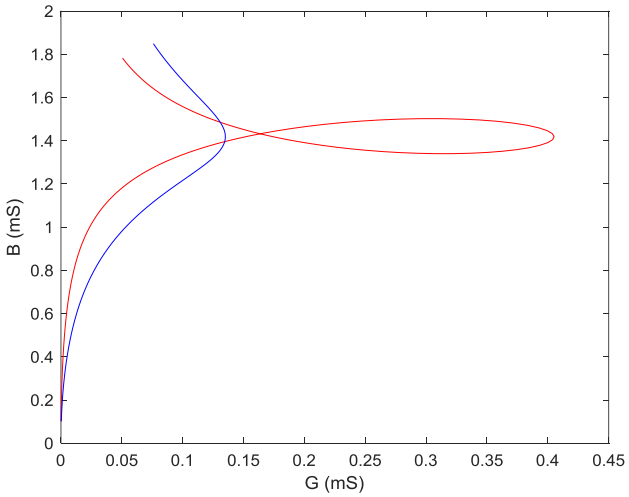

Fig. 2.5. The G-B characteristics derived from the equivalent circuit of a piezoelectric ceramic transducer with two resonances in the band of interest [81].

In Fig. 2.6, analytical results computed using M_r=M_z=0 are compared with those obtained using I=16 and J=12 elements in ATILA for a (50, 38, 8) ring. 10 Hz resolution is used in both methods. The conductance, G, and susceptance, B, in the neighborhood of the first resonance frequency are shown in Figs. 2.6(a) and 2.6(b), respectively. The admittance of the hollow PZT cylinder is obtained by integration over the flat electroded surface and accurate values can be obtained even if the spatial dependence of the variables is not accurate. However, the spatial dependence of the primary variables is also accurate as shown in the figure. The real part of the axial displacement, and the real and imaginary parts of the radial displacement at the first resonance frequency, are shown along the radial direction, at $z = 0$, in Figs. 2.6(c), 2.6(d), and 2.6(e), respectively. It is seen from Fig. 2.6(c) that the analytical axial displacement is zero everywhere, as discussed earlier. When ATILA is used, the axial displacement is not exactly zero. However, it is of the order of 1e-15 times the radial displacement shown in Figs. 2.6(d) and 2.6(e). It is noted that 15 digits are used in double precision calculations using C and that ATILA uses C. The conductance and susceptance in the neighborhood of the second resonance frequency, 359.63 kHz, and resistance in the neighborhood of the second anti-resonance frequency, 364.35 kHz, are shown in Figs. 2.6(f), 2.6(g), and 2.6(h), respectively.

The computed electric potential, $\emptyset(z)$, along the axis at the inner curved surface, r=b, is shown in Fig. 2.6(i). It satisfies the applied boundary conditions on potential; as the potential is one on the top flat surface and zero on the bottom flat surface. In between it varies linearly. The radial displacement at the second resonance, f_{s2}, is shown in Figs. 2.6(j) to 2.6(m). The real and imaginary parts of W are shown in Figs. 2.6(j) and 2.6(k),

respectively at the plane midway between the flat ends of the cylinder; and in Figs. 2.6(l) and 2.6(m) on the top flat surface of the cylinder. The conductances in the neighborhood of the third resonance frequency, f_{s3}, computed using the analytical method and ATILA are shown in Fig. 2.6(n). The magnitudes of the radial displacement at $z = 0$, at f_{s3}, are shown in Fig. 2.6(o). The displacement is plotted along the radial direction. All results computed using ATILA are in good agreement with the exact analytical results. This shows that ATILA yields accurate results and that it has been correctly used here.

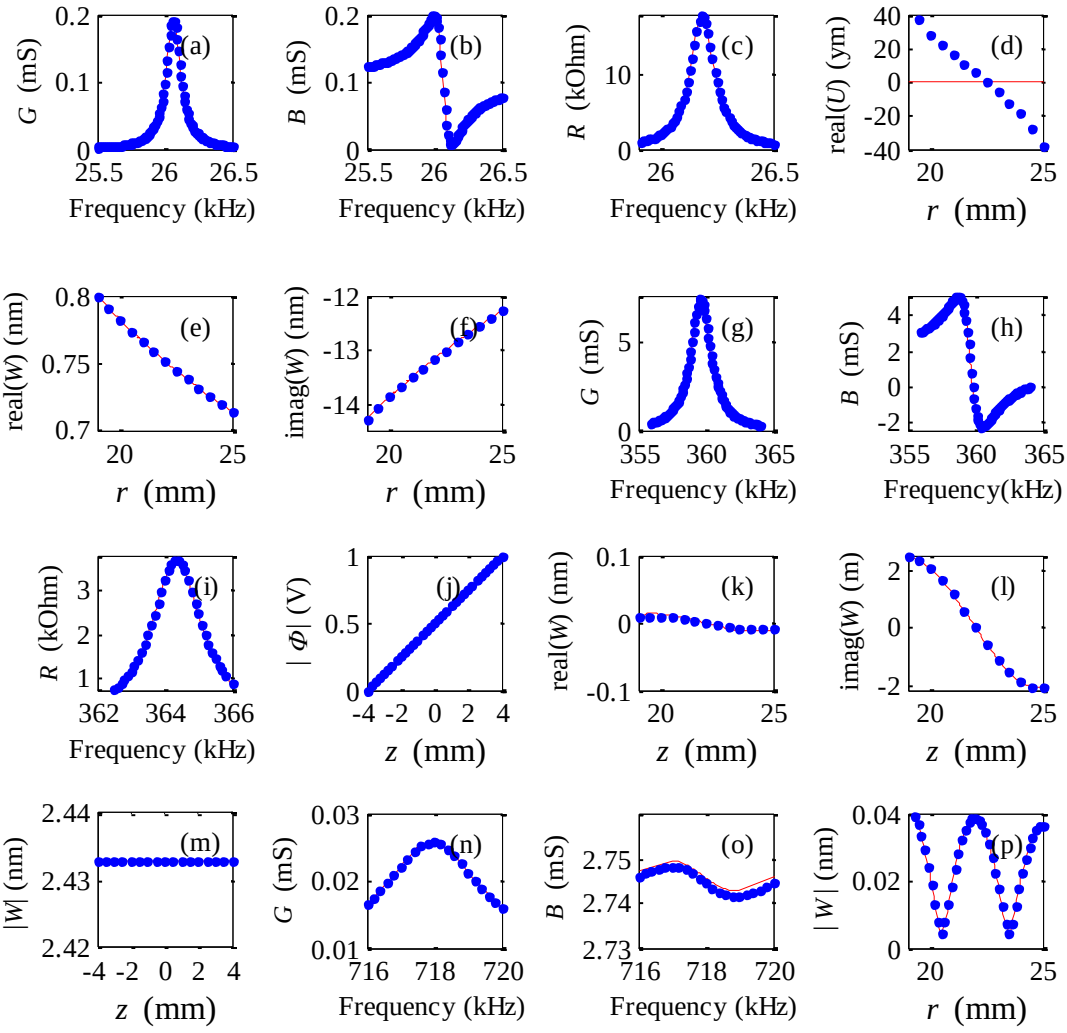

Fig. 2.6. Axial and radial displacement, electric potential, conductance, susceptance, and resistance for Case 1. The dimensions of the cylinder are (50, 38, 8). Solid line: Model and Dots: ATILA.

Next, results are presented for two other rings with *L*/*D* ratios of 1/3 and 1/15. The dimensions of the rings are (12, 6, 3) and (100, 80, 6). The first three resonance and anti-resonance frequencies of these rings and the conductance and resistance, respectively at these frequencies, are shown in Table 2.4. For the first ring, when 24×24 finite elements

are used, the frequencies computed using ATILA and the analytical model are the same upto the fifth significant digit for all the frequencies except for f_{s3} where it differs by 1. Further, the fourth significant digits of *G* and *R* differ from the exact analytical values by less than or equal to 2. For the second and larger ring of size (100, 80, 6), when 12×20 and 24×40 finite elements are used, the fifth significant digits of the resonance frequencies computed using ATILA and the analytical model differ at most by 1. The fourth significant digits of *G* differ by at most 1 and third significant digits of *R* by at most 4.

Table 2.4. Critical frequencies and associated electrical parameters for Case 1. The dimensions of the rings are (12, 6, 3) and (100, 80, 6).

Parameter	(12, 6, 3)			(100, 80, 6)		
	Model	ATILA		Model	ATILA	
		I=6, J=6	I=24, J=24		I=12, J=20	I=24, J=40
f_{s1}(kHz)	134.08	134.08	134.08	12.699	12.699	12.699
G_1(mS)	0.3047	0.3045	0.3047	0.4204	0.4199	0.4199
f_{p1}(kHz)	134.78	134.78	134.78	12.757	12.757	12.757
$R_1(\Omega)$	14.44k	14.44k	14.44k	7.995k	7.949k	7.949k
f_{s2}(kHz)	729.77	729.81	729.77	215.59	215.60	215.60
G_2(mS)	3.846	3.844	3.844	20.04	20.03	20.03
f_{p2}(kHz)	738.87	738.90	738.87	218.44	218.44	218.44
$R_2(\Omega)$	6.371k	6.374k	6.373k	1.367k	1.368k	1.368k
f_{s3}(kHz)	1440.8	1441.9	1440.9	430.67	430.67	430.67
G_3(mS)	0.0609	0.0610	0.0609	0.0545	0.0544	0.0544
f_{p3}(kHz)	1440.9	1442.1	1440.9	430.67	430.68	430.67
$R_3(\Omega)$	26.97	26.99	26.98	0.9713	0.9717	0.9717

Table 2.5. Computed resonances of a (10, 5, 10) cylinder for Case 1.

Mode	Model	ATILA (I= J=20)
1	160.892	160.893
2	875.735	875.728
3	1729.19	1729.01

The first three resonance frequencies of an electrically excited hollow piezoceramic cylinder with a thick wall are shown in Table 2.5. The dimensions of the cylinder are (10, 5, 10). The natural frequencies of a steel cylinder with the same dimension are shown

in Ref. [79]. The L/D ratio of this cylinder is 4/3. The fifth significant digits of the values of frequencies computed using ATILA and the analytical model differ by at most 2 when 20x20 finite elements are used. The forced PZT cylinder has only three resonances that are less than 2 MHz, but there are 19 resonances for a free hollow elastic cylinder of same dimension with zero axial displacement on its flat surfaces [79].

2.6.2 **Case 2: Zero radial displacement on cylindrical surfaces**

In this case, the radial displacement is zero on both the curved surfaces. All stresses on the flat surfaces and shear stress on the curved surfaces are zero. The boundary conditions are $\bar{T}_{zz} = 0,\ \bar{T}_{rz} = 0,\ \hat{W}_a = 0,\ \hat{T}_{rza} = 0,\ \hat{W}_b = 0,\ \hat{T}_{rzb} = 0,\ \emptyset = 0$ on $z = -L/2$ and $\emptyset = \emptyset_0$ on $z = L/2$. The resonance and anti-resonance frequencies upto 4 MHz are determined for a (50, 38, 8) ring and are presented in Table 2.6. They are computed with $M_r = M_z = 0$ as the series terms are not required to satisfy the boundary conditions.

Table 2.6. Resonance and anti-resonance frequencies of a (50, 38, 8) ring for Case 2.

Mode	Method	f_r (kHz)	G (mS)	f_p (kHz)	R (Ω)
1	Model	251.13	55.959	283.34	41.692k
	ATILA	251.13	55.959	283.34	41.689k
2	Model	840.30	16.541	850.02	1.545k
	ATILA	840.29	16.541	850.01	1.545k
3	Model	1410.9	9.8554	1416.7	334.11
	ATILA	1410.9	9.8554	1416.7	334.09
4	Model	1979.2	7.0360	1983.4	121.97
	ATILA	1979.2	7.0361	1983.4	121.96
5	Model	2546.8	5.4799	2550.1	57.518
	ATILA	2546.9	5.4802	2550.1	57.515
6	Model	3114.1	4.4943	3116.7	31.593
	ATILA	3114.2	4.4946	3116.9	31.591
7	Model	3681.2	3.8148	3683.4	19.205
	ATILA	3681.3	3.8153	3683.6	19.204

ATILA results are computed with *I*=80 and *J*=60. All the computed parameters, except the conductance value at the 5th resonance frequency, are in excellent agreement. The fifth significant digits of the resonance and anti-resonance frequencies differ at most by one and two, respectively; those of the conductances differ at most by five; and those of the resistances differ at most by three. This again shows that ATILA is accurate and is correctly

used. The largest side of the finite element used in ATILA is approximately $\lambda^E/10$ where $\lambda^E = v^E/f_{max}$ and f_{max} is 4000 kHz.

2.6.3 Case 3: Free flat and cylindrical surfaces

In this case, the stresses are zero on all the surfaces. The boundary conditions are $\bar{T}_{zz} = 0$, $\bar{T}_{rz} = 0$, $\hat{T}_{rra} = 0$, $\hat{T}_{rza} = 0$, $\hat{T}_{rrb} = 0$, $\hat{T}_{rzb} = 0$, $\emptyset = 0$ on $z = -L/2$ and $\emptyset = \emptyset_0$ on $z = L/2$. In this case, all the series terms in Eq. (2.7) are required, and therefore used.

The critical frequencies and admittance in and around the first four resonances computed using the present method and ATILA are presented for (50, 25, 50) cylinder in Table 2.7. In the present method, $M_r = M_z = 5$ is used and in ATILA $I = 100$ and $J = 25$ elements are used. In this case, both the present method and ATILA yield approximate results. However, it has been shown for Cases 1 and 2 that ATILA yields accurate results by comparison with exact analytical results. Therefore, in this case, values obtained using ATILA are considered to be the correct values. The values of f_s, G_{max}, $f_{-1/2s}$, B_{max}, $f_{1/2s}$, B_{min}, f_p, and R_{max}, computed using the present method and ATILA are presented in Table 2.7.

The F matrix in Eq. (2.29) is rank-deficient even when only the A, B, C, D, and E terms are used to build it and the elements of the matrix are computed using the above equations. It becomes a full-rank matrix when the rows are normalized by dividing each row in the equation by the largest element in the row. It is noted that, for this case, only one element in the G matrix is non-zero. When the series terms are also used to build the F matrix, it remains rank-deficient even after the row normalization even though the condition number improves. A study of the rank-deficient matrix shows that no row (or column) is a multiple of some other row (or column). This indicates that some rows (or columns) are linear combinations of other rows (or columns). In some rows (and columns) some elements are much smaller than others and this could lead to the numerical difficulties.

The rank-deficiency of the F matrix gradually increases when the values of M_r and M_z are increased gradually after starting at one. However, the resonance and anti-resonance frequencies converge, the conductance is always positive, and they converge towards the values obtained using ATILA. This indicates that the coefficients that are significant for the computation of the critical frequencies and conductance are correctly determined even though the F matrix is rank-deficient. The conductance becomes negative at some frequencies when the values of M_r and M_z are increased beyond a critical value; and this

indicates that rank-deficiency is affecting the values of the significant coefficients. This is used to choose the maximum values of M_r and M_z used in the computations; and in this case they are both five.

Table 2.7. Critical parameters of a (50, 25, 50) cylinder for Case 3.

Mode		1	2	3	4
f_r (kHz)	Model	25.21	31.08	38.31	113.3
	ATILA	25.20	30.86	38.30	113.1
	% Error	-0.04	-0.7	-0.03	-0.2
G_{max} (mS)	Model	3.607	0.1115	1.572	1.088
	ATILA	3.567	0.1299	1.570	1.063
	% Error	1.1	-14	0.13	2.4
$f_{-1/2s}$ (kHz)	Model	25.15	31.01	38.22	113.1
	ATILA	25.13	30.78	38.21	112.9
	% Error	0.08	0.7	0.03	0.2
B_{max} (mS)	Model	1.837	0.0679	0.8075	0.6675
	ATILA	1.829	0.0752	0.8059	0.6542
	% Error	0.4	-9.7	0.2	2
$f_{+1/2s}$ (kHz)	Model	25.27	31.16	38.41	113.6
	ATILA	25.26	30.93	38.40	113.4
	% Error	0.04	0.7	0.03	0.2
B_{min} (mS)	Model	-1.767	-0.0409	-0.7632	-0.4174
	ATILA	-1.757	-0.0525	-0.7617	-0.4053
	% Error	-0.6	22	-0.2	-3
f_a (kHz)	Model	29.54	31.54	42.81	115.3
	ATILA	29.45	31.42	42.80	115.1
	% Error	0.3	0.4	0.02	0.2
R_{max} (Ω)	Model	746.4k	264.6k	1.116M	61.37k
	ATILA	702.9k	323.1k	1.118M	60.19k
	% Error	6	-18	-0.2	2

The percentage error, with ATILA as the reference, is computed using the equation $(Analysis - ATILA) \times 100 \,/\, ATILA$ and are given. The percentage errors are in general

very small. They are smallest for the first and third rows, a little higher for the fourth row, and highest for the second row. An examination of the displacement at 30.86 kHz (second row) using ATILA shows that the relative edge displacement is much higher than at 25.20 (first row), 38.30 (third row), and 113.1 kHz (fourth row). Higher values of M_r and M_z are required to accurately compute edge modes but it is not possible to use them because of rank-deficiency and ill-conditioning. Even for the case where edge vibrations are dominant, the percentage errors in the resonance and anti-resonance frequencies are very small and much less than that due to typical variation in values of piezoelectric coefficients of samples in one production batch.

Contour maps and wireframes of the axial and radial displacements, computed using ATILA, at the four resonance frequencies 25.20, 30.86, 38.30, 113.1 kHz are shown in Figs. 2.7 to 2.10, respectively. In each figure, the real and imaginary parts of U are shown in (a) and (b), respectively; the real and imaginary parts of W are shown in (c) and (d), respectively. Wireframes of the real and imaginary parts of the total displacement are shown in (e) and (f), respectively. The real and imaginary parts of the electric potential are shown in (g) and (h), respectively.

In all the figures, it is seen that the real and imaginary parts of U are zero on the plane that is midway between the flat ends of the cylinder and anti-symmetric about this plane. Further, W is symmetric about the plane. The form of the solution in Eq. 2.7 is appropriate for this displacement. In Figs. 2.7 to 2.10, the imaginary parts of U and W are greater than the corresponding real parts. This shows that the vibration is nearly out of phase with the applied voltage. In all the figures, the electric potential is 0 at $z = -L/2$ and +1 at $z = +L/2$ because of the boundary conditions. However, its maximum lies within the cylinder and is greater than one.

At the first three resonance frequencies, U is zero only on the $z = 0$ plane. This indicates that B_{qs}, or C_{qs}, or both, in Eqs. (2.7c) and (2.7d), are large when $q = 1$. At the fourth resonance frequency of 113.1 kHz Im(U) = 0 contours lie approximately on three z = constant planes. This indicates that that B_{qs}, or C_{qs}, or both, in Eqs. (2.7c) and (2.7d), are large when q = 3. At 25.20 kHz, the constant W contours lie almost on constant z lines. At 38.30 kHz, they lie almost on constant r lines. At both frequencies, the constant U contours lie approximately on constant z lines. However, at 25.20 kHz, the inner surface has greater axial displacement than the outer curved surface; whereas at 38.30 kHz, the outer surface has greater axial displacement than the inner surface. At 30.86 kHz, the axial

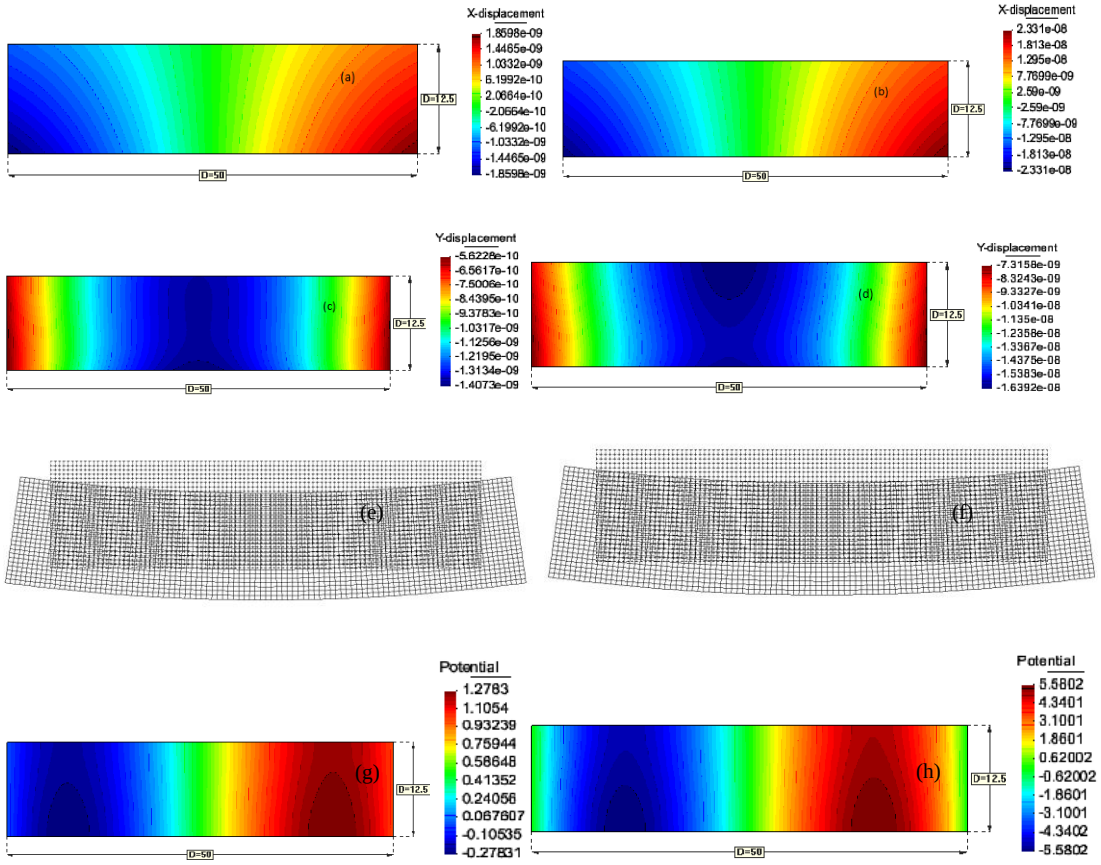

Fig. 2.7. Contour maps of the axial and radial displacements of a (50, 25, 50) mm cylinder at its first resonance 25.20 kHz. (a) Real and (b) imaginary part of the axial displacement; (c) real and (b) imaginary part of the radial displacement; (e) real and (f) imaginary part of the total displacement in wireframe view; and (g) real and (h) imaginary part of the electric potential.

displacement is quite different from that at 25.20 and 38.30 kHz. On the flat ends, U has opposite signs on the inner and outer curved surfaces and a Im(U)=0 contour line lies approximately on $r = (a + b)/2$. Im(W) has opposite signs at the center and ends of the cylinder. Therefore, the radius of the cylinder increases at the center and decreases at the ends. This is in contrast to the pattern at 25.20 kHz where the radius decreases throughout the length of the cylinder. At 25.20, 38.30, 113.1 kHz, max($|U|$) is a little greater than max($|W|$). However, at 30.86 kHz, max($|U|$) is about half of max($|W|$). In long, thin, elastic, circular cylindrical shells, the axial and radial displacements have the same shape in two branches. In one branch, max($|U|$) $>$ max($|W|$); and max($|U|$) $<$ max($|W|$) in the other branch.

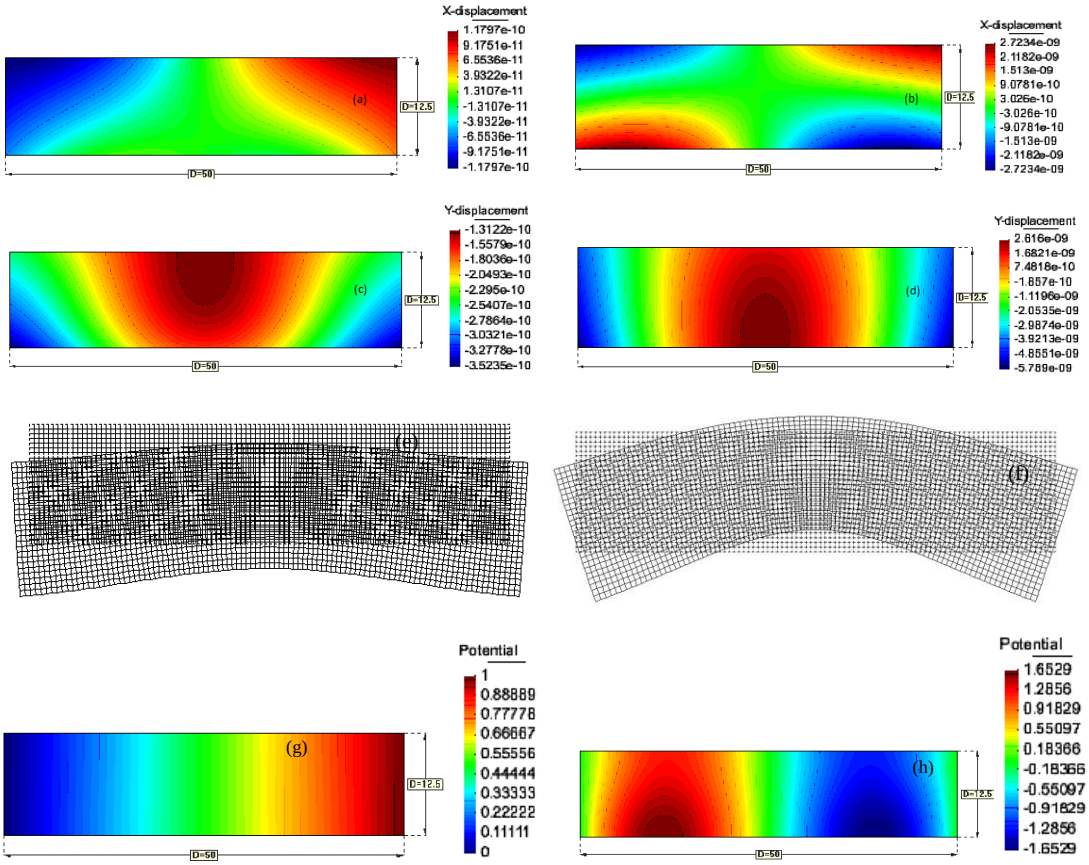

Fig. 2.8. Contour maps of the axial and radial displacements of a (50, 25, 50) cylinder at its second resonance 30.86 kHz. (a) Real and (b) imaginary part of the axial displacement; (c) real and (b) imaginary part of the radial displacement; (e) real and (f) imaginary part of the total displacement in wireframe view; and (g) real and (h) imaginary part of the electric potential.

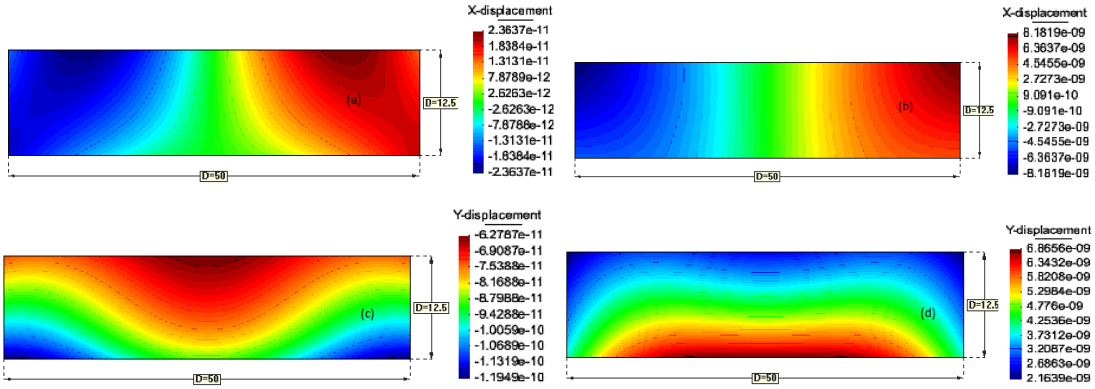

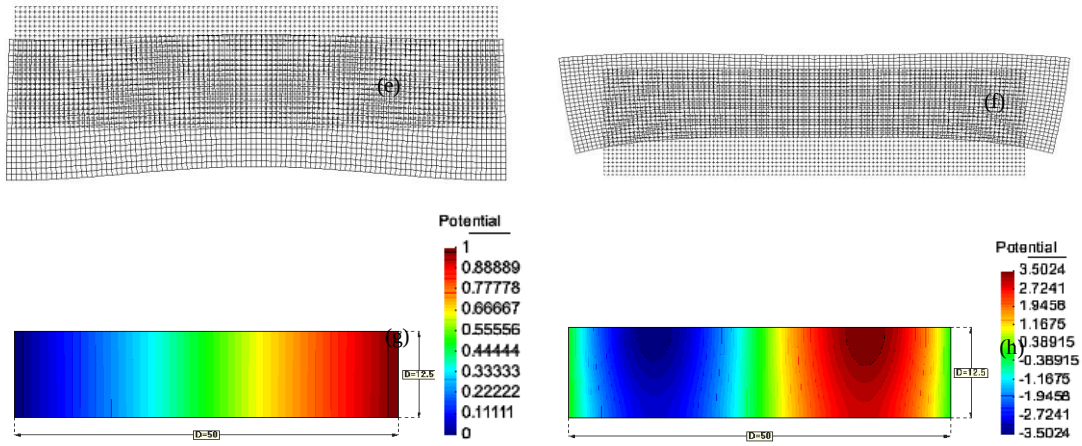

Fig. 2.9. Contour maps of the axial and radial displacements of a (50, 25, 50) cylinder at its third resonance 38.30 kHz. (a) Real and (b) imaginary part of the axial displacement; (c) real and (b) imaginary part of the radial displacement; (e) real and (f) imaginary part of the total displacement in wireframe view; and (g) real and (h) imaginary part of the electric potential.

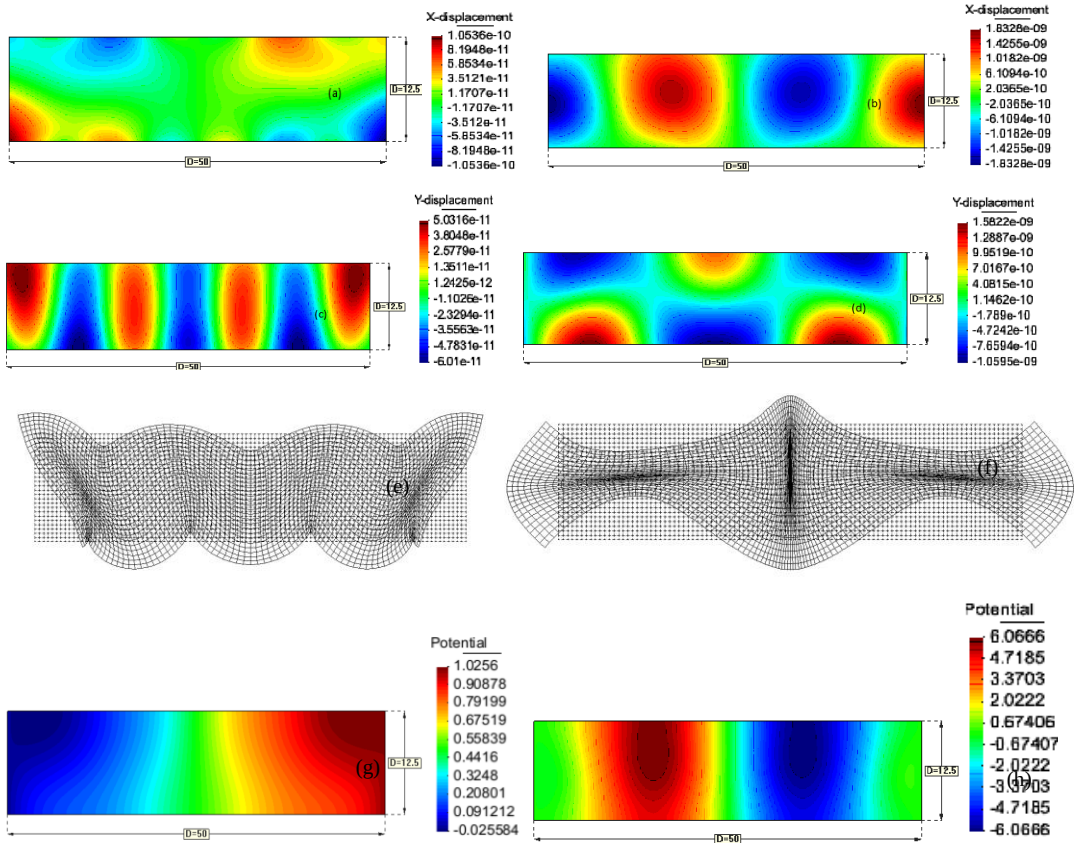

Fig. 2.10. Contour maps of the axial and radial displacements a (50, 25, 50) cylinder at its fourth resonance 113.10 kHz. (a) Real and (b) imaginary part of the axial displacement; (c) real and (b) imaginary part of the radial displacement.

The first two resonance and antiresonance frequencies of (50, 38, 8) and (50, 38, 50) rings are presented in Table 2.8. L/D ratios of these rings are 0.18 and 1.14, respectively. Computed frequencies are in good agreement with those computed using ATILA. The percentage errors are also shown. For both dimensions, the maximum percentage error is 0.3 %. No M_z term is required for a (50, 38, 8) ring to achieve the same level of convergence as that of a (50, 38, 50) ring with M_z terms because it is shorter by a factor of 6.25. The f_{s2} of a (50, 38, 8) cylinder computed using M_r = M_z = 0 is 192.2 kHz [30] and using M_r = 5 yields more nearly accurate results.

Table 2.8. First two resonance and antiresonance frequencies of hollow piezoelectric cylinders of various dimensions for Case 3.

Frequencies (kHz)	(50, 38, 8)			(50, 38, 50)		
	Model M_r=5, M_z=0	ATILA I=32, J=24	% Error	Model M_r=5, M_z=5	ATILA I=200, J=24	% Error
f_{s1}	23.97	23.96	0.04	22.32	22.30	0.09
f_{p1}	25.42	25.41	0.04	25.02	24.94	0.3
f_{s2}	189.9	189.4	0.3	35.58	35.57	0.03
f_{p2}	236.0	236.0	0	236.0	42.05	0

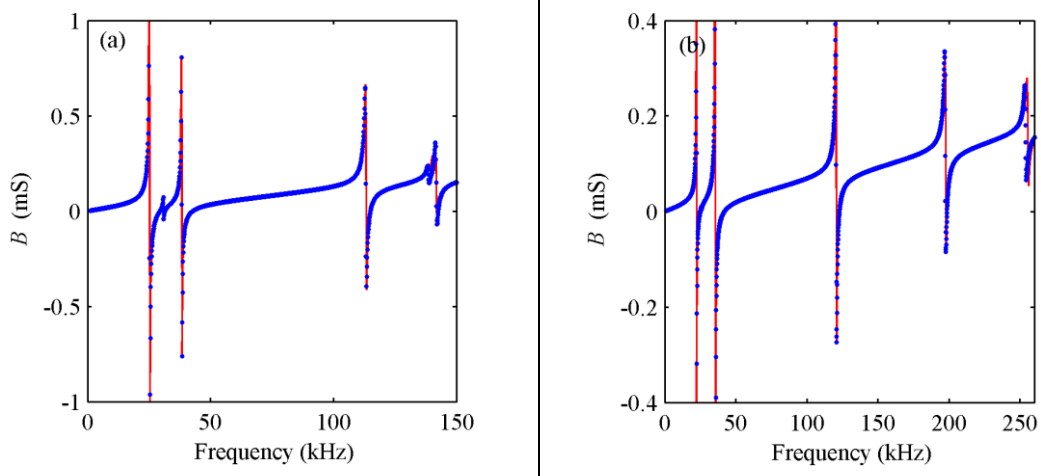

Fig. 2.11. Susceptance (B) for Case 3. The dimensions of the cylinder are (a) (50, 25, 50) and (b) (50, 38, 50). Solid line: Model and Dots: ATILA.

The computed susceptance of (50, 25, 50) and (50, 38, 50) cylinders are shown in Figs. 2.11(a) and 2.11(b), respectively. Six resonances of the (50, 25, 50) cylinder are less than 150 kHz and five resonances of a (50, 38, 50) cylinder are less than 280 kHz. It is shown in the tables that the critical frequencies and the conductance, susceptance, and resistance at the critical frequencies are accurately determined by using the present method. Therefore, in the figures, the upper and lower limits of the Y axis are chosen to highlight the accuracy of the susceptance at frequencies that are not close to the critical frequencies. The rate of convergence is good for admittance because it is computed by evaluating an integral over the flat surfaces of the cylinder and thus represents an average effect. Admittance depends only on the coefficients B, C, and D and is independent of the series terms A_{ms}, B_{ms}, and C_{ms} - as seen in Eq. (2.18).

The first three resonance and anti-resonance frequencies of a (12, 6, 3) and a (12, 6, 6) cylinders are presented in Table 2.9. The L/D ratios are 0.33 and 0.667, respectively. The values are computed with M_r=10 and M_z =1 and I=J=24 for the (12, 6 3) cylinder; and M_r= M_z =2 and I=48 and J =24 for the (12, 6, 6) cylinder. It is noted that sizes of the elements are the same in both cases. Comparison of the resonance frequencies of the cylinders of different sizes indicates that the first resonance is strongly dependent on the diameter; and the second and third resonances are strongly dependent on the length.

Table 2.9. Critical parameters of (12, 6, 3) and (12, 6, 6) cylinders for Case 3.

Parameter	(12, 6, 3)			(12, 6, 6)		
	Model	ATILA	% Error	Model	ATILA	% Error
f_{s1} (kHz)	120.87	120.85	-0.02	118.9	118.79	-0.08
G_1 (mS)	6.473	6.466	-0.1	3.919	3.903	-0.4
f_{p1} (kHz)	129.4	129.4	0	128.9	128.74	-0.2
R_1 (Ω)	0.1106M	0.1106M	0	249.9k	249.4k	0
f_{s2} (kHz)	440.32	436.44	-0.9	201.5	196.26	-2.6
G_2 (mS)	2.804	2.417	-16	0.0783	0.0723	-7.7
f_{p2} (kHz)	441.49	437.5	-0.9	201.7	196.48	-2.6
R_2 (Ω)	412.7	408.7	-0.9	1.585k	2.194k	27
f_{s3} (kHz)	470.9	468.61	-0.5	275.8	275.64	-0.07
G_3 (mS)	52.81	51.29	-3	16.15	16.11	-0.2
f_{p3} (kHz)	551.4	541.7 (1.8)	551.4	339.9	339.70	-0.06
R_3 (Ω)	51.59k	44.38k	-17	419.4k	419.1k	-0.07

2.7 CONCLUSIONS

A method is presented to determine the forced responses of axially polarized, hollow piezoelectric ceramic cylinders of finite length with internal losses. In this method, exact solutions to the governing equations are used and all field variables; displacements, potential, stress, and electric displacement are expressed in terms of complete sets of functions. Therefore, arbitrary, piecewise continuous boundary conditions can be satisfied. The method is illustrated by presenting many critical frequencies and critical parameters for various piezoceramic cylinders subjected to different sets of boundary conditions. Numerical values of the complex input electrical admittance and the complex displacement are computed and compared with finite element results. For cylinders with internal losses, critical frequencies - f_s, $f_{-1/2s}$, $f_{1/2s}$, and f_a - and the electrical parameters - G_{max}, B_{max}, B_{min}, and R_{max} - are all in excellent agreement with ATILA. These parameters are of interest in the design of transducers with hollow piezoceramic cylinders in it and in the characterization of piezoelectric material. The displacements and electrical parameters computed are in good agreement with ATILA even at high frequencies. The level of convergence achieved here is sufficient for most practical applications. In the next chapter, the model is used to analyze a stack of hollow piezoceramic cylinders. It can also be used to model composite transducers where such stacks are used as components.

CHAPTER 3

STACK OF AXIALLY POLARIZED HOLLOW PIEZOCERAMIC CYLINDERS

3.1 INTRODUCTION

Electromechanical systems are often composed of different components that are interconnected to give reinforced mechanical motion. This chapter describes the analysis of such a system of an even number of identical axially polarized hollow piezoceramic cylinders (rings) in the form of a stack. This is used in Tonpilz type transducers for generation of underwater sound. This multilayered structure of piezoceramic rings is combined mechanically in series and electrically in parallel. Each ring is coated on both flat surfaces with electrodes and then glued together to create the stack. The schematic of a stack of axially polarized piezoelectric ceramic rings is shown in Fig. 3.1. Adjacent rings have opposite poling directions. The electrode and glue are neglected in this analysis as their thicknesses are much smaller than the length of each ring. When a voltage is applied across the stack, each ring receives the same voltage and allows 'large' expansions for a reasonable voltage. The input electrical admittance and some characteristic frequencies in the neighborhood of the resonance frequencies of the stack are of interest.

In this chapter, the model of an axially polarized piezoceramic ring developed in Chapter 2 is extended to analyze an electrically excited stack of a finite number of axially polarized piezoceramic rings. As in Chapter 2, in the analysis of a stack, the primary variables are the displacements and the electric potential. The stresses and electric field components are treated as the secondary variables and those are expressed in terms of the same coefficients that are used to describe the primary variables. In Chapter 2, these coefficients are determined by using the boundary conditions on the flat and curved surfaces of the ring. The coefficients are then used to find the primary and secondary variable and the Input Electrical Admittance (IEA) in the ring. In this Chapter, each ring is in contact with one or two neighbors as shown in Fig. 3.1. The normal and shear stresses are zero on both the curved surfaces of each ring. However, the stresses and displacements on the flat boundaries of the rings that are not at the ends are not known a priori and cannot be directly used to determine the coefficients. Therefore, a transfer matrix approach is used.

In the transfer matrix approach, the coefficients for each ring are not initially determined. Instead, the normal stress and displacement on one flat surface are expressed in terms of the same functions on the other flat surface of the ring and the applied electric potential. Then, the continuity conditions are applied to develop a model of the stack. Then, the zero-normal-stress boundary conditions on the flat ends of the stack are used to determine displacements at the ends of the stack. At this stage, the normal stress and displacement at one end of the two rings at the ends of the stack are known. They are used to determine the normal stress and displacement at the other end of the ring by using the transfer matrix for the rings. The procedure is repeated until all the normal stresses and displacements at both flat ends of all the rings are known. Then, the coefficients for each ring are determined and used to find the current in each ring. They can also be used to find the primary and secondary variable within each ring.

The series solution used in Chapter 2 is labeled as an anti-symmetric series because the axial displacement is anti-symmetric with respect to the mid-plane of the cylinder. The radial displacement is, however, symmetric. A symmetric series solution also exists in which the axial displacement is symmetric with respect to the mid-plane of the cylinder and the radial displacement is anti-symmetric. In the anti-symmetric series and in the symmetric series, the electric potential is neither purely anti-symmetric nor purely symmetric.

In Chapter 2, only the axial displacement that is anti-symmetric with respect to the plane that is midway between the flat ends of the cylinder has been considered. This is sufficient because only zero boundary conditions are considered and application of the electric potential causes the axial vibration of the cylinder to be anti-symmetric. However, with appropriate boundary conditions, the axial displacement can be symmetric with respect to the plane. This analysis is, however, not done in Chapter 2. In the general case, the axial displacement is a combination of anti-symmetric and symmetric components. Ebenezer et al. [55, 56] analyze purely anti-symmetric and purely symmetric axial vibrations of solid elastic cylinders in 2005 and 2008, respectively. A combination of anti-symmetric and symmetric axial vibration is considered in Chapters 3 and 4.

In this Chapter, anti-symmetric and symmetric axial vibrations of hollow piezoelectric cylinders are considered. This is necessary as the vibration of a ring in a stack is neither purely anti-symmetric nor purely symmetric. However, as a stack with several rings is of interest, and the ratio of the length to mean diameter is usually more than one, only the

leading terms in the series are used. Numerical results are presented to show that this is sufficient for many cases of practical interest. A simple extension of the method yields a model based on series solutions.

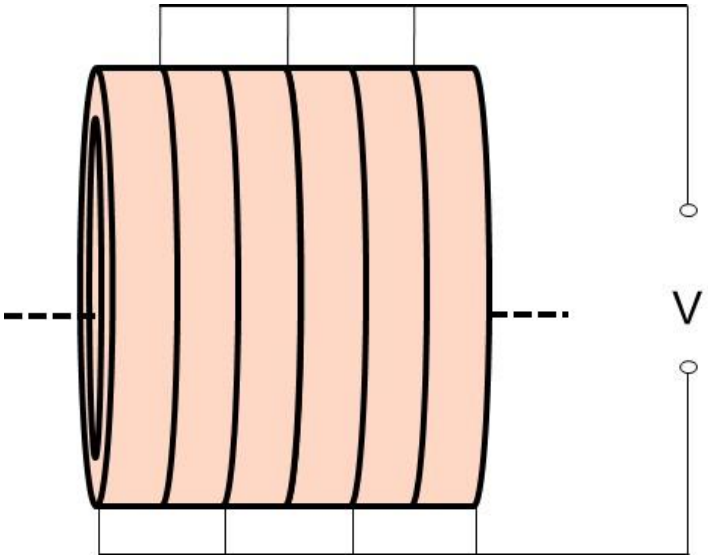

Fig. 3.1. Schematic of a stack of piezoelectric ceramic rings.

3.2 AN EXACT SOLUTION

In this Chapter, a model of a ring that is suitable for use as a building block to model a stack is first developed. The origin of the cylindrical local coordinate system is placed at the geometric center of each ring in the stack. Only the leading terms of the exact anti-symmetric and symmetric series solutions to the exact governing equations (2.5) are used. The solution that is used in this Chapter for each ring is the sum of five solutions. Each solution is a function of only the axial or radial coordinate. It is expressed in the form

$$\begin{Bmatrix} U \\ W \\ \emptyset \end{Bmatrix} = \begin{Bmatrix} U_1 \\ W_1 \\ \emptyset_1 \end{Bmatrix} + \begin{Bmatrix} U_2 \\ W_2 \\ \emptyset_2 \end{Bmatrix} + \begin{Bmatrix} U_3 \\ W_3 \\ \emptyset_3 \end{Bmatrix} + \begin{Bmatrix} U_4 \\ W_4 \\ \emptyset_4 \end{Bmatrix} + \begin{Bmatrix} U_5 \\ W_5 \\ \emptyset_5 \end{Bmatrix} \tag{3.1a}$$

where

$$\begin{Bmatrix} U_1 \\ W_1 \\ \emptyset_1 \end{Bmatrix} = \begin{Bmatrix} A_1 \sin(k_{z0} z) \\ 0 \\ A_1 \frac{e_{33}}{\varepsilon_{33}^S} \sin(k_{z0} z) \end{Bmatrix} \tag{3.1b}$$

$$\begin{Bmatrix} U_2 \\ W_2 \\ \emptyset_2 \end{Bmatrix} = \begin{Bmatrix} A_2 \cos(k_{z0} z) \\ 0 \\ A_2 \frac{e_{33}}{\varepsilon_{33}^S} \cos(k_{z0} z) \end{Bmatrix} \tag{3.1c}$$

$$\begin{Bmatrix} U_3 \\ W_3 \\ \emptyset_3 \end{Bmatrix} = \begin{Bmatrix} 0 \\ B_1 J_1(k_{r0} r) + B_2 Y_1(k_{r0} r) \\ 0 \end{Bmatrix} \tag{3.1d}$$

$$\begin{Bmatrix} U_4 \\ W_4 \\ \emptyset_4 \end{Bmatrix} = \begin{Bmatrix} Q_1 J_0(k_{r0} r) + Q_2 Y_0(k_{r0} r) \\ 0 \\ Q_1 \frac{e_{15}}{\varepsilon_{11}^S} J_0(k_{r0} r) + Q_2 \frac{e_{15}}{\varepsilon_{11}^S} Y_0(k_{r0} r) \end{Bmatrix} \tag{3.1e}$$

and

$$\begin{Bmatrix} U_5 \\ W_5 \\ \emptyset_5 \end{Bmatrix} = \begin{Bmatrix} 0 \\ 0 \\ Dz + E \end{Bmatrix}. \tag{3.1f}$$

Here A_1, A_2, Q_1, Q_2, B_1,B_2, D, and E are the coefficients to be determined. k_{z0}, k_{r0}, $J_n(.)$ and $Y_n(.)$, $n = 0, 1$ follows the same definition as in Chapter2.

The axial displacement, U, is expressed as the sum of anti-symmetric terms in Eq. (3.1b) and symmetric terms in Eq. (3.1c) and (3.1e). It is a function of r and z. The radial displacement, W, is expressed as the sum of symmetric terms in Eqs. (3.1d). It is a function of only r. The electric potential, $\emptyset$, is expressed as the sum of anti-symmetric terms in Eq. (3.1b) and symmetric terms in Eq. (3.1c) and a combination of anti-symmetric and symmetric terms in Eq. (3.1f). It is a function of r and z.

Substituting the expressions for displacements and electric potential in Eq. (3.1) in the stress-strain and strain-displacement relations in Eqs. (2.3) and (2.2), respectively, yields the stress and electric displacement. The axial and radial components of normal stress are expressed as

$$T_{zz} = A_1 c_{33}^D k_{z0} \cos(k_{z0} z) - A_2 c_{33}^D k_{z0} \sin(k_{z0} z) + B_1 c_{13}^E k_{r0} J_0(k_{r0} r) + B_2 c_{13}^E k_{r0} Y_0(k_{r0} r) + D e_{33} \tag{3.2}$$

and

$$T_{rr} = A_1(c_{13}^E + e_{31}e_{33}/\varepsilon_{33}^S)k_{z0}\cos(k_{z0}z) - A_2(c_{13}^E + e_{31}e_{33}/\varepsilon_{33}^S)k_{z0}\sin(k_{z0}z) +$$
$$B_1\left\{c_{11}^E k_{r0}J_0(k_{r0}r) + \frac{c_{12}^E - c_{11}^E}{r}J_1(k_{r0}r)\right\} + B_2\left\{c_{11}^E k_{r0}Y_0(k_{r0}r) + \frac{c_{12}^E - c_{11}^E}{r}Y_1(k_{r0}r)\right\} + De_{31}, \quad (3.3)$$

respectively; and both are functions of the axial and radial coordinates. The shear stress is expressed as

$$T_{rz} = -\left(c_{44}^E + \frac{{e_{15}}^2}{\varepsilon_{11}^S}\right)k_{r0}\{Q_1J_1(k_{r0}r) + Q_2Y_1(k_{r0}r)\} \quad (3.4)$$

and is a function of only the radial coordinate. The axial component of electric displacement is expressed as

$$D_z = B_1e_{31}k_{r0}J_0(k_{r0}r) + B_2e_{31}k_{r0}Y_0(k_{r0}r) - D\varepsilon_{33}^S \quad (3.5)$$

and is a function of only the radial coordinate. The radial component of the electric field displacement D_r vanishes everywhere. Finally, the current in the ring is expressed as

$$I = -\int_a^b j\omega D_z\, 2\pi r dr$$
$$= -2\pi j\omega\left\{B_1e_{31}[bJ_1(k_{r0}b) - aJ_1(k_{r0}a)] + B_2e_{31}[bY_1(k_{r0}b) - aY_1(k_{r0}a)] - D\varepsilon_{33}^S\frac{b^2 - a^2}{2}\right\} \quad (3.6)$$

and the input electrical admittance is determined by using $Y = \frac{I}{\emptyset_0}$.

The solutions in Eq. (3.1) contain eight coefficients that are determined by using the boundary conditions. As there are only eight coefficients, only eight boundary conditions can be satisfied. In Chapter 2, ten boundary conditions are specified: Two for the potential and two stress or displacement conditions on each of the four surfaces. Here, in order to simplify the model, only eight coefficients are used and appropriate conditions are to be specified and satisfied. This is done in the following sections for one ring and a stack of rings.

3.3 ONE RING

It is shown in Chapter 2 that the anti-symmetric series solution is necessary and sufficient to satisfy all the special cases for one cylinder or ring considered there. In this Chapter, the leading terms of the anti-symmetric and the symmetric series are used. Both are necessary to analyze a stack. In this Section, analysis of one ring is presented by using

the solution in Eq. (3.1). For the special case of a stress-free ring, all the coefficients of the leading terms of the symmetric series are expected to become zero - and it is shown that this happens.

In the one-dimensional model of a long thin rod or a stack of piezoelectric ceramic rings, it is assumed that the transverse stresses are zero. Therefore, the zero normal and shear stress boundary conditions on the inner and outer curved surfaces are to be satisfied. This accounts for four of the eight boundary conditions that can be satisfied by using the solution in Eq. (3.1). The two boundary conditions on the electric potential are essential for a model of a stack and they are to be specified and satisfied. This leaves two boundary conditions to be chosen. They are chosen to be either the specified normal stress or the normal displacement on each of the two flat ends of the ring. Alternatively, the normal stress and the normal displacement are specified on one of the flat ends and there are no boundary conditions at the other flat end. The latter set of conditions is used to develop the transfer matrix for the ring. This is in contrast with Chapter 2 where two boundary conditions are specified on each of the two flat ends of the ring. The boundary condition that is not considered in this Chapter is on the shear stress on the flat surfaces. However, if the shear stress is zero on both the curved surfaces it will be small everywhere within the stack. If the shear stress is zero on one or both ends of the stack, it will be even smaller throughout the stack. It is shown later that, as expected, the present model yields results that are in better agreement with exact axisymmetric finite element results for a stress-free stack than the one-dimensional rod model [3]. The stress-free stack is of special interest because the stack is a component of underwater transducers and is tested in the stress-free condition before it is used in the assembly of transducer.

In this Section, a model of a ring with zero stress on all the surfaces is presented and the results are compared with those obtained using the series solution for Case 3 in Chapter 2.

The boundary conditions on the electric potential $\emptyset$ are:

$$\emptyset = \emptyset_0 \text{ on } = L/2, \tag{3.7a}$$

and

$$\emptyset = 0 \text{ on } z = -L/2 \tag{3.7b}$$

on the top and bottom flat surface of the ring, respectively. Substituting the expression for electric potential $\emptyset$ in Eq. (3.1a) into the boundary conditions in Eq. (3.7) yields

$$A_1 \frac{e_{33}}{\varepsilon_{33}^S} \sin(k_{z0}\, L/2) + A_2 \frac{e_{33}}{\varepsilon_{33}^S} \cos(k_{z0}\, L/2) + D\, L/2 = \emptyset_0 \qquad (3.8a)$$

and

$$-A_1 \frac{e_{33}}{\varepsilon_{33}^S} \sin(k_{z0}\, L/2) + A_2 \frac{e_{33}}{\varepsilon_{33}^S} \cos(k_{z0}\, L/2) - D\, L/2 = 0. \qquad (3.8b)$$

These conditions are independent of r and can, therefore, be exactly satisfied at every point on the flat surfaces.

The normal and shear stresses are specified to be zero at every point on the surface. The expression for T_{zz} in Eq. (3.2) is dependent on the radial coordinate r. Therefore, uniform or zero T_{zz} at every point can be achieved only by choosing B_1=B_2=0. This results in W=0 which is unrealistic. Therefore, boundary conditions on the normal component of stress, on the two flat surfaces, are satisfied only in an average sense by equating the integral of the stress over the area to zero:

$$\int_a^b T_{zz}\, 2\pi r dr = 0 \text{ on } z = \pm L/2. \qquad (3.9a, 3.9b)$$

Substituting the expression for T_{zz} in Eq. (3.9) yields

$$A_1 c_{33}^D S k_{z0} \cos(k_{z0}\mathrm{L}/2) - A_2 c_{33}^D S k_{z0} \sin(k_{z0}\mathrm{L}/2) + B_1 c_{13}^E 2\pi k_{r0}[bJ_1(k_{r0}b) - aJ_1(k_{r0}a)] + B_2 c_{13}^E 2\pi k_{r0}[bY_1(k_{r0}b) - aY_1(k_{r0}a)] + De_{33}S = 0, \qquad (3.10a)$$

at $z = L/2$ and

$$A_1 c_{33}^D S k_{z0} \cos(k_{z0}\mathrm{L}/2) + A_2 c_{33}^D S k_{z0} \sin(k_{z0}\mathrm{L}/2) + B_1 c_{13}^E 2\pi k_{r0}[bJ_1(k_{r0}b) - aJ_1(k_{r0}a)] + B_2 c_{13}^E 2\pi k_{r0}[bY_1(k_{r0}b) - aY_1(k_{r0}a)] + De_{33}S = 0. \qquad (3.10b)$$

at $z = -L/2$ where $c_{33}^D = c_{33}^E + \mathrm{e}_{33}^2/\varepsilon_{33}^S$ and $S = \pi(b^2 - a^2)$.

Similarly, T_{rr} is independent of z only when $A_1 = A_2 = 0$. This makes U indepdent of z. Therefore, $T_{rr} = 0$ or a constant on the curved surfaces is satisfied only in an average sense:

$$\int_{-L/2}^{L/2} T_{rr}\, 2\pi r dz = 0 \text{ on } r = a \text{ and } r = b. \qquad (3.11a, 3.11b)$$

Substituting the expression for T_{rr} in Eq. (3.4) into Eq. (3.11) yields

$$A_1 c_{13}^D 4\pi a \sin(k_{z0}\mathrm{L}/2) + B_1 2\pi aL \left[c_{11}^E k_{r0} J_0(k_{r0}a) + \frac{c_{12}^E - c_{11}^E}{a} J_1(k_{r0}a)\right] + B_2 2\pi aL \left[c_{11}^E k_{r0} Y_0(k_{r0}a) + \frac{c_{12}^E - c_{11}^E}{a} Y_1(k_{r0}a)\right] + De_{31} 2\pi aL = 0 \qquad (3.12a)$$

on $r = a$ and

$$A_1 c_{13}^D 4\pi b \sin(k_{z0}\mathrm{L}/2) + B_1 2\pi bL\left[c_{11}^E k_{r0} J_0(k_{r0}b) + \frac{c_{12}^E - c_{11}^E}{b} J_1(k_{r0}b)\right] +$$

$$B_2 2\pi bL\left[c_{11}^E k_{r0} Y_0(k_{r0}b) + \frac{c_{12}^E - c_{11}^E}{b} Y_1(k_{r0}b)\right] + De_{31} 2\pi bL = 0. \quad (3.12b)$$

on $r = b$ where $c_{13}^D = c_{13}^E + e_{31}e_{33}/\varepsilon_{33}^S$.

The averaged conditions on shear stress T_{rz} are

$$\int_{-L/2}^{L/2} T_{rz}\, 2\pi r dz = 0 \text{ on } r = a \text{ and } r = b. \quad (3.13a, 3.13b)$$

Substituting the expression of T_{rz} in Eq. (3.5) into the conditions in Eq. (3.13) yields

$$-Q_1\left(c_{44}^E + \frac{{e_{15}}^2}{\varepsilon_{11}^S}\right) 2\pi aLk_{r0} J_1(k_{r0}a) - Q_2\left(c_{44}^E + \frac{{e_{15}}^2}{\varepsilon_{11}^S}\right) 2\pi aLk_{r0} Y_1(k_{r0}a) = 0 \quad (3.14a)$$

on $r = a$ and

$$-Q_1\left(c_{44}^E + \frac{{e_{15}}^2}{\varepsilon_{11}^S}\right) 2\pi bLk_{r0} J_1(k_{r0}b) - Q_2\left(c_{44}^E + \frac{{e_{15}}^2}{\varepsilon_{11}^S}\right) 2\pi bLk_{r0} Y_1(k_{r0}b) = 0. \quad (3.14b)$$

on $r =$ b.

The boundary conditions in Eqs. (3.8), (3.10), (3.12), and (3.14) are expressed in the matrix form,

$$[\mathrm{R}]\begin{bmatrix} A_1 \\ A_2 \\ B_1 \\ B_2 \\ D \\ E \\ Q_1 \\ Q_2 \end{bmatrix} = \begin{bmatrix} \emptyset_0 \\ 0 \\ 0 \\ 0 \\ 0 \\ 0 \\ 0 \\ 0 \end{bmatrix} \quad (3.15a)$$

where

$$[\mathrm{R}] = \begin{bmatrix} e_{33}\sin(Z)/\varepsilon_{33}^S & e_{33}\cos(Z)/\varepsilon_{33}^S & 0 & 0 & L/2 & 1 & 0 & 0 \\ -e_{33}\sin(Z)/\varepsilon_{33}^S & e_{33}\cos(Z)/\varepsilon_{33}^S & 0 & 0 & -L/2 & 1 & 0 & 0 \\ Sc_{33}^D k_{z0}\cos(Z) & -Sc_{33}^D k_{z0}\sin(Z) & 2\pi c_{13}^E J_{ba} & 2\pi c_{13}^E Y_{ba} & Se_{33} & 0 & 0 & 0 \\ Sc_{33}^D k_{z0}\cos(Z) & Sc_{33}^D k_{z0}\sin(Z) & 2\pi c_{13}^E J_{ba} & 2\pi c_{13}^E Y_{ba} & Se_{33} & 0 & 0 & 0 \\ 2ac_{13}^D\sin(Z) & 0 & LJ_{ca} & LY_{ca} & aLe_{31} & 0 & 0 & 0 \\ 2bc_{13}^D\sin(Z) & 0 & LJ_{cb} & LY_{cb} & bLe_{31} & 0 & 0 & 0 \\ 0 & 0 & 0 & 0 & 0 & 0 & k_{r0}c_{45}^D J_{1a} & k_{r0}c_{45}^D Y_{1a} \\ 0 & 0 & 0 & 0 & 0 & 0 & k_{r0}c_{45}^D J_{1b} & k_{r0}c_{45}^D Y_{1b} \end{bmatrix}$$

(3.15b)

is an 8th order square matrix, $Z = k_{z0}L/2$, $c_{13}^D = c_{13}^E + e_{31}e_{33}/\varepsilon_{33}^S$, $c_{45}^D = c_{44}^E + {e_{15}}^2/\varepsilon_{11}^S$, $J_{1b} = bJ_1(k_{r0}b)$, $J_{1a} = aJ_1(k_{r0}a)$, $J_{0b} = bJ_0(k_{r0}b)$, $J_{0a} = aJ_0(k_{r0}a)$, $Y_{1b} = bY_1(k_{r0}b)$, $Y_{1a} = aY_1(k_{r0}a)$, $Y_{0b} = bY_0(k_{r0}b)$, $Y_{0a} = aY_0(k_{r0}a)$, $J_{ca} = c_{11}^E k_{r0} J_{0a} + \frac{c_{12}^E - c_{11}^E}{a} J_{1a}$, $Y_{ca} = c_{11}^E k_{r0} Y_{0a} + \frac{c_{12}^E - c_{11}^E}{a} Y_{1a}$, $J_{cb} = c_{11}^E k_{r0} J_{0b} + \frac{c_{12}^E - c_{11}^E}{b} J_{1b}$, $Y_{cb} = c_{11}^E k_{r0} Y_{0b} + \frac{c_{12}^E - c_{11}^E}{b} Y_{1b}$, $J_{ba} = J_{1b} - J_{1a}$, and $Y_{ba} = Y_{1b} - Y_{1a}$.

The eight coefficients are determined by solving Eq. (3.15). The current and the input electrical admittance are then computed using these coefficients and Eq. (3.6). Numerical results for one ring are presented in Section 3.5.

It is noted that the matrix [R] in Eq. (3.15) is sparse and Eq. (3.15) can be rewritten as two independent matrix equations. One independent matrix equation is formed by using Eqs. (3.14a) and (3.14b) with the coefficients Q_1 and Q_2. In Eq. (3.15), they are the last two of the eight Eqs. It is to be satisfied at all frequencies. This is done by using $Q_1 = Q_2 = 0$. It is seen from the matrix equation that the determinant is zero at some frequencies and that Q_1 and Q_2 become indeterminate and need not be zero at these frequencies. Therefore, $Q_1 = Q_2 = 0$ is used at all frequencies. It is seen from Eq. (3.4) that this results in zero shear stress everywhere in the ring. Therefore, non-zero shear stress boundary conditions cannot be satisfied on the flat surfaces. In many applications, in addition to zero shear stress on the inner and outer curved surfaces, one end of the ring or stack or the device has zero shear stress. For example, in Tonpilz transducers in water, the radiating face of the head has zero shear stress and the end of the tail mass has zero shear stress. Therefore, it is reasonable to assume that shear stress is zero everywhere in the stack and transducer.

It is important to note, at this stage, that the normal radial and tangential stresses are not assumed to be zero everywhere. These assumptions are used in the classic rod model [3]. Martin [5] presents a model of a cylinder in which the membrane approximation is used and the normal radial stress is assumed to be zero everywhere because it is zero on the inner and outer curved surfaces. Therefore, the exact solution in Eq. (3.1) to the exact governing equations in Eq. (2.5) is expected to yield results that are in better agreement with exact axisymmetric finite element results for a stack than the one-dimensional rod model [3] based on approximate solutions to Eq. (2.5).

3.4 STACK

Analysis of one ring is extended to analyze a stack of a finite number of axially polarized piezoceramic rings. First, a transfer matrix for one ring is developed by using the solution in Eq. (3.1) and the stress-free boundary conditions on the inner and outer curved surfaces and the specified potentials of zero and one on the flat ends of the ring. Then, a model of the stack is easily developed by using the transfer matrix for each ring. The details are presented below.

The transfer matrix for a ring is expressed in terms of the functions that are continuous at the interfaces between rings and the applied electric potential. In an exact model, the normal and shear stresses and axial and radial displacements are continuous at the interfaces. Here, only the normal stress and the axial displacement are continuous at the interfaces. The same continuity conditions are used in the rod model of the stack. Therefore, in the transfer matrix, the normal stress and the axial displacement at one end of the ring are expressed in terms of the normal stress and the axial displacement at the other end of the ring and the potential difference applied across its ends.

If either the normal stress or the axial displacement are specified at each end of the ring, these boundary conditions together with the two boundary conditions on the applied potential form a system of six equations that can be solved to determine the coefficients A_1, A_2, B_1, B_2, D, and E. Then, the coefficients can be used to determine all the functions of interest at the ends of the ring and within the ring. Similarly, if the normal stress and the axial displacement are specified at one end of the ring, the coefficients can be determined and used to find the functions of interest on the other end of the ring. Alternatively, the normal stress and the axial displacement at one end can be expressed in terms of the normal stress and the axial displacement at the other end, the applied potential, and the transfer matrix. The details of the method to find the transfer matrix are presented next.

In the stack, the axial displacement and axial stress are specified on one flat end. The conditions on electric potential on the flat surfaces of each ring and normal and shear stress on the curved surfaces remains the same. At the interface between two adjacent rings, the axial displacement and axial stress is continuous.

Consider the case where the normal stress and the axial displacement at $z = -L/2$ of the nth ring of the stack are specified:

$T_{zz} = T_n^-$ on $z = -L/2$

and

$$U = U_n^- \text{ on } z = -L/2. \tag{3.16}$$

Using the expressions for T_{zz} in Eq. (3.2) and U in Eq. (3.1), yields

$$A_1 c_{33}^D S k_{z0} \cos(k_{z0}\mathrm{L}/2) + A_2 c_{33}^D S k_{z0} \sin\left(\frac{k_{z0}\mathrm{L}}{2}\right) + B_1 c_{13}^E 2\pi k_{r0}[bJ_1(k_{r0}b) -$$

$$aJ_1(k_{r0}a)] + B_2 c_{13}^E 2\pi k_{r0}[bY_1(k_{r0}b) - aY_1(k_{r0}a)] + De_{33}S = T_n^-. \tag{3.17}$$

and

$$-A_1 \sin(k_{z0}L/2) + A_2 \cos(k_{z0}L/2) + Q_1 J_0(k_{r0}r) + Q_2 Y_0(k_{r0}r) = U_n^-. \tag{3.18}$$

These equations are combined with the boundary conditions on the normal stresses on the inner and outer curved surfaces in Eq. (3.12), the potential on the flat surfaces in Eq. (3.8), and expressed as

$$[M_n^-]\begin{Bmatrix} A_1 \\ A_2 \\ B_1 \\ B_2 \\ D \\ E \end{Bmatrix} = \begin{Bmatrix} T_n^- \\ U_n^- \\ 0 \\ 0 \\ 0 \\ \emptyset_0 \end{Bmatrix}. \tag{3.19a}$$

where

$$[M_n^-] = \begin{bmatrix} c_{33}^D S k_{z0} \cos(k_{z0}\mathrm{L}/2) & c_{33}^D S k_{z0} \sin(k_{z0}\mathrm{L}/2) & 2\pi c_{13}^E J_{ba} & 2\pi c_{13}^E Y_{ba} & e_{33}S & 0 \\ -\sin(k_{z0}L/2) & \cos(k_{z0}L/2) & 0 & 0 & 0 & 0 \\ 2ac_{13}^D \sin(Z) & 0 & LJ_{ca} & LY_{ca} & aLe_{31} & 0 \\ 2bc_{13}^D \sin(Z) & 0 & LJ_{cb} & LY_{ca} & bLe_{31} & 0 \\ e_{33}\sin(Z)/\varepsilon_{33}^S & e_{33}\cos(Z)/\varepsilon_{33}^S & 0 & 0 & L/2 & 1 \\ -e_{33}\sin(Z)/\varepsilon_{33}^S & e_{33}\cos(Z)/\varepsilon_{33}^S & 0 & 0 & -L/2 & 1 \end{bmatrix} \tag{3.19b}$$

Here $[M_n^-]$ is a square matrix of order 6. Similarly, the matrix equation corresponding to a specified stress T_n^+ and axial displacement U_n^+ on $z = L/2$, zero normal stress on the curved surfaces and a known potential applied between the electrodes on the flat surfaces of the nth ring is expressed as,

$$[M_n^+]\begin{Bmatrix} A_1 \\ A_2 \\ B_1 \\ B_2 \\ D \\ E \end{Bmatrix} = \begin{Bmatrix} T_n^+ \\ U_n^+ \\ 0 \\ 0 \\ 0 \\ \emptyset_0 \end{Bmatrix}. \tag{3.20a}$$

where

$$[M_n^+] = \begin{bmatrix} c_{33}^D S k_{z0}\cos(k_{z0}\mathrm{L}/2) & -c_{33}^D S k_{z0}\sin(k_{z0}\mathrm{L}/2) & 2\pi c_{13}^E J_{ba} & 2\pi c_{13}^E Y_{ba} & e_{33}S & 0 \\ \sin(k_{z0}L/2) & \cos(k_{z0}L/2) & 0 & 0 & 0 & 0 \\ 2ac_{13}^D\sin(Z) & 0 & LJ_{ca} & LY_{ca} & aLe_{31} & 0 \\ 2bc_{13}^D\sin(Z) & 0 & LJ_{cb} & LY_{ca} & bLe_{31} & 0 \\ e_{33}\sin(Z)/\varepsilon_{33}^S & e_{33}\cos(Z)/\varepsilon_{33}^S & 0 & 0 & L/2 & 1 \\ -e_{33}\sin(Z)/\varepsilon_{33}^S & e_{33}\cos(Z)/\varepsilon_{33}^S & 0 & 0 & -L/2 & 1 \end{bmatrix}. \tag{3.20b}$$

Eqs. (3.19) and (3.20) can be combined into the following form:

$$\begin{Bmatrix} T_n^+ \\ U_n^+ \\ 0 \\ 0 \\ 0 \\ \emptyset_0 \end{Bmatrix} = [M_n]\begin{Bmatrix} T_n^- \\ U_n^- \\ 0 \\ 0 \\ 0 \\ \emptyset_0 \end{Bmatrix} \tag{3.21}$$

where $[M_n] = [M_n^+][M_n^-]^{-1}$.

The first two equations of Eq. (3.21) can be rewritten as

$$[T_n^+ \quad U_n^+]^T = [D_n][T_n^- \quad U_n^-]^T + \{d_n\}\emptyset_0 \tag{3.22}$$

where $[D_n]$ and $\{d_n\}$ are submatrices of $[M_n]$ of order 2×2 and 2×1, respectively. In Eq. (3.22), the normal stress and displacement at one end of the *n*th ring are expressed in terms of the normal stress and displacement at the other end of the ring and the potential difference.

When N rings are assembled to form a stack, the top flat surface of the *n*th ring ($1 \le n < N$) is pasted to the bottom flat surface of the (*n*+1)th ring. Hence, the continuity of axial displacement and stress at the interface between the top flat surface of the *n*th ring and bottom flat surface of the (*n*+1)th ring are expressed as,

$$[T_n^+ \quad U_n^+]^T = [T_{n+1}^- \quad U_{n+1}^-]^T. \tag{3.23}$$

Then, substitution of Eq. (3.22) for each ring in the continuity equation in Eq. (3.23) yields

$$[T_N^+ \quad U_N^+]^T = [D_N D_{N-1} \dots D_2 D_1][T_1^- \quad U_1^-]^T + \{D_N D_{N-1} \dots D_3 D_2 d_1 + D_N D_{N-1} \dots D_4 D_3 d_2 + \cdots + D_N d_{N-1} + d_N\}\emptyset_0. \quad (3.24)$$

Here, the normal stress and axial displacement at one end of the stack are expressed in terms of the normal stress and axial displacement at the other end of the stack and the potential difference. Each ring has its own influences in the stack performance. This is taken in to account in Eq. (3.24), since the equation is expressed in terms of the products of the matrices associated with each ring in the stack. This equation has two unknowns because normal stress is zero at the ends of the stack. The displacements at both ends of the stack are determined by using the specified stresses at the ends of the stack and the applied potential difference.

The normal stress and the axial displacement are now known at bottom end of the 1st ring and the top end of the Nth ring. Therefore, the normal stress and the axial displacement at the top of the 1st ring is determined by using Eq. (3.22). Then, the normal stress and the axial displacement at the bottom of the 2nd ring are determined by using the continuity condition in Eq. (3.23). Then, the process is repeated until the normal stress and the axial displacement are known at both ends of each ring in the stack.

Next, the coefficients for each ring are determined by using Eq. (3.19). Then, the coefficients are used to determine the current in the nth ring, I_n, by using Eq. (3.7) and the total current in the stack is obtained using

$$I = \sum_{n=1}^{N} I_n. \quad (3.25)$$

Finally, the complex admittance, Y, is expressed as $Y = G + jB = I/\emptyset_0$.

3.5 NUMERICAL RESULTS

Numerical results are presented for different stacks with different rings but the PZT material is the same in all stacks - PZT 4 with losses. Analytically computed results are compared with those computed using ATILA. Second order, eight-noded, quadrilateral, axisymmetric, piezoelectric elements are used in ATILA with internal losses represented by complex coefficients. The basic set of piezoelectric coefficients and the density of the material that is used both in the analytical model and ATILA are shown in Tables 2.1 and 2.2.

Critical frequencies of the rings and stacks with zero stresses on all the surfaces are computed in the neighborhood of the resonance frequencies and compared with ATILA and existing 1-D model. The details of the 1-D model is described in the Appendix of this Chapter. The model presented in this Chapter is to be used primarily for stacks in which the resonance frequency of interest is associated with predominantly axial vibration. However, all the resonance frequencies are discussed. In all the figures, a red line is used to show the results computed by the present method, a green line to show the results computed by the 1-D model, and blue dots are used to show those computed using ATILA, unless and otherwise specified. Both analytical and ATILA results are shown with same resolution of 10 Hz. The results are produced for three different cases. The description of the piezoceramic rings follows the same notation as in Chapter 2.

3.5.1 **Case 1**

In this case, the dimensions of the axially polarized piezoceramic rings are (12, 6, 3). The input electrical admittances of a single ring and stack of 4 such rings are computed and the critical parameters are compared. The input conductance (G) of the single ring, in the 100-600 kHz band, computed by the present model is shown in Fig. 3.2(a). The model predicts two resonances in this band; one at 121.60 kHz and other at 481.03 kHz. When the complete series solution is used, there are three resonances in the band at 120.87, 440.32, and 470.90, kHz as seen in Table 2.9 and there are three corresponding resonances in ATILA. The conductance computed using a one-dimensional model of a ring [3] is shown by a green line. This model has only one resonance in the band at 511.4 kHz.

The input conductance in the neighborhood of the first resonance is shown in Fig. 3.2(b). In the one-dimensional model, only the axial stress is considered and this model does not predict the radial resonance - as seen in Fig. 3.2(a). However, in the present model, radial stress is not assumed to be zero everywhere within the ring and the resonance frequency differs from that computed using ATILA by only 0.5%. Moreover, the computed conductance at the resonance frequency, G_{max}, is nearly equal to that computed using ATILA as can be seen in Fig. 3.2(b). Similar good agreement is reported in [30] for rings of other dimensions. The second resonance is primarily a function of the length of the ring. The resonance frequency computed using ATILA is 468.8 kHz and the G_{max} is 51.26 mS. The present model yields 481.03 kHz and G_{max} of 62.76 mS. The resonance predicted by the 1-D model is at 511.40 kHz. It is seen from Fig. 3.2(a) that 1-D model overestimates the resonance frequency and the conductance at this resonance.

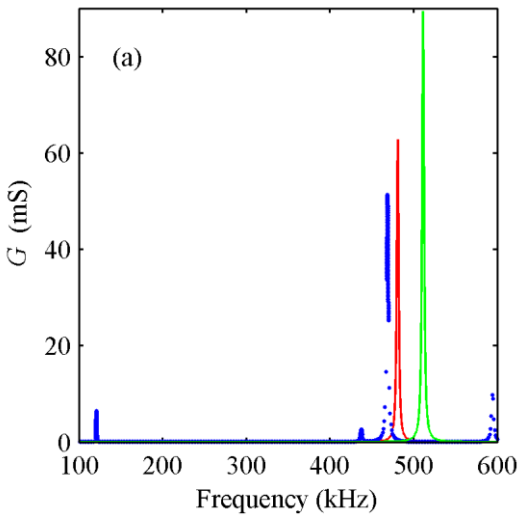

Fig. 3.2(a). Conductance in the 100-600 kHz band of a (12, 6, 3) ring. Red Line: Model; Dots: ATILA; and Green Line: 1-D model.

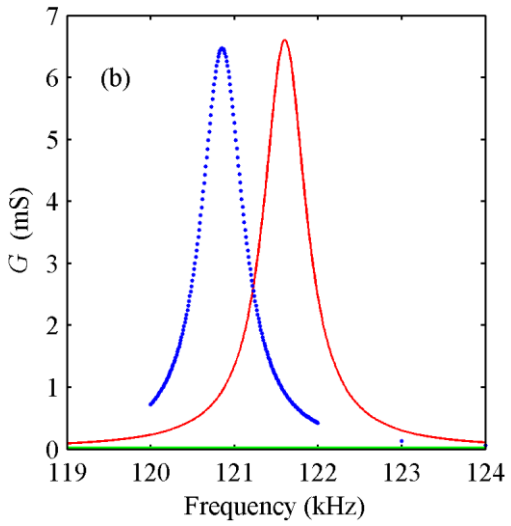

Fig. 3.2(b). Conductance in the neighborhood of the first resonance of a (12, 6, 3) ring. Red Line: Model; Dots: ATILA; and Green Line: 1-D model.

The magnitudes of the axial (blue line) and radial (red line) components of the displacements of the ring at the two resonances computed using the present method are shown in Fig. 3.3. Fig. 3.3(a) shows the axial and radial displacements at the first resonance frequency of 121.60 kHz at the mean radius, 4.5 mm. The magnitude of the radial displacement is about 7 times that of the axial displacement at this frequency and is uniform. This is the hoop mode resonance of the ring. The magnitudes of both the displacement components at the second resonance are shown in Fig. 3.3(b). Here, the magnitude of the axial displacement is about 7 times that of the radial displacement. This resonance is associated with the axial mode of the ring.

A stack of four (12, 6, 3) rings is then analyzed. In the stack, the length is equal to its diameter. The input conductance of the stack computed by the present model, ATILA, and the 1-D model are shown in Fig. 3.4(a) upto the third resonance frequency. The present model predicts the three resonances with G and B values approximately equal to those obtained using ATILA. But the 1-D model predicts only the resonance near 120 kHz. The input susceptance in this band is shown in Fig. 3.4(b).

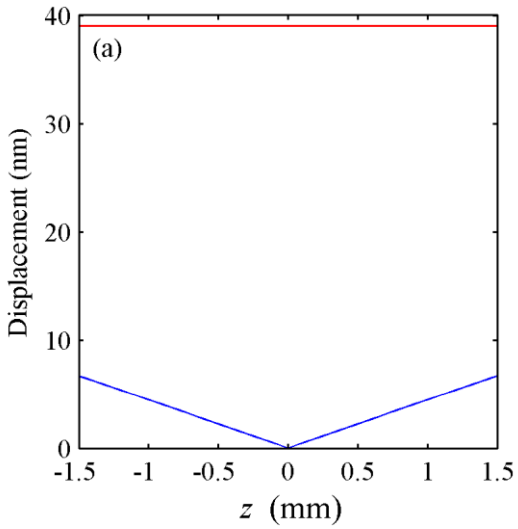

Fig. 3.3(a). Displacements at the first resonance, 121.6 kHz, of the (12, 6, 3) ring. Red line: Radial and blue line: axial displacements.

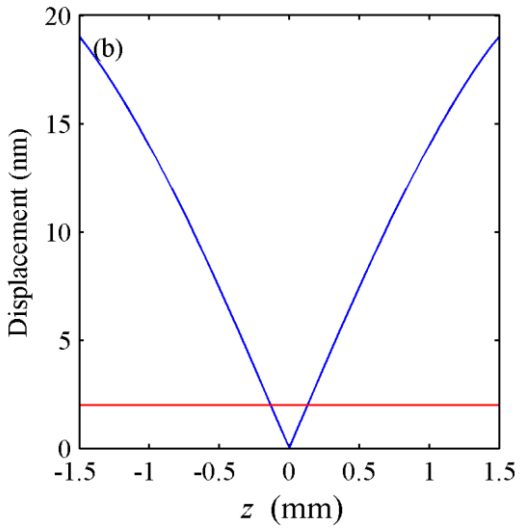

Fig. 3.3(b). Displacements at the second resonance, 481 kHz, of the (12, 6, 3) ring. Red line: Radial and blue line: axial displacements.

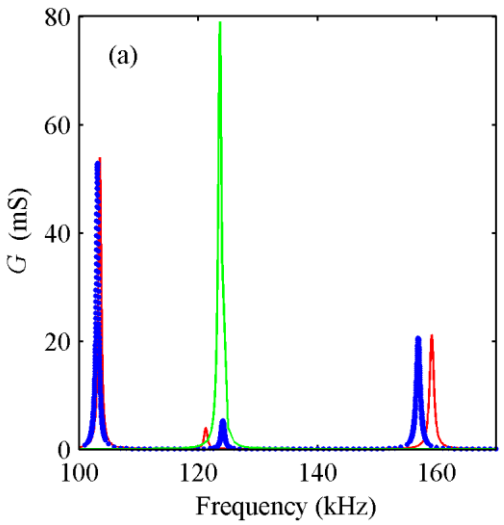

Fig. 3.4(a). Conductance of a stack of four (12, 6, 3) rings. Red Line: Present Method, Dots: ATILA, and Green Line: 1-D model.

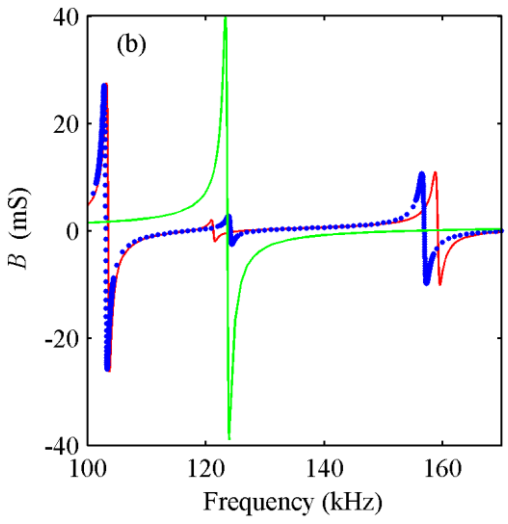

Fig. 3.4(b). Susceptance of a stack of four (12, 6, 3) rings. Red Line: Present Method, Dots: ATILA, and Green Line: 1-D model.

The critical frequencies and critical parameters in the neighborhood of the first three resonance frequencies of the four ring stack of (12, 6, 3) rings are presented in Table 3.1. Both analytical and ATILA values are given. Here, the second resonance is associated with the hoop mode of the stack that does not change by increasing the length of the stack. The resonance near 103 kHz is the length mode resonance of the stack. The maximum percentage error in the critical frequencies in the neighborhood of this resonance is 0.4%. Analytically computed values of the critical parameters are also in good agreement with ATILA values.

Table 3.1. G and B in the neighborhood of the first three resonances of the four ring stack of (12, 6, 3) rings.

Mode	Method	f_s (kHz)	G_{max} (mS)	$f_{-1/2s}$ (kHz)	B_{max} (mS)	$f_{1/2s}$ (kHz)	B_{min} (mS)
First	ATILA	103.1	52.85	102.9	27.04	103.4	-25.77
	Model	103.5	53.91	103.3	27.55	103.8	-26.34
	% Error	0.4	2	0.4	1.8	0.4	-2.2
Second	ATILA	124.1	5.253	123.8	2.711	124.4	-2.502
	Model	121.3	4.012	121	1.899	121.6	-2.059
	% Error	-2.2	-23.6	-2.3	-29.9	-2.25	17.7
Third	ATILA	156.9	20.51	156.5	10.62	157.3	-9.875
	Model	159.2	21.16	158.8	10.97	159.6	-10.17
	% Error	1.5	3.16	1.46	3.3	1.46	-2.9

3.5.2 **Case 2**

In case 2, numerical results are presented for stacks with rings of dimensions (50, 38, 8). The susceptance of the two ring stack in the neighborhood of its length mode resonance is shown in Fig. 3.5(a). The radial and length mode resonances of a (50, 38, 8) ring computed by the model described in Chapter 2 are at 23.98 kHz and at 192.2 kHz, respectively. The first two resonances of the two ring stack computed using the present model are at 23.91 kHz and 103.1 kHz. These frequencies are in good agreement with the ATILA computed resonance frequencies at 23.88 kHz and at 102.1 kHz.

The conductances in the neighborhood of the length mode resonance of the ten ring stack computed by the present method and by ATILA are shown in Fig. 3.5(b). The length mode resonances of the ten ring stack computed using the present model and ATILA are at 17.09 kHz. The G values at this frequency are also the same and equal to 94.7 mS. The

resonance frequency computed using the 1-D model is at 18.37 kHz and the G_{max} is 104.2 mS.

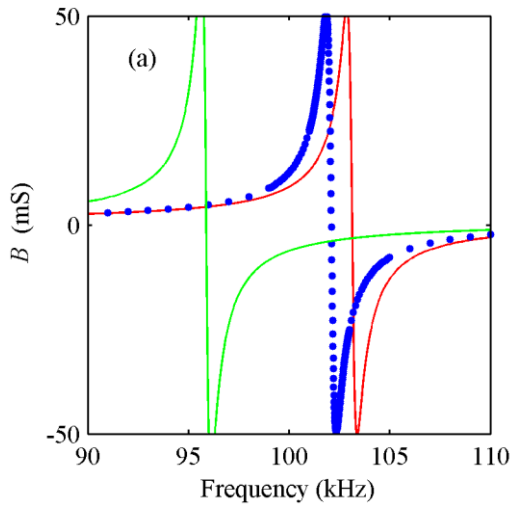

Fig. 3.5(a). Susceptance of a stack of two (50, 38, 8) mm rings. Red Line: Model, Dots: ATILA, and Green Line: 1-D model.

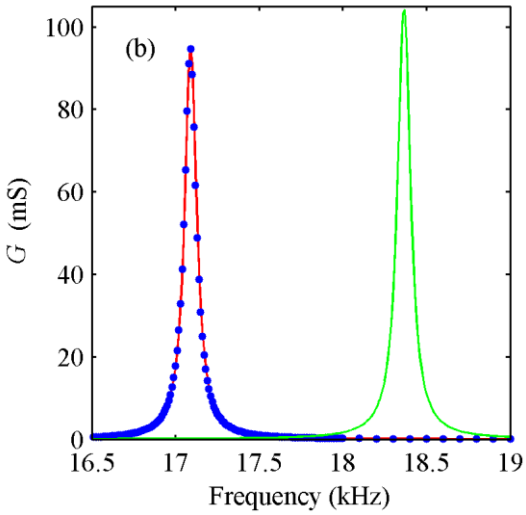

Fig. 3.5(b). Conductance of a stack of ten (50, 38, 8) mm rings at the length mode resonance of 17.09 kHz. Red Line: Model, Dots: ATILA, and Green Line: 1-D model.

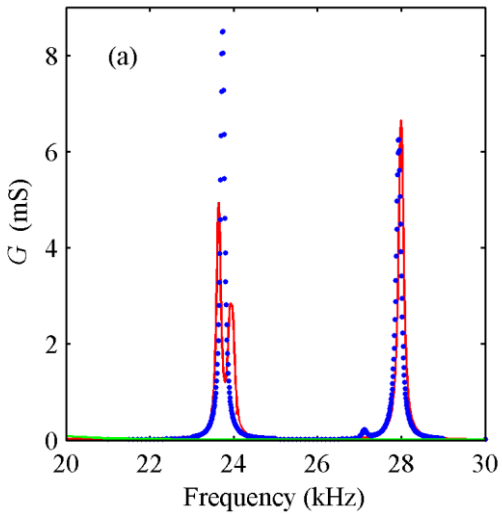

Fig. 3.6(a). Conductance in the neighborhood of the second and third resonances of the stack of ten (50, 38, 8) rings. Red Line: Model, Blue Dots: ATILA, and Green Line: 1-D model.

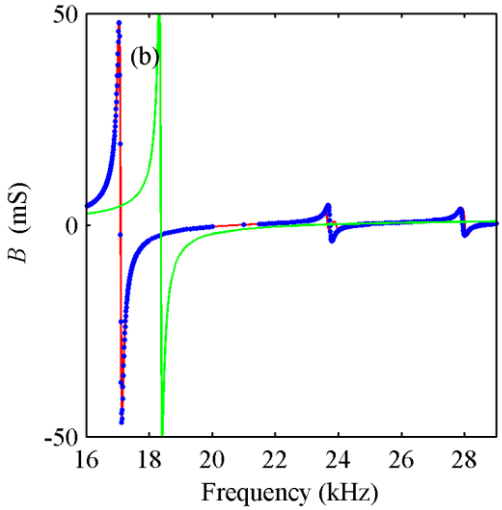

Fig. 3.6(b). Susceptance at the first three resonances of a stack of ten (50, 38, 8) rings. Red Line: Model, Blue Dots: ATILA, and Green Line: 1-D model.

The second, third, and fourth resonances of stack of ten rings are shown in Fig. 3.6(a). In ATILA, the second resonance is at 23.74 kHz and the first resonance of a single ring is at the same frequency. Therefore, it is concluded that it is a hoop mode resonance. In the present analysis, the second resonance is at 23.64 kHz and corresponds to the hoop mode. The third resonance is at 27.12 kHz in ATILA and at 23.93 kHz in the present model. The fourth resonance is at 27.94 kHz in ATILA and at 27.99 kHz in the present model. The error is 0.2%. The conductances are also in good agreement as seen in Fig. 3.6(a). These resonances are not predicted by the 1-D model. The susceptance, B, in the neighborhood of the first three resonances of this stack is shown in Fig. 3.6(b). The first two resonance frequencies and B values computed by the present model are in good agreement with ATILA.

The critical frequencies and associated values in the neighborhood of the length mode resonance of a single ring, two ring stack, and ten ring stack are given in Table 3.2. It can be seen from the table that the length mode resonance of the single ring computed using the present model is greater than those computed using ATILA. The difference decreases as the length of the stack increases. The maximum percentage error in critical frequencies is 1.5% and that occurs at the length mode resonance of a single ring.

Table 3.2. Critical parameters in the neighborhood of the length mode resonance of various stacks of (50, 38, 8) rings.

No. of rings in the stack	Method	f_s (kHz)	G_{max} (mS)	$f_{-1/2s}$ (kHz)	B_{max} (mS)	$f_{1/2s}$ (kHz)	B_{min} (mS)
1	Model	192.2	101.5	191.7	51.4	192.7	-50.1
	ATILA	189.4	95.87	188.9	48.61	189.9	-47.25
	% Error	1.5	5.8	1.1	5.7	1.5	-6.03
2	Model	103.1	102.6	102.9	53.18	103.4	-49.38
	ATILA	102.1	100	101.8	50.73	102.3	-49.3
	% Error	0.9	2.6	1	4.8	1.07	-0.016
10	Model	17.09	94.7	17.05	48.1	17.13	-46.63
	ATILA	17.09	94.7	17.05	47.89	17.13	-46.42
	% Error	0	0	0	0.4	0	-0.45

3.5.3 **Case 3**

In case 3, the ring considered have dimensions (100, 80, 6). The input electrical admittance of three different stacks with 12, 20, and 22 rings are computed in this case.

A single ring of the above dimension has the hoop mode resonance at 11.7 kHz and length mode resonance at 215.59 kHz. The critical frequencies and associated admittance values of different stacks with these rings are shown in Table 3.3. As the number of rings increases, the resonance near 11 kHz remains nearly unchanged. Therefore, it is the hoop mode resonance of the stack. The length mode resonance is approximately inversely proportional to the length when the length of the stack is not much less than the outer diameter. It is seen from Table 3.3 that it is at 22.8 kHz, 10.14 kHz, and 9.67 kHz for stacks with 12, 20, and 22, rings.

Table 3.3. Critical parameters in the neighborhood of the first two resonances of various stacks of (100, 80, 6) rings.

No. of rings in the stack	Resonance	Method	f_s (kHz)	G_{max} (mS)	$f_{-1/2s}$ (kHz)	B_{max} (mS)	$f_{1/2s}$ kHz)	B_{min} (mS)
12	I	Model	11.33	127.2	11.31	70.02	11.36	-58.93
		ATILA	11.36	147.9	11.33	77.93	11.39	-69.76
		% Error	-0.3	-14	-0.3	-10.15	-0.3	15.5
	II	Model	22.8	456.6	22.75	232.2	22.86	-224
		ATILA	22.78	456.7	22.73	232.4	22.84	-224.1
		% Error	0.08	-0.02	0.08	-0.09	0.09	-0.04
20	I	Model	10.14	382.3	10.12	201.7	10.17	-190.9
		ATILA	10.14	391.8	10.11	199	10.16	-185.8
		% Error	0	-2.4	0.09	1.36	0.09	-2.74
	II	Model	11.61	20.09	11.59	12.52	11.72	-12.39
		ATILA	11.69	35.62	11.66	17.51	11.72	-17.86
		% Error	-0.68	-43.6	-0.6	-28.5	0	30.6
22	I	Model	9.67	451.8	9.64	235.8	9.69	-226.3
		ATILA	9.66	458	9.64	234.8	9.69	-223.1
		% Error	0.1	-1.4	0	0.42	0	-1.4
	II	Model	11.59	22.09	11.56	14.51	11.72	-11.94
		ATILA	11.64	41.06	11.61	20.94	11.67	-19.87
		% Error	-0.43	-46	-0.43	-30.7	0.43	40

It is seen from Table 3.3 that, in all the stacks, the maximum error occurs at the hoop mode resonance. But, in most of the practical situations where we are dealing with piezoceramic stacks, we are interested in the length mode resonance. In all the stacks, the

error in the length mode resonance frequency computed using the present model is less than 0.1%.

The conductance of the twelve ring stack is shown in Fig. 3.7(a) upto the first three resonances. Only two of them are predicted by the 1-D model. Analytical and ATILA values are in very good agreement. The susceptance computed by the present method in the neighborhood of the first resonance is shown in Fig. 3.7(b). It can be seen that, *B* values are also in good agreement with ATILA computed values.

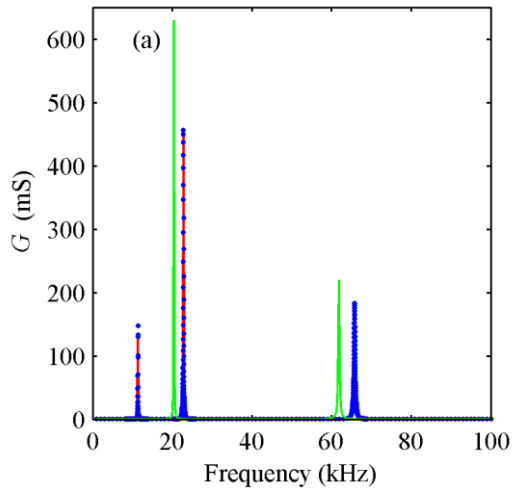

Fig. 3.7(a). Conductance of a stack of twelve (100, 80, 6) rings. Red Line: Model, Dots: ATILA, and Green Line: 1-D model.

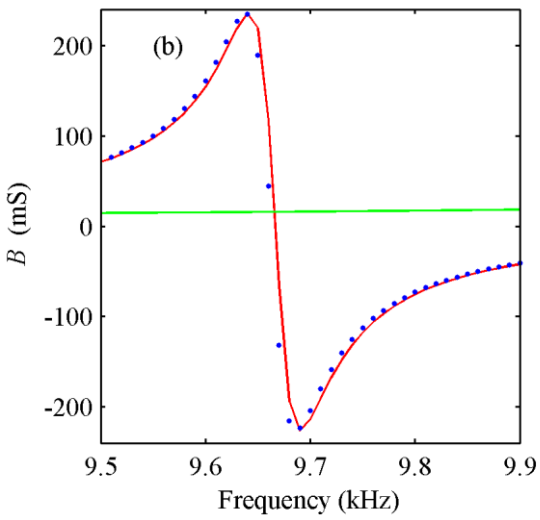

Fig. 3.7(b). Susceptance of a 22 ring stack of (100, 80, 6) rings at its length mode resonance. Red Line: Model, Dots: ATILA, and Green Line: 1-D model.

3.6 CONCLUSIONS

A method is presented here to compute the complex input electrical admittance and critical parameters of a stack of finite number of axially polarized piezoelectric ceramic rings with internal losses. The method is approximate in the sense that the exact series solution to the governing equations is not used and only the leading terms are used. Numerical results are presented for different stacks and are compared with ATILA - a finite element package for the analysis of sonar transducers. The proposed approximate axisymmetric two-dimensional model of the stack yields accurate results for the length mode resonances that are used in devices such as the Tonpilz transducer.

In Chapter 2, the complete series solution is used and a large number of the resonances are accurately determined. In this Chapter, only the leading terms in the series are used and the focus is on the resonances of the stack that will affect the performance of the Tonpilz transducer or device in the operating band of interest. Therefore, a simpler model that is able to accurately model the first few resonances of stacks with length that is greater than 0.5 times the mean diameter is presented.

APPENDIX A: 1-D model

In the classic one-dimensional model referred in [3], only the axial normal stress is considered and it is assumed that all other stresses are negligible. The axial displacement of the ring is expressed as

$$\xi = A\sin(kz) + B\cos(kz) \tag{A1}$$

where

$$k = \frac{\omega}{c} \text{ and } c = 1/\sqrt{\rho s_{33}^{D}}. \tag{A2}$$

The transfer matrix is expressed as

$$\begin{Bmatrix} F^{+} \\ U^{+} \\ I \end{Bmatrix} = \begin{bmatrix} 1+\frac{Z_1}{Z_2} & Z_1(2+\frac{Z_1}{Z_2}) & -\kappa\frac{Z_1}{Z_2} \\ \frac{1}{Z_2} & 1+\frac{Z_1}{Z_2} & \frac{-\kappa}{Z_2} \\ \frac{\kappa}{Z_2} & \kappa\frac{Z_1}{Z_2} & \frac{-\rho c\omega S C_0}{Z_2 \sin kL} \end{bmatrix} \begin{Bmatrix} F^{-} \\ U^{-} \\ \emptyset_0 \end{Bmatrix} \tag{A3}$$

where $U = \frac{\partial \xi}{\partial t}$ is the velocity, F is the axial force,

$$\kappa = \frac{g_{33} C_0}{s_{33}^{D}}, \tag{A4}$$

$$Z_1 = -j\rho cS \tan\left({}^{kL}/_{2}\right), \tag{A5}$$

and

$$Z_2 = \frac{j\rho cS}{\sin kL} - j\frac{\kappa^2}{\omega C_0}. \tag{A6}$$

In order to develop the model of the stack, Eq. (A3) is rewritten in the form

$$\begin{Bmatrix} F_n^{+} \\ U_n^{+} \end{Bmatrix} = [T] \begin{Bmatrix} F_n^{-} \\ U_n^{-} \end{Bmatrix} + \{t\}\,\emptyset_0 \tag{A7}$$

and

$$I = \tau_1 F_n^{-} + \tau_2 U_n^{-} + \tau_3 \emptyset_0 \tag{A8}$$

for the nth ring in the stack. T and t are the 2×2 and 2×1 submatrices respectively. For N identical rings in a stack,

$$\begin{Bmatrix} F_N^{+} \\ U_N^{+} \end{Bmatrix} = [T]^N \begin{Bmatrix} F_1^{-} \\ U_1^{-} \end{Bmatrix} + \left\{[T]^{N-1} + [T]^{N-2} + \cdots + T + \begin{bmatrix} 1 & 0 \\ 0 & 1 \end{bmatrix}\right\} t\,\emptyset_0. \tag{A9}$$

CHAPTER 4

CLASSICAL LANGEVIN TRANSDUCER

4.1 INTRODUCTION

Analytical multi-dimensional modeling of transducer components and the transducer itself is challenging due to difficulties in solving the partial differential equations governing the system and satisfying the space-dependent boundary and continuity conditions. A few components are analyzed using 1-D [3], 2-D [4, 10-13, 34], finite element [64-65] and exact axisymmetric models [25, 29-32, 55-56]. In this chapter, an exact series method is presented to analyze a classical Langevin transducer with internal losses.

A classical Langevin transducer is a type of sandwich transducer that comprises an axially polarized piezoelectric ceramic cylinder sandwiched between two elastic cylinders as shown in Fig. 4.1. All three cylinders have the same radius, a. The bottom and top elastic cylinders are referred to as the tail mass and head mass, respectively of the transducer. The head mass is usually shorter and lighter so that it vibrates more than the tail mass at the fundamental resonance frequency of the transducer. The piezoelectric cylinder is electrically excited. It is the predecessor of the Tonpilz transducer that is often used for generation of intense underwater sound.

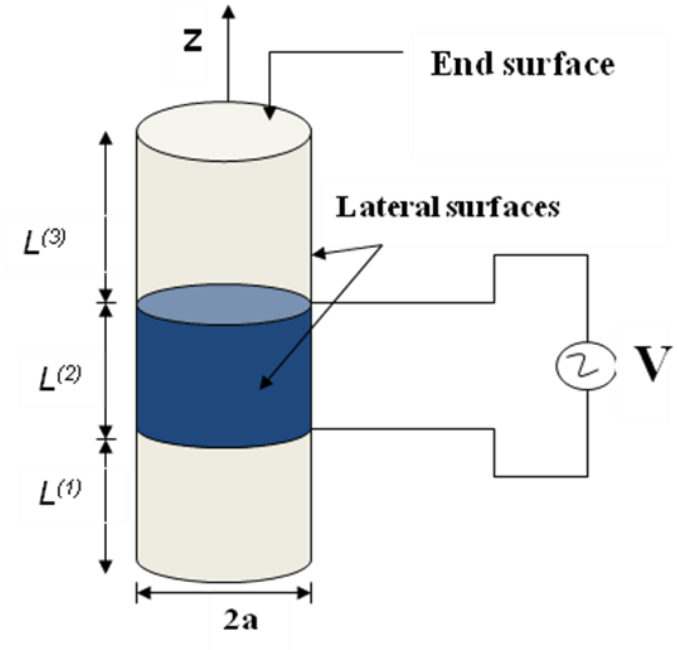

Fig. 4.1. Schematic of a Langevin Transducer.

In chapter 2, an axially polarized piezoceramic ring is analyzed using exact, linearized, and axisymmetric governing equations and exact series solutions. There are eight boundary conditions on surfaces and all of them are satisfied in a weighted average sense to get very accurate results for several resonance frequencies and other functions. Only the antisymmetric axial vibration with respect to the plane midway between the ends of the ring is excited by the application of electric potential difference across the electrodes and the only corresponding series solutions are chosen. In chapter 3, the complexity of the structure increases as there are several rings in the stack. In this case, there are boundary conditions on the inner and outer curved surfaces of each ring and the continuity conditions at the interfaces between rings are to be satisfied. The axial vibration of each ring is neither purely symmetric nor antisymmetric about the plane that is midway between the ends of each ring. However, only the lowest length mode resonance frequency is of primary interest. Therefore, exact series solutions are not expected to be necessary. Only the leading terms in the symmetric and antisymmetric series solutions are used to develop a model based on the transfer matrix of each ring. The error in finding the lowest length mode resonance frequency is less than that when using the classic one-dimensional model even when the length is much less than the outer diameter.

In this Chapter, a model of a stack of solid piezoelectric and elastic cylinders is developed by using exact series solutions. In Chapters 2 and 3, hollow cylinders are considered and it is necessary to include additional solutions to the governing equations to satisfy the boundary conditions on the inner curved surface. Here, there is only one curved surface. In Chapter 2, only one cylinder is considered and exact series solutions are used. In Chapter 3, only the leading terms in the series are used. Therefore, the boundary conditions are satisfied in only an average sense, the shear stress is zero everywhere, and continuity of radial displacement could not be considered. In this Chapter, a transducer with non-identical head and tail masses is modeled. Therefore, symmetric and antisymmetric series solutions are needed not only for the elastic cylinders but also for the piezoelectric cylinder. Antisymmetric solutions for the elastic cylinder have been studied earlier [55] but the same has not been done earlier for piezoelectric cylinders. Here, symmetric and antisymmetric series solutions are used to satisfy all the boundary and continuity conditions in a weighted average sense. As a large number of weights are used to satisfy the conditions in an average sense, the conditions are nearly satisfied at every point on the surface.

Therefore, several resonance frequencies and the corresponding primary and secondary variables are accurately determined.

All the three cylinders in the transducer are analyzed using functions that are symmetric and anti-symmetric with respect to the plane midway between the ends of the cylinders. The axial and radial components of displacement are the primary variables in both piezoelectric and elastic cylinders. Electric potential is also a primary variable for piezoelectric cylinder. Secondary variables including stresses and electric field displacements are expressed in terms of the weighted functions used to describe the primary variables.

Arbitrary piecewise continuous boundary conditions on the flat and curved surfaces and all the continuity conditions at the interfaces can be satisfied because of the completeness property of the solution sets. The coefficients in the series solutions are determined by satisfying the boundary and continuity conditions in a weighted average sense, as explained in Chapter 2, by using the orthogonal property of the Bessel and trigonometric functions. Numerical results are presented for different Langevin transducers to illustrate the good agreement between the values computed using the present method and ATILA.

4.2 GOVERNING EQUATIONS

Consider the Langevin transducer shown in Fig. 4.1. Cylindrical coordinates (r, θ, z) are used in the analysis. Local coordinates are used for each cylinder and the origin of the local system is at the centre of each cylinder. The three cylinders in the transducer are numbered 1, 2, and 3 starting from the bottom elastic cylinder. Superscripts denote the number of the cylinder but are omitted for convenience when it is clear from the context. The radius of each cylinder is a. The length of the nth cylinder is $L^{(n)}$, n = 1, 2, 3. The top and bottom flat surfaces of the piezoceramic cylinder are fully electroded. The electrical excitation and the response of the transducer have a $e^{j\omega t}$ variation in time that is suppressed everywhere for convenience.

The Langevin transducer, the boundary conditions, and the electrical excitation are axisymmetric. The axisymmetric governing differential equations for a piezoceramic cylinder are shown in Eq. (2.5). The axisymmetric governing differential equations for the elastic cylinder are presented in the following sub-section. Let $U^{(p)}$ and $W^{(p)}$ be the axial and radial displacements, respectively and $\emptyset$ be the electric potential.

4.2.1.1 Elastic Cylinder

The exact axisymmetric governing equations of the elastic cylinder are derived from the stress-strain, strain-displacement, and dynamic equilibrium by following a procedure similar to that used to derive the equations for a piezoelectric cylinder. Consider a solid, elastic, isotropic cylinder of radius a and finite length, $L^{(e)}$, where e is one or three. The dynamic equilibrium equations of an axisymmetric elastic cylinder [74] expressed in cylindrical coordinates (r, θ, z) are

$$\frac{\partial T_{rr}^{(e)}}{\partial z} + \frac{\partial T_{rz}^{(e)}}{\partial r} + \frac{1}{r} T_{rz}^{(e)} = -\rho^{(e)} \omega^2 U^{(e)} \tag{4.1a}$$

and

$$\frac{\partial T_{rr}^{(e)}}{\partial r} + \frac{\partial T_{rz}^{(e)}}{\partial z} + \frac{1}{r}\left(T_{rr}^{(e)} - T_{\theta\theta}^{(e)}\right) = -\rho^{(e)} \omega^2 W^{(e)}. \tag{4.1b}$$

Here, $U^{(e)}$ and $W^{(e)}$ are the axial and radial displacements, respectively, $T_{rr}^{(e)}$, $T_{zz}^{(e)}$, and $T_{\theta\theta}^{(e)}$ are the normal components of stress, $T_{rz}^{(e)}$ is the shear component of stress, $\rho^{(e)}$ is the density of the elastic material. The components of strain [74] are expressed as

$$\begin{bmatrix} S_{rr}^{(e)} & S_{\theta\theta}^{(e)} & S_{zz}^{(e)} & S_{rz}^{(e)} \end{bmatrix} = \begin{bmatrix} \frac{\partial W^{(e)}}{\partial r} & \frac{W^{(e)}}{r} & \frac{\partial U^{(e)}}{\partial z} & \frac{\partial U^{(e)}}{\partial r} + \frac{\partial W^{(e)}}{\partial z} \end{bmatrix}. \tag{4.2}$$

The constitutive relations for an isotropic elastic cylinder [74] are:

$$\begin{Bmatrix} T_{rr}^{(e)} \\ T_{\theta\theta}^{(e)} \\ T_{zz}^{(e)} \\ T_{rz}^{(e)} \end{Bmatrix} = \begin{bmatrix} \lambda^{(e)} + 2\mu^{(e)} & \lambda^{(e)} & \lambda^{(e)} & 0 \\ \lambda^{(e)} & \lambda^{(e)} + 2\mu^{(e)} & \lambda^{(e)} & 0 \\ \lambda^{(e)} & \lambda^{(e)} & \lambda^{(e)} + 2\mu^{(e)} & 0 \\ 0 & 0 & 0 & \mu^{(e)} \end{bmatrix} \begin{Bmatrix} S_{rr}^{(e)} \\ S_{\theta\theta}^{(e)} \\ S_{zz}^{(e)} \\ S_{rz}^{(e)} \end{Bmatrix}. \tag{4.3}$$

Combining Eqs. (4.1) – (4.3), the axisymmetric governing equations of the elastic cylinder are expressed as

$$\begin{bmatrix} \left(\lambda^{(e)} + 2\mu^{(e)}\right)\frac{\partial^2}{\partial z^2} + \mu^{(e)}\left[\frac{\partial^2}{\partial r^2} + \frac{1}{r}\frac{\partial}{\partial r}\right] + \rho^{(e)}\omega^2 & \left(\lambda^{(e)} + \mu^{(e)}\right)\left[\frac{\partial^2}{\partial r \partial z} + \frac{1}{r}\frac{\partial}{\partial z}\right] \\ \left(\lambda^{(e)} + \mu^{(e)}\right)\frac{\partial^2}{\partial r \partial z} & \left(\lambda^{(e)} + 2\mu^{(e)}\right)\left[\frac{\partial^2}{\partial r^2} + \frac{1}{r}\frac{\partial}{\partial r} - \frac{1}{r^2}\right] + \mu^{(e)}\frac{\partial^2}{\partial z^2} + \rho^{(e)}\omega^2 \end{bmatrix} \begin{Bmatrix} U^{(e)} \\ W^{(e)} \end{Bmatrix} = \begin{Bmatrix} 0 \\ 0 \end{Bmatrix} \tag{4.4}$$

where the superscripts e = 1 and 3 are used to denote the bottom and top elastic cylinders, respectively, and $\lambda^{(e)}$ and $\mu^{(e)}$ are the Lame constants.

The governing differential equations for the piezoelectric and elastic cylinders, the boundary conditions, and the continuity conditions are to be satisfied to determine the displacement and electric potential within the transducer and other functions of interest such as the admittance and impedance of the transducer.

4.3 SOLUTIONS

The primary variables in the governing equations are the axial and radial components of displacements. Electric potential is also a primary variable in case of a piezoceramic cylinder. These parameters are obtained by solving the governing partial differential equations by the method of separation of variables [82].

4.3.1 **Piezoelectric Ceramic Cylinder**

The solution to Eq. 2.5 of an axially polarized piezoceramic cylinder is expressed as the sum of five independent exact solutions:

$$\{U^{(p)} \quad U^{(p)} \quad \emptyset\} = \{U_1^{(p)} \quad W_1^{(p)} \quad \emptyset_1\} + \{U_2^{(p)} \quad W_2^{(p)} \quad \emptyset_2\} + \{U_3^{(p)} \quad W_3^{(p)} \quad \emptyset_3\} + \{U_4^{(p)} \quad W_4^{(p)} \quad \emptyset_4\} + \{U_5^{(p)} \quad W_5^{(p)} \quad \emptyset_5\} \tag{4.6a}$$

where

$$\begin{Bmatrix} U_1^{(p)} \\ W_1^{(p)} \\ \emptyset_1 \end{Bmatrix} = \begin{Bmatrix} 0 \\ 0 \\ Dz + E \end{Bmatrix}; \tag{4.6b}$$

$$\begin{Bmatrix} U_2^{(p)} \\ W_2^{(p)} \\ \emptyset_2 \end{Bmatrix} = \begin{Bmatrix} A^{(p)} \sin(k_{z0} z) \\ 0 \\ A^{(p)} \frac{e_{33}}{\varepsilon_{33}^S} \sin(k_{z0} z) \end{Bmatrix} + \begin{Bmatrix} \sum_{m=1}^{M_r} \sum_{s=1}^{3} A_{ms}^{(p)} J_0(k_{rm} r) \sin(k_{zms}^{(p)} z) \\ \sum_{m=1}^{M_r} \sum_{s=1}^{3} A_{ms}^{(p)} \psi_{ms} J_1(k_{rm} r) \cos(k_{zms}^{(p)} z) \\ \sum_{m=1}^{M_r} \sum_{s=1}^{3} A_{ms}^{(p)} \chi_{ms} J_0(k_{rm} r) \sin(k_{zms}^{(p)} z) \end{Bmatrix} \tag{4.6c}$$

where

$$k_{z0} = \omega \sqrt{\frac{\rho}{c_{33}^E + \frac{e_{33}^2}{\varepsilon_{33}^S}}}; \tag{4.6d}$$

$$\begin{Bmatrix} U_3^{(p)} \\ W_3^{(p)} \\ \emptyset_3 \end{Bmatrix} = \begin{Bmatrix} 0 \\ B^{(p)} J_1(k_{r0} r) \\ 0 \end{Bmatrix} + \begin{Bmatrix} \sum_{m=1}^{M_r} \sum_{s=1}^{3} B_{ms}^{(p)} J_0(k_{rms}^{(p)} r) \sin(k_{zm}^{(p)} z) \\ \sum_{m=1}^{M_r} \sum_{s=1}^{3} B_{ms}^{(p)} \phi_{ms} J_1(k_{rms}^{(p)} r) \cos(k_{zm}^{(p)} z) \\ \sum_{m=1}^{M_r} \sum_{s=1}^{3} B_{ms}^{(p)} \gamma_{ms} J_0(k_{rms}^{(p)} r) \sin(k_{zm}^{(p)} z) \end{Bmatrix} \tag{4.6e}$$

where

$$k_{r0} = \omega\sqrt{\frac{\rho}{c_{11}^E}}; \tag{4.6f}$$

$$\begin{Bmatrix} U_4^{(p)} \\ W_4^{(p)} \\ \emptyset_4 \end{Bmatrix} = \begin{Bmatrix} P^{(p)}\cos(k_{z0}z) \\ 0 \\ P^{(p)}\frac{e_{33}}{\varepsilon_{33}^S}\cos(k_{z0}z) \end{Bmatrix} + \begin{Bmatrix} \sum_{m=1}^{M_r}\sum_{s=1}^{3} P_{ms}^{(p)} J_0(k_{rm}r)\cos(k_{zms}^{(p)}z) \\ \sum_{m=1}^{M_r}\sum_{s=1}^{3} P_{ms}^{(p)} \upsilon_{ms} J_1(k_{rm}r)\sin(k_{zms}^{(p)}z) \\ \sum_{m=1}^{M_r}\sum_{s=1}^{3} P_{ms}^{(p)} \zeta_{ms} J_0(k_{rm}r)\cos(k_{zms}^{(p)}z) \end{Bmatrix}, \tag{4.6g}$$

and

$$\begin{Bmatrix} U_5^{(p)} \\ W_5^{(p)} \\ \emptyset_5 \end{Bmatrix} = \begin{Bmatrix} \sum_{m=1}^{M_q}\sum_{s=1}^{3} Q_{ms}^{(p)} J_0(K_{rms}^{(p)}r)\cos(K_{zm}^{(p)}z) \\ \sum_{m=1}^{M_q}\sum_{s=1}^{3} Q_{ms}^{(p)} \upsilon_{ms} J_1(K_{rms}^{(p)}r)\sin(K_{zm}^{(p)}z) \\ \sum_{m=1}^{M_r}\sum_{s=1}^{3} Q_{ms}^{(p)} \vartheta_{ms} J_0(K_{rms}^{(p)}r)\cos(K_{zm}^{(p)}z) \end{Bmatrix}. \tag{4.6h}$$

It is noted that Eqs. (4.6g) and (4.6h) are not used in Chapter 2 as the boundary conditions are symmetric with respect to the plane that is midway between the ends. The weights $A^{(p)}$, $B^{(p)}$, D, E, $P^{(p)}$, $A_{ms}^{(p)}$, $B_{ms}^{(p)}$, $P_{ms}^{(p)}$, and $Q_{ms}^{(p)}$ are to be determined and chosen such that the specified boundary conditions on all surfaces of the transducer are satisfied.

In the above expressions, J_ν is the ν^{th} order Bessel function of the first kind. Eqs. (4.6c) and (4.6e) are exact solutions for arbitrary values of k_{rm}, m = 1,2,3, …, M_r, and for $k_{zm}^{(p)}$, m = 1,2,3, …, M_z, by suitably choosing the frequency dependent values of $k_{zms}^{(p)}$, $k_{rms}^{(p)}$, ψ_{ms}, χ_{ms}, ϕ_{ms}, and γ_{ms}. For each value of k_{rm}, the frequency-dependent values of $k_{zms}^{(p)}$ are determined by substituting one term in the series in Eq. (4.6c) into Eq. (2.5) and equating the determinant of the resulting equation to zero. The characteristic equation is cubic in ${k_{zms}^{(p)}}^2$. Similarly, the frequency-dependent values of $k_{rms}^{(p)}$ are determined by substituting one term in the series in Eq. (4.6e) into Eq. (2.5) and equating the determinant of the resulting equation to zero. The characteristic equation is cubic in ${k_{rms}^{(p)}}^2$. The expressions for ψ_{ms}, χ_{ms}, ϕ_{ms}, and γ_{ms} are obtained by substituting Eqs. (4.6c) and (4.6e) and the known values of $k_{zms}^{(p)}$ and $k_{rms}^{(p)}$ in the homogenous Eq. (2.5) and rearranging the terms. This yields:

$$\psi_{ms} = \frac{\left\{\left[\rho\omega^2 - c_{33}^E {k_{zms}^{(p)}}^2 - c_{44}^E {k_{rm}}^2\right]\left[\varepsilon_{33}^S {k_{zms}^{(p)}}^2 + \varepsilon_{11}^S {k_{rm}}^2\right] - \left[e_{33}\,{k_{zms}^{(p)}}^2 + e_{15}\,{k_{rm}}^2\right]^2\right\}}{\Delta_k} \tag{4.7a}$$

$$\chi_{ms} = \frac{\left\{\left[\rho\omega^2 - c_{33}^E {k_{zms}^{(p)}}^2 - c_{44}^E {k_{rm}}^2\right]\left[(e_{15}+e_{31})k_{rm}k_{zms}^{(p)}\right] + \left[e_{33}\,{k_{zms}^{(p)}}^2 + e_{15}\,{k_{rm}}^2\right]\left[(c_{13}^E + c_{44}^E)k_{rm}k_{zms}^{(p)}\right]\right\}}{\Delta_k} \tag{4.7b}$$

where

$$\Delta_k = \left[e_{33}\, k_{zms}^{(p)\,2} + e_{15}\, k_{rm}{}^2\right]\left[(e_{15}+e_{31})k_{rm}k_{zms}^{(p)}\right] + \left[\varepsilon_{33}^S k_{zms}^{(p)\,2} + \varepsilon_{11}^S k_{rm}{}^2\right]\left[(c_{13}^E + c_{44}^E)k_{rm}k_{zms}^{(p)}\right]; \quad (4.7c)$$

and

$$\phi_{ms} = \frac{\left\{\left[\rho\omega^2 - c_{33}^E k_{zm}^{(p)\,2} - c_{44}^E k_{rms}^{(p)\,2}\right]\left[\varepsilon_{33}^S k_{zm}^{(p)\,2} + \varepsilon_{11}^S k_{rms}^{(p)\,2}\right] - \left[e_{33}\, k_{zm}^{(p)\,2} + e_{15}\, k_{rms}^{(p)\,2}\right]^2\right\}}{\Delta_p}; \quad (4.7d)$$

$$\gamma_{ms} = \frac{\left\{\left[\rho\omega^2 - c_{33}^E k_{zm}^{(p)\,2} - c_{44}^E k_{rms}^{(p)\,2}\right]\left[(e_{15}+e_{31})k_{rms}^{(p)}k_{zm}^{(p)}\right] + \left[e_{33}\, k_{zm}^{(p)\,2} + e_{15}\, k_{rms}^{(p)\,2}\right]\left[(c_{13}^E + c_{44}^E)k_{rms}^{(p)}k_{zm}^{(p)}\right]\right\}}{\Delta_p} \quad (4.7e)$$

where

$$\Delta_p = \left[e_{33}\, k_{zm}^{(p)\,2} + e_{15}\, k_{rms}^{(p)\,2}\right]\left[(e_{15}+e_{31})k_{rms}^{(p)}k_{zm}^{(p)}\right] + \left[\varepsilon_{33}^S k_{zm}^{(p)\,2} + \varepsilon_{11}^S k_{rms}^{(p)\,2}\right]\left[(c_{13}^E + c_{44}^E)k_{rms}^{(p)}k_{zm}^{(p)}\right]. \quad (4.7f)$$

Similarly, Eq. (4.6g) and (4.6h) are exact solutions for arbitrary values of k_{rm}, m = 1,2,3, …, M_r and $K_{zm}^{(p)}$, m = 1,2,3, …, M_q and corresponding frequency-dependent values of $k_{zms}^{(p)}$, $K_{rms}^{(p)}$, ν_{ms}, ζ_{ms}, υ_{ms} and ϑ_{ms}. The frequency-dependent values of $k_{zms}^{(p)}$ and $K_{rms}^{(p)}$ are determined by substituting each term in the series solutions in Eq. (4.6g) and (4.6h), respectively in Eq. (2.5) and then equating the determinant of the resulting equation to zero. Both the equations are cubic in respective variables. Then, substituting Eq. 4.4(g) and 4.4(h) and the known values of $k_{zms}^{(p)}$ and $K_{rms}^{(p)}$ in the homogenous Eq. (2.5), yields the following expressions for ν_{ms}, ζ_{ms}, υ_{ms} and ϑ_{ms}:

$$\nu_{ms} = \frac{\left\{-\left[\rho\omega^2 - c_{33}^E k_{zms}^{(p)\,2} - c_{44}^E k_{rm}{}^2\right]\left[\varepsilon_{33}^S k_{zms}^{(p)\,2} + \varepsilon_{11}^S k_{rm}{}^2\right] + \left[e_{33}\, k_{zms}^{(p)\,2} + e_{15}\, k_{rm}{}^2\right]^2\right\}}{\Delta_k}; \quad (4.7g)$$

$$\zeta_{ms} = \frac{\left\{\left[\rho\omega^2 - c_{33}^E k_{zms}^{(p)\,2} - c_{44}^E k_{rm}{}^2\right]\left[(e_{15}+e_{31})k_{rm}k_{zms}^{(p)}\right] + \left[e_{33}\, k_{zms}^{(p)\,2} + e_{15}\, k_{rm}{}^2\right]\left[(c_{13}^E + c_{44}^E)k_{rm}k_{zms}^{(p)}\right]\right\}}{\Delta_k}; \quad (4.7h)$$

$$\upsilon_{ms} = \frac{\left\{-\left[\rho\omega^2 - c_{33}^E K_{zm}^{(p)\,2} - c_{44}^E K_{rms}^{(p)\,2}\right]\left[\varepsilon_{33}^S K_{zm}^{(p)\,2} + \varepsilon_{11}^S K_{rms}^{(p)\,2}\right] + \left[e_{33}\, K_{zm}^{(p)\,2} + e_{15}\, K_{rms}^{(p)\,2}\right]^2\right\}}{\Delta_q}; \quad (4.7i)$$

and

$$\vartheta_{ms} = \frac{\left\{-\left[\rho\omega^2 - c_{33}^E K_{zm}^{(p)^2} - c_{44}^E K_{rms}^{(p)^2}\right]\left[(e_{15}+e_{31})K_{rms}^{(p)}K_{zm}^{(p)}\right] + \left[e_{33}K_{zm}^{(p)^2} + e_{15}K_{rms}^{(p)^2}\right]\left[(c_{13}^E + c_{44}^E)K_{rms}^{(p)}K_{zm}^{(p)}\right]\right\}}{\Delta_k}$$

(4.7j)

where

$$\Delta_q = \left[e_{33}K_{zm}^{(p)^2} + e_{15}K_{rms}^{(p)^2}\right]\left[(e_{15}+e_{31})K_{rms}^{(p)}K_{zm}^{(p)}\right] + \left[\varepsilon_{33}^S K_{zm}^{(p)^2} + \varepsilon_{11}^S K_{rms}^{(p)^2}\right]\left[(c_{13}^E + c_{44}^E)K_{rms}^{(p)}K_{zm}^{(p)}\right].$$ (4.7k)

As noted earlier, the origin of the coordinate system is at the center of each cylinder. The radial displacement which represents the symmetric part with respect to the axial direction is given in Eq. (4.6e), because it is expressed in terms of cosine function in z. Antisymmetric part of the radial displacement in terms of sine functions in z is shown in Eq. (4.6h). Similarly, the symmetric and antisymmetric components of the axial displacement and electric potential are expressed in Eqs. (4.6h) and (4.6e) respectively. The solutions contain Bessel functions of the first kind, but the Bessel function of the second kind has not been included in this Chapter in order to satisfy the finiteness condition at the origin.

Substituting the expressions for displacement and potential in the stress-strain and strain displacement equations [Eqs. (2.2) - (2.3)] yields the following expressions for stress and electric field displacement. The normal component of stress along the axis of the piezoceramic cylinder is,

$$T_{zz}^{(p)} = A^{(p)}\left(c_{33}^E + \frac{e_{33}^2}{\varepsilon_{33}^S}\right)k_{z0}\cos(k_{z0}z) + B^{(p)}c_{13}^E k_{r0}J_0(k_{r0}r) + De_{33} - P^{(p)}\left(c_{33}^E + \frac{e_{33}^2}{\varepsilon_{33}^S}\right)k_{z0}\sin(k_{z0}z) + \sum_{m=1}^{M_r}\sum_{s=1}^{3}A_{ms}^{(p)}\left\{c_{13}^E\psi_{ms}k_{rm} + (c_{33}^E + e_{33}\chi_{ms})k_{zms}^{(p)}\right\}J_0(k_{rm}r)\cos\left(k_{zms}^{(p)}z\right) + \sum_{m=1}^{M_r}\sum_{s=1}^{3}B_{ms}^{(p)}\left\{c_{13}^E\phi_{ms}k_{rms}^{(p)} + (c_{33}^E + e_{33}\gamma_{ms})k_{zm}^{(p)}\right\}J_0\left(k_{rms}^{(p)}r\right)\cos\left(k_{zm}^{(p)}z\right) + \sum_{m=1}^{M_r}\sum_{s=1}^{3}P_{ms}^{(p)}\left\{c_{13}^E\nu_{ms}k_{rm} - (c_{33}^E + e_{33}\xi_{ms})k_{zms}^{(p)}\right\}J_0(k_{rm}r)\sin\left(k_{zms}^{(p)}z\right) + \sum_{m=1}^{M_r}\sum_{s=1}^{3}Q_{ms}^{(p)}\left\{c_{13}^E\upsilon_{ms}K_{rms}^{(p)} - (c_{33}^E + e_{33}\vartheta_{ms})K_{zm}^{(p)}\right\}J_0\left(K_{rms}^{(p)}r\right)$$ (4.8)

and the normal component of stress along the radial direction is,

$$T_{rr}^{(p)} = A^{(p)}\left(c_{13}^{E} + \frac{e_{31}e_{33}}{\varepsilon_{33}^{S}}\right)k_{z0}\cos(k_{z0}z) + B^{(p)}\left\{c_{11}^{E}k_{r0}J_0(k_{r0}r) + \frac{c_{12}^{E}-c_{11}^{E}}{r}J_1(k_{r0}r)\right\} +$$

$$De_{31} - P^{(p)}\left(c_{13}^{E} + \frac{e_{31}e_{33}}{\varepsilon_{33}^{S}}\right)k_{z0}\sin(k_{z0}z) + \sum_{m=1}^{M_r}\sum_{s=1}^{3}A_{ms}^{(p)}\left\{\left[c_{11}^{E}\psi_{ms}k_{rm} +\right.\right.$$

$$\left.\left.(c_{13}^{E} + e_{31}\chi_{ms})k_{zms}^{(p)}\right]J_0\left(k_{rm}^{(p)}r\right) + \frac{c_{12}^{E}-c_{11}^{E}}{r}\psi_{ms}J_1\left(k_{rm}^{(p)}r\right)\right\}\cos\left(k_{zms}^{(p)}z\right) +$$

$$\sum_{m=1}^{M_r}\sum_{s=1}^{3}B_{ms}^{(p)}\left\{\left[c_{11}^{E}\phi_{ms}k_{rms}^{(p)} + (c_{13}^{E} + e_{31}\gamma_{ms})k_{zm}^{(p)}\right]J_0\left(k_{rms}^{(p)}r\right) +\right.$$

$$\left.\frac{c_{12}^{E}-c_{11}^{E}}{r}\phi_{ms}J_1\left(k_{rms}^{(p)}r\right)\right\}\cos\left(k_{zm}^{(p)}z\right) + \sum_{m=1}^{M_r}\sum_{s=1}^{3}P_{ms}^{(p)}\left\{\left[c_{11}^{E}\nu_{ms}k_{rm} - (c_{13}^{E} +\right.\right.$$

$$\left.\left.e_{31}\xi_{ms})k_{zms}^{(p)}\right]J_0(k_{rm}r) + \frac{c_{12}^{E}-c_{11}^{E}}{r}\nu_{ms}J_1\left(k_{rm}^{(p)}r\right)\right\}\sin\left(k_{zms}^{(p)}z\right) +$$

$$\sum_{m=1}^{M_r}\sum_{s=1}^{3}Q_{ms}^{(p)}\left\{\left[c_{13}^{E}\upsilon_{ms}K_{rms}^{(p)} - (c_{13}^{E} + e_{31}\vartheta_{ms})K_{zm}^{(p)}\right]J_0\left(K_{rms}^{(p)}r\right) +\right.$$

$$\left.\frac{c_{12}^{E}-c_{11}^{E}}{r}\upsilon_{ms}J_1\left(K_{rms}^{(p)}r\right)\right\}\sin\left(K_{zm}^{(p)}z\right). \qquad (4.9)$$

The shear stress is expressed as,

$$T_{rz}^{(p)} = -\sum_{m=1}^{M_r}\sum_{s=1}^{3}A_{ms}^{(p)}\left\{c_{44}^{E}\left[k_{rm} + \psi_{ms}k_{zms}^{(p)}\right] + e_{15}\chi_{ms}k_{rm}\right\}J_1(k_{rm}r)\sin\left(k_{zms}^{(p)}z\right) +$$

$$\sum_{m=1}^{M_r}\sum_{s=1}^{3}B_{ms}^{(p)}\left\{c_{44}^{E}\left[k_{rms}^{(p)} + \phi_{ms}k_{zm}^{(p)}\right] + e_{15}\gamma_{ms}k_{rms}^{(p)}\right\}J_1\left(k_{rms}^{(p)}r\right)\sin\left(k_{zm}^{(p)}z\right) +$$

$$\sum_{m=1}^{M_r}\sum_{s=1}^{3}P_{ms}^{(p)}\left\{c_{44}^{E}\left[-k_{rm} + \nu_{ms}k_{zms}^{(p)}\right] - e_{15}\xi_{ms}k_{rm}\right\}J_1(k_{rm}r)\cos\left(k_{zms}^{(p)}z\right) +$$

$$\sum_{m=1}^{M_r}\sum_{s=1}^{3}Q_{ms}^{(p)}\left\{c_{44}^{E}\left[-K_{rms}^{(p)} + \upsilon_{ms}K_{zm}^{(p)}\right] - e_{15}\vartheta_{ms}K_{rms}^{(p)}\right\}J_1\left(K_{rms}^{(p)}r\right)\cos\left(K_{zm}^{(p)}z\right). \quad (4.10)$$

Now, the components of electric field displacement are expressed as

$$D_r = \sum_{m=1}^{M_r}\sum_{s=1}^{3}A_{ms}^{(p)}\left\{-e_{15}\left[k_{rm} + \psi_{ms}k_{zms}^{(p)}\right] + \varepsilon_{11}^{S}\chi_{ms}k_{rm}\right\}J_1(k_{rm}r)\sin\left(k_{zms}^{(p)}z\right) +$$

$$\sum_{m=1}^{M_r}\sum_{s=1}^{3}B_{ms}^{(p)}\left\{-e_{15}\left[k_{rms}^{(p)} + \phi_{ms}k_{zm}^{(p)}\right] + \varepsilon_{11}^{S}\gamma_{ms}k_{rms}^{(p)}\right\}J_1\left(k_{rms}^{(p)}r\right)\sin\left(k_{zm}^{(p)}z\right) +$$

$$\sum_{m=1}^{M_r}\sum_{s=1}^{3}P_{ms}^{(p)}\left\{-e_{15}\left[k_{rm} - \nu_{ms}k_{zms}^{(p)}\right] + \varepsilon_{11}^{S}\xi_{ms}k_{rm}\right\}J_1(k_{rm}r)\cos\left(k_{zms}^{(p)}z\right) +$$

$$\sum_{m=1}^{M_r}\sum_{s=1}^{3}Q_{ms}^{(p)}\left\{-e_{15}\left[K_{rms}^{(p)} - \upsilon_{ms}K_{zm}^{(p)}\right] + \varepsilon_{11}^{S}\vartheta_{ms}K_{rms}^{(p)}\right\}J_1\left(K_{rms}^{(p)}r\right)\cos\left(K_{zm}^{(p)}z\right) \quad (4.11)$$

and

$$D_z = B^{(p)} e_{31} k_{r0} J_0(k_{r0} r) - D\varepsilon_{33}^S + \sum_{m=1}^{M_r} \sum_{s=1}^{3} A_{ms}^{(p)} \left\{ e_{31} \psi_{ms} k_{rm} + (e_{33} - \varepsilon_{33}^S \chi_{ms}) k_{zms}^{(p)} \right\} J_0(k_{rm} r) \cos\left(k_{zms}^{(p)} z\right) + \sum_{m=1}^{M_r} \sum_{s=1}^{3} B_{ms}^{(p)} \left\{ e_{31} \phi_{ms} k_{rms}^{(p)} + (e_{33} - \varepsilon_{33}^S \gamma_{ms}) k_{zm}^{(p)} \right\} J_0\left(k_{rms}^{(p)} r\right) \cos\left(k_{zm}^{(p)} z\right) + \sum_{m=1}^{M_r} \sum_{s=1}^{3} P_{ms}^{(p)} \left\{ e_{31} \upsilon_{ms} k_{rm} - (e_{33} - \varepsilon_{33}^S \xi_{ms}) k_{zms}^{(p)} \right\} J_0(k_{rm} r) \sin\left(k_{zms}^{(p)} z\right) + \sum_{m=1}^{M_q} \sum_{s=1}^{3} Q_{ms}^{(p)} \left\{ e_{31} \upsilon_{ms} K_{rms}^{(p)} - (e_{33} - \varepsilon_{33}^S \vartheta_{ms}) K_{zm}^{(p)} \right\} J_0\left(K_{rms}^{(p)} r\right) \sin\left(K_{zm}^{(p)} z\right). \quad (4.12)$$

Now, the current along the piezoceramic cylinder is computed and is expressed as

$$I = -\int_0^a j\omega D_z 2\pi r dr = -j\omega\pi a \left(2B^{(p)} e_{31} J_1(k_{r0} a) - D\varepsilon_{33}^S a\right) - j\omega 2\pi \sum_{m=1}^{M_z} \cos\left(k_{zm}^{(p)} z\right) \sum_{s=1}^{3} B_{ms}^{(p)} \left\{ e_{31} \phi_{ms} k_{rms}^{(p)} + (e_{33} - \varepsilon_{33}^S \gamma_{ms}) k_{zm}^{(p)} \right\} \frac{a}{k_{rms}^{(p)}} J_1\left(k_{rms}^{(p)} a\right) - j\omega 2\pi \sum_{m=1}^{M_q} \sin\left(K_{zm}^{(p)} z\right) \sum_{s=1}^{3} Q_{ms}^{(p)} \left\{ e_{31} \upsilon_{ms} K_{rms}^{(p)} - (e_{33} - \varepsilon_{33}^S \vartheta_{ms}) K_{zm}^{(p)} \right\} \frac{a}{K_{rms}^{(p)}} J_1\left(K_{rms}^{(p)} a\right), \quad (4.13)$$

because [77]

$$\int_0^a J_0(k_{rm} r)\, r dr = 0, m = 1,2,\dots,M_r. \quad (4.14)$$

The current in Eq. (4.13) should be independent of *z*, from the Gauss zero-divergence condition of Eq. (2.4). Hence, the series terms in Eq. (4.13) should be zero. Finally, the input electrical admittance $Y = G + jB = \frac{I}{\emptyset_0}$ is obtained from Eq. (4.13) and from the specified applied voltage, $\emptyset_0$. Here, the real part, *G*, of admittance (*Y*) is the conductance and the imaginary part, *B*, is the susceptance of the transducer.

4.3.2 **Elastic Cylinder**

The solutions to the exact governing equations for an elastic cylinder in Eq. (4.4) are obtained by the method of separation of variables and are expressed as the sum of four exact solutions:

$$\{U^{(e)} \quad W^{(e)}\}^T = \{U_1^{(e)} \quad W_1^{(e)}\}^T + \{U_2^{(e)} \quad W_2^{(e)}\}^T + \{U_3^{(e)} \quad W_3^{(e)}\}^T + \{U_4^{(e)} \quad W_4^{(e)}\}^T \quad (4.15a)$$

where

$$\begin{Bmatrix} U_1^{(e)} \\ W_1^{(e)} \end{Bmatrix} = \begin{Bmatrix} A^{(e)}\sin(k_1^{(e)}z) \\ 0 \end{Bmatrix} + \begin{Bmatrix} \sum_{m=1}^{M_r}\sum_{s=1}^{2} A_{ms}^{(e)} J_0(k_{rm}r)\sin(k_{zms}^{(e)}z) \\ \sum_{m=1}^{M_r}\sum_{s=1}^{2} A_{ms}^{(e)}\alpha_{ms}^{(e)} J_1(k_{rm}r)\cos(k_{zms}^{(e)}z) \end{Bmatrix}, \quad (4.15b)$$

$$\begin{Bmatrix} U_2^{(e)} \\ W_2^{(e)} \end{Bmatrix} = \begin{Bmatrix} 0 \\ B^{(e)} J_1(k_2^{(e)}r) \end{Bmatrix} + \begin{Bmatrix} \sum_{m=1}^{M_r}\sum_{s=1}^{2} B_{ms}^{(e)} J_0(k_{rms}^{(e)}r)\sin(k_{zm}^{(e)}z) \\ \sum_{m=1}^{M_r}\sum_{s=1}^{2} A_{ms}^{(e)}\beta_{ms}^{(e)} J_1(k_{rms}^{(e)}r)\cos(k_{zm}^{(e)}z) \end{Bmatrix}, \quad (4.15c)$$

$$\begin{Bmatrix} U_3^{(e)} \\ W_3^{(e)} \end{Bmatrix} = \begin{Bmatrix} P^{(e)}\cos(k_1^{(e)}z) \\ 0 \end{Bmatrix} + \begin{Bmatrix} \sum_{m=1}^{M_r}\sum_{s=1}^{2} P_{ms}^{(e)} J_0(k_{rm}r)\cos(k_{zms}^{(e)}z) \\ \sum_{m=1}^{M_r}\sum_{s=1}^{2} P_{ms}^{(e)}\varsigma_{ms}^{(e)} J_1(k_{rm}r)\sin(k_{zms}^{(e)}z) \end{Bmatrix}, \quad (4.15d)$$

and

$$\begin{Bmatrix} U_4^{(e)} \\ W_4^{(e)} \end{Bmatrix} = \begin{Bmatrix} \sum_{m=1}^{M_q}\sum_{s=1}^{2} Q_{ms}^{(e)} J_0(K_{rms}^{(e)}r)\cos(K_{zm}^{(e)}z) \\ \sum_{m=1}^{M_r}\sum_{s=1}^{2} Q_{ms}^{(e)}\eta_{ms}^{(e)} J_1(K_{rms}^{(e)}r)\sin(K_{zm}^{(e)}z) \end{Bmatrix} \quad (4.15e)$$

where

$$k_s^{(e)} = \omega/c_s^{(e)}, s = 1,2 \text{ and } {c_1^{(e)}}^2 = \frac{\lambda^{(e)}+2\mu^{(e)}}{\rho^{(e)}}, {c_2^{(e)}}^2 = \frac{\mu^{(e)}}{\rho^{(e)}}. \quad (4.15f)$$

Here, $A^{(e)}$, $B^{(e)}$, $P^{(e)}$, $A_{ms}^{(e)}$, $B_{ms}^{(e)}$, $P_{ms}^{(e)}$, and $Q_{ms}^{(e)}$ are weights that depend on the excitation. Eqs. (4.15b) to (4.15e) are exact solutions for arbitrary values of $k_{rm}, m = 1,2,3,\dots,M_r$; for $k_{zm}^{(e)}$, $m = 1,2,3,\dots,M_z$; and for $K_{zm}^{(e)}$, $m = 1,2,3,\dots,M_q$ by suitably choosing the frequency dependent values of $k_{zms}^{(e)}$, $k_{rms}^{(e)}$, and $K_{rms}^{(e)}$, respectively.

The frequency dependent values of $k_{zms}^{(e)}$ and $k_{rms}^{(e)}$ are determined by substituting each term in the series in Eqs. (4.15b) and (4.15c), respectively, in Eq. (4.4) and then equating the determinant of the resulting equation to zero. This characteristic equation is quadratic in ${k_{zms}^{(e)}}^2$ in the first case and quadratic in ${k_{rms}^{(e)}}^2$ in the second case. Solving these equations yields:

$$k_{zms}^{(e)} = \sqrt{{k_s^{(e)}}^2 - {k_{rm}}^2}; m = 1,2,3,\dots,M_r; s = 1,2 \quad (4.16a)$$

and

$$k_{rms}^{(e)} = \sqrt{{k_s^{(e)}}^2 - {k_{rm}}^2}; m = 1,2,3,\dots,M_z; s = 1,2. \quad (4.16b)$$

Similarly, the values of $K_{rms}^{(e)}$ are determined by substituting each term in the series in Eq. (4.15e) in Eq. (4.4) and equating the determinant of the resulting equation to zero. They are given by,

$$K_{rms}^{(e)} = \sqrt{k_s^{(e)^2} - K_{zm}^{(e)^2}}; m = 1,2,3,\dots,M_q; s = 1,2. \quad (4.16c)$$

The values of $\alpha_{ms}^{(e)}$ and $\beta_{ms}^{(e)}$ are then obtained by substituting Eq. (4.15b) and (4.15c), respectively, in Eq. (4.4) and rearranging them. They are computed as:

$$\alpha_{ms}^{(e)} = \frac{(\lambda^{(e)}+\mu^{(e)})k_{zms}^{(e)}k_{rm}}{\rho^{(e)}\omega^2-(\lambda^{(e)}+2\mu^{(e)})k_{rm}{}^2-\mu^{(e)}k_{zms}^{(e)}{}^2}; m = 1,2,3,\dots,M_r; s = 1,2 \quad (4.17a)$$

and

$$\beta_{ms}^{(e)} = \frac{(\lambda^{(e)}+\mu^{(e)})k_{zm}^{(e)}k_{rms}^{(e)}}{\rho^{(e)}\omega^2-(\lambda^{(e)}+2\mu^{(e)})k_{rms}^{(e)}{}^2-\mu^{(e)}k_{zm}^{(e)}{}^2}; m = 1,2,3,\dots,M_r; s = 1,2. \quad (4.17b)$$

Similarly, substituting Eqs. (4.15d) and (4.15e), respectively, in Eq. (4.4), will yield $\varsigma_{ms}^{(e)}$ and $\eta_{ms}^{(e)}$ as:

$$\varsigma_{m1}^{(e)} = -\frac{k_{rm}}{k_{zm1}^{(e)}}, \varsigma_{m2}^{(e)} = \frac{k_{zm2}^{(e)}}{k_{rm}}; m = 1,2,3,\dots,M_r \quad (4.18c,d)$$

and

$$\eta_{m1}^{(e)} = -\frac{K_{rm1}^{(e)}}{K_{zm}^{(e)}}, \eta_{m2}^{(e)} = \frac{K_{zm}^{(e)}}{K_{rm2}^{(e)}}; m = 1,2,3,\dots,M_q. \quad (4.18e,f)$$

In Eq. (4.15c), the axial displacement is antisymmetric and the radial displacement is symmetric about the plane midway between the ends of the cylinder. Axial and radial displacements are symmetric and antisymmetric, respectively, in Eq. (4.15d). The stress components of the elastic cylinder are computed by using the stress-strain and strain displacement relations in Eqs. (4.3) and (4.2), respectively. The normal components of the axial stress is expressed as

$$T_{zz}^{(e)} = A^{(e)}\left[\lambda^{(e)} + 2\mu^{(e)}\right]k_1^{(e)}\cos\left(k_1^{(e)}z\right) + B^{(e)}\lambda^{(e)}k_1^{(e)}J_0\left(k_1^{(e)}r\right) - P^{(e)}\left[\lambda^{(e)} + 2\mu^{(e)}\right]k_1^{(e)}\sin\left(k_1^{(e)}z\right) + \sum_{m=1}^{M_r}\sum_{s=1}^{2}A_{ms}^{(e)}\left\{\left[\lambda^{(e)} + 2\mu^{(e)}\right]k_{zms}^{(e)} + \lambda^{(e)}\alpha_{ms}^{(e)}k_{rm}\right\}J_0(k_{rm}r)\cos\left(k_{zms}^{(e)}z\right) + \sum_{m=1}^{M_z}\sum_{s=1}^{2}B_{ms}^{(e)}\left\{\left[\lambda^{(e)} + 2\mu^{(e)}\right]k_{zm}^{(e)} + \lambda^{(e)}\beta_{ms}^{(e)}k_{rms}^{(e)}\right\}J_0\left(k_{rms}^{(e)}r\right)\cos\left(k_{zm}^{(e)}z\right) + \sum_{m=1}^{M_r}\sum_{s=1}^{2}P_{ms}^{(e)}\left\{-\left[\lambda^{(e)} + 2\mu^{(e)}\right]k_{zms}^{(e)} + \lambda^{(e)}\varsigma_{ms}^{(e)}k_{rm}\right\}J_0(k_{rm}r)\sin\left(k_{zms}^{(e)}z\right) + \sum_{m=1}^{M_q}\sum_{s=1}^{2}Q_{ms}^{(e)}\left\{-\left[\lambda^{(e)} + 2\mu^{(e)}\right]K_{zm}^{(e)} + \lambda^{(e)}\eta_{ms}^{(e)}K_{rms}^{(e)}\right\}J_0\left(K_{rms}^{(e)}r\right)\sin\left(K_{zm}^{(e)}z\right) \quad (4.19)$$

and the normal component of the radial stress is expressed as

$$T_{rr}^{(e)} = A^{(e)}\lambda^{(e)}k_1^{(e)}\cos\left(k_1^{(e)}z\right) + B^{(e)}\left\{\left[\lambda^{(e)} + 2\mu^{(e)}\right]k_1^{(e)}J_0\left(k_1^{(e)}r\right) - \frac{2\mu^{(e)}}{r}J_1\left(k_1^{(e)}r\right)\right\} -$$

$$P^{(e)}\lambda^{(e)}k_1^{(e)}\sin\left(k_1^{(e)}z\right) + \sum_{m=1}^{M_r}\sum_{s=1}^{2}A_{ms}^{(e)}\left\{\left(\lambda^{(e)}k_{zms}^{(e)} + \left[\lambda^{(e)} +\right.\right.\right.$$

$$\left.\left.\left.2\mu^{(e)}\right]\alpha_{ms}^{(e)}k_{rm}\right)J_0(k_{rm}r) - \frac{2\mu^{(e)}}{r}\alpha_{ms}^{(e)}J_1(k_{rm}r)\right\}\cos\left(k_{zms}^{(e)}z\right) +$$

$$\sum_{m=1}^{M_z}\sum_{s=1}^{2}B_{ms}^{(e)}\left\{\left(\lambda^{(e)}k_{zm}^{(e)} + \left[\lambda^{(e)} + 2\mu^{(e)}\right]\beta_{ms}^{(e)}k_{rms}^{(e)}\right)J_0\left(k_{rms}^{(e)}r\right) -\right.$$

$$\left.\frac{2\mu^{(e)}}{r}\beta_{ms}^{(e)}J_1\left(k_{rms}^{(e)}r\right)\right\}\cos\left(k_{zm}^{(e)}z\right) + \sum_{m=1}^{M_r}\sum_{s=1}^{2}P_{ms}^{(e)}\left\{\left(-\lambda^{(e)}k_{zms}^{(e)} + \left[\lambda^{(e)} +\right.\right.\right.$$

$$\left.\left.\left.2\mu^{(e)}\right]\varsigma_{ms}^{(e)}k_{rm}\right)J_0\left(k_{rm}^{(e)}r\right) - \frac{2\mu^{(e)}}{r}\varsigma_{ms}^{(e)}J_1(k_{rm}r)\right\}\sin\left(k_{zms}^{(e)}z\right) +$$

$$\sum_{m=1}^{M_q}\sum_{s=1}^{2}Q_{ms}^{(e)}\left\{\left(-\lambda^{(e)}K_{zm}^{(e)} + \left[\lambda^{(e)} + 2\mu^{(e)}\right]\eta_{ms}^{(e)}K_{rms}^{(e)}\right)J_0\left(K_{rms}^{(e)}r\right) -\right.$$

$$\left.\frac{2\mu^{(e)}}{r}\eta_{ms}^{(e)}J_1\left(K_{rms}^{(e)}r\right)\right\}\sin\left(K_{zm}^{(e)}z\right). \tag{4.20}$$

The shear stress is obtained as,

$$\mathrm{T}_{rz}^{(e)} = -\mu^{(e)}\sum_{m=1}^{M_r}\sum_{s=1}^{2}A_{ms}^{(e)}\left\{k_{rm} + \alpha_{ms}^{(e)}k_{zms}^{(e)}\right\}J_1(k_{rm}r)\sin\left(k_{zms}^{(e)}z\right) -$$

$$\mu^{(e)}\sum_{m=1}^{M_z}\sum_{s=1}^{2}B_{ms}^{(e)}\left\{k_{rms}^{(e)} + \beta_{ms}^{(e)}k_{zm}^{(e)}\right\}J_1\left(k_{rms}^{(e)}r\right)\sin\left(k_{zm}^{(e)}z\right) +$$

$$\mu^{(e)}\sum_{m=1}^{M_r}\sum_{s=1}^{2}P_{ms}^{(e)}\left\{-k_{rm} + \varsigma_{ms}^{(e)}k_{zms}^{(e)}\right\}J_1(k_{rm}r)\cos\left(k_{zms}^{(e)}z\right) +$$

$$\mu^{(e)}\sum_{m=1}^{M_q}\sum_{s=1}^{2}Q_{ms}^{(e)}\left\{-K_{rms}^{(e)} + \eta_{ms}^{(e)}K_{zm}^{(e)}\right\}J_1\left(K_{rms}^{(e)}r\right)\cos\left(K_{zm}^{(e)}z\right). \tag{4.21}$$

All the primary and secondary variables for the piezoelectric and elastic cylinders are expressed in terms of Bessel and trigonometric functions that are orthogonal and complete in the radial and axial directions, respectively. The orthogonality properties of trigonometric functions were described in Eqs. (2.9) and (2.10). The orthogonality property of the Bessel functions [77] are shown below.

$$\int_0^a J_\nu(Xr)J_\nu(k_{rm}r)rdr = \begin{cases} 0, \ X = k_{rm}, m \neq n \\ (a^2/2)J_0^2(k_{rn}a), \ X = k_{rn}, m = n \\ \frac{Xa}{X^2 - k_{rn}^{(c)^2}}J_0(k_{rn}a)J_1(Xa), X \neq k_{rn}, n = 1,2,3,\ldots \end{cases} \quad \nu = 0,1. \tag{4.22}$$

Here, $k_{rm}a$ are chosen to be the roots of $J_1(k_{rm}a) = 0$ and are approximately equal to 0, 3.83, 7.02, … for m = 0, 1, 2, ... respectively. For $M_r = \infty$, $J_\nu(k_{rm}r)$ form a point-wise

complete set of functions when $\nu = 0$ and norm-wise complete sets of functions when $\nu = 1$. Sets of functions that are not all zero at the same point and form a norm-wise complete sets of functions are known as point-wise complete sets.

Here, $k_{zm}^{(c)}$ are chosen such that $k_{zm}^{(c)} = m\pi; m = 0,1,2, \ldots, M_z$, where M_z is ∞. The series begins with the m = 0 term. In the second set, $K_{zm}^{(c)}L/2$ are chosen such that $\frac{K_{zm}^{(c)}L}{2} = \frac{(2m-1)\pi}{2}, m = 1,2,3, \ldots, M_z$, where M_z is ∞. Here, the series begins with the m = 1 term. In both sets, for $M_z = \infty$, sin and cos are complete sets of functions.

The primary and secondary variables of the piezoelectric and elastic cylinders are expressed as the sum of a point-wise or norm-wise complete set of functions and other functions. On the flat surfaces of the cylinders, U and T_{zz} are expressed in terms of $J_0(k_{rm}r), m = 0,1,2, \ldots$ and W and T_{rz} are expressed in terms of $J_1(k_{rm}r), m = 0,1,2, \ldots$. On the curved surfaces, U and T_{rz} are expressed in terms of $\cos(k_{zm}^{(c)}z)$ and $\cos(K_{zm}^{(c)}z)$; and W and T_{rr} are expressed in terms of $\sin(k_{zm}^{(c)}z)$ and $\cos(K_{zm}^{(c)}z)$. Hence, arbitrary boundary conditions and continuity conditions can be satisfied on the flat and curved surfaces of the cylinders of the transducer.

4.4 BOUNDARY AND CONTINUITY CONDITIONS

Various boundary and continuity conditions can be considered on the flat and curved surfaces of the Langevin transducer. The case considered in this analysis has zero stress on all the exposed surfaces of the elastic and piezoelectric cylinders and specified electric field on the flat surfaces of the piezoceramic cylinder. Similar procedure can be followed, when the displacements are specified. The continuity of axial and radial displacements and that of normal and shear components of stress are used at the two piezoelectric - elastic cylinder interfaces.

The normal and shear stresses on the flat surfaces are denoted by $\bar{T}_{zz}^{(c)}$ and $\bar{T}_{rz}^{(c)}$, respectively and that on the curved surface are denoted by $\hat{T}_{rr}^{(c)}$ and $\hat{T}_{rz}^{(c)}$, respectively; where $c = p$ or e. The potential is zero on the bottom electrode and uniform on the top electrode, i.e. $\emptyset = \emptyset_0$ on the top flat surface of the piezoceramic cylinder. $\emptyset_0$ is specified for the applied potential condition, zero for the short circuit condition, and is to be determined for the open-circuit condition. The normal components of electric field displacement on the flat and curved surface are denoted by, $\bar{D}_z$ and $\hat{D}_r$, respectively. The axial and radial displacements on the flat surfaces are denoted by $\bar{U}^{(c)}$ and $\bar{W}^{(c)}$, respectively.

4.4.1 **Boundary Conditions**

The Langevin transducer has four flat surfaces, one at the bottom and one at the top of the transducer and two at the flat ends of the piezoceramic cylinder. It also has three curved surfaces, one for each cylinder. Since the piezoceramic cylinder has both electrical and mechanical vibrations, the boundary conditions are categorized into two: electrical and mechanical.

4.4.1.1 Electrical Boundary Conditions

The electrical boundary conditions on the flat electrodes of the piezoceramic cylinder are specified as follows for electrical excitation:

$$\emptyset = 0 \text{ at } z = -L^{(p)}/2 \tag{4.23a}$$

and

$$\emptyset = \emptyset_0 \text{ at } z = L^{(p)}/2. \tag{4.23b}$$

These conditions are satisfied in an average sense by using the orthogonal property of $J_0(k_{rm}r)$ in Eq. (4.22). Substituting the specified values of potential, in Eq. (4.6), multiplying both sides of Eq. (4.23) by $rJ_0(k_{rn}r)$ and integrating over r yields one set of equations each for the top and bottom flat surfaces. For the top flat surface of the piezoceramic cylinder ($z = L^{(2)}/2, 0 \le r \le a$), using n = 0 yields

$$A^{(p)}\frac{e_{33}}{\varepsilon_{33}^S}\frac{a^2}{2}\sin\left(\frac{k_{z0}L^{(p)}}{2}\right) + D\frac{a^2L^{(p)}}{4} + E\frac{a^2}{2} + P^{(p)}\frac{e_{33}}{\varepsilon_{33}^S}\frac{a^2}{2}\cos\left(\frac{k_{z0}L^{(p)}}{2}\right) +$$

$$\sum_{m=1}^{M_q}\sum_{s=1}^{3} Q_{ms}^{(p)}\vartheta_{ms}\cos\left(\frac{K_{zm}^{(p)}L^{(p)}}{2}\right)\frac{a}{K_{rms}^{(p)}}J_1\left(K_{rms}^{(p)}a\right) = \emptyset_0\frac{a^2}{2} \tag{4.24a}$$

and using $n = m = 1, 2, \ldots, M_r$ yields

$$\frac{a^2}{2}J_0^2(k_{rn}a)\sum_{s=1}^{3}A_{ns}^{(p)}\chi_{ns}\sin\left(k_{zns}^{(p)}\frac{L^{(p)}}{2}\right) + \frac{a^2}{2}J_0^2(k_{rn}a)\sum_{s=1}^{3}P_{ns}^{(p)}\xi_{ns}\cos\left(k_{zns}^{(p)}\frac{L^{(p)}}{2}\right) +$$

$$\sum_{m=1}^{M_q}\sum_{s=1}^{3} Q_{ms}^{(p)}\vartheta_{ms}\cos\left(\frac{K_{zm}^{(p)}L^{(p)}}{2}\right)\frac{K_{rms}^{(p)}aJ_0\left(k_{rm}^{(p)}a\right)J_1\left(K_{rms}^{(p)}a\right)}{{K_{rms}^{(p)}}^2 - {k_{rn}}^2} = 0. \tag{4.24b}$$

Similarly, for the bottom flat surface of the piezoceramic cylinder (($z = -L^{(2)}/2, 0 \le r \le a$), using n = 0 yields

$$A^{(p)}\frac{e_{33}}{\varepsilon_{33}^{S}}\frac{a^2}{2}\sin\left(\frac{k_{z0}L^{(p)}}{2}\right)-D\frac{a^2L^{(p)}}{4}+E\frac{a^2}{2}+P^{(p)}\frac{e_{33}}{\varepsilon_{33}^{S}}\frac{a^2}{2}\cos\left(\frac{k_{z0}L^{(p)}}{2}\right)+$$

$$\sum_{m=1}^{M_q}\sum_{s=1}^{3}Q_{ms}^{(p)}\vartheta_{ms}\cos\left(\frac{K_{zm}^{(p)}L^{(p)}}{2}\right)\frac{a}{K_{rms}^{(p)}}J_1\left(K_{rms}^{(p)}a\right)=0 \qquad (4.25a)$$

and using n=m=1, 2, ..., M_r yields

$$-\frac{a^2}{2}J_0^2(k_{rn}a)\sum_{s=1}^{3}A_{ns}^{(p)}\chi_{ns}\sin\left(k_{zns}^{(p)}\frac{L^{(p)}}{2}\right)+\frac{a^2}{2}J_0^2(k_{rn}a)\sum_{s=1}^{3}P_{ns}^{(p)}\xi_{ns}\cos\left(k_{zns}^{(p)}\frac{L^{(p)}}{2}\right)+$$

$$\sum_{m=1}^{M_q}\sum_{s=1}^{3}Q_{ms}^{(p)}\vartheta_{ms}\cos\left(\frac{K_{zm}^{(p)}L^{(p)}}{2}\right)\frac{K_{rms}^{(p)}aJ_0\left(k_{rm}^{(p)}a\right)J_1\left(K_{rms}^{(p)}a\right)}{{K_{rms}^{(p)}}^2-{k_{rn}}^2}=0. \qquad (4.25b)$$

The boundary conditions are separately written for n = 0, since $J_0(k_{rn}r)=1$ when $n=0$. Electrical conditions are specified only at the two flat surfaces of the piezoceramic cylinder.

On the curved surface of the piezoceramic cylinder, i.e. on $|z|\le L^{(p)}/2$; the electric field displacement in the radial direction, D_r, is specified as zero, i.e. $\widehat{D}_r=0$. This condition is satisfied by multiplying D_r in Eq. 4.11 by 1, $\cos(K_{zn}^{(c)}z)$ and $\sin(k_{zn}^{(c)}z)$ respectively, and integrating over z and equating them to zero. Using the orthogonality property of trigonometric functions this yields:

$$\sum_{m=1}^{M_q}\sum_{s=1}^{3}Q_{ms}^{(p)}\left\{-e_{15}\left(K_{rms}^{(p)}-\upsilon_{ms}K_{zm}^{(p)}\right)+\varepsilon_{11}^{S}\vartheta_{ms}K_{rms}^{(p)}\right\}J_1\left(K_{rms}^{(p)}a\right)\frac{2}{K_{zm}^{(p)}}\sin\left(K_{zm}^{(p)}\frac{L^{(p)}}{2}\right)=$$

$$\int_{-L^{(p)}/2}^{L^{(p)}/2}\widehat{D}_r\,dz=0 \text{ for } n=0, \qquad (4.26)$$

$$\frac{L^{(p)}}{2}\sum_{s=1}^{3}Q_{ns}^{(p)}\left\{e_{15}\left(-K_{rns}^{(p)}+\upsilon_{ns}K_{zn}^{(p)}\right)+\varepsilon_{11}^{S}\vartheta_{ns}K_{rns}^{(p)}\right\}J_1\left(K_{rns}^{(p)}a\right)=$$

$$\int_{-L^{(p)}/2}^{L^{(p)}/2}\widehat{D}_r\cos\left(K_{zn}^{(p)}z\right)dz=0 \quad \text{for } n=1,2,\dots,M_q, \qquad (4.27)$$

and

$$\frac{L^{(p)}}{2}\sum_{s=1}^{3}B_{ns}^{(p)}\left\{-e_{15}\left(k_{rns}^{(p)}+\phi_{ns}k_{zn}^{(p)}\right)+\varepsilon_{11}^{S}\gamma_{ns}k_{rns}^{(p)}\right\}J_1\left(k_{rns}^{(p)}a\right)=$$

$$\int_{-L^{(p)}/2}^{L^{(p)}/2}\widehat{D}_r\sin\left(k_{zn}^{(p)}z\right)dz=0 \quad \text{for } n=1,2,\dots,M_z. \qquad (4.28)$$

4.4.1.2 Mechanical Boundary Conditions

The mechanical boundary conditions are specified on the normal and shear components of stresses on the flat and curved boundaries of the transducer.

4.4.1.2.1 Flat Surfaces

At the flat ends of the transducer, the following boundary conditions are specified for $|r| \leq a$:

$$\begin{Bmatrix} \bar{T}_{zz}^{(1)} \\ \bar{T}_{rz}^{(1)} \end{Bmatrix} = \begin{Bmatrix} 0 \\ 0 \end{Bmatrix} \text{ at } z = -L^{(1)}/2 \tag{4.29a}$$

and

$$\begin{Bmatrix} \bar{T}_{zz}^{(3)} \\ \bar{T}_{rz}^{(3)} \end{Bmatrix} = \begin{Bmatrix} 0 \\ 0 \end{Bmatrix} \text{ at } z = L^{(3)}/2. \tag{4.29b}$$

Here, the conditions in Eq. (4.29a) are specified on the bottom flat surface of the bottom elastic cylinder and those in Eq. (4.29b) are specified on the top flat surface of the top elastic cylinder. The boundary conditions on the normal component of stress at the bottom flat surface of the transducer is satisfied by multiplying both sides of the equation $\bar{T}_{zz}^{(e)} = 0$ by $rJ_0(k_{rn}r)$, n = 0, 1, 2, 3, …, M_r, at $z = -L^{(1)}/2$, and integrating over r. This yields M_r+1 equations instead of the original one, $\bar{T}_{zz}^{(e)} = 0$. The coefficients in these equations are solved after combining these equations with similar equations obtained by using other boundary and continuity conditions. Thus each boundary condition is satisfied in a weighted-average sense. When M_r is large, the expression for $\bar{T}_{zz}^{(e)}$ evaluated on the flat surface is nearly zero at all points.

Using $T_{zz}^{(e)}$ in Eq. (4.19), multiplying $\bar{T}_{zz}^{(e)} = 0$ by $rJ_0(k_{rn}r)$, integrating over r, and using the orthogonality of Bessel functions in Eq. (4.22) yields

$$A^{(e)}\left[\lambda^{(e)} + 2\mu^{(e)}\right]k_1^{(e)}\frac{a^2}{2}\cos\left(k_1^{(e)}z\right) + B^{(e)}\lambda^{(e)}aJ_1\left(k_1^{(e)}a\right) - P^{(e)}\left[\lambda^{(e)} + 2\mu^{(e)}\right]k_1^{(e)}\frac{a^2}{2}\sin\left(k_1^{(e)}z\right) + \sum_{m=1}^{M_z}\sum_{s=1}^{2}B_{ms}^{(e)}\left\{\left[\lambda^{(e)} + 2\mu^{(e)}\right]k_{zm}^{(e)} + \lambda^{(e)}\beta_{ms}^{(e)}k_{rms}^{(e)}\right\}\frac{aJ_1\left(k_{rms}^{(e)}a\right)}{k_{rms}^{(e)}}\cos\left(k_{zm}^{(e)}z\right) + \sum_{m=1}^{M_q}\sum_{s=1}^{2}Q_{ms}^{(e)}\left\{-\left[\lambda^{(e)} + 2\mu^{(e)}\right]K_{zm}^{(e)} + \lambda^{(e)}\eta_{ms}^{(e)}K_{rms}^{(e)}\right\}\frac{aJ_1\left(K_{rms}^{(e)}a\right)}{K_{rms}^{(e)}}\sin\left(K_{zm}^{(e)}z\right) = \int_0^a \bar{T}_{zz}^{(e)}\,rdr = 0, \text{ for n = 0} \tag{4.30a}$$

and

$$B^{(e)}\lambda^{(e)}ak_1^{(e)\,2}\frac{J_0(k_{rn}a)J_1\left(k_1^{(e)}a\right)}{k_1^{(e)\,2}-k_{rn}{}^2}+\frac{a^2}{2}J_0{}^2(k_{rn}a)\sum_{s=1}^{2}A_{ns}^{(e)}\left\{\left[\lambda^{(e)}+2\mu^{(e)}\right]k_{zns}^{(e)}+\right.$$

$$\left.\lambda^{(e)}\alpha_{ns}^{(e)}k_{rn}\right\}\cos\left(k_{zns}^{(e)}z\right)+\sum_{m=1}^{M_z}\sum_{s=1}^{2}B_{ms}^{(e)}\left\{\left[\lambda^{(e)}+2\mu^{(e)}\right]k_{zm}^{(e)}+\right.$$

$$\left.\lambda^{(e)}\beta_{ms}^{(e)}k_{rms}^{(e)}\right\}ak_{rms}^{(e)}\frac{J_0(k_{rn}a)J_1\left(k_{rms}^{(e)}a\right)}{k_{rms}^{(e)\,2}-k_{rn}{}^2}\cos\left(k_{zm}^{(e)}z\right)+\frac{a^2}{2}J_0{}^2(k_{rn}a)\sum_{s=1}^{2}P_{ns}^{(e)}\left\{-\left[\lambda^{(e)}+\right.\right.$$

$$\left.\left.2\mu^{(e)}\right]k_{zns}^{(e)}+\lambda^{(e)}\varsigma_{ns}^{(e)}k_{rn}\right\}\sin\left(k_{zns}^{(e)}z\right)+\sum_{m=1}^{M_q}\sum_{s=1}^{2}Q_{ms}^{(e)}\left\{-\left[\lambda^{(e)}+2\mu^{(e)}\right]K_{zm}^{(e)}+\right.$$

$$\left.\lambda^{(e)}\eta_{ms}^{(e)}K_{rms}^{(e)}\right\}aK_{rms}^{(e)}\frac{J_0\left(k_{rn}^{(e)}a\right)J_1\left(K_{rms}^{(e)}a\right)}{K_{rms}^{(e)\,2}-k_{rn}{}^2}\sin\left(K_{zm}^{(e)}z\right)=\int_0^a\bar{T}_{zz}^{(e)}rJ_0(k_{rn}r)dr=0$$

for n=1, 2, ..., M_r. (4.30b)

Similarly, the zero shear stress boundary conditions on the two flat ends of the transducer are replaced by several equations. Specifically, equating the expression for $T_{rz}^{(e)}, e=1,3$ in Eq. (4.21) to zero on the flat surface, multiplying both sides by $rJ_1(k_{rn}r)$ and integrating with respect to r yields:

$$-\mu^{(e)}\frac{a^2}{2}J_0{}^2(k_{rn}a)\sum_{s=1}^{2}A_{ns}^{(e)}\left\{k_{rn}+\alpha_{ns}^{(e)}k_{zns}^{(e)}\right\}\sin\left(k_{zns}^{(e)}z\right)+$$

$$\mu^{(e)}\frac{a^2}{2}J_0{}^2(k_{rn}a)\sum_{s=1}^{2}P_{ns}^{(e)}\left\{-k_{rn}+\varsigma_{ns}^{(e)}k_{zns}^{(e)}\right\}\cos\left(k_{zns}^{(e)}z\right)+$$

$$\mu^{(e)}\sum_{m=1}^{M_q}\sum_{s=1}^{2}Q_{ms}^{(e)}\left\{-K_{rms}^{(e)}+\eta_{ms}^{(e)}K_{zm}^{(e)}\right\}ak_{rn}^{(e)}\frac{J_0\left(k_{rn}^{(e)}a\right)J_1\left(K_{rms}^{(e)}a\right)}{K_{rms}^{(e)\,2}-k_{rn}{}^2}\cos\left(K_{zm}^{(e)}z\right)=$$

$\int_0^a\bar{T}_{rz}^{(e)}rJ_1(k_{rn}r)\,dr=0$ for n= 1,2,…,M_r. (4.31)

It can be seen from Eqs. (4.30) - (4.31) that the zero stress conditions on the flat ends of the transducer are satisfied in a weighted average sense by equating the weighted integral of stress to zero.

4.4.1.2.2 Curved Surfaces

On the curved surface of each cylinder, the normal and shear stresses are zero. These conditions are expressed as

$$\begin{Bmatrix}\hat{T}_{rr}^{(c)}\\ \hat{T}_{rz}^{(c)}\end{Bmatrix}=\begin{Bmatrix}0\\0\end{Bmatrix}\text{ on } r=a \text{ and } |z|\le\frac{L^{(c)}}{2} \tag{4.32}$$

where $c=p$ or e. These are also satisfied in a weighted average sense after replacing them by a large number of equations that are simplified by using the orthogonal property of

$\cos(k_{zn}^{(c)}z)$ and $\sin(K_{zn}^{(c)}z)$. The details are presented below first for the normal radial stress for the piezoelectric and elastic cylinders and then for the shear stress for both types of cylinders.

The resulting equations for $\hat{T}_{rr}^{(p)}$, obtained by using Eq. (4.20), and integrating over z, are

$$A^{(p)}2\left(c_{13}^{E}+\frac{e_{31}e_{33}}{\varepsilon_{33}^{S}}\right)\sin\left(k_{z0}\frac{L^{(p)}}{2}\right)+B^{(p)}L^{(p)}\left\{c_{11}^{E}k_{r0}J_0(k_{r0}a)+\frac{c_{12}^{E}-c_{11}^{E}}{a}J_1(k_{r0}a)\right\}+$$

$$De_{31}L^{(p)}+\sum_{m=1}^{M_r}\sum_{s=1}^{3}A_{ms}^{(p)}2\left[c_{11}^{E}\psi_{ms}\frac{k_{rm}}{k_{zms}^{(p)}}+c_{13}^{E}+e_{31}\chi_{ms}\right]J_0(k_{rm}a)\sin\left(k_{zms}^{(p)}\frac{L^{(p)}}{2}\right)=$$

$$\int_{-L^{(p)}/2}^{L^{(p)}/2}\hat{T}_{rr}^{(p)}dz\ =\ 0\ \text{for}\ n=0. \tag{4.33a}$$

Multiplying $\hat{T}_{rr}^{(p)}=0$ by $\cos(k_{zn}^{(c)}z)$ and integrating over z yields:

$$A^{(p)}2\left(c_{13}^{E}+\frac{e_{31}e_{33}}{\varepsilon_{33}^{S}}\right)\left[\frac{k_{zn}^{(p)}\sin\left(k_{zn}^{(p)}\frac{L^{(p)}}{2}\right)\cos\left(k_{z0}\frac{L^{(p)}}{2}\right)-k_{z0}\cos\left(k_{zn}^{(p)}\frac{L^{(p)}}{2}\right)\sin\left(k_{z0}\frac{L^{(p)}}{2}\right)}{{k_{zn}^{(p)}}^2-{k_{z0}}^2}\right]+$$

$$\sum_{m=1}^{M_r}\sum_{s=1}^{3}A_{ms}^{(p)}\left\{\left[c_{11}^{E}\psi_{ms}k_{rm}+(c_{13}^{E}+\right.\right.$$

$$\left.\left.e_{31}\chi_{ms})k_{zms}^{(p)}\right]J_0(k_{rm}a)\right\}2\left[\frac{k_{zms}^{(p)}\sin\left(k_{zn}^{(p)}\frac{L^{(p)}}{2}\right)\cos\left(k_{zms}^{(p)}\frac{L^{(p)}}{2}\right)-k_{zms}^{(p)}\cos\left(k_{zn}^{(p)}\frac{L^{(p)}}{2}\right)\sin\left(k_{zms}^{(p)}\frac{L^{(p)}}{2}\right)}{{k_{zn}^{(p)}}^2-{k_{zms}^{(p)}}^2}\right]+$$

$$\frac{L^{(p)}}{2}\sum_{s=1}^{3}B_{ns}^{(p)}\left\{\left[c_{11}^{E}\Phi_{ns}k_{rns}^{(p)}+(c_{13}^{E}+e_{31}\gamma_{ns})k_{zn}^{(p)}\right]J_0\left(k_{rns}^{(p)}a\right)+\frac{c_{12}^{E}-c_{11}^{E}}{a}\Phi_{ns}J_1\left(k_{rns}^{(p)}a\right)\right\}=$$

$$\int_{-L^{(p)}/2}^{L^{(p)}/2}\hat{T}_{rr}^{(p)}\cos\left(k_{zn}^{(p)}z\right)dz=0\ \ \text{for}\ \ n\ =\ 1,2,3,\ldots\ M_z, \tag{4.33b}$$

and multiplying $\hat{T}_{rr}^{(p)}=0$ by $\sin(K_{zn}^{(c)}z)$, and integrating over z yields

$$-P^{(p)}2\left(c_{13}^{E}+\frac{e_{31}e_{33}}{\varepsilon_{33}^{S}}\right)k_{z0}\left[\frac{k_{z0}\sin\left(K_{zn}^{(p)}\frac{L^{(p)}}{2}\right)\cos\left(k_{z0}\frac{L^{(p)}}{2}\right)-K_{zn}^{(p)}\cos\left(K_{zn}^{(p)}\frac{L^{(p)}}{2}\right)\sin\left(k_{z0}\frac{L^{(p)}}{2}\right)}{{K_{zn}^{(p)}}^2-{k_{z0}}^2}\right]+$$

$$\sum_{m=1}^{M_r}\sum_{s=1}^{3}P_{ms}^{(p)}\left[c_{11}^{E}\nu_{ms}k_{rm}^{(p)}-(c_{13}^{E}+\right.$$

$$\left.e_{31}\xi_{ms})k_{zms}^{(p)}\right]J_0(k_{rm}a)\,2\left[\frac{k_{zms}^{(p)}\sin\left(K_{zn}^{(p)}\frac{L^{(p)}}{2}\right)\cos\left(k_{zms}^{(p)}\frac{L^{(p)}}{2}\right)-K_{zn}^{(p)}\cos\left(k_{zn}^{(p)}\frac{L^{(p)}}{2}\right)\sin\left(k_{zms}^{(p)}\frac{L^{(p)}}{2}\right)}{{K_{zn}^{(p)}}^2-{k_{zms}^{(p)}}^2}\right]+$$

$$\frac{L^{(p)}}{2}\sum_{s=1}^{3}Q_{ns}^{(p)}\left\{\left[c_{11}^{E}\upsilon_{ns}K_{rns}^{(p)}-(c_{13}^{E}+e_{31}\vartheta_{ns})K_{zn}^{(p)}\right]J_0\left(K_{rns}^{(p)}a\right)+\frac{c_{12}^{E}-c_{11}^{E}}{a}\upsilon_{ns}J_1\left(K_{rns}^{(p)}a\right)\right\}=$$

$$\int_{-L^{(p)}/2}^{L^{(p)}/2}\hat{T}_{rr}^{(p)}\sin\left(K_{zn}^{(p)}z\right)dz=0\ \text{for}\ \ n\ =\ 1,2,3,\ldots\ M_q. \tag{4.33c}$$

Multiplying $\hat{T}_{rr}^{(e)} = 0$ in by 1 and integrating over z yields

$$A^{(e)} 2\lambda^{(e)} \sin\left(k_1^{(e)} \frac{L^{(e)}}{2}\right) + B^{(e)} L^{(e)} \left\{\left[\lambda^{(e)} + 2\mu^{(e)}\right] k_1^{(e)} J_0\left(k_1^{(e)} a\right) - \frac{2\mu^{(e)}}{a} J_1\left(k_1^{(e)} a\right)\right\} +$$

$$\sum_{m=1}^{M_r} \sum_{s=1}^{2} A_{ms}^{(e)} 2\left(\lambda^{(e)} + \left[\lambda^{(e)} + 2\mu^{(e)}\right] \frac{\alpha_{ms}^{(e)} k_{rm}}{k_{zms}^{(e)}}\right) J_0(k_{rm} a) \sin\left(k_{zms}^{(e)} \frac{L^{(e)}}{2}\right) =$$

$$\int_{-L^{(e)}/2}^{L^{(e)}/2} \hat{T}_{rr}^{(e)}\, dz = 0, \qquad (4.34a)$$

and multiplying $\hat{T}_{rr}^{(e)} = 0$ by $\cos(k_{zn}^{(c)} z)$ and integrating over z yields

$$A^{(e)} \lambda^{(e)} k_1^{(e)} 2 \left[\frac{k_{zn}^{(e)} \sin\left(k_{zn}^{(e)} \frac{L^{(e)}}{2}\right) \cos\left(k_1^{(e)} \frac{L^{(e)}}{2}\right) - k_1^{(e)} \cos\left(k_{zn}^{(e)} \frac{L^{(e)}}{2}\right) \sin\left(k_1^{(e)} \frac{L^{(e)}}{2}\right)}{{k_{zn}^{(e)}}^2 - {k_1^{(e)}}^2}\right] +$$

$$\sum_{m=1}^{M_r} \sum_{s=1}^{2} A_{ms}^{(e)} \left\{\lambda^{(e)} k_{zms}^{(e)} + \left[\lambda^{(e)} +\right.\right.$$

$$\left.\left. 2\mu^{(e)}\right] \alpha_{ms}^{(e)} k_{rm}\right\} J_0(k_{rm} a)\, 2 \left[\frac{k_{zn}^{(e)} \sin\left(k_{zn}^{(e)} \frac{L^{(e)}}{2}\right) \cos\left(k_{zms}^{(e)} \frac{L^{(e)}}{2}\right) - k_{zms}^{(e)} \cos\left(k_{zn}^{(e)} \frac{L^{(e)}}{2}\right) \sin\left(k_{zms}^{(e)} \frac{L^{(e)}}{2}\right)}{{k_{zn}^{(e)}}^2 - {k_{zms}^{(e)}}^2}\right] +$$

$$\frac{L^{(e)}}{2} \sum_{s=1}^{2} B_{ns}^{(e)} \left\{\left(\lambda^{(e)} k_{zn}^{(e)} + \left[\lambda^{(e)} + 2\mu^{(e)}\right] \beta_{ns}^{(e)} k_{rns}^{(e)}\right) J_0\left(k_{rns}^{(e)} a\right) - \frac{2\mu^{(e)}}{a} \beta_{ns}^{(e)} J_1\left(k_{rns}^{(e)} a\right)\right\} =$$

$$\int_{-L^{(e)}/2}^{L^{(e)}/2} \hat{T}_{rr}^{(e)} \cos\left(k_{zn}^{(e)} z\right) dz, \qquad \text{for} \quad n = 1, 2, \ldots, M_z \qquad (4.34b)$$

and multiplying $\hat{T}_{rr}^{(e)} = 0$ by $\sin(K_{zn}^{(e)} z)$ and integrating over z yields

$$-P^{(e)} 2\lambda^{(e)} k_1^{(e)} \left[\frac{k_1^{(e)} \sin\left(K_{zn}^{(e)} \frac{L^{(e)}}{2}\right) \cos\left(k_1^{(e)} \frac{L^{(e)}}{2}\right) - K_{zn}^{(e)} \cos\left(K_{zn}^{(e)} \frac{L^{(e)}}{2}\right) \sin\left(k_1^{(e)} \frac{L^{(e)}}{2}\right)}{{K_{zn}^{(e)}}^2 - {k_1^{(e)}}^2}\right] +$$

$$\sum_{m=1}^{M_r} \sum_{s=1}^{2} P_{ms}^{(e)} \left\{-\lambda^{(e)} k_{zms}^{(e)} + \left[\lambda^{(e)} +\right.\right.$$

$$\left.\left. 2\mu^{(e)}\right] \varsigma_{ms}^{(e)} k_{rm}\right\} J_0(k_{rm} a)\, 2 \left[\frac{k_{zms}^{(e)} \sin\left(K_{zn}^{(e)} \frac{L^{(e)}}{2}\right) \cos\left(k_{zms}^{(e)} \frac{L^{(e)}}{2}\right) - K_{zn}^{(e)} \cos\left(K_{zn}^{(e)} \frac{L^{(e)}}{2}\right) \sin\left(k_{zms}^{(e)} \frac{L^{(e)}}{2}\right)}{{K_{zn}^{(e)}}^2 - {k_{zms}^{(e)}}^2}\right] +$$

$$\frac{L^{(e)}}{2} \sum_{s=1}^{2} Q_{ns}^{(e)} \left\{\left(-\lambda^{(e)} K_{zn}^{(e)} + \left[\lambda^{(e)} + 2\mu^{(e)}\right] \eta_{ns}^{(e)} K_{rns}^{(e)}\right) J_0\left(k_{rns}^{(e)} a\right) - \frac{2\mu^{(e)}}{a} \eta_{ns}^{(e)} J_1\left(K_{rns}^{(e)} a\right)\right\} =$$

$$\int_{-L^{(e)}/2}^{L^{(e)}/2} \hat{T}_{rr}^{(e)} \sin\left(K_{zn}^{(e)} z\right) dz = 0 \text{ for } n = 1, 2, \ldots, M_q. \qquad (4.34c)$$

The boundary conditions on $\hat{T}_{rz}^{(c)}$, $c = p$ or e are also satisfied in a weighted average sense. For the piezoceramic cylinder, multiplying $\hat{T}_{rz}^{(p)} = 0$ in by 1, $\cos(K_{zn}^{(c)} z)$ and $\sin(k_{zn}^{(c)} z)$ respectively, and integrating over z yields

$$\sum_{m=1}^{M_q} \sum_{s=1}^{3} Q_{ms}^{(p)} \left\{ c_{44}^{E} \left[-K_{rms}^{(p)} + \upsilon_{ms} K_{zm}^{(p)} \right] - e_{15} \vartheta_{ms} K_{rms}^{(p)} \right\} J_1\left(K_{rms}^{(p)} a \right) \frac{2}{K_{zm}^{(p)}} \sin\left(K_{zm}^{(p)} \frac{L^{(p)}}{2} \right) =$$

$$\int_{-L^{(p)}/2}^{L^{(p)}/2} \hat{T}_{rz}^{(p)} dz \quad \text{for } n = 0, \tag{4.35a}$$

$$\frac{L^{(p)}}{2} \sum_{s=1}^{3} Q_{ns}^{(p)} \left\{ c_{44}^{E} \left[-K_{rns}^{(p)} + \upsilon_{ns} K_{zn}^{(p)} \right] - e_{15} \vartheta_{ns} K_{rns}^{(p)} \right\} J_1\left(K_{rns}^{(p)} a \right) =$$

$$\int_{-L^{(p)}/2}^{L^{(p)}/2} \hat{T}_{rz}^{(p)} \cos\left(K_{zn}^{(p)} z \right) dz \quad \text{for } n = 1, 2, \ldots, M_q, \tag{4.35b}$$

and

$$-\frac{L^{(p)}}{2} \sum_{s=1}^{3} B_{ns}^{(p)} \left\{ c_{44}^{E} \left[k_{rns}^{(p)} + \phi_{ns} k_{zn}^{(p)} \right] + e_{15} \gamma_{ns} k_{rns}^{(p)} \right\} J_1\left(k_{rns}^{(p)} a \right) =$$

$$\int_{-L^{(p)}/2}^{L^{(p)}/2} \hat{T}_{rz}^{(p)} \sin\left(k_{zn}^{(p)} z \right) dz \quad \text{for } n = 1, 2, \ldots, M_z. \tag{4.35c}$$

For the elastic cylinders, the same procedure is followed by using $\hat{T}_{rz}^{(e)} = 0$, Eq. (4.21), and the orthogonality properties in Eq. (2.9) and (2.10). This yields

$$\sum_{m=1}^{M_q} \sum_{s=1}^{2} Q_{ms}^{(e)} \left[-K_{rms}^{(e)} + \eta_{ms}^{(e)} K_{zm}^{(e)} \right] J_1\left(K_{rms}^{(e)} a \right) \frac{2}{K_{zm}^{(e)}} \sin\left(K_{zm}^{(e)} \frac{L^{(e)}}{2} \right) = \int_{-L^{(e)}/2}^{L^{(e)}/2} \hat{T}_{rz}^{(e)} dz$$

for $n = 0$, (4.36a)

$$\mu^{(e)} \frac{L^{(e)}}{2} \sum_{s=1}^{2} Q_{ns}^{(e)} \left[-K_{rns}^{(e)} + \eta_{ns}^{(e)} K_{zn}^{(e)} \right] J_1\left(K_{rns}^{(p)} a \right) = \int_{-L^{(e)}/2}^{L^{(e)}/2} \hat{T}_{rz}^{(e)} \cos\left(K_{zn}^{(e)} z \right) dz$$

for $n = 1, 2, \ldots, M_q$, (4.36b)

and

$$\mu^{(e)} \frac{L^{(e)}}{2} \sum_{s=1}^{2} B_{ns}^{(e)} \left[k_{rns}^{(e)} + \beta_{ns}^{(e)} k_{zn}^{(e)} \right] J_1\left(k_{rns}^{(p)} a \right) = \int_{-L^{(e)}/2}^{L^{(e)}/2} \hat{T}_{rz}^{(e)} \sin\left(k_{zn}^{(e)} z \right) dz$$

for $n = 1, 2, \ldots, M_z$. (4.36c)

4.4.2 **Continuity Conditions**

The classical Langevin transducer has two flat interfaces in addition to the boundary surfaces; one is between the bottom elastic and middle piezoceramic cylinders and the other is between the piezoceramic and top elastic cylinders. The continuity of the axial and radial

displacements and the normal and shear components of stress are used to build the model of the Langevin transducer. In order to satisfy the continuity conditions, the stresses and displacements are equated at the corresponding interfaces. At the bottom interface between the bottom elastic and middle piezoceramic cylinder, the following conditions are satisfied for $|r| \leq a$:

$$\begin{Bmatrix} \bar{U}^{(1)} \\ \bar{W}^{(1)} \\ \bar{T}_{zz}^{(1)} \\ \bar{T}_{rz}^{(1)} \end{Bmatrix}_{z=L^{(1)}/2} = \begin{Bmatrix} \bar{U}^{(p)} \\ \bar{W}^{(p)} \\ \bar{T}_{zz}^{(p)} \\ \bar{T}_{rz}^{(p)} \end{Bmatrix}_{z=-L^{(p)}/2} . \tag{4.37}$$

Similarly, at the top interface between the piezoceramic and top elastic cylinders, the following conditions are satisfied for$|r| \leq a$:

$$\begin{Bmatrix} \bar{U}^{(p)} \\ \bar{W}^{(p)} \\ \bar{T}_{zz}^{(p)} \\ \bar{T}_{rz}^{(p)} \end{Bmatrix}_{z=L^{(p)}/2} = \begin{Bmatrix} \bar{U}^{(3)} \\ \bar{W}^{(3)} \\ \bar{T}_{zz}^{(3)} \\ \bar{T}_{rz}^{(3)} \end{Bmatrix}_{z=-L^{(3)}/2} . \tag{4.38}$$

All the continuity equations are satisfied in a weighted average sense and they are simplified by using the orthogonal properties of the Bessel functions in the sets.

4.4.2.1 Continuity of Displacement

Multiplying the continuity condition for the axial displacement, U, by $rJ_0(k_{rn}r)$, integrating over r, and using the orthogonal properties of $J_0(k_{rn}r)$ yields weighted average equations for $n = 0, 1, 2, ...$This is done in two steps. In the first step, performing the above operations on the functions on either side of the equations yields the following intermediate equations for arbitrary z. In the second step, the weighted average continuity conditions are obtained by equating the appropriate intermediate equations evaluated at appropriate specific values of z.

The continuity condition for U is presented first. The expression for $U^{(p)}$ in the piezoelectric cylinder is in Eq. (4.6). Performing the multiplication and integration operations yields, for arbitrary z,

$$A^{(p)}\frac{a^2}{2}\sin(k_{z0}z) + P^{(p)}\frac{a^2}{2}\cos(k_{z0}z) + \sum_{m=1}^{M_q}\sum_{s=1}^{3} Q_{ms}^{(p)} \cos\left(K_{zm}^{(p)}z\right)\frac{a}{K_{rms}^{(p)}}J_1\left(K_{rms}^{(p)}a\right) =$$

$$\int_0^a \bar{U}^{(p)} r dr \quad \text{for } n = 0 \tag{4.39a}$$

and

$$\frac{a^2}{2}J_0^2(k_{rn}a)\sum_{s=1}^{3}A_{ns}^{(p)}\sin\left(k_{zns}^{(p)}z\right)+\frac{a^2}{2}J_0^2(k_{rn}a)\sum_{s=1}^{3}P_{ns}^{(p)}\cos\left(k_{zns}^{(p)}z\right)+$$

$$\sum_{m=1}^{M_q}\sum_{s=1}^{3}Q_{ms}^{(p)}\cos\left(K_{zm}^{(p)}z\right)K_{rms}^{(p)}a\frac{J_0(k_{rn}a)J_1\left(K_{rms}^{(p)}a\right)}{{K_{rms}^{(p)}}^2-{k_{rn}}^2}=\int_0^a\bar{U}^{(p)}rJ_0(k_{rn}r)dr$$

for $n=1,2,\ldots,M_r$. (4.39b)

For elastic cylinders, multiplication of $U^{(e)}$ in Eq. (4.15) by $rJ_0(k_{rn}r), e=1,3$ and integrating with respect to *r* yields:

$$A^{(e)}\frac{a^2}{2}\sin\left(k_1^{(e)}z\right)+P^{(e)}\frac{a^2}{2}\cos\left(k_1^{(e)}z\right)+\sum_{m=1}^{M_q}\sum_{s=1}^{2}Q_{ms}^{(e)}\cos\left(K_{zm}^{(e)}z\right)\frac{a}{K_{rms}^{(e)}}J_1\left(K_{rms}^{(e)}a\right)=$$

$\int_0^a\bar{U}^{(e)}rdr$ for $n=0$ (4.40a)

and

$$\frac{a^2}{2}J_0^2(k_{rn}a)\sum_{s=1}^{2}A_{ns}^{(e)}\sin\left(k_{zns}^{(e)}z\right)+\frac{a^2}{2}J_0^2(k_{rn}a)\sum_{s=1}^{e}P_{ns}^{(e)}\cos\left(k_{zns}^{(e)}z\right)+$$

$$\sum_{m=1}^{M_q}\sum_{s=1}^{2}Q_{ms}^{(e)}\cos\left(K_{zm}^{(e)}z\right)K_{rms}^{(e)}a\frac{J_0(k_{rn}a)J_1\left(K_{rms}^{(e)}a\right)}{{K_{rms}^{(e)}}^2-{k_{rn}}^2}=\int_0^a\bar{U}^{(e)}rJ_0(k_{rn}r)dr$$

for $n=1,2,\ldots,M_r$. (4.40b)

The continuity condition on U at the interface between the bottom elastic cylinder and the piezoelectric cylinder is obtained by using $z=-L^{(2)}/2$ in Eq. (4.39) and $z=L^{(1)}/2$ in Eq. (4.40) and equating them. Similarly, the continuity condition on U at the interface between the piezoelectric cylinder and the top elastic cylinder is obtained by using $z=L^{(2)}/2$ in Eq. (4.39) and $z=-L^{(3)}/2$ in Eq. (4.40) and equating them.

The continuity of the radial displacement W at the interfaces is also satisfied in a similar manner. It is satisfied by using the orthogonal property of $J_1(k_{rn}r)$ in Eq. (4.22). In the first step, the following intermediate equations are obtained by multiplying the expressions for W for the piezoceramic and elastic cylinders in Eqs. (4.6) and (4.15), respectively, by $rJ_1(k_{rn}r)$ and integrating with respect to *r*:

$$B^{(p)}k_{rn}a\frac{J_0(k_{rn}a)J_1(k_{r0}a)}{{k_{r0}}^2-{k_{rn}}^2}+\frac{a^2}{2}J_0^2(k_{rn}a)\sum_{s=1}^{3}A_{ns}^{(p)}\psi_{ns}\cos\left(k_{zns}^{(p)}z\right)+$$

$$\sum_{m=1}^{M_z}\sum_{s=1}^{3}B_{ms}^{(p)}\phi_{ms}\cos\left(k_{zm}^{(p)}z\right)k_{rn}^{(p)}a\frac{J_0(k_{rn}a)J_1\left(k_{rms}^{(p)}a\right)}{{k_{rms}^{(p)}}^2-{k_{rn}}^2}-$$

$$\frac{a^2}{2}J_0^2(k_{rn}a)\sum_{s=1}^{3}P_{ns}^{(p)}\nu_{ns}\sin\left(k_{zns}^{(p)}z\right)+$$

$$\sum_{m=1}^{M_z}\sum_{s=1}^{3} Q_{ms}^{(p)}\upsilon_{ms}\sin\left(K_{zm}^{(p)}z\right)k_{rn}^{(p)}a\frac{J_0(k_{rn}a)J_1\left(K_{rms}^{(p)}a\right)}{{K_{rms}^{(p)}}^2-{k_{rn}}^2}=\int_0^a \bar{W}^{(p)}rJ_1(k_{rn}r)dr \quad \text{for} \quad n=$$

$$1,2,\ldots,M_r \tag{4.41}$$

for the piezoceramic cylinder, and

$$B^{(e)}k_{rn}^{(e)}a\frac{J_0(k_{rn}a)J_1\left(k_1^{(e)}a\right)}{{k_1^{(e)}}^2-{k_{rn}}^2}+\frac{a^2}{2}J_0^2(k_{rn}a)\sum_{s=1}^{2}A_{ns}^{(e)}\alpha_{ns}^{(e)}\cos\left(k_{zns}^{(e)}z\right)+$$

$$\sum_{m=1}^{M_z}\sum_{s=1}^{2}B_{ms}^{(e)}\beta_{ms}^{(e)}\cos\left(k_{zm}^{(e)}z\right)k_{rn}a\frac{J_0(k_{rn}a)J_1\left(k_{rms}^{(e)}a\right)}{{k_{rms}^{(e)}}^2-{k_{rn}}^2}+$$

$$\frac{a^2}{2}J_0^2(k_{rn}a)\sum_{s=1}^{2}P_{ns}^{(e)}\varsigma_{ns}^{(e)}\sin\left(k_{zns}^{(e)}z\right)+$$

$$\sum_{m=1}^{M_z}\sum_{s=1}^{2}Q_{ms}^{(e)}\eta_{ms}^{(e)}\sin\left(K_{zm}^{(e)}z\right)k_{rn}a\frac{J_0(k_{rn}a)J_1\left(K_{rms}^{(e)}a\right)}{{K_{rms}^{(e)}}^2-{k_{rn}}^2}=\int_0^a \bar{W}^{(e)}rJ_1(k_{rn}r)dr \text{ for } n=$$

$$1,2,\ldots,M_r \tag{4.42}$$

for the elastic cylinders.

The continuity condition on W at the interfaces between the cylinders is obtained by using the appropriate values of z in Eqs. (4.41) and (4.42) and equating them.

4.4.2.2 Continuity of Stress

The normal stress T_{zz} and the shear stress T_{rz} are also continuous at the two interfaces. The weighted average continuity equations are obtained here by following the two steps used earlier for continuity of displacements.

For the piezoceramic cylinder, multiplying the expression for $T_{zz}^{(p)}$ in Eq. (4.8) by $rJ_0(k_{rn}r)$ and integrating with respect to *r* yields:

$$A^{(p)}\left(c_{33}^E+\frac{e_{33}^2}{\varepsilon_{33}^S}\right)k_{z0}\frac{a^2}{2}\cos(k_{z0}z)+B^{(p)}c_{13}^E a J_1(k_{r0}a)+De_{33}\frac{a^2}{2}-P^{(p)}\left(c_{33}^E+\right.$$

$$\left.\frac{e_{33}^2}{\varepsilon_{33}^S}\right)k_{z0}\frac{a^2}{2}\sin(k_{z0}z)+\sum_{m=1}^{M_z}\sum_{s=1}^{3}B_{ms}^{(p)}\left\{c_{13}^E\phi_{ms}k_{rms}^{(p)}+(c_{33}^E+\right.$$

$$\left.e_{33}\gamma_{ms})k_{zm}^{(p)}\right\}\frac{a}{k_{rms}^{(p)}}J_1\left(k_{rms}^{(p)}a\right)\cos\left(k_{zm}^{(p)}z\right)+\sum_{m=1}^{M_q}\sum_{s=1}^{3}Q_{ms}^{(p)}\left\{c_{13}^E\upsilon_{ms}K_{rms}^{(p)}-(c_{33}^E+\right.$$

$$\left.e_{33}\vartheta_{ms})K_{zm}^{(p)}\right\}\frac{a}{K_{rms}^{(p)}}J_1\left(K_{rms}^{(p)}a\right)\sin\left(K_{zm}^{(p)}z\right)=\int_0^a \bar{T}_{zz}^{(p)}rdr \text{ for } n=0 \tag{4.43a}$$

and

$$B^{(p)}c_{13}^{E}{k_{r0}}^{2}a\frac{J_0(k_{rn}a)\,J_1(k_{r0}a)}{{k_{r0}}^{2}-{k_{rn}}^{2}}+\frac{a^2}{2}{J_0}^{2}(k_{rn}a)\sum_{s=1}^{3}A_{ns}^{(p)}\left\{c_{13}^{E}\psi_{ns}k_{rn}+(c_{33}^{E}+e_{33}\chi_{ns})k_{zns}^{(p)}\right\}\cos\left(k_{zns}^{(p)}z\right)+\sum_{m=1}^{M_z}\sum_{s=1}^{3}B_{ms}^{(p)}\left\{c_{13}^{E}\phi_{ms}k_{rms}^{(p)}+(c_{33}^{E}+e_{33}\gamma_{ms})k_{zm}^{(p)}\right\}\frac{k_{rms}^{(p)}a}{{k_{rms}^{(p)}}^{2}-{k_{rn}}^{2}}J_0(k_{rn}a)\,J_1\left(k_{rms}^{(p)}a\right)\cos\left(k_{zm}^{(p)}z\right)+\frac{a^2}{2}{J_0}^{2}(k_{rn}a)\sum_{s=1}^{3}P_{ns}^{(p)}\left\{c_{13}^{E}\nu_{ns}k_{rn}-(c_{33}^{E}+e_{33}\xi_{ns})k_{zns}^{(p)}\right\}\sin\left(k_{zns}^{(p)}z\right)+\sum_{m=1}^{M_z}\sum_{s=1}^{3}Q_{ms}^{(p)}\left\{c_{13}^{E}\upsilon_{ms}K_{rms}^{(p)}-(c_{33}^{E}+e_{33}\vartheta_{ms})K_{zm}^{(p)}\right\}\frac{K_{rms}^{(p)}a}{{K_{rms}^{(p)}}^{2}-{k_{rn}}^{2}}J_0(k_{rn}a)\,J_1\left(K_{rms}^{(p)}a\right)\sin\left(K_{zm}^{(p)}z\right)=\int_0^a\bar{T}_{zz}^{(p)}r\,J_0(k_{rn}r)\,dr$$

for $=1,2,\dots,M_r$. (4.43b)

For the elastic cylinder, Eqs. (4.30) correspond to Eqs. (4.43) for the piezoceramic cylinder. The continuity condition on T_{zz} at the interface between the bottom elastic cylinder and the piezoelectric cylinder is obtained by using $z=-L^{(2)}/2$ in Eq. (4.43) and $z=L^{(1)}/2$ in Eq. (4.30) and equating them. Similarly, the continuity condition on T_{zz} at the interface between the piezoelectric cylinder and the top elastic cylinder is obtained by using $z=L^{(2)}/2$ in Eq. (4.43) and $z=-L^{(3)}/2$ in Eq. (4.30) and equating them.

The continuity condition on T_{rz} is also satisfied by performing the two steps. For the piezoceramic cylinder, multiplying T_{rz} by $r\,J_1(k_{rn}r)$ and integrating with respect to r yields the following intermediate equations for arbitrary z:

$$-\frac{a^2}{2}{J_0}^{2}(k_{rn}a)\sum_{s=1}^{3}A_{ns}^{(p)}\left\{c_{44}^{E}\left[k_{rn}+\psi_{ns}k_{zns}^{(p)}\right]+e_{15}\chi_{ns}k_{rn}\right\}\sin\left(k_{zns}^{(p)}z\right)+\frac{a^2}{2}{J_0}^{2}(k_{rn}a)\sum_{s=1}^{3}P_{ns}^{(p)}\left\{c_{44}^{E}\left[-k_{rn}+\nu_{ns}k_{zns}^{(p)}\right]-e_{15}\xi_{ns}k_{rn}\right\}\cos\left(k_{zns}^{(p)}z\right)+\sum_{m=1}^{M_q}\sum_{s=1}^{3}Q_{ms}^{(p)}\left\{c_{44}^{E}\left[-K_{rms}^{(p)}+\upsilon_{ms}K_{zm}^{(p)}\right]-e_{15}\vartheta_{ms}K_{rms}^{(p)}\right\}\frac{k_{rn}a}{{K_{rms}^{(p)}}^{2}-{k_{rn}}^{2}}J_0(k_{rn}a)\,J_1\left(K_{rms}^{(p)}a\right)\cos\left(K_{zm}^{(p)}z\right)=\int_0^a\bar{T}_{rz}^{(p)}r\,J_1(k_{rn}r)\,dr.$$

for $n=1,2,\dots,M_r$. (4.44)

For the elastic cylinder, Eqs. (4.31) correspond to Eqs. (4.44) for the piezoceramic cylinder. The continuity condition on T_{rz} at the interfaces between the cylinders is obtained by using the appropriate values of z in Eqs. (4.44) and (4.31) and equating them.

4.5 MATRIX FORM

In order to compute numerical results, all the boundary and continuity conditions are truncated, combined, and expressed in a matrix form as,

$$[F]\{X\} = \{G\} \tag{4.45a}$$

where

$$\{X\}^T = \left[A^{(1)}, B^{(1)}, P^{(1)}, A_{11}^{(1)}, A_{12}^{(1)}, A_{21}^{(1)}, A_{22}^{(1)}, \dots, A_{M_r1}^{(1)}, A_{M_r2}^{(1)}, B_{11}^{(1)}, B_{12}^{(1)}, B_{21}^{(1)}, B_{22}^{(1)}, \dots, B_{M_z1}^{(1)}, B_{M_z2}^{(1)},\right.$$
$$P_{11}^{(1)}, P_{12}^{(1)}, \dots, P_{M_r1}^{(1)}, P_{M_r2}^{(1)}, Q_{11}^{(1)}, Q_{12}^{(1)}, \dots, Q_{M_q1}^{(1)}, Q_{M_q2}^{(1)}, A^{(2)}, B^{(2)}, D, E, P^{(2)}, A_{11}^{(2)}, A_{12}^{(2)}, A_{13}^{(2)}, \dots,$$
$$A_{M_r1}^{(2)}, A_{M_r2}^{(2)}, A_{M_r3}^{(2)}, B_{11}^{(2)}, B_{12}^{(2)}, B_{13}^{(2)}, \dots, B_{M_z1}^{(2)}, B_{M_z2}^{(2)}, B_{M_z3}^{(2)}, P_{11}^{(2)}, P_{12}^{(2)}, P_{13}^{(2)}, \dots, P_{M_r1}^{(2)}, P_{M_r2}^{(2)}, P_{M_r3}^{(2)}$$
$$Q_{11}^{(2)}, Q_{12}^{(2)}, Q_{13}^{(2)}, \dots, Q_{M_q1}^{(2)}, Q_{M_q2}^{(2)}, Q_{M_q3}^{(2)}, A^{(1)}, B^{(1)}, P^{(1)}, A_{11}^{(3)}, A_{12}^{(3)}, \dots, A_{M_r1}^{(3)}, A_{M_r2}^{(3)}, B_{11}^{(3)}, B_{12}^{(3)}, \dots,$$
$$\left.B_{M_z1}^{(3)}, B_{M_z2}^{(3)}, P_{11}^{(3)}, P_{12}^{(3)}, \dots, P_{M_r1}^{(3)}, P_{M_r2}^{(3)}, Q_{11}^{(3)}, Q_{12}^{(3)}, \dots, Q_{M_q1}^{(3)}, Q_{M_q2}^{(3)}\right] \tag{4.45b}$$

is a column matrix of coefficients that are to be determined, $[F]$is a square matrix of size $[14M_r+7M_z+7M_q+14]$, and M_r, M_z, and M_q are the number of terms in the series solutions. The elements of the column matrix $\{G\}$ are non-zero only when the corresponding boundary conditions on the surfaces are non-zero. In the special case mentioned here, the only non-zero element of $\{G\}$ is

$$G_{M_r+2} = \int_0^a \emptyset_0 r dr = \emptyset_0 \frac{a^2}{2}. \tag{4.46}$$

Solving Eq. (4.45) for $\{X\}$, yields the coefficients and the parameters of interest are then determined by using Eqs. (4.6), (4.8) – (4.21). It is noted that the number of equations is equal to the number of coefficients in Eq. (4.45) irrespective of the values of M_r, M_z, and M_q.

4.6 NUMERICAL RESULTS AND SPECIAL CASES

Numerical results are presented for four different Langevin transducers and are compared with those computed using ATILA to illustrate the accuracy of the analytical model. Values of certain critical frequencies, the input electrical admittance, displacement

and stresses are presented. In ATILA, second order, axisymmetric, rectangular elements are used. The elements used are equisized. The results are computed using $I \times J$ elements, i.e. I elements in the axial direction and J elements in the radial direction. The number of finite elements that is necessary for accurate analysis depends on the frequency and spatial distribution of the excitation and is determined through convergence studies. Convergence is illustrated for one of the transducers. All the ATILA results presented in this report are computed with I=J=40 unless specified.

A PZT 4 piezoceramic cylinder of length 10 mm is used in all the Langevin transducers considered and the properties of PZT 4 are shown in Table 2.1. In this analysis, losses are considered only for the piezoceramic cylinder.

The Young's modulus Y, Poisson's ratio σ, and density ρ, of the elastic cylinder (steel) are 200 GPa, 0.3, and 7800 kg/m^3 respectively, i.e., the Lame's constants are $\lambda \approx$ 115.38 GPa and $\mu \approx$76.923 GPa. Similarly, the Young's modulus, Y, Poisson's ratio σ, and density ρ, of the elastic cylinder (Aluminium) are 71 GPa, 0.33, and 2700 kg/m^3 respectively, i.e., the Lame's constants are $\lambda \approx$ 51.813 GPa and $\mu \approx$ 26.692 GPa.

Numerical results are presented for four different Langevin transducers with stress-free boundary conditions. Details of the four transducers are shown in Table 4.1. In all the cases, both elastic and piezoceramic cylinders are of radius 5 mm and the bottom elastic cylinder is of Steel. In case 1, the piezoelectric cylinder is sandwiched between two elastic steel cylinders. All the three cylinders have the same length, 10 mm. In the second case, the length of the top elastic steel cylinder is reduced to 5 mm. The third transducer has an Aluminium head of length 10 mm and in case 4, the length of the Aluminium head is reduced to 5 mm. In all the cases, the critical frequencies associated with each transducer are computed in the neighborhood of the first three resonances. The critical frequencies f_s, $f_{-1/2s}$, and $f_{1/2s}$ and the corresponding electrical parameters at these frequencies G_{max}, B_{max}, and B_{min}, respectively, are computed using the present method and by ATILA and are shown in tables. The percentage error is also shown. In all the figures, a solid line is used to show the values computed using the present method and dots are used to show those computed using ATILA, unless specified.

Table 4.1. Different cases considered for the analysis.

Case No.	Elastic Cylinder (Bottom)	Piezoceramic Cylinder	Elastic Cylinder 3 (Top)
1	Length, L_1=10 mm Radius, a = 5 mm Material: Steel	Length, L_2= 10 mm Radius, a = 5 mm Material: PZT 4	Length, L_3 = 10 mm Radius, a = 5 mm Material: Steel
2			Length, L_3 = 5 mm Radius, a = 5 mm Material: Steel
3			Length, L_3 = 10 mm Radius, a = 5 mm Material: Aluminium
4			Length, L_3 = 5 mm Radius, a = 5 mm Material: Aluminium

4.6.1 **Case 1**

As mentioned in Table 4.1, in the first case considered, the piezoelectric cylinder is sandwiched between two elastic steel cylinders. All the three cylinders have the same length 10 mm. The stress is zero at the free ends of the elastic cylinders and at the curved surface of each cylinder. The transducer is symmetric. The critical frequencies are shown in Table 4.2. Analytical results are computed using M_r= M_z= M_q=10.

The critical frequencies in the neighborhood of the first three resonances are in good agreement with those computed using ATILA. The first resonance of the transducer where G has a maximum is at 55.66 kHz by present approach and ATILA shows it is at 55.65 kHz. In the neighborhood of this resonance, four significant digits of the critical frequencies and three significant digits of the admittance are shown in Table 4.1. The maximum percentage error in the critical frequencies and admittance is 0.02%. In the neighborhood of the second resonance, the maximum error in the critical frequencies is 0.02% but the error in the admittance is about 0.4%. M_r= M_z= M_q=10 is used to generate the analytical results. The conductance (G) and susceptance (B) of the transducer are shown in Fig. 4.2(a) and 4.2(b), respectively. The results are shown upto 500 kHz with 1 kHz resolution and the agreement between analysis and ATILA is very good in the entire band. All the peaks in G are clearly predicted by the present method.

Table 4.2. Critical frequencies and G and B values of the transducer in Case 1.

Resonance	Method	f_s (kHz)	G_{max} (mS)	$f_{-1/2s}$ (kHz)	B_{max} (mS)	$f_{1/2s}$ (kHz)	B_{min} (mS)
First	ATILA	55.65	2.88	55.54	1.45	55.76	-1.43
	Present Method	55.66	2.88	55.54	1.45	55.77	-1.43
	% Error	0.02	0	0	0	0.02	0
Second	ATILA	205.61	5.04	205.49	2.58	205.74	-2.46
	Present Method	205.65	5.02	205.52	2.57	205.77	-2.45
	% Error	0.02	-0.39	0.01	-0.39	0.01	-0.41
Third	ATILA	269.68	0.02	269.26	0.08	270.08	0.06
	Present Method	269.71	0.02	269.29	0.08	270.11	0.06
	% Error	0.01	0	0.01	0	0.01	0

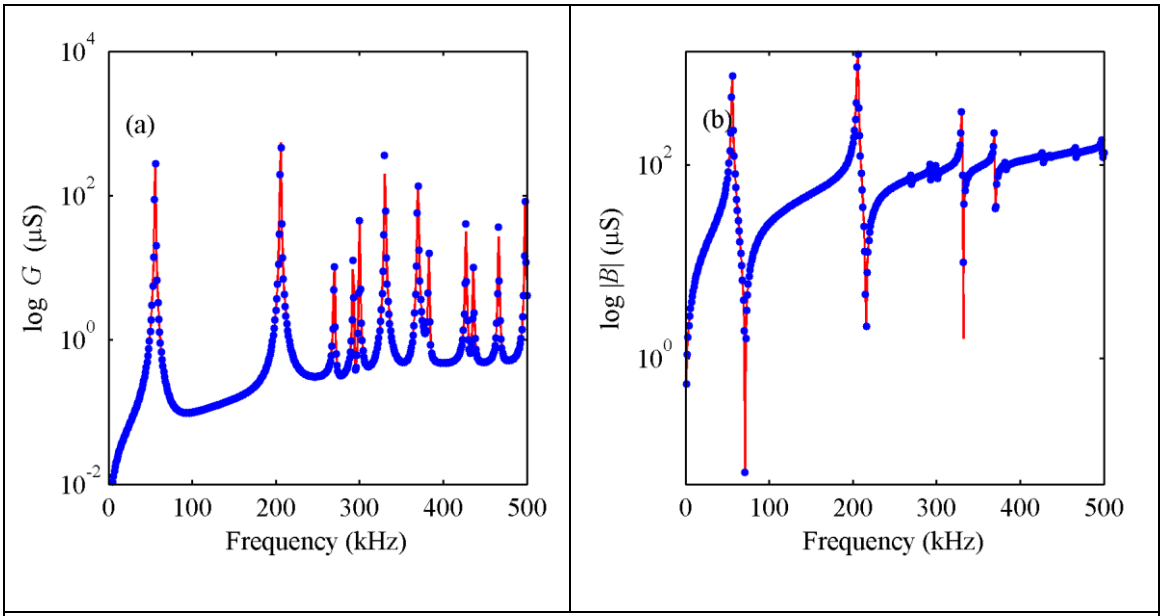

Fig. 4.2. (a) Conductance (G) and (b) Susceptance (B) of the transducer in Case 1. Solid line: Present Method and Dots: ATILA.

The axial displacement, U, along the axis of the transducer ($r = 0, -L^{(1)}/2 \leq z \leq L^{(3)}/2$) at the first resonance frequency, 55.66 kHz, is shown in Fig. 4.3. The real and imaginary parts of U are shown in Fig. 4.3(a) and 4.3(b) respectively. In Fig. 4.3, zero on

the x-axis is the axial center of the Langevin transducer, i.e. the center of the piezoceramic cylinder on the axis; the negative value on the left side represents the center of the bottom flat surface of the bottom elastic cylinder and that on the right end corresponds to the center of top flat surface of the top elastic cylinder. The real and imaginary parts of the displacement are in very good agreement with ATILA values. As the transducer is symmetric about the middle plane of the piezoceramic cylinder, the real and imaginary parts are anti-symmetric about zero - as seen in Fig. 4.3.

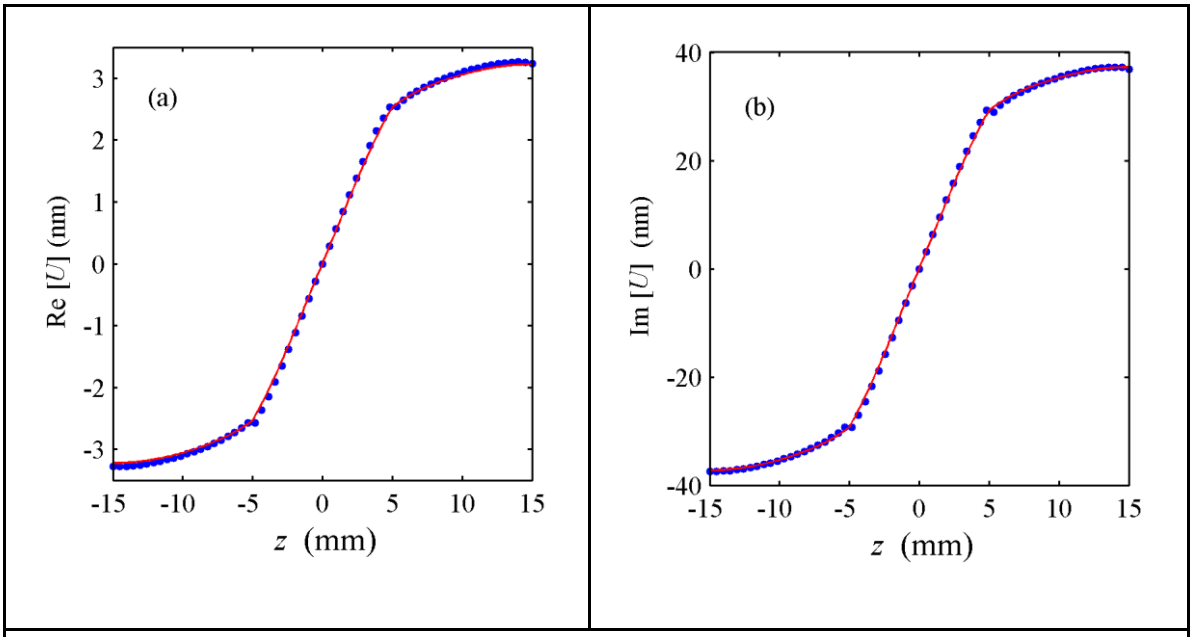

Fig. 4.3. (a) Real and (b) imaginary parts of the axial displacement, U, on the axis of the transducer at its first resonance frequency, 55.66 kHz. Solid line: Present Method and Dots: ATILA.

4.6.2 **Case 2**

The Langevin transducer in case 2 has a lighter head than in case 1. Here, the length of the steel head is reduced to 5 mm and the tail is 10 mm. The transducer is not symmetric. The critical frequencies and the corresponding *G*-*B* values are shown in Table 4.3.

The percentage errors between the analytical and ATILA values are also shown in Table 4.3. The present method predicts the first resonance frequency with a percentage error of 0.02. The corresponding G value differs from ATILA by 0.3%. The rest of the critical frequencies and associated B values are computed with zero percent error in the neighborhood of the first resonance. The maximum percentage error in critical frequencies

is 0.07 and that in the corresponding *G*-*B* values is less than 3%, which occurs in the neighborhood of the third resonance frequency.

Table 4.3. Critical frequencies and *G* and *B* values of the transducer in Case 2.

Resonance	Method	f_s (kHz)	G_{max} (mS)	$f_{-1/2s}$ (kHz)	B_{max} (mS)	$f_{1/2s}$ (kHz)	B_{min} (mS)
First	ATILA	65.41	3.38	65.28	1.71	65.55	-1.68
	Present Method	65.42	3.39	65.28	1.71	65.55	-1.68
	% Error	0.02	0.30	0	0	0	0
Second	ATILA	172.32	1.32	172.17	0.71	172.47	-0.61
	Present Method	172.36	1.32	172.21	0.71	172.51	-0.61
	% Error	0.02	0	0.02	0	0.02	0
Third	ATILA	229.67	0.64	229.38	0.38	229.95	-0.26
	Present Method	229.81	0.65	229.53	0.39	230.09	-0.26
	% Error	0.06	1.56	0.07	2.63	0.06	0

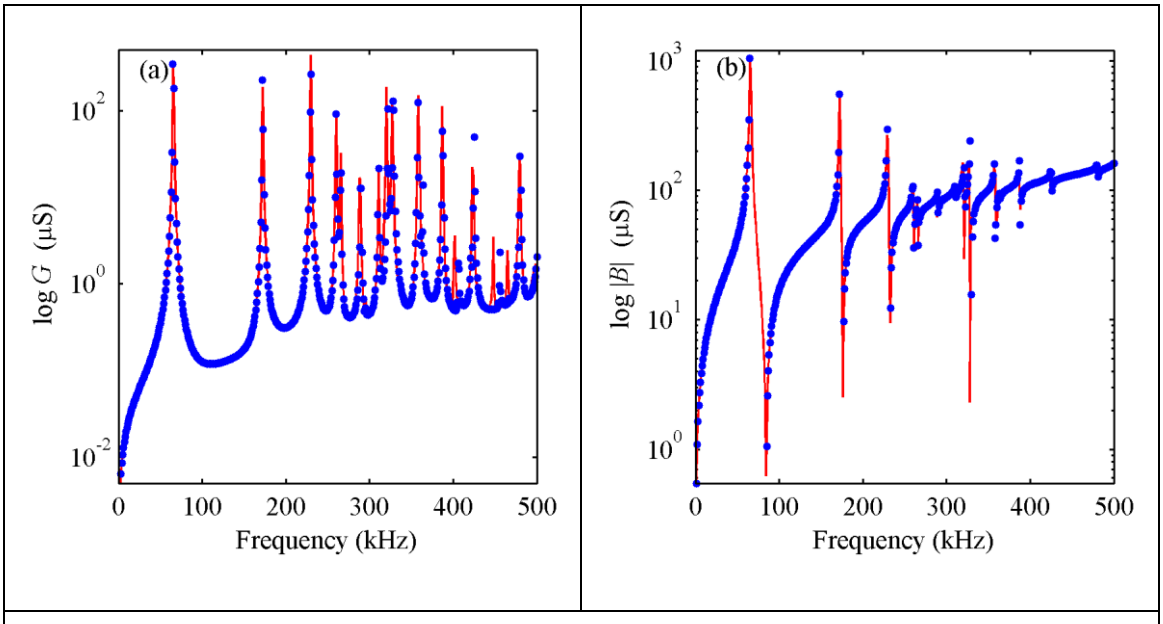

Fig. 4.4. (a) Conductance (*G*) and (b) Susceptance (*B*) of the Langevin transducer in Case 2. Solid line: ATILA and Dots: Present Method.

The conductance (G) and susceptance (B) of this transducer are shown in Fig. 4.4 upto 500 kHz with 1 kHz resolution. The y-axis values are shown in log scale. There is good agreement at all frequencies. $M_r = M_z = M_q$=5 is used to compute model values.

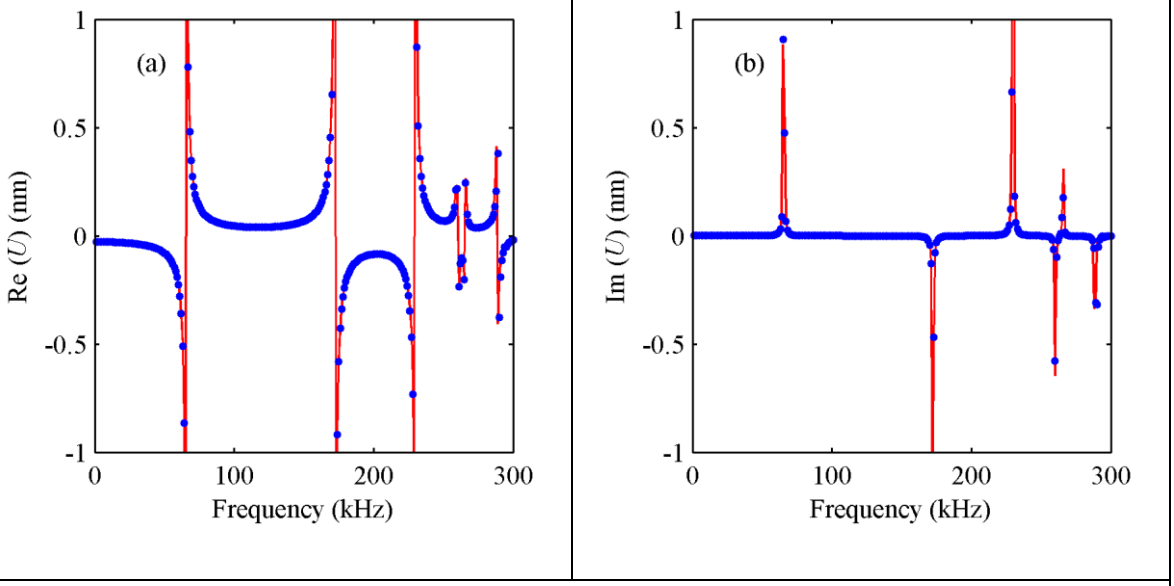

Fig. 4.5. (a) Real and (b) imaginary parts of the axial displacement U at the centre of the PZT cylinder of the asymmetric transducer in Case 2. Solid line: Present Method and Dots: ATILA.

The axial displacement at the center of the piezoelectric ceramic cylinder on the axis ($z = 0, r = 0$ on the PZT cylinder) of the transducer is shown in Fig. 4.5. The real part is shown in Fig. 4.5(a) and imaginary part is shown in Fig. 4.5(b). The results are shown upto 300 kHz. The displacement pattern does not have any symmetry as the transducer is not symmetric. Both real and imaginary parts and hence the absolute values of the displacement are in good agreement at all frequencies.

4.6.3 **Case 3**

In case 3, the transducer is similar to that in case 1 except for the head mass. This transducer has an Aluminium head. Both the Aluminium head and steel tail are of length 10 mm. Because this has a lighter head mass and heavier tail mass, this transducer is analyzed extensively. The critical frequencies and corresponding G-B values for this transducer are shown in Table 4.4.

Table 4.4. Critical frequencies and G and B values of the transducer in Case 3.

Resonance	Method	f_s (kHz)	G_{max} (mS)	$f_{-1/2s}$ (kHz)	B_{max} (mS)	$f_{1/2s}$ (kHz)	B_{min} (mS)
First	ATILA	67.00	3.51	66.86	1.77	67.13	-1.74
	Present Method	67.00	3.51	66.87	1.77	67.13	-1.74
	% Error	0	0	0.01	0	0	0
Second	ATILA	146.53	0.23	146.46	0.17	146.61	-0.06
	Present Method	146.54	0.23	146.47	0.16	146.62	-0.06
	% Error	0.01	0	0.01	-5.9	0.01	0
Third	ATILA	198.67	5.03	198.53	2.57	198.82	-2.46
	Present Method	198.71	5.02	198.57	2.57	198.86	-2.45
	% Error	0.02	-0.2	0.02	0	0.02	0.41

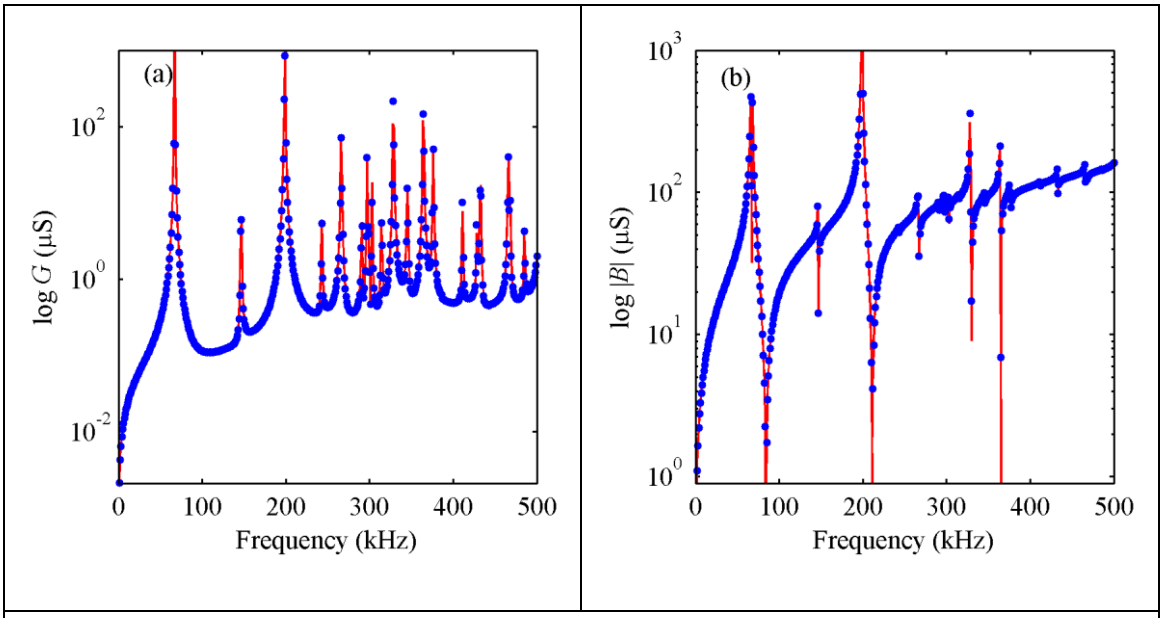

Fig. 4.6(a) Conductance (G) and (b) susceptance (B) of the transducer in Case 3. Solid line: ATILA and Dots: Present Method.

The critical frequencies in the neighborhood of the first and second resonances, computed using ATILA and the present method, are the same upto 4 significant digits. The values of G and B at the critical frequencies, in the neighborhood of the first resonance, are

the same upto 3 significant digits. The errors are shown upto the third resonance. The conductance (G) and susceptance (B) of this transducer upto 500 kHz are shown in Fig. 4.6(a) and 4.6(b) respectively. Analytical results are computed using $M_r = M_z = M_q$=10. The agreement between present method and ATILA is very good in the entire band.

The convergence of ATILA result is shown in Table 4.5 for this particular transducer. The conductance (G) and susceptance (B) values are shown at some spot frequencies of 100, 200, …, 500 kHz for different mesh densities. In ATILA, I and J values specify the mesh densities; the increase in which increases the mesh density. The results are shown for I=J=20, 40, and 80. The conductance and susceptance of the transducer computed analytically using various M_r, M_z, and M_q values are shown in Table 4.5. The total number of coefficients to be determined, is, for example, 154 when $M_r = M_z = M_q$=5. In Table 4.5, the G-B values have not converged with $M_r = M_z = M_q$=5. But, most of them have converged with $M_r = M_z = M_q$=10 as further increase of M_r, M_z, and M_q to 15 does not result in any significant changes in the values. It is clear from table that, ATILA values have converged with I=J=40.

Table 4.5. Convergence studies for the transducer in Case 3.

G (μS)						
ATILA				Present Method		
Frequency (kHz)	I=J=20	I=J=40	I=J=80	$M_r = M_z = M_q$=5	$M_r = M_z = M_q$= 10	$M_r = M_z = M_q$= 15
100	0.0001	0.0001	0.0001	0.0001	0.0001	0.0001
200	0.0619	0.0618	0.0617	0.0748	0.0655	0.0646
300	0.0013	0.0012	0.0012	0.0030	0.0015	0.0015
400	0.0005	0.0005	0.0005	0.0005	0.0005	0.0005
500	0.0019	0.0020	0.0020	0.0017	0.0019	0.0019
B (μS)						
100	0.0195	0.0195	0.0195	0.0195	0.0195	0.0195
200	-0.4952	-0.4948	-0.4948	-0.5481	-0.5106	-0.5038
300	0.0781	0.0782	0.0782	0.0763	0.0777	0.0777
400	0.1100	0.1100	0.1100	0.1100	0.1100	0.1100
500	0.1616	0.1619	0.1619	0.1601	0.1612	0.1612

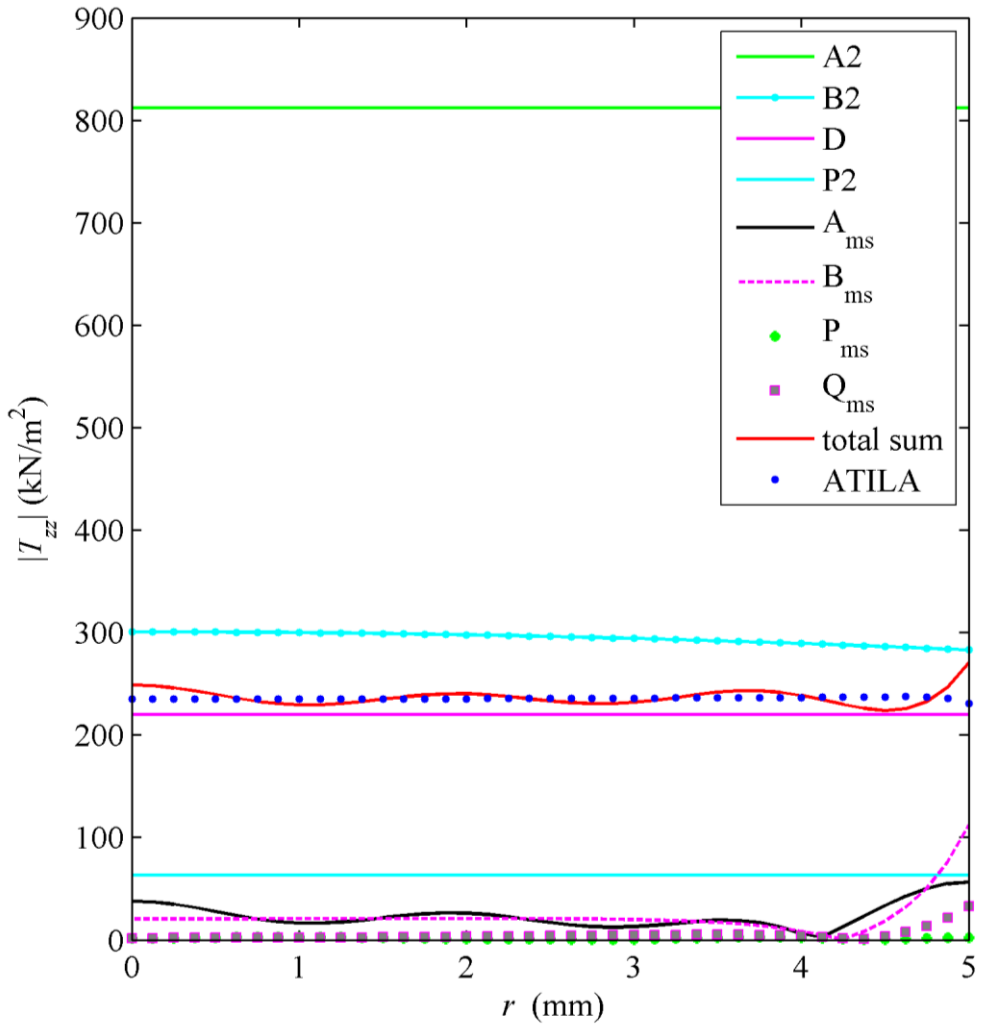

Fig. 4.7. Case 3. Contributions of terms associated with coefficients shown in the legend to the normal stress component T_{zz} at the top flat surface of the piezoceramic cylinder at 67 kHz.

The contribution of various terms, in the expression for T_{zz} of the piezoceramic cylinder in Eq. (4.8), to the total stress T_{zz} on the top flat surface of the piezoceramic cylinder is shown in Fig. 4.7 at the first resonance frequency of the transducer, i.e. at 67 kHz. There are $6M_r+3M_z+3M_q+5$ coefficients for the piezoceramic cylinder alone. All the coefficients except E, are present in the expression of T_{zz} of the piezoceramic cylinder. The total stress computed using the analytical method is in good agreement with that computed using ATILA. It is nearly uniform on the surface and approximately equal to 250 kN/m^2. The contributions by various terms are also nearly independent of r. The legend shows the contributions in descending order. The contributions from the $A^{(2)}$ and $B^{(2)}$ terms are very

large and of opposite sign. The absolute values of stress due to these terms are greater than the total stress. The sums of contributions from $P_{ms}^{(2)}$; m = 1,2,…, M_r, and $Q_{ms}^{(2)}$; m = 1,2,…, M_q and s=1, 2, 3 are the least.

The normal component of stress T_{zz}, along the axis of the transducer ($r = 0$) at the first resonance frequency, 67 kHz, is shown in Fig. 4.8. The length of the transducer is 30 mm. The analytical results are computed using $M_r = M_z = M_q$=5. The absolute stress is maximum at the center. It is zero at the ends because of the boundary conditions. The stress is nearly out of phase with the applied voltage and the imaginary part of the stress is therefore much greater than the real part.

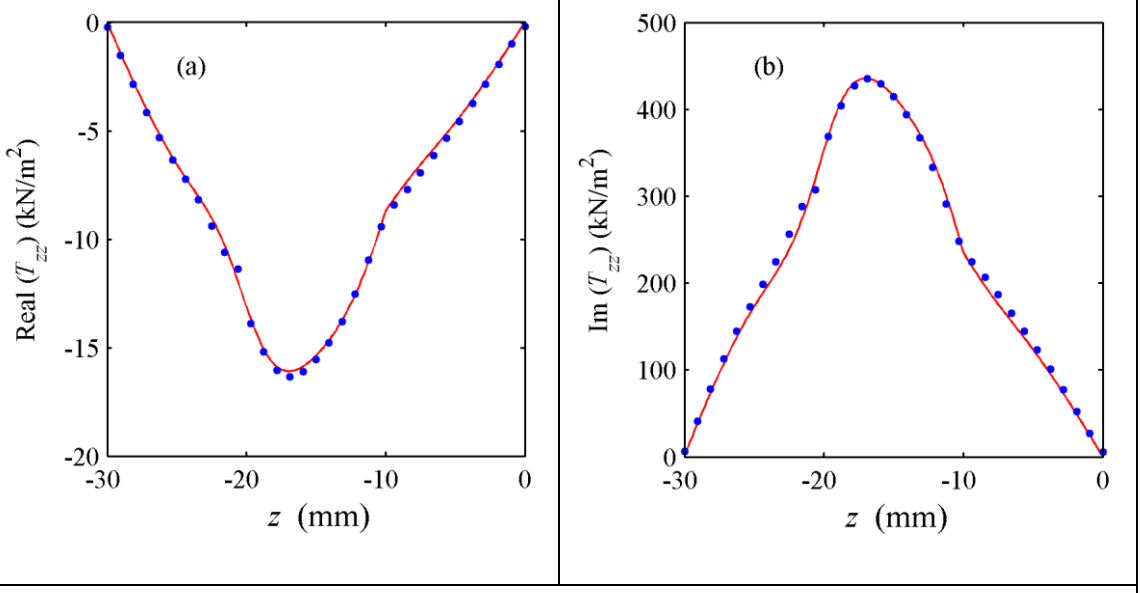

Fig. 4.8. (a) Real and (b) imaginary parts of the normal component of stress T_{zz} along the axis of the transducer at 67 kHz. Solid line: Present method and Dots: ATILA.

The absolute value of the axial displacement, U, on the plane midway between the ends of the transducer, is shown in Fig. 4.9, at various r values ($0 \leq r \leq a$) at the first resonance of 67 kHz. The values obtained using the present method and ATILA are in good agreement. They are nearly independent of r but the same small variation with r is seen in the values obtained using both methods.

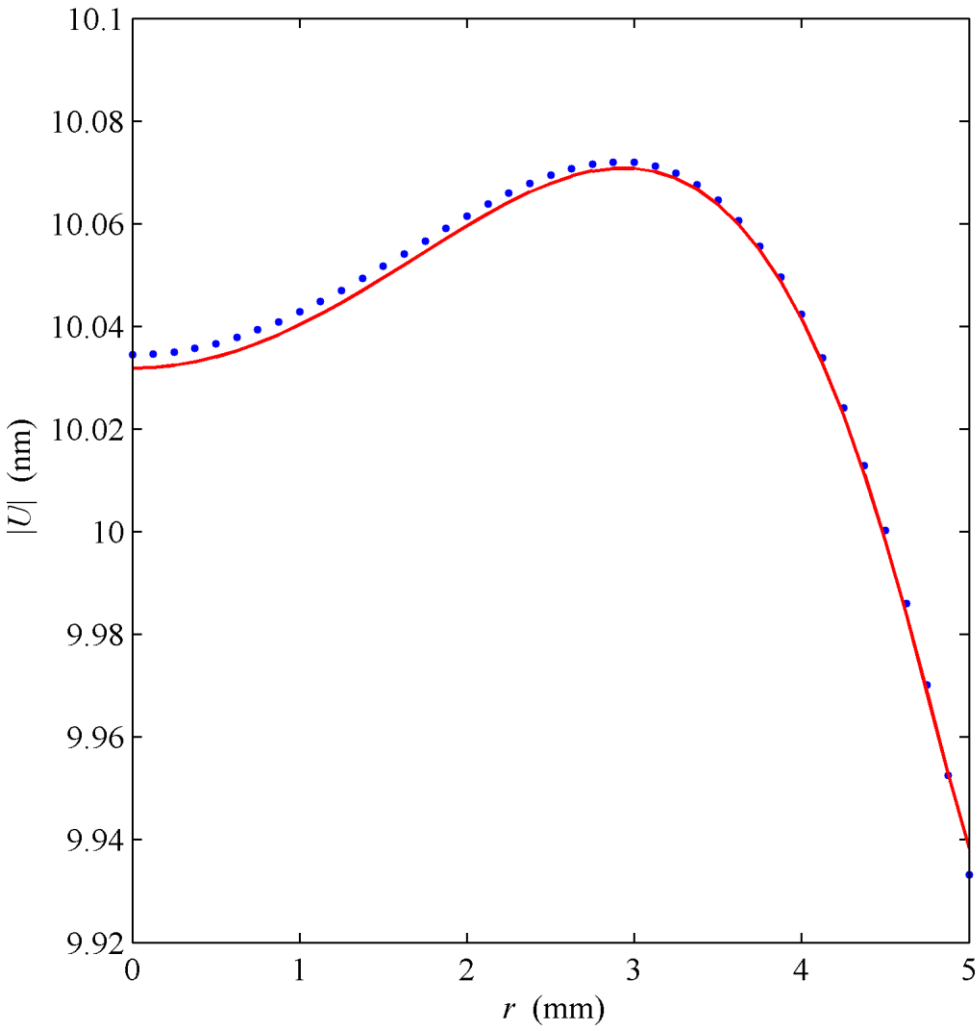

Fig. 4.9. Axial displacement U along the axis of the transducer at its first resonance, 67 kHz. Solid line: Present Method and dots: ATILA.

The bottom interface of the Langevin transducer is at $z = L^{(1)}/2$ for the bottom elastic cylinder and at $z = -L^{(2)}/2$ for the piezoceramic cylinder. Similarly, the top interface is at $z = L^{(2)}/2$ for the piezoceramic cylinder and at $z = -L^{(3)}/2$ for the top elastic cylinder. At these interfaces, two analytical values can be computed for the same variable; one on the elastic cylinder and the other on the piezoceramic cylinder. The arithmetic average of these two values at any point on the interface is considered as the value of the parameter at that point. The axial displacement U at the top interface of the Langevin transducer is shown in Fig. 4.10, at the first resonance, i.e. at 67 kHz. Present method is used to compute the

displacement for both the cylinders separately; at $z = L^{(2)}/2$ for the piezoceramic cylinder and at $z = -L^{(3)}/2$ for the top elastic cylinder, and their arithmetic average is shown here as the model values. The displacement is nearly uniform at the top interface. Both ATILA and analytical values are in good agreement.

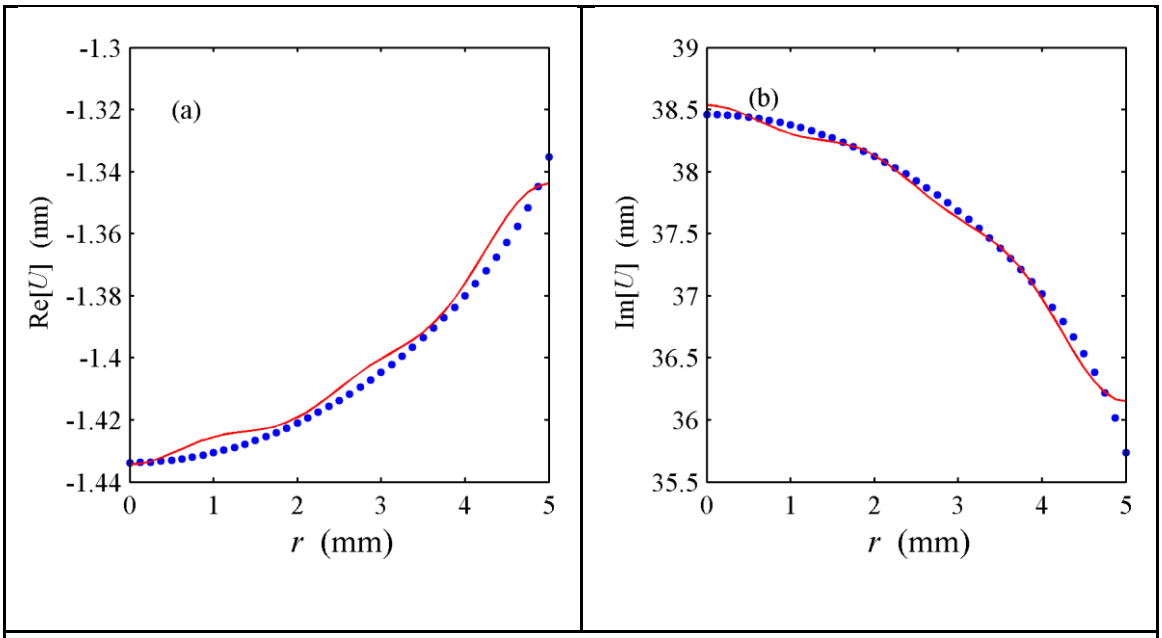

Fig. 4.10. Axial displacement U at the top piezoceramic-elastic cylinder interface at 67 kHz. (a) Real part and (b) Imaginary part. Solid line: Present method and Dots: ATILA.

The normal component of stress T_{zz} at the top interface is shown in Figs. 4.11 and 4.12 at the first resonance frequency, 67 kHz of the transducer. The real part is shown in Fig. 4.11 and the imaginary part is shown in Fig. 4.12. Here, the stress values computed from the elastic and piezoelectric cylinders are shown separately and their average value is shown as the model value. A solid line with stars is used to show the stress values at $z = L^{(2)}/2$ on the PZT cylinder and a dashed line is used to show values computed at $z = -L^{(3)}/2$ on the elastic cylinder. Dots are used to show the arithmetic average of these two values. All these values are compared with ATILA, shown in solid line. Though the values of T_{zz}, given by the PZT cylinder and the elastic cylinder at the top interface are different, their arithmetic average, which is the value of the parameter at any point on the interface, is nearly equal to the ATILA value and is nearly uniform over the surface. Analytical results are computed with $M_r = M_z = M_q = 5$.

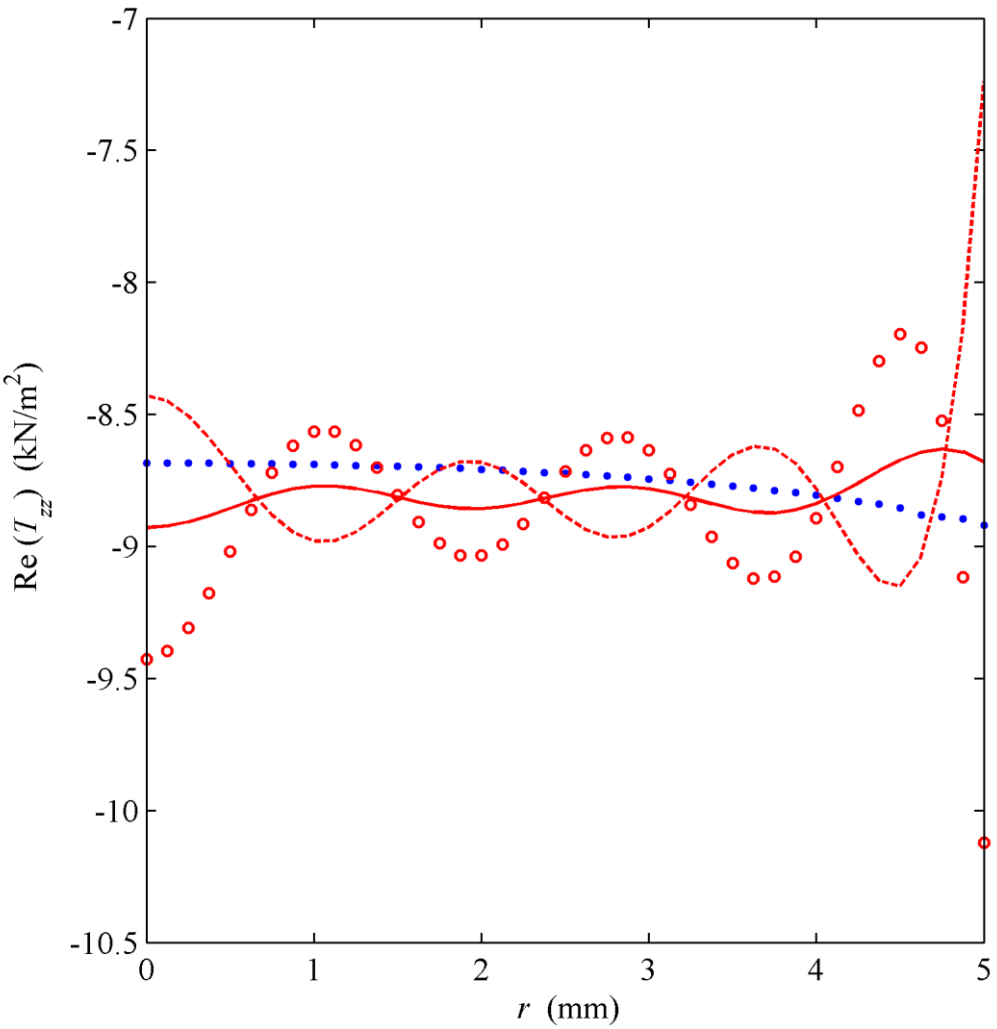

Fig. 4.11. Real part of T_{zz} at the piezoceramic-top elastic cylinder interface. Solid line: average T_{zz} of the PZT and elastic cylinders at the interface computed analytically, Dashed line: T_{zz} at the bottom of the top elastic cylinder computed analytically, Circles: T_{zz} at the top of the piezoceramic cylinder computed analytically. Dots: ATILA.

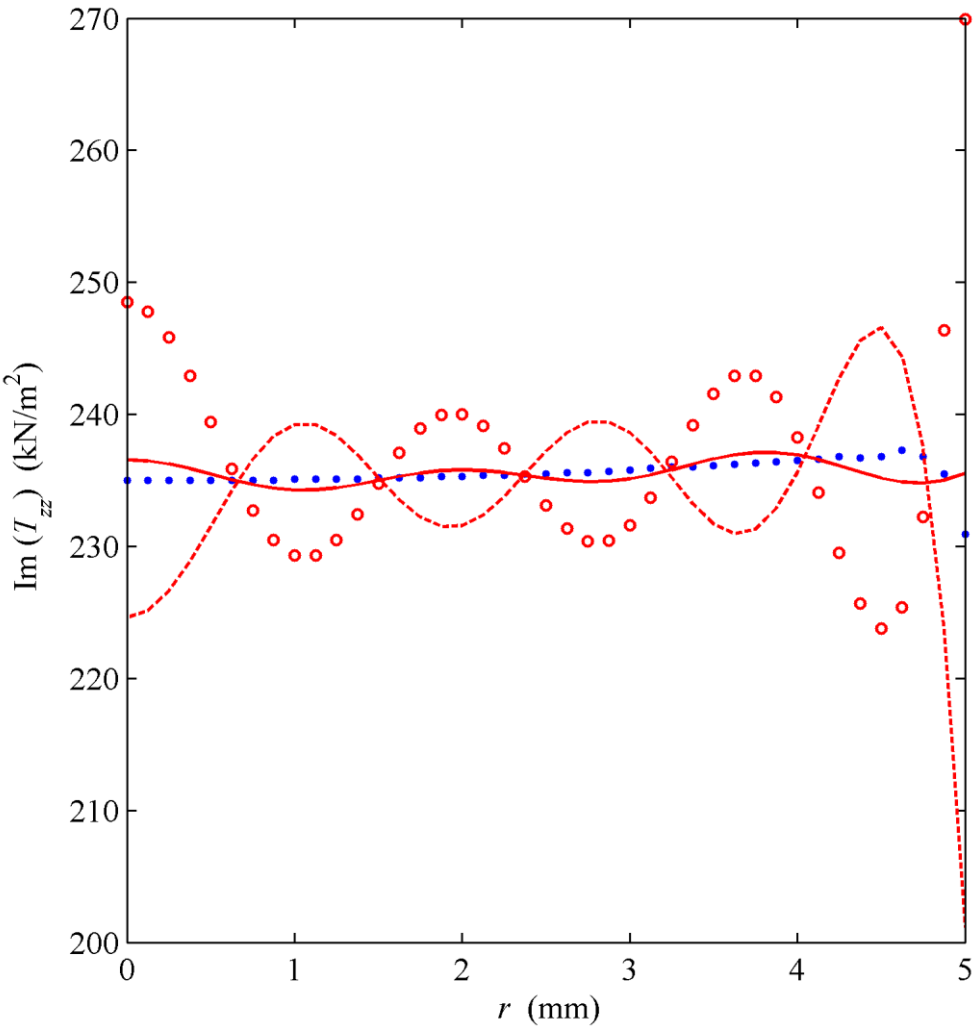

Fig. 4.12. Imaginary part of T_{zz} at the piezoceramic-top elastic cylinder interface Solid line: average T_{zz} of the PZT and elastic cylinders at the interface computed analytically, Dashed line: T_{zz} at the bottom of the top elastic cylinder computed analytically, Circles: T_{zz} at the top of the piezoceramic cylinder computed analytically. Dots: ATILA.

The normal component of stress, T_{zz}, at the midplane of the two elastic cylinders is shown in Fig. 4.13 as a function of r, at 100 kHz. $M_r = M_z = M_q = 5$ is used to compute the analytical results. Stress values are shown at two different locations of the transducer; one at the center of the bottom elastic cylinder ($z = 0,\ 0 \leq r \leq a$) and other at the center of the top elastic cylinder ($z = 0,\ 0 \leq r \leq a$). The stress is maximum at the center of the

cylinders and minimum at the ends. The two elastic cylinders are made of different materials and the magnitudes of the stresses generated are, therefore, different.

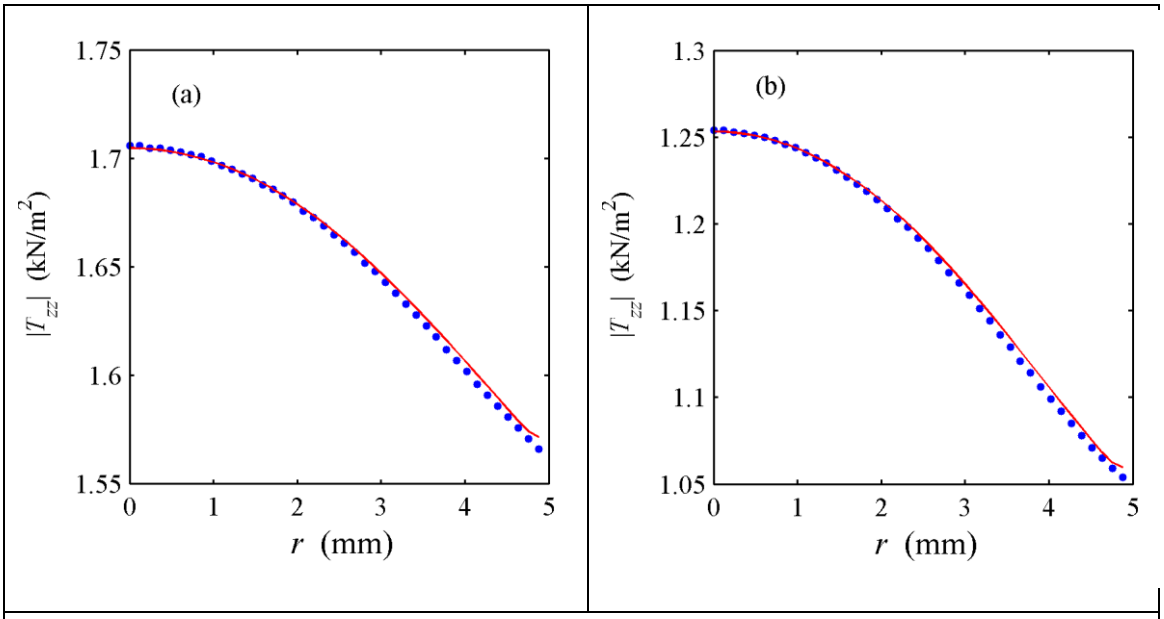

Fig. 4.13. T_{zz} at 100 kHz for the transducer in Case 3; (a) at the center of the bottom elastic cylinder, (b) at the center of the top elastic cylinder. Solid line: Present Method and Dots: ATILA.

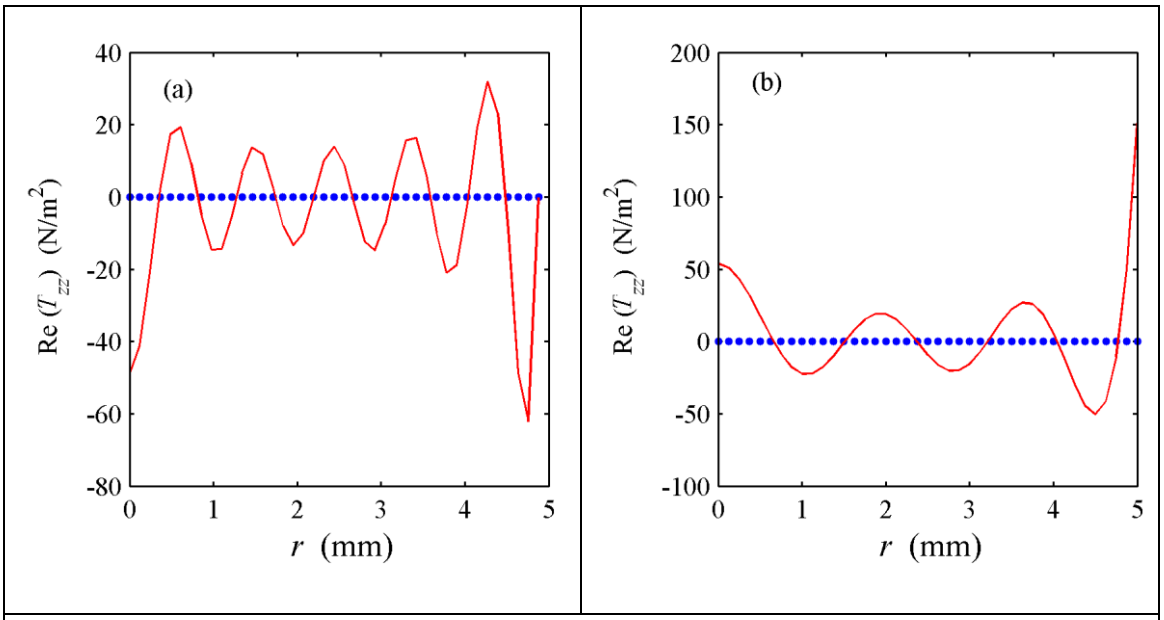

Fig. 4.14. Stress values at the free ends of the elastic cylinders at 100 kHz; (a) T_{zz} at the bottom flat surface of the bottom elastic cylinder, (b) T_{zz} at the top flat surface of the top elastic cylinder. Solid line: Present Method and Dots: ATILA.

After determining the coefficients in Eqs. (4.6) and (4.15), the functions that are specified at the boundaries are computed using the present method and ATILA. In the present method, all the boundary conditions are satisfied in a weighted average sense. The normal stress T_{zz} at the bottom and top flat surfaces of the transducer at 100 kHz are shown in Fig. 4.14(a) and 4.14(b), respectively and those at the first resonance frequency, i.e. 67 kHz are shown in Fig. 4.15(a) and 4.15(b), respectively.

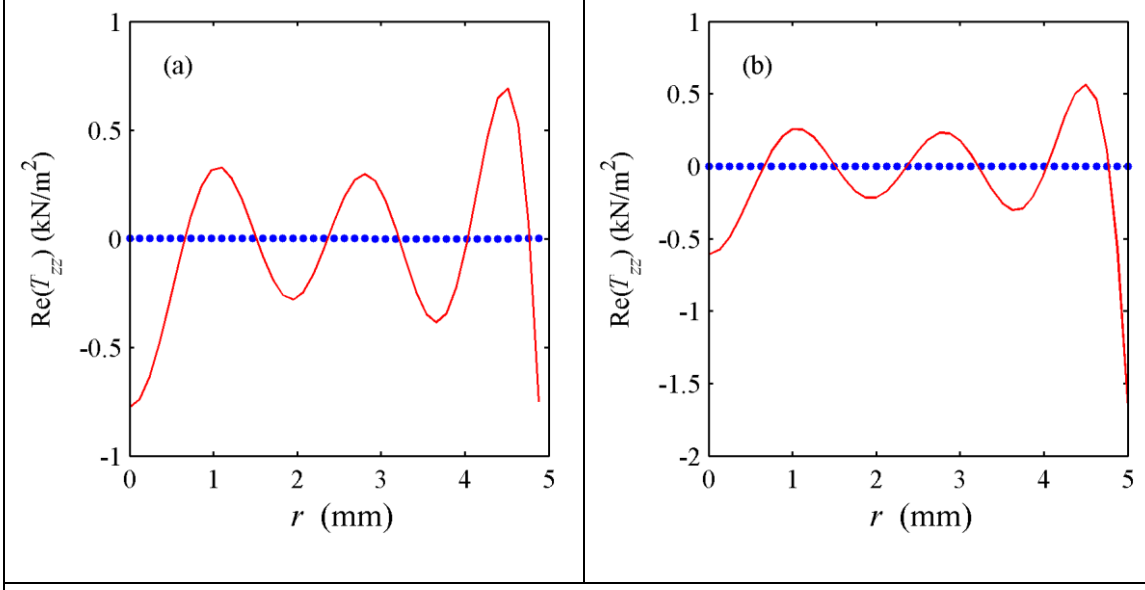

Fig. 4.15. Stress values at the free ends of the elastic cylinders at the first resonance frequency, 67 kHz; (a) T_{zz} at the bottom flat surface of the bottom elastic cylinder, (b) T_{zz} at the top flat surface of the top elastic cylinder. Solid line: Present Method and Dots: ATILA.

In the analysis, T_{zz} is specified to be zero in an average sense at both the free ends of the transducer. This is a weaker condition than the exact condition. Hence, the analytical values are not exactly zero, but, their integral average is zero. Moreover, magnitude of these values computed at the ends of the cylinders are much less than those computed at the center of the cylinder (Fig. 4.13). In ATILA, T_{zz} at a point is determined by using the primary variables (displacement and electric potential). The stress at a point that lies on two adjacent finite elements is computed using the displacements in both the elements. The average of these two values is shown in the Figure and it is everywhere nearly zero in Figs. 4.14(a) and 4.14(b). T_{zz} values at the first resonance frequency of 67 kHz are shown in Fig. 4.15. Here also, the average analytical values are zero and the ATILA values are nearly zeros. As seen in Figs. 4.14 and 4.15, the error in satisfying the zero normal stress boundary

condition is less in ATILA than the present method. The error in the present method may due to numerical methods used to solve the equations.

4.6.4 **Case 4**

In case 4, the piezoceramic cylinder is placed in between an Aluminium head of 5 mm length and a Steel tail of 10 mm length. The critical frequencies of this transducer around the first three resonances are shown in Table 4.6.

Table 4.6. Critical frequencies and the G, B values of the transducer in Case 4.

Resonance	Method	f_s (kHz)	G_{max} (mS)	$f_{-1/2s}$ (kHz)	B_{max} (mS)	$f_{1/2s}$ (kHz)	B_{min} (mS)
First	ATILA	76.65	3.96	76.49	2.00	76.81	-1.96
	Present Method	76.66	3.96	76.51	2.00	76.82	-1.96
	% Error	0.01	0	0.03	0	0.01	0
Second	ATILA	179.08	2.52	178.92	1.31	179.23	-1.21
	Present Method	179.08	2.51	178.93	1.31	179.23	-1.20
	% Error	0	-0.4	0.01	0	0	0.8
Third	ATILA	228.21	0.46	227.95	0.29	228.48	-0.17
	Present Method	228.14	0.48	227.88	0.30	228.41	-0.18
	% Error	-0.03	4.3	-0.03	3.45	-0.03	-5.9

The maximum percentage error in the critical frequencies is 0.03% and that in the associated G and B values is less than 6%. The conductance and susceptance values are shown in Fig. 4.16 upto 500 kHz with 1 kHz resolution. The agreement between analytical and ATILA values is very good. The analytical results are computed with $M_r = M_z = M_q$=5.

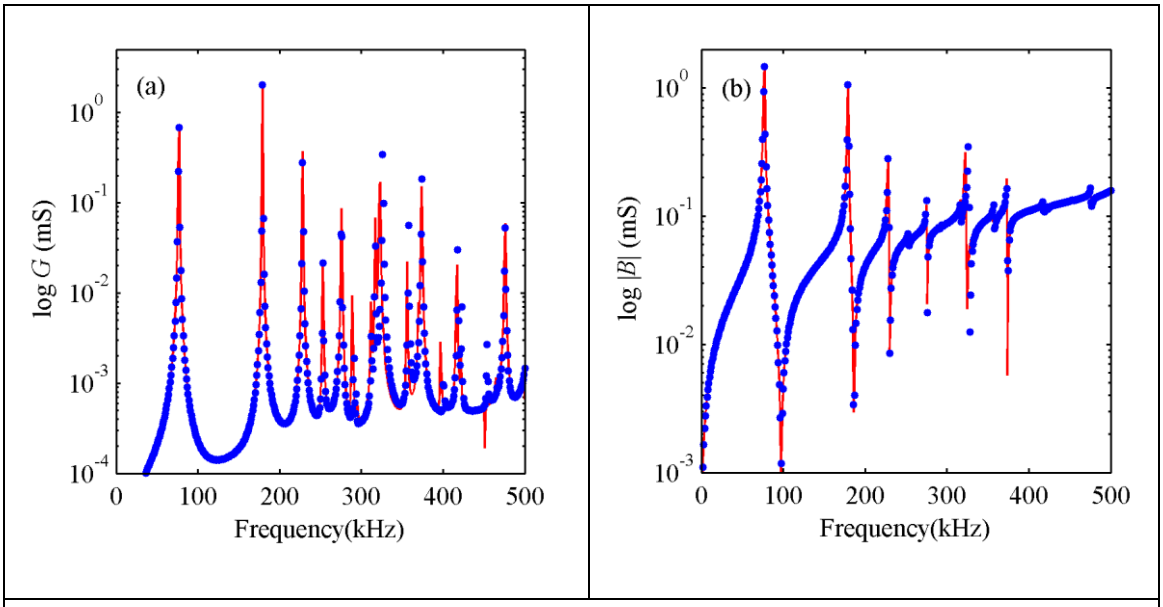

Fig. 4.16. (a) Conductance (*G*) and (b) Susceptance (*B*) of the transducer for Case 4 in 1-500 (kHz) frequency band. Solid line: Present Method and Dots: ATILA.

In Fig. 4.17, the axial displacement, *U*, at the center of the top interface between cylinders, computed using the present method is compared with that computed using ATILA. There is good agreement at all frequencies.

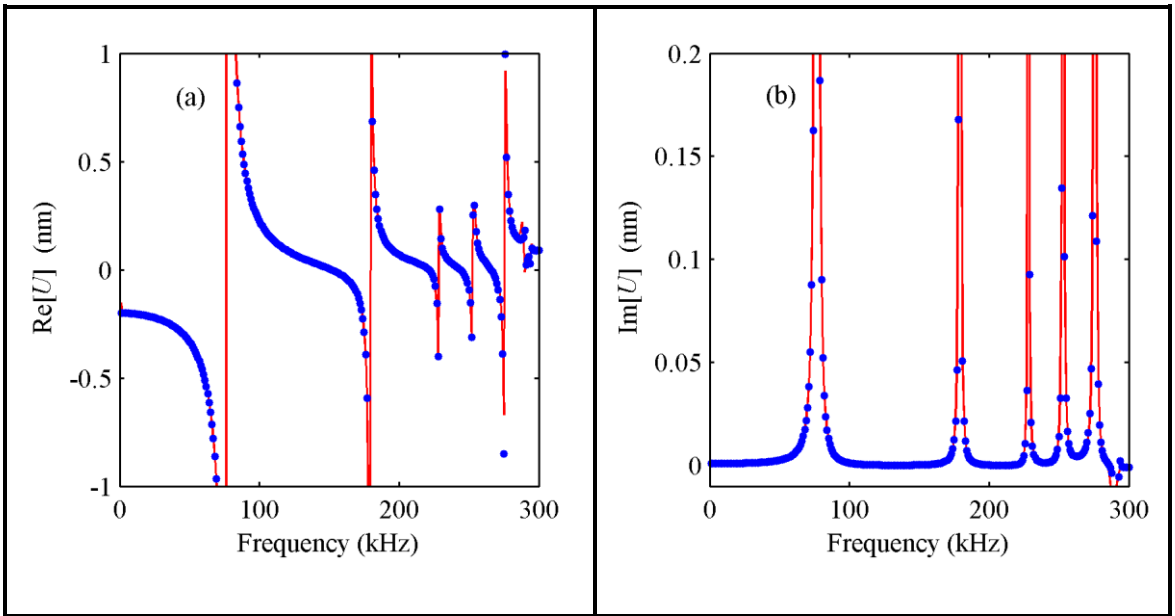

Fig. 4.17. (a) Real and (b) imaginary parts of the axial displacement *U* at *r=0* at the top interface of the transducer. Solid line: Present Method and Dots: ATILA.

4.7 CONCLUSIONS

An analytical method to analyze the response of a Langevin transducer to excitation is presented. Exact series solutions to the exact governing equations are used and the displacement, potential, stress, and electric displacement fields are expressed in terms of complete sets of functions. Therefore, arbitrary boundary conditions and continuity conditions can be satisfied. Numerical values of the complex input electrical admittance and the complex displacement are computed and compared with finite element results. The critical frequencies, input electrical admittance, the primary and secondary variables are all in excellent agreement with ATILA. The method can be extended to analyze Tonpilz transducers with conical heads. Further extensions are required to include the effect of fluid loading and to analyze an array of Tonpilz transducers.

CHAPTER 5

SUMMARY

Mathematical models are presented of axisymmetric piezoelectric transducers that are based on models of their components. The components are axially polarized piezoelectric solid or hollow cylinders and solid elastic cylinders. The transducers are co-axial cylinders stacked end to end. Exact, second order, linear, partial differential equations are used to describe the dynamics of the components. For elastic cylinders, they are obtained by using the exact dynamic equilibrium equations and the equations of state; and, for piezoelectric cylinders, the Gauss electrostatic condition as well. The axial and radial components of displacement and the electric potential are used as the primary variables. The governing equations are homogeneous because the excitation acts on the boundaries or on the interfaces between components. Cylindrical coordinates are used because the components and the transducers are axisymmetric circular cylinders of finite length. Infinite series solutions to the governing differential equations are used and each term in the series is an exact solution to the governing equations. Therefore, the governing equations are exactly satisfied even when the series are truncated to find numerical solutions. Thus the approach is appropriate for modeling cylinders with arbitrary dimensions. Some existing models of the components and the transducers are based on one-dimensional analysis in which it is assumed that the longitudinal stress along the axis of the transducer is the only significant stress. Therefore, they are appropriate only for modeling transducers with a high length to diameter ratio. In others, it is assumed that only the radial stress is significant and they are appropriate when the diameter to length ratio is high. Other existing models are based on approximate solutions to the governing partial differential equations.

Boundary conditions complement the governing equations. Together they form a mathematical model that has a unique steady-state solution. The boundaries of the components are flat and curved surfaces. On each boundary, one of the cylindrical coordinates is a constant. A combination of the normal and shear stresses and the normal and tangential displacements is specified on each boundary. Electrical boundary conditions are specified by using the electric potential and the electric charge density.

Each term in the series solutions to the governing equations has two components (axial and radial components of displacement) for elastic cylinders and three components (electric potential being the third) for piezoelectric cylinders. The number of components is equal to the number of primary variables for each type of material. Each component is a

product of an independent coefficient, a Bessel function with the radial coordinate in its argument, and a sinusoidal function with the axial coordinate in its argument. One of the arguments in the Bessel and sinusoidal functions can be arbitrarily chosen. The other is then determined by using a relationship between the arguments that they should satisfy in order to satisfy the governing equations. The number of components in each term of the series is also equal to the number of boundary conditions that are to be satisfied on each boundary. For elastic components, there are two boundary conditions on each face. For piezoelectric components, a third boundary condition in terms of the electric potential or the charge density or both is prescribed. The coefficients are determined by using the boundary conditions.

As noted earlier, one of the arguments of the Bessel and sinusoidal functions can be arbitrarily chosen. For each choice, there is an associated series. Here, two choices are made. In the first, the arguments of the sinusoidal functions are chosen such that they form a complete set in the axial direction. In the second, the arguments of the Bessel functions are chosen such that they form a complete in the radial direction. This is done so that the sets can be used to satisfy arbitrary boundary conditions by appropriately choosing the coefficients. It is shown that the functions that form a complete set are also orthogonal to each other.

All functions that are specified on a boundary are expressed in terms of complete sets. Therefore, piecewise continuous boundary conditions can be satisfied by appropriately choosing the coefficients. Uniform ring loads that do not act over the entire length of the cylinder and uniform circular loads that do not act over the entire flat surface are simple examples of such loads. All boundary conditions are satisfied in a weighted average sense. The weights are the elements of the complete set. Therefore, each boundary condition is approximated by several conditions or equations. The number of equations is equal to the number of weights used.

The orthogonal property of the functions reduces the number of coefficients in each boundary equation. In the one-dimensional case, arbitrary functions are expressed as the weighted sum of a complete set of functions. If the elements of the set are orthogonal, multiplying both sides of the equation by one of the elements of the set and integrating over the domain yields an equation that has only one weight. In other words, the resulting matrix equation is of size one and is diagonal. On the two-dimensional boundary surfaces considered here, all functions are expressed in terms of a complete set of functions and

other series. Therefore, the boundary equations obtained by using each boundary condition yield, after using the orthogonal property of the functions, a matrix equation where the number of coefficients is greater than the number of equations and only a part of the matrix is diagonal. All the equations obtained by using the boundary conditions are assembled to obtain a large matrix equation that has several diagonal sub-matrices.

The series solutions are truncated in order to find numerical solutions. The number of terms that are to be retained depends on the spatial distribution of the boundary loads. More terms have to be retained to get an accurate solution if the load is concentrated. In many transducer applications, the load acts over the entire face of the cylinder. Therefore, only a few terms are needed to get accurate results.

An arbitrary number of terms can be retained after truncating each series. The number of coefficients in the matrix equation will always be equal to the number of equations. More terms are needed along the axial direction when the length of a cylinder is much greater than its diameter; and vice versa.

In Chapter 2, an exact series solution is presented for hollow axially polarized piezoelectric ceramic cylinders. The excitation is electrical and a potential is applied across the flat ends. Therefore, the axial and radial displacements are anti-symmetric and symmetric, respectively, about the plane that is midway between the flat ends. A few sets of boundary conditions are used to illustrate the approach. It is shown that closed form solutions are obtained and series solutions are not necessary when zero axial displacement and zero shear stress on the flat ends and zero stress on the inner and outer curved surfaces are prescribed. This is also the case when zero radial displacement and zero shear stress on the curved surfaces ends and zero stress on the flat ends are prescribed. The results for these special cases are compared with those obtained using the finite element package ATILA. The excellent agreement shows that ATILA yields accurate results. The case of zero stress on all the surfaces is also presented. Here, truncated series are used and the analytical results are in good agreement with ATILA. The values of the critical frequencies, the frequency-dependent complex input electrical admittance, and the components of stress and displacement are compared. Only a few terms in the series are required to achieve excellent agreement upto many significant digits even at frequencies that are many times the fundamental resonance frequency.

In Chapter 3, a stack of hollow piezoelectric ceramic cylinders (rings) is analyzed by the using only the leading terms of the series solution. These stacks are used in Tonpilz

transducers and are frequently analyzed under stress free conditions. Only stress free stacks are analyzed in the thesis and its input electrical conductance and resonance frequencies are computed. Stacks with various number of identical rings are analyzed. It is shown that the fundamental length mode resonance computed using the axisymmetric model that includes the radial stress in the interior of the stack yields is in better agreement with ATILA results than the 1-D model in which it is assumed that the radial stress is zero everywhere. The fundamental radial mode resonance frequency is also accurately determined in the present model but cannot be obtained by using the 1-D model. As the length of the stack increases, the difference between the values computed using the present model and ATILA decreases.

In Chapter 4, classical Langevin transducers that comprise a solid piezoelectric cylinder sandwiched between elastic cylinders are analyzed using exact series solutions. The model is illustrated for transducers with identical or different elastic cylinders with stress free boundaries. In all the cases, the critical parameters are computed with excellent agreement with those computed using ATILA. Though the model is illustrated for stress free transducers, it can be used to analyze transducers with specified stress or displacements at the ends.

CHAPTER 6
APPLICATIONS AND FUTURE WORK

The analytical models of piezoceramic cylinders and stacks of cylinders developed here can be used to characterize them. Here, a forward problem is solved. The material properties and dimensions of the cylinders are used to determine the electrical and mechanical responses of the cylinder to electrical excitation. In the inverse characterization problem, the electrical and mechanical responses of the cylinder to electrical excitations are measured and it is of interest to determine the material properties of the cylinder. Stress-free conditions on all surfaces are used in the inverse problem as they are easy to achieve experimentally. The values of ten coefficients of a piezoelectric cylinder that result in excellent agreement between the measured and calculated responses are determined by iteration.

The models presented here can also be used to design components and transducers. It is often of interest to design a component with specific resonance frequencies or other characteristics and the dimensions of the transducer are to be chosen. It is convenient if the model used to determine the resonance frequencies and the method to iterate the dimensions are executed using the same software such as MATLAB.

The work done here can be extended to model other devices. For example, concentric cylinders of elastic and piezoelectric materials are of interest. In this case, the continuity condition is to be applied at the curved surfaces whereas it is applied on the flat surfaces in a stack.

Devices may have components in other shapes and models of all components are required to build a model of the device. For example, a Tonpilz transducer has a head in the shape of a frustum of a cone, piezoelectric cylinders, and elastic cylinders. A model of a frustum of a cone can be developed by using solutions to exact linearized equations. Then, a model of a Tonpilz transducer can be developed.

REFERENCES

1. ATILA Users Manual, Version 5.1.1., ISEN, Lille CEDEX, France, 1997.
2. H. H. Ding, L. E. McCleary, and J. A. Ward, "Computerized sonar transducer analysis and design based on multiport network interconnection techniques," U.S. Naval Undersea Center, San Diego, CA, NUC TP 228, 1973.
3. W. P. Mason, *Electromechanical transducers and wave filters*, D. Van Nostrand Company, Inc., New York, 2nd ed., 399-404,1948.
4. R. A. Langevin, "The electro-acoustic sensitivity of cylindrical ceramic tubes," J. Acoust. Soc. America, 26(3), 421-427, 1954.
5. G. E. Martin, "Vibrations of longitudinally polarized ferroelectric cylindrical tubes," J. Acoust. Soc. America, 35(4), 510-520, 1963.
6. H. S. Paul, "Vibrations of circular cylindrical shells of piezoelectric silver iodide crystals," J. Acoust. Soc. America, 40(5), 1077-1080, 1966.
7. P. H. Rogers, "Mathematical model for a free-flooded piezoelectric cylinder transducer," J. Acoust. Soc. America, 80(1), 13-18, 1986.
8. G. R. Buchanan and J. Peddieson, "Axisymmetric vibration of infinite piezoelectric cylinders using one-dimensional finite elements," IEEE Trans. Ultrasonics, Ferroelectrics, and Freq. Control, 36(4), 459-465, 1989.
9. G. R. Buchanan and J. Peddieson, "Vibration of infinite piezoelectric cylinders with anisotropic properties using cylindrical finite elements," IEEE Trans. Ultrasonics, Ferroelectrics, and Freq. Control, 38(3), 291-296, 1991.
10. H. A. Kunkel, S. Locke, and B. Pikeroen, "Finite-element analysis of vibrational modes in piezoelectric ceramic disks," IEEE Trans. Ultrasonics, Ferroelectrics, and Freq. Control, 37(4), 316-328, 1990.
11. M. Brissaud, "Characterzation of piezoceramics," IEEE Trans. Ultrasonics, Ferroelectrics, and Freq. Control, 38(6), 316-328, 1991.
12. N. Lamberti and M. Pappalardo, "A general approximated two-dimensional model for piezoelectric array elements," IEEE Trans. Ultrasonics, Ferroelectrics, and Freq. Control, 42(2), 316-328, 1995.
13. A. Iula, N. Lamberti, and M. Pappalardo, "An approximated 3-D model of cylinder-shaped piezoceramic elements for transducer design," IEEE Trans. Ultrasonics, Ferroelectrics, and Freq. Control, 45(54), 1056-1064, 1998.

14. D. D. Mancic and M. Dj. Radmanovic, “Piezoceramic ring loaded on each face: a three- dimensional approach,” Technical Acoustics, 2, 1.1-1.7, 2002.
15. S. Lin and F. Zhang, “Vibrational modes and frequency spectra in piezoelectric ceramic rectangular resonators,” J. Acoust. Soc. America, 94(5), 2481-2484, 1993.
16. S. Lin, “Three-dimensional equivalent circuit and the natural frequencies of rectangular piezoelectric ceramic resonators,” J. Acoust. Soc. America, 96(3), 1620-1626, 1994.
17. S. Lin, “Coupled vibration analysis of piezoelectric ceramic disk resonators,” J. Sound and Vib., 218(2), 205-217, 1998.
18. S. Lin, “Coupled vibration in hollow cylinders of longitudinally polarized piezoelectric ceramics,” J. Acoust. Soc. America, 97(6), 3599-3604, 1995.
19. S. Lin, “Analysis of the equivalent circuit of piezoelectric ceramic disk resonators in coupled vibration,” J. sound and Vib., 231(2), 277-290, 2000.
20. S. Lin, “Study on the equivalent circuit and coupled vibration for the longitudinally polarized piezoelectric ceramic hollow cylinders,” J. Sound and Vib., 275, 859-875, 2004.
21. F. Feng, J. Shen, and J. Deng, “A 2-D equivalent circuit of piezoelectric ceramic ring for transducer design,” Ultrasonics, 44,723-726, 2006.
22. Z. G. Ying, Y. Wang, Y. Q. Ni, and J. M. Ko, “Stochastic response analysis of piezoelectric axisymmetric hollow cylinders,” J. Sound and Vib., 321, 735-761, 2009.
23. D. J. Griffiths, *Introduction to Eectrodynamics*, 3rd Ed., Cambridge University Press, Sec 2.2, 2007.
24. H. Jalili and H. Goudarzi, “Modeling the hollow cylindrical piezo-ceramics with axial polarization using equivalent electro-mechanical admittance matrix,” Sensors and Actuators A: Physical, 149(2), 266-276, 2009.
25. M. Brissaud, “Three-dimensional modeling of piezoelectric materials,” IEEE Trans. Ultrasonics, Ferroelectrics, and Freq. Control, 57(9), 2051-2065, 2010.
26. D. D. Ebenezer and Pushpa Abraham, “Analysis of axially polarized piezoelectric ceramic cylindrical shells of finite length with internal losses,” J. Acoust. Soc. America, 112(5), 1953-1960, 2002.
27. D. D. Ebenezer and Pushpa Abraham, “Eigenfunction analysis of radially polarized piezoelectric ceramic cylindrical shells of finite length,” J. Acoust. Soc. America, 102(3), 1549-1558, 1997.

28. D. D. Ebenezer and Pushpa Abraham, “Closed form analysis of thin radialy polarized piezoelectric ceramic cylindrical shells with loss,” Curr. Sci., 83, 981-988, 2002.
29. D. D. Ebenezer and R. Ramesh, “Exact analysis of axially polarized piezoelectric ceramic cylinders with certain uniform boundary conditions,” Curr. Sci., 85(8), 1173-1179, 2003.
30. R. Ramesh and D. D. Ebenezer, “Analysis of axially polarized piezoelectric ceramic rings,” Ferroelectrics, 323, 17-23, 2005.
31. D. D. Ebenezer and R. Ramesh, “Analysis of axially polarized piezoelectric cylinders with arbitrary boundary conditions on flat surfaces,” J. Acoust. Soc. America, 113(4), 1900-1908, 2003.
32. D. D. Ebenezer, K. Ravichandran, R. Ramesh, and C. Padmanabhan, “Forced responses of solid axially polarized piezoelectric ceramic finite cylinders with internal losses,” J. Acoust. Soc. America, 117(6), 3645-3656, 2005.
33. C. R. Wylie and L. C. Barret, *Advanced Engineering Mathematics*, Fifth Ed., McGraw-Hill Company, pp F511, 1985.
34. G. E. Martin, “On the theory of segmented electromechanical systems,” J. Acoust. Soc. America, 36(7), 1366-1370, 1964.
35. W. J. Toulis “Electromechanical coupling and composite transducers,” J. Acoust. Soc. America 35, 74-80, 1963.
36. S. Sherrit, S. P. Leary, Y. Bar-Cohen, B. P. Dolgin, and R. Tasker, “Analysis of the impedance resonance of piezoelectric stacks,” IEEE Ultrasonics Symp., San Juan, Puerto Rico, 2000.
37. H. Nowotny and E. Benes, “General one-dimensional treatment of the layered piezoelectric resonator with two electrodes,” J. Acoust. Soc. America, 82(2), 513-521, 1987.
38. H. Nowotny, E. Benes, and M. Schmid, “Layered piezoelectric resonators with an arbitrary number of electrodes (general one-dimensional treatment),” J. Acoust. Soc. America, 90(3), 1238-1245, 1991.
39. E. Flint, C. Liang, and C. A. Rogers, “Electromechanical analysis of piezoelectric stack active member power consumption,” J. Intelligent Mat. Sys. and Structures, 6, 117-124, 1995.
40. K. F. Graf, *Wave motion in elastic solids*, Columbus, Ohio, Ohio State University Press, 1975.

41. L. Pochhammer, “Beitrag zur Theorie der Biegung des Kreiszylinders,” J. Reine Angrew. Maths. 81, 33-47, 1876.
42. C. Chree, “Longitudinal vibrations of a circular bar,” Q. J. Pure Applied Math. 21, 287-298, 1886.
43. L. N. G. Filon, “On the elastic equilibrium of circular cylinders under certain practical systems of load,” Proc. Roy. Soc. Lon. A 198, 147-233, 1901.
44. V. V. Meleshko, “Selected topics in the history of the two-dimensional biharmonic problem,” Appl. Mech. Rev. 56(1), 33-85, 2003.
45. F. Purser, “On the application of Bessel’s functions to the elastic equilibrium of a homogeneous isotropic cylinder,” Trans. R. Irish Acad. A 32, 31-60, 1902.
46. R. R. Aggarwal, “Axially symmetric vibrations of a finite isotropic disk,” J. Acoust. Soc. America, 24(5), 463-467, 1952.
47. J. R. Hutchinson, “Axisymmetric vibrations of solid elastic cylinder encased in a rigid container,” J. Acoust. Soc. America, 42(2), 398-402, 1967.
48. J. R. Hutchinson, “Axisymmetric vibrations of a free finite-length rod,” J. Acoust. Soc. America, 51(1), 233-240, 1972.
49. V. T. Grinchenko, “The axisymmetric problem of the theory of elasticity for a thick walled cylinder of finite length,” Soviet Appl. Mech. 65, 93-102, 1967.
50. G, W. McMahon, “Finite-difference analysis of the vibrations of solid cylinders,” J. Acoust. Soc. America, 48(1), 307-312, 1970.
51. V. T. Grinchenko and V. V. Meleshko, “High frequency axisymmetric vibrations of circular disks,” Int. Appl. Mech. ISSN 1573-8582, 12, 1251-1258, 1976.
52. A. W. Leissa and J. So, “Comparisons of vibration frequencies for rods and beams from one-dimensional and three-dimensional analyses,” J. Acoust. Soc. America, 98(4), 2122-2135, 1995.
53. A. W. Leissa and J. So, “Accurate vibration frequencies of circular cylinders from three-dimensional analysis,” J. Acoust. Soc. America, 98(4), 2136-2141, 1995.
54. V. V. Meleshko, “Equilibrium of a elastic finite cylinder: Filon’s problem revisited,” J. Eng. Math. 46, 355-376, 2003.
55. D. D. Ebenezer, K. Ravichandran, and C. Padmanabhan, “Forced vibrations of solid elastic cylinders,” J. Sound and Vibration, 282, 991-1007, 2005.
56. D. D. Ebenezer, K. Nirnimesh, R. Barman, R. Kumar, and S. B. Singh, "Analysis of solid elastic cylinders with internal losses using complete sets of functions," J. Sound and Vibration, 310, 197-216, 2008.

57. R. Sburlati, “Three-dimensional analytical solution for an axisymmetric biharmonic problem,” J. Elast., 95, 79-97, 2009.
58. D. Stansfield, *Underwater electroacoustic transducers*, Bath University Press and Inst. Acoust., 1990.
59. R. S. Woollett, *Sonar transducer fundamentals*, Naval Underwater Systems Centre, New Port, Rhode Island.
60. D. F. McCammon and W. Thompson, “The design of Tonpilz piezoelectric transducers using nonlinear goal programming,” J. Acoust. Soc. America, 68(3), 754-757, 1980.
61. M. V. Crombrugge and W. Thompson, “Optimization of the transmitting characteristics of a Tonpilz-type transducer by proper choice of impedance matching layers,” J. Acoust. Soc. America, 77(2), 747-752, 1985.
62. J. N. Decarpigny, J. C. Dubus, B. Torcquet and D. Boucher, “In-air analysis of piezoelectric Tonpilz transducers in a wide frequency band using a mixed finite element-plane wave method,” J. Acoust. Soc. America, 78(5), 1499-1507, 1985.
63. Q. Yao and L. Bjorno, “Broadband Tonpilz underwater acoustic transducers based on multimode optimization,” IEEE Trans. Ultrasonics, Ferroelectrics, and Freq. Control, 44(5), 1060-1066, 1997.
64. A. Iula, R. Carotenuto, M. Pappalrdo, and N. Lamberti, “An approximated 3-D model of the Langevin transducer and its experimental validation,” J. Acoust. Soc. America, 111(6), 2675-2680, 2002.
65. A. Iula, D. Cerro, and M. Pappalardo, “3-D Finite element analysis of the Langevin transducer,” IEEE Ultrasonics Symp., 2003.
66. S. Lin, “Analysis of the sandwich piezoelectric ultrasonic tranducer in coupled vibration,’ J. Acoust. Soc. America, 117(2), 653-661, 2005.
67. S. Lin, “Analysis of multifrequency Langevin composite ultrasonic transducers,” IEEE Trans. Ultrasonics, Ferroelectrics, and Freq. Control, 56(9), 1990-2009, 2009.
68. F. J. Arnold, “Resonance frequencies of the multilayered piezotransducers,” Acoustics 08, Paris, 2008.
69. Z. Liang, X. Mo, and G. Zhou, “A method for improving the electrical limit of a Langevin ultrasonic transducer,” IEEE SPAWDA, Shanghai, Nov. 2012.
70. S. C. Butler, “Triple resonant transducers,” IEEE Trans. Ultrasonics, Ferroelectrics, and Freq. Control, 59(6) 1292-1300, 2012.

71. P. A. Nishamol and D. D. Ebenezer, 'Exact series model of axially polarized hollow piezoelectric cylinders of finite length,' J. Acoust. Soc. America, 144 (2), 1028-1039, 2018.
72. P. A. Nishamol and D. D. Ebenezer, 'Piezoelectric ceramic stacks for underwater transducers,' Proc. of the IEEE International Symposium on Underwater Technology 2015 (UT15), DOI: 10.1109/UT.2015.7108217.
73. P. A. Nishamol and D. D. Ebenezer, 'Exact series model of Langevin transducers with internal losses," J. Acoust. Soc. America, 135 (3), 1159-1170, 2014.
74. W. P. Mason, *Physical Acoustics - Principles and Methods*, Vol. I - Part A, Academic Press, New York and London, 1964.
75. R. Holland, "Representation of dielectric, elastic, and piezoelectric losses by complex coefficients," IEEE Trans. Sonics and Ultrasonics, 14(1), 18-20, 1967.
76. S. I. Hayek, *Advancd Mathematical methods in Science and Engineering*, Second Ed., CRC Press, Taylor & Francis Group, pp-319, 2011.
77. M. Abramowitz and I. A. Stegun (Eds.), *Handbook of Mathematical Functions*, Dover, New York, 1965.
78. C. R. Wylie and L. C. Barrett, *Advanced Engineering Mathematics*, 5th Edn., McGraw-Hill international Editions, Singapore, 1985.
79. D. D. Ebenezer, K. Ravichandran, and C. Padmanabhan, "Free and forced vibrations of hollow elastic cylinders of finite length," J. Acoust. Soc. America, 137(5), 2927-2938, 2015.
80. C. H. Sherman and J. L. Butler, *Transducers and Arrays for Underwater Sound* Springer, USA, 2007, pp 517.
81. R. Ramesh and D. D. Ebenezer, "Equivalent Circuit for Broadband Underwater Transducers," IEEE UFFC, 55(9), 2079-2083, 2008.
82. E. Kreyzig, *Advanced Engineering Mathematics*, 3rd Edn., Wiley Publications, 1972.

LIST OF PAPERS BASED ON THE THESIS

1. P. A. Nishamol and D. D. Ebenezer, ‘Exact series model of Langevin transducers with internal losses,’ J. Acoust. Soc. America, 135 (3), 1159-1170, 2014.
2. P. A. Nishamol and D. D. Ebenezer, ‘Piezoelectric ceramic stacks for underwater transducers,’ Proc. of the IEEE International Symposium on Underwater Technology 2015 (UT15), DOI: 10.1109/UT.2015.7108217.
3. P. A. Nishamol and D. D. Ebenezer, ‘Exact series model of axially polarized hollow piezoelectric cylinders of finite length,’ J. Acoust. Soc. America, 144 (2), 1028-1039, 2018.
4. P. A. Nishamol and D. D. Ebenezer, “Analytical model of axially polarized hollow piezoelectric cylinders of finite length,” Proc. Intl. Conf. Sonar Systems and Sensors, Kochi, 2018.

OTHER PUBLICATIONS AND CONFERENCE PROCEEDINGS

1. D. D. Ebenezer and P. A. Nishamol, “Exact model of Langevin transducers with internal losses,” ACOUSTICS08, Paris, 2008.
2. P. A. Nishamol, J. Mathew, and D. D. Ebenezer, “Acoustic radiation from cylindrical transducer arrays,” J. Sound and Vibration, 323, 989-1002, 2009.
3. P. A. Nishamol and D. D. Ebenezer, “Approximate but accurate model of Langevin transducer with internal losses,” Proc. of National Symposium on Acoustics, 2009.
4. J. Mathew, D. D. Ebenezer and P. A. Nishamol, “Effect of an Elastic Cylinder near an array on the pressure field due to a plane acoustic wave,” Proc. of National Symposium on Acoustics, 2010.
5. P. A. Nishamol and D. D. Ebenezer, “Analytical model of a stack of axially polarized piezoelectric ceramic rings,” Proc. Natl. Symp. Acoustics, Rishikesh, 2010.

CURRICULUM VITAE

Name in full (in capital letters) : **NISHAMOL P. A.**

Date of Birth : **21.05.1982**

Ph.D. Registration No. and Date : **4069, 04.10.2011**

Educational Qualifications:

Degree	Subject	Year	University
B.Sc.	Mathematics	2002	Mahatma Gandhi University, Kottayam, Kerala
M.Sc.	Mathematics	2004	Cochin University of Science and Technology, Kochi, Kerala